Department of Civil, Environmental
and Geomatic Engineering
University College London

An experimental investigation of tsunami forces on coastal structures

Tristan Oliver Lloyd

Submitted in partial fulfilment of the requirements
for the degree of Doctor of Philosophy
at University College London

September 3, 2016

I, Tristan Oliver Lloyd confirm that the work presented in this thesis is my own. Where information has been derived from other sources, I confirm that this has been indicated in the thesis.

Signed: _____ Date: _____

Abstract

This thesis explores the complex fluid interactions between inundating long-period waves and buildings. Several aspects of these are found to be poorly described in the literature, particularly the flow conditions around, and forces applied to, emergent structures. Numerical models capable of reproducing the propagation phase of tsunami waves reliably are insufficiently detailed to capture the complex behaviour near structures. They also have no means of directly determining the force on a building, are agnostic to its presence and often lack reliable validation data. By critically reviewing the literature this thesis shows that experimental modelling to date has been confined to short-wave tests, commonly using paddle type wavemakers, which are not comparable to tsunami waves at scale. These experiments form the basis of many current design guidelines.

The loading imposed by long-period wave inundation on buildings is characterised through experimental modelling and development of a simple numerical model capable of predicting the force on a building. Large-scale testing with a novel pneumatic long-wave generator and complementary smaller-scale steady-flow experiments are carried out. The experiments are unique and examine onshore long-wave inundation loading on emergent bodies at wave periods never before tested in a laboratory. Significant differences between the loading regime of long- and short-period waves are observed in the experiments, demonstrating that short-period waves are insufficient models for tsunami inundation. The experiments to date also represent the only known database of long-period wave tests at scale which are representative of actual tsunami periods, so can provide an excellent validation resource for numerical models.

The numerical model presented within this thesis is novel because of its inclusion

of flow blocking and drag to estimate forces on buildings. It is firstly applied to steady experiments which are used to parameterise the drag inclusion, secondly to externally published unsteady bore/surge experiments and finally to a set of large-scale unsteady long-period wave experiments. Results of this very simple model show that it performs very well in all three situations examined in this thesis. Excellent estimations of measured full-body force on a blockage, as well as the flow conditions around it are achieved.

Acknowledgements

The research presented in this thesis was funded through an EPSRC Industrial Collaborative Studentships Award (CASE), and the industrial partner was Arup. I thank both of these organisations for their financial support over the course of this project.

I also give thanks for the industrial supervision from Ziggy Lubkowski at Arup. I thank my secondary supervisor Ian Eames for providing guidance on the interpretation of my experimental results, and William Allsop at HR Wallingford for his valuable advice at various stages throughout.

I acknowledge the many research colleagues who have been involved with my work in some way. In particular I thank Ingrid Charvet, Ioanna Ioannou and Tristan Robinson for their support over the years. Thanks to my family and those close to me for being understanding, and my friends for their subtle yet persistent "are you ever going to get a real job?" comments. They were greatly appreciated.

I would like to give thanks to my primary supervisor, Tiziana Rossetto for her continued support throughout the PhD. The delivery of this thesis, particularly after I commenced full-time employment, would've been very difficult without her drive, enthusiasm and occasional early morning meeting at the UCL café!

Finally the greatest thank you belongs to my wife Michelle. Your patience has been incredible over the years and I couldn't have finished this thesis without you. I have a lot to make up for...

Contents

List of Figures

List of Tables

Nomenclature

Δx the spatial resolution, page 40

η_0 the still water elevation, page 27

η the free-surface elevation relative to datum, page 27

λ a coefficient used by Qi et al. (2014) to relate up and downstream flow to force components, page 50

λ_{sf} the length scale factor, page 140

λ_w the wavelength, page 33

μ the dynamic viscosity, page 29

$\oslash$ the diameter, page 46

ϕ local blocking fraction, page 67

ρ the density of the fluid (sea water approximately 1200kgm^{-3}), page 29

$\boldsymbol{\sigma}_{\mathrm{T}}$ the total stress tensor, page 29

$\boldsymbol{\tau}_b$ the contribution due to bottom shear stresses, page 34

$\boldsymbol{\tau}_{\mathbf{D}}$ the deviatoric stress tensor which contains viscous stresses, page 42

θ is the beach slope, page 48

$\boldsymbol{\varepsilon}$ the residuals, page 76

A the horizontal diffusion coefficient, page 34

A_W the wetted frontal area of a body or building, page 46

$[\mathbf{A}]$ a time averaged image, page 205

a the amplitude of the wave, page 28

b the width of an element, page 39

C_H the hydrostatic coefficient, page 49

C_K an empirical constant accounting for hydrostatic and hydrodynamic components, page 92

C_L the transverse force coefficient, page 101

C_R the resistance coefficient, page 48

C_{a} the added mass coefficient, page 52

C_{m} the inertia coefficient, page 52

C_f the Chézy coefficient, page 36

C_{D0} the unbounded drag coefficient, page 46

C_{D} the drag coefficient, page 46

C_{df} the general form of friction coefficient inclusion, page 36

Co the Courant number, a ratio of physical wave velocity to computational signal transmission velocity, page 106

c_0 the celerity of the wave, page 28

D the still water depth, page 33

$\mathrm{d}S$ an element of a surface, page 43

F_L the transverse force, page 101

F_x the force in the direction of the flow, page 130

F_{Df} the friction drag force, page 45

F_{Dp} the pressure drag force, page 45

F_{D} the drag force, page 45

F_{H} the hydrostatic force, page 43

F_{T} the total force due to external stresses, page 42

Fr the Froude number, a ratio of inertial to gravitational forces, page 49

$\boldsymbol{f}_D$ a depth averaged resistive force per unit mass, page 67

f_s the sample frequency, page 156

f_{DW} the Darcy-Weisbach friction factor, page 36

g the acceleration due to gravity ($9.81\mathrm{ms}^{-2}$), page 30

H the specific energy, page 71

H_b height of the building, block or roughness element, page 40

$\hat{H}_d$ dimensionless specific energy, page 89

$\hat{h}$ dimensionless local water depth, page 72

h the total water height, page 27

h_1 is the total upstream water height, page 50

h_2 is the total downstream water height away from the block, page 70

h_c the critical depth, page 164

h_d is the total water height immediately downstream of the block, page 50

h_e the effective height, page 44

h_e the end depth, page 164

h_i initial reference water depth, page 79

$I(z)$ the light intensity at depth z, page 80

I_0 the light intensity at depth $z = 0$, page 80

I_t the turbulence intensity, page 46

$[\mathbf{I}]$ an image intensity matrix, page 212

$[\mathbf{I}_{\text{norm}}]$ the normalised intensity image, page 212

$\mathbf{I}$ the identity tensor, page 42

L a characteristic length, in the case of a building this is taken as the streamwise length, page 30

L_A the lever arm, page 78

l is the maximum horizontal run-up distance measured from the initial shoreline, page 48

M the sum of the specific momentum flux and hydrostatic force on a vertical plane, page 49

M_{a} the added mass, page 52

M_f the momentum flux in the x-direction, page 34

M_{D} the drag moment, page 76

M_{L} the transverse moment, page 76

M_{yy} the total moment about the y-axis from a force on the front face of a body, page 53

$\mathbf{M_T}$ the total moment on a body, page 53

N_f the momentum flux in the y-direction, page 34

$\hat{\mathbf{n}}$ a unit vector normal to the surface, page 43

n the Manning coefficient, page 36

p the pressure, page 30

Q the flow or volume flux, page 70

$\hat{Q}$ dimensionless flow, page 72

R the ground height at the maximum penetration of tsunami run-up, measured from the initial shoreline. Also sometimes known as the run-up, page 47

Re the Reynolds number, a ratio of inertial forces to viscous forces, page 30

S a control surface, page 43

T the wave period, page 20

t the time in seconds, page 28

$\bar{u}$ the mean flow velocity, page 44

$\mathbf{u}$ the velocity vector in 3D (u, v, w), or 2D (u, v), page 29

u the velocity in the x-direction, page 28

u_{RMS} the root-mean-squared of the velocity fluctuations, page 46

(u^2h) the momentum flux, page 47

V the volume, page 44

v the velocity in the y-direction, page 34

w the width of the channel, cell, or spacing between buildings, page 39

x the distance in metres, usually chosen positive in the direction of propagation or flow, page 28

z the ground height of the location of interest also measured from the initial shoreline, page 48

z_0 the datum, page 27

z_b the bed elevation, page 27

Chapter 1

Introduction, Literature Review, Aims and Objectives

1.1 Introduction

Tsunamis are long-period waves generated by the rapid displacement of a significant volume of water, most commonly due to the vertical movement of the sea floor associated with a large earthquake. Both aerial and submarine landslides as well as volcanic eruptions are also known to produce tsunamis. Additionally, models of impact by celestial bodies (Ward, 2000) along with supporting sediment records associated with the Cretaceous-Paleogene extinction boundary (Smit et al., 1996) and other large events, show asteroid impacts to be another generation mechanism. In the open ocean, tsunamis have very small amplitudes in comparison to their wavelength, but in shallower water they can shoal to tens of metres, causing inundation and the potential destruction of large areas of coast most recently seen in Japan (Chian et al., 2011), Chile (Lubkowski et al., 2010) and coastlines of the Indian Ocean (Rossetto et al., 2006). In the most extreme and infrequent cases, tsunami heights can exceed tens of metres depending on the source mechanism and specifics of the bathymetry. Typical periods, T, are between 5 and 90 minutes (Murty et al., 1977), depending on the source and its geometry.

Due to several source mechanisms, incomplete historical records and long time-scales

involved, quantifying the frequency of tsunamis is an extremely difficult exercise. Reliable recordings of offshore tsunami wave profiles have only become available over the last decade or so and these have been used to validate and improve numerical models. These profiles have mainly been recorded by the US National Oceanic and Atmospheric Administration (NOAA), who have deployed numerous Deep-ocean Assessment and Reporting of Tsunami (DART) buoys as part of the National Data Buoy Centre, discussed by Bernard et al. (2006). The high uncertainty associated with tsunami recurrence prediction has huge implications for the management of tsunami risk and engineered design options for coastal structures and mitigation. Furthermore, due to the low frequency of tsunami events, observational data for past tsunamis are scarce.

Current numerical simulations, while remarkably good at reproducing offshore wave signals, can have difficulty in the transitional near-shore region and are sometimes poor in the inundation zone without high resolution bathymetry data, the use of very complex numerical codes and extensive run times. Velocities cannot be measured reliably in post-tsunami surveys and where they exist are usually inferred from hydrodynamic force calculations of bent railings (Shimamoto et al., 1995) or differences in water level between the front and rear of a structure (Matsutomi and Okamoto, 2010). The validation of tsunami inland flows from models is therefore problematic. Recently, studies have emerged that use security video data obtained during the 2011 Great Eastern Japan (Tohoku) tsunami to estimate inundation velocities (Roh et al., 2012; Fritz et al., 2012) so that models can be validated more comprehensively. Greater detail and the trend towards more complex equations required for modelling interactions lead to more computationally expensive model runs which are still a problem even with today's rapid computing power increases. Additionally, the link between flow parameters and the force on structures is not yet clear.

The Indian Ocean Tsunami in 2004 had taken the majority of the world by surprise. Despite clear evidence of past large magnitude tsunamigenic earthquake events having occurred along the Sunda Trench (Newcomb and McCann, 1987), few were prepared for the level of devastation caused by the 2004 tsunami to coastlines bounding the Indian Ocean. However, the financial losses to the insurance industry were largely mitigated by low insurance penetration across the vast affected region, and there remained no demand for tsunami loss models. Some six years on the 2011

Great Eastern Japan Tsunami offshore of Tohoku surprised the scientific community, where the consensus was that a Mw9.0 earthquake could not occur on the Japan Trench. The resulting USD 35bn insured losses experienced (≈ USD 300bn economic loss) (Swiss Re, 2012), where 15-25% of those losses were due to tsunami (AIR, 2013), caused a change in perception across risk management sectors. The large reinsurance brokers, as well as all major catastrophe modelling firms began developing tsunami loss models as extensions to their earthquake loss models as a matter of urgency. Research on tsunami design increased at the same time.

Despite this activity there remains a deficiency in the understanding of tsunami impact and the processes in the near shore region, which means that the necessary tools to analyse adequately the vulnerability of coastal infrastructure are not presently in place. The level of risk analysis expected of more well-established natural hazard mitigation and risk analysis techniques is currently impossible, and ten years ago tsunami engineering stood where earthquake engineering was in 1971 (Synolakis and Bernard, 2006). Progressive research in earthquake engineering motivated by large earthquake events e.g. San Fernando 1971, caused wide changes to building codes in the United States and worldwide. A similar response is now occurring with tsunami engineering as happened in the 1970s for earthquake engineering, and many countries (United States (Bernard et al., 2006), Chile, Japan (Okada et al., 2005)) and smaller island nations are pro-actively incorporating tsunami hazard, risk assessment and evacuation measures into their urban planning policies. More rigorous design codes are developing in the form of FEMA (2012), and ASCE (2016) as well as others, yet tsunamis are still not considered across many susceptible regions (e.g. it is not considered by Eurocodes at the time of writing). Raby et al. (2015) provide a good discussion of recent design code efforts.

Fundamental to the production of design procedures is a thorough understanding of the forces and pressure distributions that are applied to structures during a tsunami inundation. For any design or engineering assessment this is essential knowledge without which calculations for the evaluation of the safety of structures cannot be carried out. Some design guidelines are available at present (described in Section 1.2), but there remain deficiencies and questions regarding the appropriateness of some of the formulations. As is demonstrated, much of the work underpinning existing guidance is based upon physical experiments of short-wave interactions, often at small-scale. Tsunamis are long-period waves, and as such have different

characteristics to those of shorter period waves.

The thesis presents a set of large-scale unsteady experiments of long-period wave inundations of a shoreline with instrumented structures installed. A complementary small-scale steady experimental study verifies a framework which describes the major processes for the unsteady tests. A simple but powerful numerical model capable of predicting forces on a structure is used to link offshore waves to actions on buildings onshore firstly on steady flows, and also for unsteady long-period wave interactions. This framework allows the prediction of time-dependent instantaneous forces on a structure from a small change to existing numerical models, and simple information about the geometry of the structure (or structures) obstructing the flow. There are important implications for this new research and many applications. The research presented in the thesis provides a contribution to the fields of coastal and structural engineering, the (re)insurance industry through the catastrophe models it uses, as well as organisations across the planning and disaster risk management sectors. It provides a validated means of force determination on a building from simple and computationally inexpensive numerical models of flows. Crucially, rather than simple estimation of the force from flow parameters not accounting for buildings, the flow conditions are themselves modified by the presence of the building. This research fills several identified gaps which are discussed in Section 1.2.6.

1.2 Literature review

Tsunami-structure interaction is a complex, multiphase and unsteady problem. In order to understand the physical processes which influence tsunami interactions with structures, it is important to build on an understanding of simpler cases. A concise outline of current literature regarding tsunami generation and propagation, inundating overland flows and interaction forces on bodies due to steady and unsteady fluid flow is presented. Throughout this chapter references are made to contributions from numerical and experimental studies, as well as building code guidance for tsunami load determination, with gaps identified. Building codes generally examine maxima for conservative design purposes, whereas academic studies tend to be more focussed on actual behaviour.

The purpose of this review is to formulate aims and objectives based on identified research gaps. As is later demonstrated, the estimation of loading patterns to structures which experience tsunamis is not currently well described, or in some cases correct. As such, a better representation of the flow around buildings is required, and the impact this flow has on structures in the path must be understood. The literature on tsunamis is varied and covers distinct areas. It is helpful to split the review into some of these sections, and a logical order to choose is the process of tsunami generation. The literature is therefore split as shown in Figure 1.1. Four distinct phases can be identified; (a) *generation*, (b) *propagation*, (c) *inundation* and (d) *interaction*, although there are clearly some overlaps. Many numerical models in particular account for more than one of these phases, however the discussion will make the distinctions where possible. The emphasis in relation to this thesis is on the inundation and interaction phases, and in part on the propagation phase also. Focus is not placed on the generation process, and only a brief discussion of the topic is included for completeness.

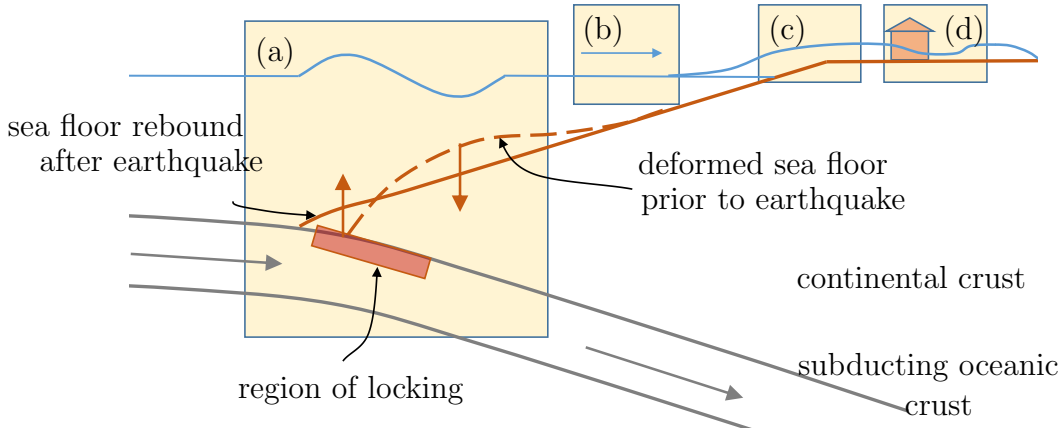

Figure 1.1: *(a) Generation, (b) propagation, (c) inundation, (d) interaction. The four phases discussed in this thesis in the context of a subduction zone mechanism.*

1.2.1 Generation

Tsunamigenic earthquakes occur most frequently on subduction zones, and as such tend to affect the regions near and around convergent plate boundaries. However, a subduction zone is not a requirement to form a tsunami. Any normal or reverse faulting earthquake mechanism which produces a large sea floor displacement, and

in turn sea surface deformation, has the potential to produce a tsunami. Due to the large fault interface areas and high characteristic slip rates, subduction zones tend to be responsible for the largest earthquake magnitudes in the world. In a subduction zone, the two sides of the fault can become locked, allowing the accumulation of strain energy over many years. This causes the plate overriding the fault to deform over time (see Figure 1.1), and when the fault finally ruptures, causing an earthquake, much of the deformation is recovered over a relatively short period of time (seconds). The resultant rapid motion of the sea floor often includes a large vertical component, which can cause an initial displacement of the water column above. With gravity as a restoring force this vertically displaced volume of water can initiate a tsunami.

Vertical motion in an earthquake source mechanism itself is not always necessary to generate a tsunami. In the case of sub-aerial and sub-marine landslides (sometimes described as sub-marine mass failures) local ground motion from an earthquake of any description can trigger unstable material on a slope to slide either into the sea, or under it. There have been several cases of relatively small earthquakes triggering large tsunamis, and the causes for these have been attributed to sub-marine landslides; e.g. 1946 Aleutian earthquake, (Fryer et al., 2004), 1998 Papua New Guinea (Synolakis et al., 2002; Tappin et al., 1999)), although it can be difficult to prove a landslide mechanism conclusively, making this sometimes a controversial topic.

Volcanic eruptions are historically another source of tsunamis. The exact mechanisms for tsunami generation in these cases are uncertain and complex, involving explosions, collapse of the volcanic cone into the magma chamber, atmospheric shock waves and in some cases the seismic movement of the sea floor (Pararas-Carayannis, 1992). Pararas-Carayannis (1992) discusses the famous caldera collapse of Santorini, in 1490BC, which the author describes as a series of progressive tsunami events and eruptions, preceding the assumed to be largest event associated with the caldera collapse. One of the largest volcanic tsunami events in recorded history is associated with the eruption of Krakatau, which is described by Nomanbhoy and Satake (1995), and again there is much speculation over the exact mechanism of tsunami generation in this case.

Significant research has been carried out on tsunami generation mechanisms, for

both earthquake (Okada, 1985; Geist, 1999), and landslide sources (Watts et al., 2003), which are generally for the purpose of initialising a numerical propagation model. Watts et al. (2003) include two slope failure mechanisms, and model an underwater slide as a rigid body moving along a straight incline subject to external forces from added mass and gravity. They also model an underwater slump as a rigid body rotating a small angle along a circular failure plane, subject to the same external forces as before, as well as the shear stress on the failure plain. Some propagation / inundation models also include a generation component, many of which are in part based on the surface deformation model of Okada (1985), which assumes an incompressible liquid layer on an underlying elastic half-space (a simplified mathematical representation of the Earth's crust) to characterise the ocean and the Earth's crust. These include TUNAMI-N2 (Imamura et al., 2006), Delft Dashboard and Delft3D-Flow (Deltares, 2014), MOST (based on the VTCS model (Titov and González, 1997; Titov and Synolakis, 1998)), and FUNWAVE (Kirby et al., 1998) which is used by Grilli et al. (2007) to initialise their 2004 Indian Ocean tsunami simulations.

Recent work of Goda and Song (2015) has demonstrated that the parameters (found by inversion analysis) of a very well studied event like Tohoku 2011 can vary enormously between authors in the geometry of the slip distribution, earthquake magnitude and fault parameters. Due to the huge variations found between different studies, Goda and Song (2015) stochastically simulated hundreds of artificial slip distributions based on the range reported in the literature, and used each of them to initialise a propagation model for the Tohoku event. Good agreement was found with the mean of the simulated events and recordings from offshore wave gauges, although large variances between different realisations of events could be seen either above or below the recorded value, highlighting the acute sensitivity of propagation models to initial conditions even when the source parameters are relatively well constrained.

Some of the generation methods used by researchers to represent these mechanisms in physical experiments of tsunamis are described further in Section 1.2.2, when discussing tsunami propagation modelling.

1.2.2 Propagation

At this point it makes sense to define a few elevation parameters, as there is abundant inconsistency across the literature regarding this. Figure 1.2 defines the terms relative to a datum as is used throughout this thesis.

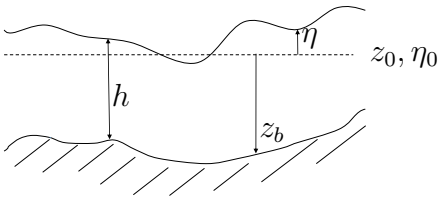

Figure 1.2: *Elevation terms in the shallow water equations. The datum, z_0, and still water elevation, η_0, are often set to be equal, although this is not always the case. The bed elevation is given by z_b.*

Here h is the total water height of the water column, η is the the free-surface elevation relative to datum.

Solitary waves, rightly or wrongly, have become synonymous with tsunamis in the context of physical modelling over the years and this research still very much underpins fledgling tsunami design codes where they exist. Madsen et al. (2008) are very critical of this assumption and there are a growing number of authors who agree with the assertion that they may not be appropriate (e.g. Constantin (2009); Goseberg et al. (2013)). Solitary waves are different to other types of water waves in that they do not have a trough, but are appealing because exact analytical solutions for their forms exist. The classic solitary wave shape was first identified as a separate and important physical phenomenon by John Scott Russell while conducting experiments on the Union Canal near Edinburgh in 1834. His experiments were designed to determine relationships between horse power and steam and the most efficient design for canal boats.

Russell (1845) describes further investigations into Solitary waves which he carried out over a period of several years. However, a theoretical explanation of Russell's observations would not be proposed until the 1870s with famous work by Boussinesq (1871) and Rayleigh (1876), leading to the development of the now classical KdV equations in Korteweg and deVries (1895). The KdV equation describes the motion

of a wave in one direction and is the basis of Cnoidal wave theory. The equation has the advantage of possessing only one unknown parameter, lending itself to analytical solutions. The version given by Miles (1980) is,

$$\frac{\mathrm{d}\eta}{\mathrm{d}t} + c_0 \left[\frac{\mathrm{d}\eta}{\mathrm{d}x} + \frac{3}{2}\left(\frac{\eta}{h}\right)\frac{\mathrm{d}\eta}{\mathrm{d}x} + \frac{1}{6}h^2\frac{\mathrm{d}^3\eta}{\mathrm{d}x^3} \right] = 0 \tag{1.1}$$

where h is the water depth, η is the free-surface elevation (relative to the still water level) and c_0 is the celerity. (1.1) admits solitary wave solutions travelling at velocity, u, for the position x at time, t, of the form,

$$\eta(x,t) = a\mathrm{sech}^2\left(\sqrt{\frac{3a}{4h^3}}(x-ut)\right), \tag{1.2}$$
$$u = c_0\left(1+\frac{a}{2h}\right)$$

The KdV equation solutions for solitary waves have amplitude, $a > 0$, and travel faster than c_0. Their speed increases with a.

There have been a variety of physical modelling methods utilised for generating solitary waves, though the majority of tests have used vertical paddle wave-makers (Maxworthy, 1976; Goring, 1979). In addition to the vertical paddle, Bukreev (1999) examined four further methods of solitary wave generation;

- by rapid removal and replacement of a baffle releasing a controlled volume of water into a flume.
- by an undular wave created by the complete removal of a baffle and cutting off the tail after the first crest by closure of a gate.
- by movement of a submerged body longitudinally along the flume, and
- by submerging a dense body into the end of a flume to displace the water

Thusyanthan and Madabhushi (2008) dropped a rectangular concrete block vertically into one end of a 4.5m long flume. This generated an inundating wave on a

sloping 1:9 bathymetry with a period around 1.5s and height approximately 0.1m. Gedik et al. (2005) used a sudden vertical displacement of a portion of the flume floor to generate waves in the form of a movable hinged flap, a technique similar to that of Hammack (1972) who used an elaborate vertical piston system to displace a portion of the flume floor upwards. In this case the displaced length of flume required to produce long-period waves would likely be prohibitive. Another method used by Lukkunaprasit et al. (2009b) involved releasing water from an elevated reservoir to create a solitary wave. All of these methods produce short-period solitary type waves, and due to instabilities created in the generation process, they often produce waves that are unstable when undergoing propagation through a long flume.

Much of the literature regarding wave propagation can be classified broadly as numerical modelling. Fundamental to all equations describing fluid motion are the principles of conservation of mass, conservation of momentum and in some cases conservation of energy. The principle of conservation of mass can be expressed as (1.3);

$$\frac{\partial \rho}{\partial t} + \nabla \cdot (\rho \mathbf{u}) = 0, \tag{1.3}$$

where $\mathbf{u}$ is the velocity vector, (u, v, w). If the fluid is assumed to be incompressible, the density of the fluid, ρ, is a constant, and (1.3) becomes (1.4).

$$\nabla \cdot \mathbf{u} = 0. \tag{1.4}$$

Conservation of linear momentum ($\rho\mathbf{u}$) for a continuum (Newton's Second Law) can be expressed as (1.5), which is known as the Cauchy momentum equation.

$$\rho \frac{D\mathbf{u}}{Dt} = \nabla \cdot \boldsymbol{\sigma}_{\mathrm{T}} + \mathbf{F}. \tag{1.5}$$

$\frac{D\mathbf{u}}{Dt}$ denotes the material derivative of $\mathbf{u}$, $(\frac{\partial \mathbf{u}}{\partial t} + \mathbf{u} \cdot \nabla \mathbf{u})$; $\boldsymbol{\sigma}_{\mathrm{T}}$ is the total stress tensor, later discussed in Section 1.2.5, and $\mathbf{F}$ represents the other body forces. For an incompressible Newtonian fluid where, μ is the dynamic viscosity, and by using a constitutive relationship for the shear stress, together with (1.4), the incompressible

Navier-Stokes Equations (NSE) (1.6) can be derived;

$$\rho\frac{D\mathbf{u}}{Dt} = -\nabla p + \mu\nabla^2\mathbf{u} + \rho\mathbf{g}, \tag{1.6}$$

where p is the pressure, $\mathbf{g}$ is the vector of acceleration due to gravity $(0, 0, -g)$, and $g \approx 9.81\text{ms}^{-2}$.

Commercial numerical packages exist to solve the NSE and are widely used to solve fluid problems in engineering. The collective name for this field is *Computational Fluid Dynamics* (CFD). CFD effectively takes the continuous partial differential NSE, and discretises the fluid domain into a number of smaller cells, or control volumes. The equations are then transformed into a discrete form often by the Finite Volume Method (FV), but also by Finite Element (FE), Finite Difference (FD), Discontinuous Galerkin (DG) (Bassi and Rebay, 1997) and Spectral Element (SE) (Patera, 1984) which can be solved by a number of different schemes. Usually the smaller the cells and time steps, the more reliable the solution, but this is not always the case and CFD is a complex field in its own right. Other Lagrangian mesh-free methods like Smoothed Particle Hydrodynamics (SPH) (Gingold and Monaghan, 1977) are also becoming more popular. Energy conservation can be incorporated as well as transport of other quantities and reactive flows. It is worth gaining a brief insight into the levels of CFD that are in general use today.

Starting at the top, *Direct Numerical Simulation* (DNS) is the most comprehensive method of solving the NSE, but is generally infeasible for all but the simplest test cases at very low Reynolds numbers ($Re = \rho uL/\mu$, where L is a characteristic length), even with today's rapidly increasing computing power. DNS simulates (as opposed to models) the turbulence in flows directly for all length-scales of turbulence, and hence requires an extremely fine grid to capture the effects of the very smallest eddies. The first level of reduced complexity CFD after DNS is *Large Eddy Simulation* (LES), which assumes that the most important turbulent transport processes arise from the large to medium size eddies and directly resolves these in the same way as DNS. It then filters out and models the smaller sub-grid scale eddies with a simpler two parameter model. Both DNS and LES are unsuitable for simulation of tsunamis at present and are likely to be for some time due to the computational overheads.

Mesh-free methods like SPH divide up the fluid into particles rather than a topological grid, and as such can have several advantages over grid based techniques. For example conservation of mass achieved by definition, as the mass of the system is represented by the particles themselves and due to the lack of topological connectivity, it is very suitable for dealing with large deformations. Tracking boundaries is natural in a mesh-free method so no special treatment of moving shorelines is needed. Special interpolating functions known as kernels are used to approximate dependent variables and their spatial derivatives from the individual particles. However, in order to produce high resolution results the number of particles required can be very large leading to increased computational cost.

A common way of solving the NSE which was pioneered in the days of far less powerful computers is by using *Reynolds-Averaged Navier-Stokes* (RANS) techniques. Again, the computational difficulty of incorporating turbulence into the simulation without making the computational expense too high is the motivation behind this methodology. RANS splits the velocity into a time-averaged, and fluctuating component $u = \bar{u} + u'$. The process of time-averaging the NSE, produces an additional term. This additional term gives rise to a closure problem, i.e. more unknowns than equations, and is known as the "Reynolds stress". The Reynolds stress can be modelled by one of several turbulence models which all have their advantages and disadvantages relating to their specific application. A discussion of turbulence models is beyond the remit of this thesis. While still fairly computationally expensive, RANS models have become practical for use on desktop computers of very reasonable specifications.

However, to model a tsunami inundation at very local scale (around a few buildings, say) currently requires the use of large computing clusters and up to a day of computation time. Examples of this are limited; Hsiao and Lin (2010) used a RANS model (COrnell BReaking And Structure (COBRAS)) to examine the run-up on a sloping bathymetry and over-topping of a breakwater. Fujima et al. (2002) and Sitanggang (2008) couple a detailed 3D RANS model to a 2D regional model and achieved good results in the specific area around the structure analysed. This still required significant computational effort to produce results for the single location meaning it is still impractical for regional, national or even city level analyses. Application to catastrophe models, where thousands of stochastic scenario events must be analysed for portfolios of hundreds of thousands of buildings for example, is totally infeasible

at present.

If one is comfortable ignoring the vertical velocity component, (assuming it is small in comparison to the horizontal motion and forces), it is possible to switch from 3D models to less demanding 2D models. By assuming an inviscid fluid, the frictional term ($\mu\nabla^2\mathbf{u}$) is ignored in the NSE, yielding the incompressible version of the Euler equations (1.7).

$$\rho\frac{D\mathbf{u}}{Dt} = -\nabla p + \rho g \tag{1.7}$$

From the Euler equations, an important approximation first made by Boussinesq (1872) is valid for the description of long weakly non-linear waves. Derived in response to the observations of Russell (1845) described earlier, the Boussinesq approximation assumes depth-averaged velocities, and thereby removes the vertical coordinate by performing a Taylor series expansion of the horizontal and vertical velocities at a certain depth, and truncating the series at a finite order (often truncated at quadratic terms). Irrotationality ($\nabla \times \mathbf{u} = 0$) and incompressibility (1.4) are used to derive a set of equations more generally known as Boussinesq-type equations. This is done by replacing terms in the Taylor expansion involving vertical partial derivatives, with equivalent terms involving horizontal partial derivatives. There is no unique Boussinesq equation - there are a great number of variations on the original equations given by Boussinesq (1872) found in the literature, most of which simply use the name "Boussinesq equations". A significant number of these authors eliminate the vertical coordinate by transforming the equations in terms of depth-averaged velocities or mass/volume fluxes (Peregrine, 1967; Madsen and Sørensen, 1992).

Conventional Boussinesq equations of the type found in Peregrine (1967) have certain limitations in terms of frequency dispersion in intermediate depths and limitations to the largest wave height that can be modelled due to the weakly non-linear assumption (Lynett et al., 2002). Improvements to the dispersive properties of the classical Boussinesq model have been made by Madsen and Sørensen (1992), who achieved this by modifying the dispersive terms, and by Nwogu (1993) who evaluated a reference velocity at a specific depth ($0.531H$) based on an optimum agreement with the linear dispersion relation (PIANC, 2010).

An example of the conventional Boussinesq-type equations as utilised by Peregrine (1967) is given below in (1.8) and (1.9);

$$\frac{\partial \eta}{\partial t} + \nabla \cdot [(D+\eta)\,\bar{\mathbf{u}}] = \quad 0 \tag{1.8}$$

$$\frac{\partial \bar{\mathbf{u}}}{\partial t} + (\bar{\mathbf{u}} \cdot \nabla)\,\bar{\mathbf{u}} + \nabla \eta = \quad \frac{1}{2} D \frac{\partial}{\partial t} \nabla \left[\nabla \cdot (D\bar{\mathbf{u}})\right] - \frac{1}{6} D^2 \frac{\partial}{\partial t} \nabla \left(\nabla \cdot \bar{\mathbf{u}}\right) \tag{1.9}$$

In this formulation D is the still water depth, (where $D = -z_b$ in Figure 1.2 assuming $z_0 = \eta_0$), and the mean, or depth-averaged velocity $\bar{\mathbf{u}}$ and free-surface elevation, η, are the dependent variables. The Boussinesq equations are often alternatively formulated in terms of total depth, h, and z_b, where $h = \eta - z_b$. The Boussinesq assumption retains some of the vertical structure, i.e. assumes a profile of velocity (usually at most quadratic in z, but this has been extended to higher order approximations for use in deeper water by Wei and Kirby (1995) and others). The resulting Boussinesq type equations derived using this technique are frequency dispersive and are often used to model tsunamis (Chen et al., 2000). Further improvements to the linear dispersion properties of Boussinesq models have been made by Madsen et al. (1991), Madsen and Sørensen (1992), Nwogu (1993).

As tsunamis of wavelength λ_w are said to be well approximated by "long-waves" ($\lambda_w \geq 20h$), several numerical models devised for tsunami use *shallow water theory*. Shallow water equations (SWE) are another common approximation used for the simplification of the equations of motion, and under these assumed "shallow-water" conditions, conservation of mass implies that the vertical acceleration will be small within the water column. Also the momentum equation implies that the horizontal velocity field will be almost constant throughout the water column. This allows the vertical velocity to be completely removed from the NSE by vertical integration and by applying boundary conditions, and is essentially how the shallow water equations are derived. The SWE are non-dispersive and as such SWE models do not produce equivalent results to Boussinesq-type models, especially in deeper water. It should be noted that generally tsunami waves far exceed the shallow water criterion in terms of λ_w or T.

This SWE approximation assumes a hydrostatic pressure distribution ($\frac{\partial p}{\partial z} = -\rho g$) and the resulting governing non-linear shallow water (NLSW) equations are some-

times written in the following form (PIANC, 2010);

$$\frac{\partial \eta}{\partial t} + \frac{\partial M_f}{\partial x} + \frac{\partial N_f}{\partial y} = 0 \tag{1.10}$$

$$\frac{\partial M_f}{\partial t} + \frac{\partial}{\partial x}\left(\frac{M_f^2}{h}\right) + \frac{\partial}{\partial y}\left(\frac{M_f N_f}{h}\right) = -gh\frac{\partial \eta}{\partial x} + A\left(\frac{\partial^2 M_f}{\partial x^2} + \frac{\partial^2 M_f}{\partial y^2}\right) - \frac{\tau_{bx}}{h} \tag{1.11}$$

$$\frac{\partial N_f}{\partial t} + \frac{\partial}{\partial x}\left(\frac{M_f N_f}{h}\right) + \frac{\partial}{\partial y}\left(\frac{N_f^2}{h}\right) = -gh\frac{\partial \eta}{\partial y} + A\left(\frac{\partial^2 N_f}{\partial x^2} + \frac{\partial^2 N_f}{\partial y^2}\right) - \frac{\tau_{by}}{h} \tag{1.12}$$

where $M_f = \int_{-z_b}^{\eta} u \mathrm{d}z$ and $N_f = \int_{-z_b}^{\eta} v \mathrm{d}z$ are the momentum fluxes in the horizontal x and y directions, respectively (v is the velocity in the y-direction). Other variables are $\boldsymbol{\tau}_b = (\tau_{bx}, \tau_{by})$, the contribution due to bottom shear stresses, and A, the horizontal diffusion coefficient. Many variants of the SWE exist in the literature, and most modifications are made to the momentum equations (1.11, 1.12) to exclude or include certain terms. (1.10:1.12) are often written in terms of total depth, h, and bed elevation, z_b which can be achieved by substituting for $\eta = h + z_b$. The time derivative of z_b is then zero in (1.10), so the mass equation still has three terms, while the momentum equations gain a term each. Generally the non-linear terms in (1.11) and (1.12) can be neglected in water over 50m deep, giving rise to the linear form of the shallow water equations (LSW). Many numerical codes automatically switch between NLSW and LSW as required to reduce computational cost, and some transform (1.10:1.12) into spherical coordinate for modelling whole ocean basins.

There are examples of hybrid simulations using coupled domains, with differing types of models used for solving each. Sitanggang and Lynett (2010) used a Boussinesq model offshore and RANS for the nearshore and interaction domain which they applied to over-topping of a breakwater. There are issues when two different types of model are coupled which Sitanggang and Lynett (2010) discuss. In general the exchange of data between two different types of model cannot be done because of differing assumptions, e.g. Boussinesq inviscid and irrotational, whereas RANS is both viscous and rotational and includes turbulence. These issues can be avoided if the interface between the domains is chosen where these effects are small enough that they can be neglected, i.e., in the non-breaking zone and if the wave satisfies

assumptions in the Boussinesq model. Other such coupled hybrid simulations are possible.

1.2.3 Inundation

Much of this topic could be presented in the previous section as many propagation models are also used for inundation purposes. However, the distinction made here is the importance of roughness inclusion. As the water depth decreases, the influence of bed roughness increases, so equations of the type (1.8:1.9) or (1.10:1.12) must include a friction term as a minimum requirement. Additionally, the ability to account for wetting and drying of cells in the model is usually required, as well as variations in topography. The literature in this space until recently had been dominated by fluvial flood modelling procedures for flood plains, but generally speaking the same equations (give or take a few terms) are solved in tsunami models, which are as discussed in Section 1.2.2. Often the equations of choice are the SWE, either in their linear or non-linear form, with or without diffusion terms, and almost always without Coriolis terms included.

The availability of remote sensing data, e.g. LiDAR, and the increase in computing power has driven the development of a range of 2D models which discretise the floodplain into fine resolution grids where the mass and momentum are calculated at each time-step. Hubbard and Dodd (2002) presented one such 2D model which was benchmarked against several 2D (and 1D) experiments. The purpose of the model was to capture wave run-up and over-topping of seawalls, so wetting and drying of cells was a problem the authors addressed by continuously tracking the shoreline. Dimensionless terms in the NSWE were formulated in order to allow the equations to capture shocks without causing instabilities. Hunter et al. (2005) presented a model which included diffusion and Bates et al. (2010) compared their inertial formulation against it favourably, but with the benefit of a large increase in the required time-step allowing faster run times.

Friction in these cases was included by assigning a Manning roughness parameterisation of the bed shear stress of the form

$$\boldsymbol{\tau}_b = \frac{\rho g n^2}{h^{1/3}} \boldsymbol{u}|\boldsymbol{u}|, \tag{1.13}$$

where n is the Manning coefficient. The form of this equation is based on a turbulent drag with a hydraulic diameter of h. The value of n is chosen to represent different forms of resistance, such as vegetation, trees, etc. See Chow (1959) for typical values based on open channel flow. Typically $0.025 < n \leq 0.045$ sm$^{-1/3}$, although for smooth man-made channels this can be as low as 0.001sm$^{-1/3}$. Other methods of including friction are by the Chézy equation which uses the Chézy coefficient, C_f, and the Darcy-Weisbach equation, which uses the Darcy-Weisbach friction factor, f_{DW}. Essentially all of these approaches assume that friction follows the form of

$$\boldsymbol{\tau}_b = \rho C_{df} \boldsymbol{u}|\boldsymbol{u}|, \tag{1.14}$$

where $C_{df} = \frac{gn^2}{h^{1/3}}$ in the Manning equation, $C_{df} = \frac{g}{C_f^2}$ in the Chézy equation and the $C_{df} = \frac{f_{DW}}{8}$ in the Darcy-Weisbach equation. There is an assumption of micro-roughness elements generating horizontal shear layers from the bed, where the depth of water is assumed to exceed the height of the roughness elements by perhaps an order of magnitude or more. Physically, the frictional shearing on a bed produces horizontal vorticity. As such formulations of the type (1.14) are appropriate for modelling bed friction within the NSWE.

Overall, the overwhelming majority of near-shore experimental studies of solitary waves, bores and surges, have tended to focus on surface profiles and run-up measurement (Rossetto et al., 2011; Charvet, 2012; Charvet et al., 2013). Hall and Watts (1953) were the first to study experimentally a single long-period wave approaching a sloping (1:1) beach and the waves they generated in the laboratory resembled those described by Russell (1845). The outcome of their experiments showed run-up R and offshore wave amplitude a, when normalised by offshore still water depth D followed a trend such that $\frac{R}{D} = \alpha(\beta)(\frac{a}{D})^{f(\beta)}$ (cited Synolakis and Bernard (2006)) where $\alpha(\beta)$ and $f(\beta)$ are empirical coefficients dependent on the gradient of the bathymetry. Other researchers over the following years extended this research (Camfield and Street (1969), Pedersen and Gjevik (1983)). Synolakis (1987) examined the run-up of solitary waves in work he carried out for his PhD thesis. Synolakis proposed his own run-up law (1.15) which fits with the data from Pedersen and Gjevik (1983) and Hall and Watts (1953).

$$\frac{R}{D} = 2.831(cot\beta)^{\frac{1}{2}} \left(\frac{a}{D}\right)^{\frac{5}{4}}. \tag{1.15}$$

Tadepalli and Synolakis (1994) investigated the run-up of so called N-waves, which are mathematical trough led forms of solitary waves.

Many of these run-up experiments and laws have been proposed as benchmark results for validating numerical codes for modelling tsunamis (Synolakis et al., 2007, 2008). This is despite the underpinning experimental studies being carried out using short-waves. An example of such numerical validations using (1.15) are Borthwick et al. (2006), who used the Boussinesq equations of Madsen et al. (1991) to compare run-ups to a set of experimental run-up measurements. More recently Schimmels et al. (2016) in a response to Rossetto et al. (2011) use the Großer Wellenkanal (GWK) 300m facility at the very limit of its operating parameters to produce long-period waves comparable to tsunamis at approximately 1:100 scale, but acknowledge that further challenges need to be overcome to reliably recreate inundating waves of periods comparable to tsunamis with paddle generators. They highlight very clearly why short-period solitary waves are not representative of tsunami by plotting measured Tohoku and Indian Ocean tsunami water surface traces with equivalent solitary wave profiles, which are dwarfed by the measured data in both cases.

1.2.4 Interaction

Modelling inundation over terrain with variable roughness has been addressed by several researchers, and standard commercial and academic codes generally perform well. Interaction could be thought of as a special case of the inundation phase, and as such has much overlap with the previous section. However, the distinction which is made regarding the specific effects that buildings have on the flow, and how this cannot be adequately captured by the physics contained in the models discussed thus far. In Section 1.2.3 the only forms of resistance appearing in source terms are generally the bed slope terms, and bed friction. Both of these have been utilised in the past by authors in order to try and account for the presence of buildings which partially obstruct the flow. One of the most interesting modelling approaches was developed by Park et al. (2013) that describes buildings as steep sided topography. Vertical walls cause difficulties with instabilities in the model so a maximum gradient is set at $2:1$ (63 degrees).

The most widely applied technique found is to model the building as an ‘equivalent

roughness'. More specifically an increased ground drag through the Manning parameterisation of drag where the base shear stress is described as (1.13). Park et al. (2014) compared the outcome from ComMIT/MOST, ADCIRC (Luettich and Westerink, 2004) and Coulwave (Lynett et al., 2002) by generating initial conditions for a hypothetical tsunami event offshore of Oregon using MOST to generate boundary conditions for the other models. MOST uses a Manning coefficient while ADCIRC and Coulwave use a Chézy friction coefficient C_f. They tested ComMIT with $n = 0.02, 0.03, 0.04$ sm$^{-1/3}$ and $C_f = 0.005, 0.010, 0.015$ m$^{1/2}$s^{-1} for Coulwave and ADCIRC. Park et al. (2014) concluded that the type of model (NLSW F-D, SWE F-E, Boussinesq) had a significant influence on water height related quantities, whereas the method of friction inclusion had the largest effect of velocities and momentum flux.

Huang et al. (2014) calibrated equivalent Manning's coefficient to sets of experiments on flow past a group of surface-piercing obstacles using a regression. The results show a reduction in water level in line with experiments on average over the whole flow domain, but water levels within the urban area are poorly predicted. The momentum loss effects appear to be too weak at the front line of buildings and so can only correctly predict the water level after the flow is past the whole urban region. Koshimura et al. (2009) uses (1.16), originally proposed by Aburaya and Imamura (2002), to apply a flow resistance in residential areas using an equivalent Manning coefficient given by

$$n^2 = n_0^2 + \frac{C_D}{2gL}\frac{\theta}{1-\theta}h^{4/3}, \tag{1.16}$$

where θ is the fraction of the flow occupied by buildings. In regions where there are no buildings, $C_D = 0$; otherwise dominates when $h \sim n_0^{3/2}(2gL/C_D)^{3/4}$. In this case,

$$\boldsymbol{\tau}_b \sim \rho\frac{C_D}{2L}h\frac{\theta}{1-\theta}\boldsymbol{u}|\boldsymbol{u}|, \tag{1.17}$$

and behaves the same as a distributed drag term. Kaiser et al. (2011) compare models of buildings as elevations, with the results of an equivalent increased roughness parameter. The authors also examined the mitigation effects of mangroves in a similar roughness approach, finding them significant in the reduction of flow velocities. They found large differences between the buildings-as-elevations and buildings-as-

roughness approaches for urban areas ($n = 0.08$), but closer agreement when the buildings were instead explicitly modelled with $n = 0.4$ and the streets $n = 0.031$. A useful table of Manning's n used for many land use classifications is given in this publication, with their individual source.

Several authors have included blocking effects in the NLSW equations in order to account for the presence of buildings. Key to this is the distinction between areal porosity, which is the fraction of a horizontal plane in a control volume (CV) free for water, and linear porosity, which is the fraction of a horizontal line of a CV's cell interface free for water to flow.

Chen et al. (2012a,b) use the complement of areal and linear porosity and introduce building coverage ratio (BCR) and anisotropic conveyance reduction factors (CRF) respectively. BCR is the proportion of a cell covered by buildings and CRF is effectively the blockage ratio of the cell boundary (b/w, where w is the width of the cell) and b is the width of a blocking element. Guinot (2012) defined multiple porosity models first assuming building areas contain no water, and defined isotropic porosity for regions of mobile and stagnant water. A mass-exchange term was introduced between the stagnant and mobile cells. Various anisotropic porosity models were later proposed by Guinot (2012) in order to account for directionality in street networks.

Liang et al. (2007) compared 2D SWE models using high Manning's number ($n = 5$) for buildings, and a porosity value, as well as as solid blocks (accounting for buildings by increasing the digital terrain model (DTM) to 1m above the flat surface). The study examined a hypothetical dam-break scenario of a 20m breach in a dyke, retaining a reservoir of 2m of impounded water. The resulting wave then impacted a 10m x 10m building located approximately 100m downstream. The authors noted that the maximum water depth in the building roughness model actually occurred inside the building for low values of n, and that there is a difficulty in assigning an appropriate roughness value highlighting a limitation of the methodology. The porosity model was used to account for some of the storage inside the buildings.

Bruwier et al. (2015) tested five models; two higher resolution (Δx =1m, 5m) classical SWE, and three lower resolution (Δx =10m) models, a SWE with calibrated roughness (Huang et al., 2014), SWE porosity and a SWE porosity with drag as $0.5 C_D A_w$, which is applied within the friction term. The results show that surface

levels and velocities are poorly represented in the urban areas using the calibrated roughness model. The inclusion of drag appears to improve the comparison with the 1m SWE model, which was used as a benchmark.

The distributed drag modelling approach is applied over the water column (of height, h), though it can be applied to a partial fraction of the water depth (for submerged buildings or vegetation). Distributed drag models have been applied to examine flow through emergent vegetation, but they are more widely known in the context of the interaction of atmospheric boundary layers with cities where the urban canopy is represented as a distributed drag force. For flows through emergent or submerged vegetation, a number of authors have used

$$\boldsymbol{f}_D \approx \frac{1}{2}\phi C_D \boldsymbol{u}|\boldsymbol{u}|b, \tag{1.18}$$

where b is the diameter of cylinder (representing the vegetation), C_D a nominal drag coefficient and ϕ is the volume fraction of vegetation. Here it is important to recognise that vegetation occupies a relatively low volume fraction (see Belcher et al. (2003) & Coceal and Belcher (2005)) and so blocking is much less significant as compared to buildings. Rosman and Hench (2011) use a two layer model for flow over coral reefs and find a wide range of C_D in the literature for this purpose, varying by as much as an order of magnitude. Their analysis shows C_D to be a function of canopy geometry and velocity profile, specifically the reference velocity chosen with respect to the roughness height.

A summary of some key literature reviewed and where they sit in terms of scales is given in Figure 1.3. H_b refers to the height of the building (or roughness element), h is the water depth, Δx is the spatial resolution, and L is the characteristic length of the buildings / roughness elements. To the left of the plot, studies using high spatial resolution models of flows around emergent buildings tend to be 3D RANS models or SPH. The significant computational expense due to the relatively high Re requiring fine meshes or many particles and small time-steps dictates that these studies tend to focus on single building or small groups. Studies which fall higher up on the plot are generally overland inundation models (without buildings) which use friction losses similar to (1.17) and the resolution of these models can vary widely from the examples shown. Large-scale regional tsunami models would tend to sit in the top right of the plot, and where buildings are included the study would fall

lower down the y-axis and slightly further to the left. This is where 2D modelling is appropriate, but drag is not generally resolved. The key separation here is between 3D simulations and SWE or Boussinesq type models. Side flow here refers to the situation where flow is forced to divert around a block.

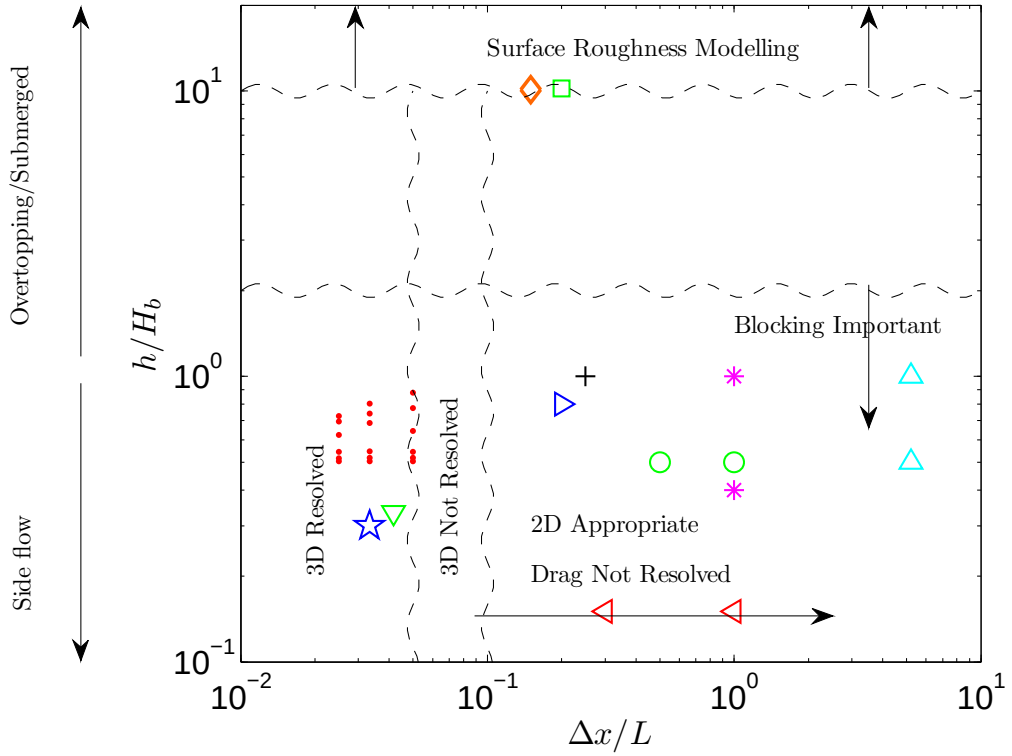

Figure 1.3: *Scatter plot summarising previous numerical analyses of inundation past obstructions and how they scale vertically and horizontally.* ○ *(Adriano et al., 2013),* ● *(Bahmanpour et al., 2015),* □ *(Bates et al., 2010),* ☆ *(Douglas and Nistor, 2015),* ∗ *(Gayer et al., 2010),* ◊ *(Hubbard and Dodd, 2002),* ◁ *(Kaiser et al., 2011),* ▷ *(Liang et al., 2007),* + *(Park et al., 2013),* △ *(Suppasri et al., 2011),* ▽ *(Wei et al., 2015). Arrows indicate increasing prevalence.*

There appears to be a gap in this kind of modelling, where drag is not resolved, but the computational expense of 3D modelling is too high to achieve this over large domains. By increasing the influence of various terms in the presence of buildings, momentum can be lost from the models, however there are fundamentally different processes occurring when flow blocking occurs. The vorticity created by a blocking object is vertical, which is at odds with a friction model which accounts for horizontal vorticity production. Blocking without drag inclusion gets us some of the way

to including the correct physics, but does not offer a means of applying a force to the oppose the flow, or an indication of what that force is. The scale and resolution is important also, and one can choose to model blocking from individual buildings ($\Delta x \leq L$) or potentially use lower resolutions ($\Delta x > L$) and account for blocking as an averaged property. The inclusion of drag by Bruwier et al. (2015) is relatively novel, and its basis is discussed in Section 1.2.5. However, the hydrodynamic drag is not the only component of force that acts on a blocking body subjected to unsteady flow, and the next part of this literature review addresses the situation under different flow conditions.

There are a number of design codes which are starting to emerge. Where relevant they are mentioned within the text in relation to the specific section to which they provide guidance. A summary of much of the design guidance can be found in Lloyd and Rossetto (2012) and Macabuag et al. (2014a), and many of the force component formulae are compiled in Appendix A.

1.2.5 Forces, moments and pressure distributions on bodies due to fluids

Any body immersed or partially immersed in fluid medium will be subject to stresses which act on every exposed surface of the body. These stresses acting on the surface cause forces per unit area, which are in addition to other body forces (like gravity) that act on the body regardless of the presence of a fluid medium.

The total stress $\boldsymbol{\sigma}_{\mathrm{T}}$, or force per unit area, acting on a body can be thought of as a combination of all inertial and viscous stresses acting on its surfaces. It can be expressed as

$$\boldsymbol{\sigma}_{\mathrm{T}} = p\mathbf{I} - \boldsymbol{\tau}_{\mathbf{D}}, \tag{1.19}$$

where $\mathbf{I}$, is the identity tensor, $p = \frac{1}{3}(\sigma_{xx}+\sigma_{yy}+\sigma_{zz})$, is the average pressure from the fluid and $\boldsymbol{\tau}$, is the deviatoric stress tensor which contains viscous stresses. It follows that the total force, F_{T}, on a body due to these external stresses is the integral of the stress distribution (1.19) over the surface of the body. This yields (1.20).

$$\mathbf{F}_{\mathrm{T}} = \int_S \boldsymbol{\sigma}_{\mathrm{T}} \cdot \hat{\mathbf{n}} \, \mathrm{d}S = \int_S (p\mathbf{I} - \boldsymbol{\tau}) \cdot \hat{\mathbf{n}} \, \mathrm{d}S \tag{1.20}$$

$\hat{\mathbf{n}}$ is a unit vector normal to the surface and $\mathrm{d}S$ is an element of the surface of the body. This is a useful formulation as it can be applied to every flow situation involving fluid-solid interactions that will be encountered in this thesis.

1.2.5.1 Forces on bodies due to fluids at rest

Forces arising from static fluids are known as *hydrostatic* forces. As the fluid is at rest, there are no velocity gradients, meaning there are no viscous stresses. For this reason, the only forces that can act on a fluid at rest in static equilibrium are: gravity acting on the fluid mass, pressure on the fluid volume, or other external forces (which are not relevant in this case, e.g. electromagnetic forces).

Assuming constant fluid density, the weight of a fluid above a point causes a pressure at that depth which varies only with immersed depth. The vertical pressure distribution in this case is triangular and can be found simply by multiplying ρg (unit weight) by the depth h. Where the water depths either side of a body are equal, there is no resultant hydrostatic force on the body. However, if the depth varies around the body or the body contains voids that do not contain fluid to the same depth as that outside the body, there will be a resultant force.

In an identical methodology to (1.20) the horizontal hydrostatic force can be found by integrating the hydrostatic pressure over the area of the body on which the pressure acts. As this is the only component of stress acting, (1.20) can be simplified. Additionally, for a flat vertical wall, the force due to the presence of static water on one side acting perpendicular to the surface is dependent only on the depth, h:

$$\begin{aligned} F_{\mathrm{H}} = \int_S p\mathbf{I} \cdot \hat{\mathbf{n}} \, \mathrm{d}S &= \rho g b \int_0^h h \, \mathrm{d}h \\ &= \frac{1}{2}\rho g b h^2, \end{aligned} \tag{1.21}$$

where b here is the width of element the fluid pressure acts on and the other side of the wall is dry and exposed to atmospheric pressure. S is a control surface. (1.21) is often quoted in terms of force per unit width of wall by dividing by b. The pressure distribution is triangular in shape, at a maximum at the bottom, at atmospheric pressure at the free-surface (zero relative to the bottom).

The formulation in (1.21) is abundant throughout coastal and draft tsunami design codes, and is valid when the wall is dry on one side. Modifications are made in some of the design codes to account for differential water levels on each side, which effectively change the pressure distributions. FEMA have a number of publications (FEMA, 2000, 2012) that specify hydrostatic forces, and all follow the form of (1.21). Some authors (CCH, 2000; IMPW, 2009; USNRC, 2009) attempt to account for the fact that water may not be static by adding an equivalent velocity head term to (1.21), by replacing h with an effective height, $h_e = h + \frac{u^2}{2g}$.

Another hydrostatic force acting on a body in a fluid at rest (and in moving fluid) is buoyancy. For an object immersed in fluid there is a vertical buoyancy force equal in magnitude to the weight of fluid it displaces, $\rho g V$, where V is the volume. If the weight of the surrounding fluid is greater than the overall weight of the object (including the air it may contain), a net buoyancy force will act on the object in a vertical direction causing it to rise in the fluid column. A list of vertical and horizontal hydrostatic force terms found in different design codes and literature can be found in Table A.1. However, it is worth mentioning the caveat that the force formulations in design codes almost exclusively relate to maxima, for conservative design reasons.

1.2.5.2 Forces on bodies due to steady uniform flow

In most cases, a structure obstructing a tsunami inundation flow will be an example of a bluff body (see Mallock (1907)). For this reason, the main focus remains on this particular case and not other forces, for example transverse oscillatory forces or lift. However, it is useful to start from the broader situation and narrow this focus down.

Let us firstly take the case of a viscous fluid moving with mean flow velocity, $\bar{u}$, past an immersed stationary body. As in 1.2.5, the contributions to total drag force F_{D} on the body can be split in to two distinct sources; those arising from tangential stresses at the body surface integrated over that surface (viscous forces) and those arising from normal stress (inertial forces) (Batchelor, 1967). The relative contribution of each of these types of stress are entirely a consequence of the shape of the body and its orientation with respect to the flow.

Objects for which the skin friction is overwhelmingly larger than the form drag, are called streamlined, while those for which the opposite is true are described as bluff (Tavoularis, 2002). In the case of the streamlined body there is minimal flow separation and the streamlines meet after the body with very little wake. The majority of the drag is caused by tangential stresses along the surface of the body which arise due to dominant viscous effects within the boundary layer. The force arising from these tangential stresses is entirely due to the internal shearing action of the fluid due to its viscosity and the *no-slip condition*, which states that at the solid boundary the fluid will have zero velocity relative to the body. As a result of its frictional nature this component of the total force is known as the *friction drag*.

The forces arising from normal stresses involves other components, but those relevant to our case are the *pressure drag* and *transverse oscillatory forces* (briefly discussed later). The others are *lift* and *induced drag* (a consequence of lift), but are not of concern here as body forms that would produce lift, i.e. aerofoils, are outside the remit of this thesis. The *pressure drag*, or "form drag", as it is sometimes known is very important for the case of a bluff body because it arises as a consequence of flow separation. In almost all cases in which flow takes place around a solid body, the boundary layer separates towards the rear of the body. Downstream of the separation position the flow is greatly disturbed by eddies, and this region of eddying motion is known as the wake. Vorticity generated at the surface of the body is convected away in the wake and as a result of the energy dissipated by the highly turbulent motion, the pressure is reduced producing a pressure-based drag on the body (Massey, 1970).

In both streamlined and bluff body cases, ignoring lift and associated induced drag, the total drag force, F_{D}, can be viewed as the sum of the friction and pressure drag, i.e. $F_{\mathrm{D}} = F_{\mathrm{Df}} + F_{\mathrm{Dp}}$. The calculation of *friction drag* and *pressure drag* is theoretically possible and the methodology is demonstrated by Douglas et al. (1995).

More commonly however, the total drag force is measured experimentally. For bluff bodies the F_{Df} component of F_{D} is negligible. F_{Df} on a streamlined body has much the same magnitude per unit surface area as a bluff body, but the F_{Dp} for a bluff body is significantly greater. Hence, bluff bodies are dominated by pressure drag and produce more total drag than streamlined bodies. For these reasons it is commonly assumed that $F_{\mathrm{Dp}} \approx F_{\mathrm{D}}$ for bluff bodies and the F_{Dp} and F_{Df} are both

taken into account by the drag coefficient, C_{D}, which is determined experimentally by measuring F_{Dp} and the mean velocity of the flow, $\bar{u}$.

$$F_{\mathrm{D}} = \frac{1}{2} C_{\mathrm{D}} \rho \bar{u}^2 A_W \tag{1.22}$$

C_{D} can be found by rearranging (1.22), in order obtain $C_D = F_{\mathrm{D}}/\frac{1}{2}\rho\bar{u}^2 A_W$, where A_W is the frontal area of the body. This drag coefficient is dimensionless. In the case of a bluff body where the separation point generally occurs at the same place, (i.e. at the sharp edges of the area perpendicular to the flow), C_{D} remains relatively constant, and drag crisis (where the C_D suddenly drops of with increasing Re because of a transition to a narrow turbulent wake) is not generally likely to occur. This is true regardless of Re, for all but the very lowest Re numbers (i.e. $Re < 100$) (Massey, 1970).

The drag coefficients given in Table 1.1 and those present in much of the literature are averages and relate to unbounded flows, i.e., far away from the influence of other blockages and minimal turbulence. In the definition of projected areas, $\oslash$ refers to the diameter and other terms have their usual meaning. These unbounded drag coefficients are referred to as C_{D0}. They also in fact relate to submerged flows, so are not entirely compatible with our surface piercing emergent case, but are close. These drag coefficients are approximately constant, but in reality do vary and are dependent on flow conditions. Key factors that influence the drag coefficients which are relevant to this work are turbulence as well as blockage ratio. Higher blockage ratio (lower proportion of area for a fluid to flow through) leads to an increase in the effective drag coefficients seen. The Reynolds number of the flow and the turbulence intensity ($I_t = u_{RMS}/\bar{u}$) also influence the values of drag coefficients, where more turbulent conditions tend to lead to a reduction in drag coefficient (Lee, 1975; Tamura and Miyagi, 1999). For square cylinders and $I_t = 5\%$, C_{D0} drops from 2.1 to 1.9. This is an important consideration for the work carried out in Chapter 2. The C_{D0} in Table 1.1 can be considered valid for the range $10^3 \lesssim Re \lesssim 10^6$. In all the experiments discussed in this thesis, Re was within this range.

In an unbounded flow at high Reynolds number, given a mean velocity, $\bar{u}$, a volume flux downstream is generated by the drag on the block of $C_{D0} b \bar{u}$. When the flow is partially blocked, the average flow outside the wake increases by $\bar{u} + C_{D0}\bar{u}b/w$. The block will therefore see an average of the flow upstream, $\bar{u}$, and the downstream

Table 1.1: *Drag coefficient (unbounded), C_{D0}. Values taken from OCDI (2002).*

Shape	Projected area	Drag coefficient, C_{D0}
Circular cylinder	$\oslash h$	$1.0 (h > \oslash)$
Rectangular prism	bh	$2.0 (h > b)$
Circular disk	$\frac{\pi}{4}\oslash^2$	1.2
Flat plate	bh	$h/b = 1 \rightarrow 1.12$
		$h/b = \infty \rightarrow 2.01$
Sphere	$\frac{\pi}{4}\oslash^2$	$0.2 \sim 0.5$
Cube	b^2	$1.3 \sim 1.6$

flow giving a mean velocity of $\bar{u}(1 + C_{D0}b/2w)$. The flow creates a drag force on the block of $\frac{1}{2}C_{D0}b\bar{u}^2(1 + C_{D0}b/2w)^2$, with an equivalent drag coefficient

$$C_D = C_{D0}(1 + C_{D0}b/2w)^2. \tag{1.23}$$

In a design context, drag coefficients are always quoted as unbounded, i.e. (1.23) is not applied. The presence of adjacent buildings on the value of C_D chosen is not therefore accounted for. While this is not important for widely spaced buildings, for densely built urban areas, the drag force could potentially be significantly underestimated.

Hydrodynamic forces are dealt with from a design perspective again in terms of maxima, but there are some variations in the formulations. In this literature review no guidelines are found to include blocking effects. FEMA (2000) is split into two cases: velocities below 10ft/sec ($3.05ms^{-1}$), and those above 10ft/sec. For low velocities a velocity head term is computed and added to the design still-water depth, (effectively, h), so the method is consistent with CCH (2000) discussed earlier. For greater velocities, the formulation is aligned with (1.22). FEMA (2012) uses the maximum momentum flux, so rather than computing $h_{\max}$, and $u^2_{\max}$ (which may not occur simultaneously), $(u^2h)_{\max}$ is used in (1.22) instead. Yeh (2006) gives an empirical relationship for $(u^2h)_{\max}$ as

$$\left(u^2h\right)_{max} = gR^2\left(0.123 - 0.235\frac{z}{R} + 0.11\left(\frac{z}{R}\right)^2\right) \tag{1.24}$$

Here, R is the run-up, defined as the ground height at the maximum penetration

of tsunami, measured from the initial shoreline. However, in adopting (1.24) of Yeh (2006), the value of R used by FEMA (2012) is factored by 1.3 where R is derived from numerical simulations or available tsunami inundation maps. z represents the ground height of the location of interest also measured from the initial shoreline. FEMA (2012) recommend that for design $(hu^2)_{max}$ should not be taken as less than 80% of the value computed by (1.24) due to uncertainties in modelling tsunami inundation. (1.24) is based on laboratory data from short-period solitary wave run-up on a constant beach slope. (1.24) was derived from a fit of data plotted for $\frac{hu^2}{g\theta^2 l^2}$ against x/l. The resulting curve was:

$$\frac{u^2 h}{g\theta^2 l^2} = 0.11\left(\frac{x}{l}\right)^2 + 0.015\left(\frac{x}{l}\right) \tag{1.25}$$

where θ is the beach slope, x is the distance from the maximum run-up location to the location of interest, and l is the maximum horizontal run-up distance measured from the initial shoreline. (1.25) was expressed in terms of ground elevations (1.24) so that it may be used on a beach of varying slope in FEMA (2012).

In relation to the work for a new tsunami loading chapter in ASCE 7-16 (ASCE, 2016), members of the Tsunami Loads and Effects Subcommittee published several conference papers detailing the recommendations that they made. One such part of their research is in relation to forces from bores. For hydrodynamic forces, Chock et al. (2011) use a similar expression to (1.22), but replace C_D with C_R, a resistance coefficient. In this case, C_R accounts for the transient condition of the initial water impact and momentary piling up of water in front of the object before a steady-state flow is eventually achieved with time.

In the cases discussed so far, assumptions are made that the fluid is deep and that there is an insignificant difference in fluid depth either side of the body. This is not true for a body submerged or partially submerged in moving shallow water. Where water depths are equal on different sides of a body, hydrostatic effects produce a zero resultant force on that body (although if there is an internal void and the internal space remains sealed and dry, the hydrostatic forces need to be evaluated on individual wall elements). However, where flow past a body causes the depth to vary, the interplay between hydrostatic and hydrodynamic force contributions is important and needs to be considered.

Qi et al. (2014) presented a steady framework which linked hydrodynamic and hydrostatic components of force which arise due to differences in water level at the front and rear of a block. The relative contribution of each component is a function of the upstream Froude number, $Fr_1 = u_1/(gh_1)^{1/2}$, and the blockage ratio, b/w. In terms of the forces on the block, Qi et al. (2014) integrated the steady Navier-Stokes (momentum) equation over the flow domain to produce (1.26).

$$\int_{S_B} (p\hat{\mathbf{n}} - \boldsymbol{\tau} \cdot \hat{\mathbf{n}}) \mathrm{d}S = -\int_{S_1+S_d} p\hat{\mathbf{n}} \mathrm{d}S - \rho \int_{S_1+S_d} (\mathbf{u} \cdot \hat{\mathbf{n}})\, \mathbf{u} \mathrm{d}S + \int_{S_1+S_d+S_W} \boldsymbol{\tau} \cdot \hat{\mathbf{n}} \mathrm{d}S \tag{1.26}$$

where, $\hat{\mathbf{n}}$, is the unit normal vector out of the fluid, p, is the pressure, and $\boldsymbol{\tau}$, is the viscous stress tensor. Subscripts of quantities indicate 1 for upstream, 2 for far downstream and d for immediately downstream. S_1, S_d are the control surfaces upstream and immediately downstream of the object, S_B is the wetted surface of the block and S_W is the wetted surface of the channel floor and walls. Taking only the direction parallel to the flow (drag), (1.26) becomes (1.27), consistent with the findings of Benjamin (1956). The final term of (1.26) is negligible as viscous stresses are weak, so,

$$\overline{F_\mathrm{D}} = \frac{1}{2}\rho g(h_1^2 - h_d^2)w + \rho(u_1^2 h_1 - u_d^2 h_d)w = \rho(M_1 - M_d), \tag{1.27}$$

where $M_i = \left(u_i^2 h_i + \frac{1}{2} g h_i^2\right) w$, is the sum of the specific momentum flux and hydrostatic force on a vertical plane. It follows that given an upstream state, Fr_1, it is desirable to determine the downstream state, Fr_2, and estimate the drag on the body. An empirical closure is necessary in order to estimate the flow state and provide an assumption about how energy or momentum is conserved across the throat of the flow. Fenton (2003, 2008) describe a momentum approach and use a mean drag force closure estimated using a summation of a hydrodynamic drag and a hydrostatic force term. Qi et al. (2014) use (1.28).

$$\overline{F_\mathrm{D}} = \frac{1}{2}\rho C_D b u^2 h + \frac{1}{2}\rho C_H b g(h_1^2 - h_d^2) \tag{1.28}$$

where C_H is the hydrostatic coefficient determined empirically. The form of this equation implies that for flow regimes that give a very small difference between

upstream h_1 and downstream h_d, the hydrostatic term is negligible as expected, and the drag component will dominate. At higher Fr where large water height differences can develop between the front and rear of a block, the hydrostatic component is larger although the drag component is also larger because of the u^2 dependency. It is possible to see how the force contributions depend on the state of the flow. As discussed earlier (see Table 1.1), there are a relative abundance of literature sources for drag coefficients, C_{D0}, for unbounded flow. C_D can be determined by (1.23) or by empirical data.

By parameterising $h = h_1$, $\bar{u} = Q/h_1 w$ and recasting (1.28) into a dimensionless form in terms of Fr_1 and Fr_d, Qi et al. (2014) were able to relate the state of downstream flow to the upstream flow as

$$\left(1 - \frac{C_H b}{w}\right) \frac{1}{2Fr_1^{4/3}} + \left(1 - \frac{C_D b}{2w}\right) Fr_1^{2/3} = \left(1 - \frac{C_H b}{w}\right) \frac{1}{2Fr_d^{4/3}} + Fr_d^{2/3}, \quad (1.29)$$

which can be solved for Fr_d as a function of Fr_1 by choosing suitable values for C_D and C_H, with a maximum value of Fr_{1c} at $\partial Fr_1/\partial Fr_d = 0$. Differentiating (1.29) gives

$$Fr_{dc} = \left(1 - \frac{C_H b}{w}\right)^{\frac{1}{2}}. \quad (1.30)$$

which means the downstream Froude number under choked conditions depends only on $C_H b/w$. The flow conditions further downstream are determined by conservation of momentum flux. A general expression for force combining both hydrostatic and drag components was determined based only on the conditions of the flow which Qi et al. (2014) expressed as (1.31), where λ is given by (1.32).

$$\overline{F_{\mathrm{D}}} = \lambda \rho b \frac{Q^{4/3} g^{1/3}}{w^{4/3}} = \lambda \rho b u_1^{4/3} g^{1/3} h_1^{4/3} \quad (1.31)$$

$$\lambda = \frac{1}{2} C_D Fr_1^{2/3} + \frac{1}{2} C_H \left(\frac{1}{Fr_1^{4/3}} - \frac{1}{Fr_d^{4/3}} \right) \quad (1.32)$$

The coefficients C_D and C_H are estimated experimentally from a set of tests covering four blockage ratios, 0.1, 0.2, 0.3 and 0.4. Q is the volume flux in m^3/s and.

1.2.5.3 Forces on bodies due to unsteady flow

In the literature the term unsteady flow can be used to mean different things. Generally the term signifies that something in the flow varies with time. One such example of unsteady behaviour is seen when the flow depth is unsteady in time, i.e. $\mathrm{d}h/\mathrm{d}t \neq 0$ as in the case of a flood, or a tsunami.

However in the "steady" example of section 1.2.5.2; the wake of a bluff body is also generally unsteady at all but the lowest Reynolds numbers. Two vortices are generated with opposite rotation in the wake of the body as the boundary layer separates symmetrically on either side. With increasing Reynolds number, these vortices become unstable and at a limiting Reynolds number one vortex will break free and move downstream. The departure of a large amount of vorticity from the region near the body affects the flow around the body causing the opposite eddy to grow larger and in turn shed. At a higher Reynolds number the shedding vortices form a regular *vortex street* downstream until the flow is increased further where the regular pattern is broken by a turbulent wake.

A consequence of the alternate shedding of vorticity is a periodic oscillation of the flow. In turn this causes a periodic force on the body in the direction perpendicular to the oncoming flow. A similar pattern can be expected for rectangular bodies and indeed, this type of vortex-induced loading is often a major design consideration for tall buildings subjected to wind loads. It can particularly be a problem when the frequency of the vortex shedding is close to one of the modal natural frequencies of the building, as this has potential to cause resonance. Davis et al. (1984) note that the presence of a confining wall, or blocking effects influence vortex shedding, as it increases the drag force.

Transverse forces from vortex shedding were detected in the experiments by Douglas and Nistor (2015), which are discussed further in later chapters of this thesis, but the RANS model with two-parameter ($k - \epsilon$) turbulence model Douglas and Nistor (2015) used to model the in-line force behaviour was unable to capture this transverse effect. In order to capture properly this effect a more detailed description of the turbulence is necessary and it is likely that accurate results would require LES modelling. Vortex shedding is an unsteady process, and this is because the velocity is unsteady in time. This means that: $\mathrm{d}u/\mathrm{d}t \neq 0$. A tsunami is unsteady in terms

of the velocity and the flow depth; it is potentially also unsteady in terms of fluid density.

An additional effect of unsteady flow around objects is the concept of *added mass* (Wakaba and Balachandar, 2007). In a physical sense the added mass is the extra mass added to a system due to the accelerating (or decelerating) body moving a volume of its surrounding fluid. This added mass force opposes the motion, so in the case of a fixed body with an accelerating flow, the force will act in the direction of the flow.

A well-known methodology used historically for describing unsteady fluid forces and widely for design of offshore structures is that of Morison et al. (1950). Morison's equation, as it is widely known, splits the loading into a viscous drag force related to the vortex-flow component of the flow, and also a component involving *added mass*, which is the inertia force associated with the irrotational flow component. Morison's equation for fixed bodies (1.33) is given as

$$F = \rho V C_{\mathrm{m}} \dot{u} + \frac{1}{2} C_{\mathrm{D}} \rho u^2 A, \tag{1.33}$$

where $C_{\mathrm{m}} = 1 + M_{\mathrm{a}}/\rho V$ is the inertia coefficient (see Table 1.2 for values), M_{a} is the added mass and $M_{\mathrm{a}}/\rho V$ represents the added mass coefficient, C_{a}.

The first term of (1.33) is a combination of the Froude-Krylov force, $\rho V \dot{u}$ and the added mass force, $\rho V \left(C_{\mathrm{m}} - 1\right) \dot{u}$, which together represent the inertia force. The Froude-Krylov force represents the integral of the wave pressure over the body surface, as if the body were not there, whereas the added mass force is due to the distortion of the fluid flow by the presence of the body.

Table 1.2: *Inertia coefficient, C_{m}. Values taken from OCDI (2002).*

Shape	Reference volume	Inertia coefficient, C_{m}
Circular cylinder	$\frac{\pi}{4} \oslash^2 h$	$2.0 (h > \oslash)$
Square based prism	$b^2 h$	$2.19 (h > b)$
Flat plate	$\frac{\pi}{4} a^2 b$	$a/b = 1 \rightarrow 0.61$
		$a/b = 2 \rightarrow 0.85$
		$a/b = \infty \rightarrow 1.0$
Sphere	$\frac{\pi}{6} \oslash^3$	1.5
Cube	b^3	1.67

1.2.5.4 Moments on bodies due to fluids

Whenever there is a variation in the forces acting over different parts of a body there is the potential to produce moments. Where the body is unfixed these moments will cause a rotation to occur without increasing internal stresses in the body. However, if a rotation occurs with a corresponding resistance to that rotation, the object will be forced to deform and this will cause an increase in internal stresses. Where this occurs it is known as bending and involves a combination of tension and compression within the material.

A moment is defined as the force multiplied by the distance between the point of application of the force to the origin where the moment is being calculated. Mathematically this is represented in vector form by a cross-product of the position vector (relative to the origin) and the force vector.

$$\mathbf{M_T} = \mathbf{x} \times \mathbf{F} \tag{1.34}$$

From (1.20), and by ignoring shear forces arising from viscous effects, this can be rewritten as (1.35):

$$\mathbf{M_T} = -\int_S p(\mathbf{x} \times \hat{\mathbf{n}}) \mathrm{d}S \tag{1.35}$$

Ramsden (1996) measured moments about the base of a vertical wall and estimated an upper bound based on hydrostatic loading. This essentially assumes a triangular pressure distribution and the point of action for the resulting force to be at $h/3$. From (1.21) and applying (1.34) it is possible to see that

$$M_{yy} = \frac{1}{6}\rho g b h^3. \tag{1.36}$$

It is observed that moments are not generally considered by any of the design codes, which is surprising. The rotations applied to buildings from flows can potentially be a source of failure and in the view of the author, have not been investigated in sufficient detail. Yeh et al. (2014) examined theoretical global structural overturning moments for a hypothetical four-story reinforced concrete structure. The authors calculated force time-histories based on video of flow conditions, which were used to parameterise ideal equations for hydrodynamic and buoyancy forces. Ultimately

the incorporation of these considerations into design codes would be desirable. In order to calculate moments and their effect on structures, the full range of force components that are discussed in this chapter must be considered, with an accurate representation of their position of application, or their distribution over a structure.

1.2.5.5 Summary of experimental studies on wave forces

In terms of force and pressure measurements of waves on structures, there has been a surge in research over recent years. Often extensions of previous work on run-up, this research has predominantly been carried out in the USA and Japan. Cross (1967) was one of the first to study surge forces experimentally, building on the theoretical work of Cumberbatch (1960), and his work is the basis of some existing design codes. Ramsden (1993) conducted experiments to determine the forces on a vertical wall by solitary waves, bores and surges. He observed that the model of Cross (1967) under-predicted the forces from bores and surges by about 30-50%.

Árnason (2005) measured forces from a bore on a circular and square column at 90 and 45 degree orientations. He derived resistance coefficients (force normalised by $\frac{1}{2}\rho bhu^2$) for the various shaped bodies tested and compared them with drag coefficients found in standard hydraulic texts and by other researchers based on steady flow. Árnason (2005) concluded that the force during the initial impact is approximately 50% higher than the resistance force during the bore passing (quasi-steady) for smaller bores. For the larger bores, blocking effects were observed to be more important, causing the quasi-steady forces to be larger than the impact force. In an extension of this work, Árnason et al. (2009) investigated interactions between a bore and columns of a square and circular cross section with a six-degree-of-freedom load cell set up. Forces were found to relate to Froude number, height of the bore and also flume and structure geometry and had drag coefficients between 1 and 2. The tests of Árnason (2005) & Árnason et al. (2009) ignore any specific effects of the changing water surface around the column, and do not capture the hydrostatic effects of a water surface difference between the front and the rear. A corresponding numerical study was carried out by Wei et al. (2015) based on Arnason's tests using an SPH method. Good agreement was found between the numerical model results and the experiments, although results for the full inundation time period were not presented and the model was cut off early. The results of Árnason et al. (2009) and

Wei et al. (2015) are used for comparative purposes later in this thesis.

Fujima et al. (2009) conducted experiments with on-shore rectangular structures and measured both pressure and forces using an array of pressure transducers and load cells fitted to the structures, varying the distance from the shore as an additional parameter. They found that estimation of the total wave force by integration of the maximum wave pressure envelope may overestimate significantly, because peak pressures occur at different times across the structure. They also observed significant inertial force components for structures located close to the shore, compared to those further away. Fujima et al. (2009) proposed a series of force equations based on their work and that of prior studies, all of which are slight empirical modifications to the components set out in Section 1.2.5. The first of these was to introduce an empirical function for C_D, where C_D is a function of the maximum inundation depth divided by the distance from the shore, h_{max}/D. The second retained a constant drag coefficient, but introduced an inertial component, and the third regressed a different drag coefficient for force based on h_{max}, u_{max}^2, rather than $(hu^2)_{max}$ as used to normalise force in the first equation. The proposed relationships appear to capture the behaviour of the forces in a log-log plot of observed force versus predicted, but there is still considerable scatter even when plotted in this way. Like the work of Arnason, Fujima et al. (2009) do not account for the change in surface profile between the front and rear of the structure.

Lukkunaprasit et al. (2009b) verified the loading described by FEMA (2012) using experimental methods. The authors used a 40m long flume and tested at 1:100 scale with a model structure fitted with a high frequency load cell. They concluded that the equations given in FEMA (2012) are a reasonable upper bound for tsunami forces, though the tests they carried out seem fairly limited in scope to verify the design formulae by themselves, as they were a relatively small set of tests. They examined peak forces, as FEMA (2012) is a design code primarily, so largely left other aspects unexplored. The primary deficiency of these tests for comparing with design loads, was that a similar set up was used to the experiments upon which much of FEMA (2012) has been based, (i.e. 1:100 scale or higher and short waves periods generally lower than 10s). Lukkunaprasit et al. (2009a) also examined the effect of openings on the pressures and forces found on structures. Models with 25 and 50% of the frontal area open to inundation respectively, were tested under wave loading and compared to a structure with no openings. A 15-25% reduction in the

overall structural force was observed in the 25% opening structure and a 30-40% reduction for the 50% opening structure, clearly demonstrating a benefit of allowing flow through a building, but no theoretical explanation is presented.

Thusyanthan and Madabhushi (2008) investigated the wave loading on a proposed "tsunami-resistant house" design and a typical coastal residential design found in Sri Lanka for comparison. The tsunami-resistant design was based on a student initiative at Harvard Design School in collaboration with Massachusetts Institute of Technology (MIT) and the general concept was to allow flow through the structure. The experiments were conducted in a small wave flume with waves generated by dropping a 100kg concrete mass in the far end of the flume, while the instrumented structures were located at the near end on a bathymetry. Impacts were filmed with high speed video. Additionally the bed was instrumented with pore pressure transducers. The house was built at a scale of 1:25, and a dimensional analysis performed using Buckingham's Π theorem (Buckingham, 1915). Thusyanthan and Madabhushi (2008) identified eight relevant variables for dimensional analysis and with the three quantities, time, length and mass, Buckingham's theorem produces five (8-3) dimensionless groups: Froude number (Fr), Reynolds number (Re), drag coefficient (C_{D}) and two non-dimensional length parameters. Re being the ratio of inertial to viscous forces, and Fr being the ratio of inertial forces to gravitational forces. The authors correctly identified that Re was not the important non-dimensional quantity to conserve as inertial forces tend to be dominant in the case of a bluff body (see section 1.2.5.2).

Scaling (discussed further in Section 3.3.7) should be based on the Froude number, Fr i.e. $(u/L^{\frac{1}{2}})_{\mathrm{model}} = (u/L^{\frac{1}{2}})_{\mathrm{prototype}}$. The authors also noted the problem with the materials and glues used to construct the scale model. The building was far stiffer than it should be under proper scaling conditions, and as such would have attracted more force. The issue of scale with respect to the very short flume and size/shape of the waves produced was not considered in the paper. Many of the water depths were extremely small, thus enhancing viscous effects (see the end of this chapter for details). The researchers concluded that the tsunami-resistant design performed well in comparison to the typical design, based on their tests. Considering the 1:25 scale chosen for the building, there are serious issues with the wave periods generated and the small size of the overall set-up.

Full-scale testing by Arikawa (2009) shows the failure mechanisms of a single wooden wall, and eight different thicknesses of reinforced concrete wall under wave loading. These experiments were carried out at the large Hydro-Geo Flume of the Port and Airport Research Institute, Japan. 2.5m waves were generated using a paddle with a 14m stroke. The purpose of the experiments appears to have been to examine the differing failure mechanisms in reinforced concrete walls depending on their thickness to inform break-away wall design for force reduction measures.

van De Lindt et al. (2009) conducted 1:6 scale tests on a residential wooden structure. The structure was instrumented to measure displacements and forces and was installed in a wave basin. In parallel, tests were also carried out using pushover analysis on a dry structure, and the resulting displacements were correlated to those of the wave experiments. Further details of the structure and tests are found in Wilson (2008) and Wilson et al. (2009). The tests demonstrated that the predominant loading to the structure is due to uplift and overturning moments. The pushover tests produced a relationship between force and displacement, but the same displacement was produced for a lower force in the wave tests. The complexity from the wave flow in comparison to the pushover tests reduced the forces between 20 and 40% of those required to produce the same displacement in the pushover tests. Assumptions for the wave forces (which are constant per metre width in the formulation) are in fact, dependent upon the aspect ratio of the structure.

Nouri et al. (2010) conducted experiments on surges impacting upon instrumented structures. The channel constriction was also varied to investigate blockage ratio. A variable pitch pump kept the impoundment depth in the reservoir topped up after release of the gate holding the water, so the tests were effectively a surge with a quasi-steady flow following it. Nouri et al. (2010) observe the overshoot in pressure upon impact of the surge front as was seen by Ramsden (1993) for square structures, but only for larger impoundment depths. These tests produced surges with steeper fronts, which is known to be a factor in the surge force (Ramsden, 1993).

Al-Faesly et al. (2012) examined the interaction between a square column and a dam-break flow produced by the rapid opening of a gate releasing water at a range of impoundment depths. Physical tests were compared to a 3D model, which showed good agreement. The RANS numerical simulations carried out show similar peak pressures as the experiments, but with initially far higher splash height and fast

relaxation of the free-surface height near the obstacle. The results of Al-Faesly et al. (2012) as well as numerical studies of this dataset by Douglas and Nistor (2015) and St-Germain et al. (2012) are used for comparison in Chapter 3 of this thesis where they are discussed further.

1.2.6 Research Gaps

Having reviewed the literature for studies of forces due to waves, there are a number of gaps which are notable. Many of the key references are summarised in Table 1.3. Firstly, the literature is overwhelmingly comprised of relatively short period tests. Limitations of the wave generation methods dictate that paddle generators have relatively short stroke lengths. It is highlighted by the period of wave produced by Arikawa (2009) which was approximately 25s, produced by a full stroke length of 14m from the actuator. This length is far longer than many of the flumes which were used in the literature reviewed, but still creates a fairly short period wave for comparison to tsunamis. Arikawa (2009) tested at full-scale, so a 25s period wave is clearly not comparable to a 5 - 90 minute tsunami period. For the purpose of this thesis, long-period waves are defined as comparable to those of tsunami waves. Generally the possible range of wave periods at experimental scale correspond to the lower end of the 5 - 90 minute prototype period range. Based on a 1:100 scale, a 5 minute prototype scale is $300/\sqrt{100} = 30$ seconds model period or above. Charvet (2012) defined long-period waves as $T > 10$s. "Long-waves" are often defined as in terms of their shallow water wavelength to depth ratio, as $\lambda_w/h < 20$, which gives periods of $T > 20/\sqrt{gh}$. On this definition the water level can be lowered for tests which can allow waves with periods of 5s or lower to be classified technically as "long-waves". In doing so, the shallow water assumptions remain valid, but the wave has very different characteristics and period to a tsunami at scale. Additionally, prototype scale periods are still well below those expected of tsunamis. For model water heights of around 0.6 - 1m at 1:100 scale the shallow water λ_w/h criterion must be modified to $T \gtrsim 120/\sqrt{gh}$ in order to achieve tsunami-like prototype periods > 5 minutes, so clearly the shallow water criterion alone is insufficient for modelling tsunamis. Generally, for the water levels commonly modelled in flumes at 1:100 scale, periods of 25s and above are probably sufficient to make a reasonable comparison. There are no such data in the literature.

Author (Year)	Generation Method	Type	Period of waves	Bathymetry Slope
Fukui et al. (1963)	Dam break	Surge	NA	0
Cross (1967)	Dam break	Surge	NA	0
Nakamura and Tsuchiya (1973)	Dam break	Surge	NA	0
Ramsden and Raichlen (1990)	Paddle	Solitary	< 10s	1:50
Ramsden (1993)	Dam break & Paddle	Surge	NA, < 10s	0, 1:50
Árnason (2005)	Dam break	Surge & Bore	NA	0
Simamora et al. (2007)	Paddle	N-Wave	< 20s	Complex, 1:3
Thusyanthan and Madabhushi (2008)	Vertically dropped concrete	Solitary	< 5s	1:9
Fujima et al. (2009)	Paddle	N-Wave	< 20s	Complex, 1:3
Lukkunaprasit et al. (2009a)	Elevated tank release	Solitary	< 10s	Complex, 1:115
van De Lindt et al. (2009)	Paddle	Solitary	< 10s	Complex, 1:30
Arikawa (2009)	Paddle	Solitary	< 25s	Complex, 1:10
Nouri et al. (2010)	Dam break	Surge	NA	0
Al-Faesly et al. (2012)	Dam break	Surge	NA	0

Table 1.3: *Table showing key experimental studies of forces from waves discussed in this review*

Many of the tests described are of too small-scale to produce results that could be reasonably scaled up to prototype. Viscous effects become important for low water depths, where the influence of the boundary layer begins to dominate the behaviour of the fluid. This can lead to an overestimation of measured drag forces when scaled up to prototype. Several of the mentioned studies use waves that at the scale tested would generally never break free of a viscous-dominated regime, particularly for the inundation zone and around structures.

Few of the tests have properly investigated the effect of adjacent structures or a blockage ratio. In fact some of the tests are for a blockage ratio of unity, because they are derived for vertical walls (Cross, 1967). The critical behaviour of a water surface in and around a surface piercing structure in a flow is changed by the structure's presence. At higher flows the modification to the surface will be significant and applies an additional net hydrostatic force components on the structure in addition to hydrodynamic forces from the moving flow. This is not accounted for by many of the studies, which tend to concentrate on the hydrodynamic force, or sometimes an unsteady force component (because the tests are of short-period waves, and therefore accelerations in the flow can be high enough for this to be significant). None of the literature properly accounts for a varying contribution between the force components as the flow changes.

Additionally, the experimental studies often involve very specific set-ups and produce data from which it is difficult to extract general empirical relationships, and many of the experiments are for limited numbers of tests. These deficiencies are difficult to address due to the obvious link to research budgets, but there is clearly a requirement for more tests, from as diverse set-ups as possible, in order to develop new relationships for long-period waves.

The major deficiencies in the current widespread application of NLSW equations for tsunami vulnerability assessment are evident and two-fold. First, it is not possible to identify the force on an individual building using these models and since the outstanding issue is to estimate building damage, this is of considerable importance. It is possible to extract local measures of water height, h, velocity, u, momentum flux, u^2h or Froude number from these simulations, but their link to the force on the buildings is debatable and still unclear. Catastrophe models in the insurance industry currently simulate thousands of hypothetical scenarios of tsunami inundations at

a regional scale, but are limited by the same problem, i.e. an indication of the force on buildings is unavailable. Correlations with the probability of levels of building damage are instead made using parameters from bare-earth flow models, namely u and h which are known as fragility curves (Macabuag et al., 2014b). Second, none of these models have been tested against the growing database of experiments for rectangular buildings in a steady channel flow or due to the impact of a bore or dam-break flow. This step should form a necessary validation exercise. Including only either blocking or drag is not sufficient to reproduce any of the salient physics of flow around a building. Drag and blocking can be resolved for flows in 3D models, but the usefulness of these models is limited to very specific detailed cases and come at a huge cost of computational expense. As such a gap is identified for a type of modelling where an estimate of forces on buildings are required for large national and regional scale modelling, but where the computational expense of 3D modelling is not feasible. An inclusion of the building effects on the flow, and the flow effects on the buildings are not available from 2D numerical models at present.

Design codes where they exist are concerned with maxima and are generally conservative in nature (Macabuag et al., 2014a). A summary of literature reviewed is found in Appendix A. However, none of the design guidelines reviewed account for the effect of flow blocking, and the increase in effective drag coefficient it has. There are clearly factors of safety on design codes, but there is a potential for the design drag forces to be underestimated in highly dense urban settings if unbounded drag coefficients are used. This requires further attention.

1.3 Aims and objectives

This thesis aims to provide better insight into the interaction between tsunami-like inundation flows and buildings. It aims to develop an experimentally validated approach for evaluating the forces imparted by these flows on buildings that is appropriate for use by engineers and by the insurance industry in their assessment of the tsunami performance of buildings. In providing the experimental validation of the proposed numerical approach to tsunami force estimation, the thesis also aims to provide a new set of published inundation tests for long-period unsteady waves at large-scale for other researchers to adopt in numerical model validation.

In order to achieve these aims the following objectives are set.

- To carry out a thorough literature review, covering not only long-waves experimental and numerical studies, but also short-period waves, steady and unsteady flow and general force descriptions.
- To devise and execute a set of steady experiments studying flow past a block measuring the forces applied to it, and the flow conditions which produce the force. Classify and parameterise this behaviour.
- To conduct a set of unsteady tests of long-period waves interacting with a sloping beach and instrumented building to capture pressures and local flow conditions using a pneumatic wave generator at a suitable comparable scale to prototype tsunamis. Present these data.
- To develop a basic numerical model capable of predicting the forces on a block, where the blockage is accounted for in the flow conditions.
- To test this model using the results of steady experiments, and apply to large-scale unsteady tests assessing the force prediction capabilities.

Chapter 2

Steady Flow Loading on a Solid Obstacle in a Laboratory Flume

2.1 Introduction

Tsunami flows are unsteady, but due to their long-period nature, for much of the inundation the temporal variation in flow is small. As such we can think of most tsunami inundations as quasi-steady flows for the majority of the flow situations (Matsutomi and Iizuka, 1998; Yeh and Li, 2008). This means that any forces of unsteady origin are likely to be small in comparison to the other components, provided that accelerations are small.

As discussed in Section 1.2, the effect of blocking on the forces that an object experiences are important and need to be understood in order to model flows in an urban context. Furthermore, there is a link between the forces imposed on the object and momentum that is lost from the flow, so it is desirable to describe this relationship in more detail. Figure 2.1 shows the differences in flow patterns between roughness modelling, and blocking.

When the flow is partially blocked, it is forced around the obstacle, and speeds up due to continuity. Momentum is lost from the flow through a drag force and vertical vorticity is generated which is shed in the wake.

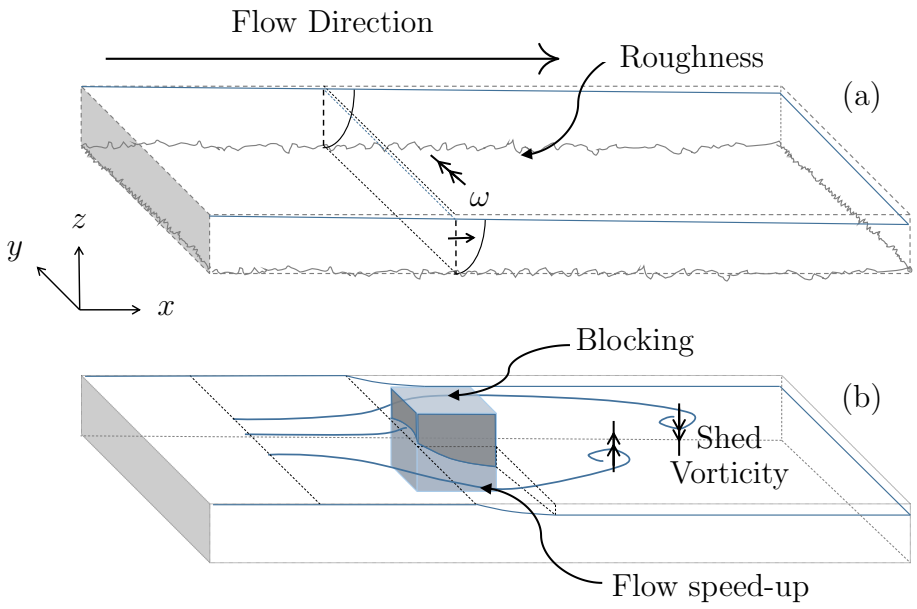

Figure 2.1: *Schematic illustrating free-surface flow (a) flow over a roughness array and (b) flow around a building. In (b) the influence of blocking and drag are highlighted. Solid blue lines indicate the deformed free-surface, dashed lines indicate the still water free-surface.*

Since the integrated effect of a building on the flow is through a drag force, it is useful to discuss recent attempts to parameterise this component in terms of upstream variables. As such it is necessary to understand the force on the building and its link to the state of the flow. Many researchers have correlated the drag force, F_{D}, in terms of a notional static pressure exerted by an incident flow as (1.22). For example, for a rectangular building, with face normal to the incident flow, u_1, $A_W \approx h_1 b$, where b, is the width of the building and so (1.22) becomes

$$F_{\mathrm{D}} \approx \frac{1}{2}\rho C_D h_1 b u_1^2. \tag{2.1}$$

This parametric form has been reported to be accurate for low blockage ratios (Fenton, 2003) and upstream Froude numbers, Fr_1, which are sufficiently low that the difference in water depth between up and downstream positions is small. In all cases the upstream Froude number is expressed as

$$Fr_1 = u_1/\sqrt{g h_1}. \tag{2.2}$$

As discussed in Section 1.2.5.2, there appears to be a consensus in the literature (Lee, 1975; Otsuki et al., 1978; Tamura and Miyagi, 1999; OCDI, 2002) about C_D for regular shapes, with $C_D \approx 2.0-2.1$ for a square cylinder and $b/w \ll 1$. Although C_D is also influenced by the Reynolds number, there are two important elements that are seen to vastly change C_D - (a) Fr_1 and (b) the blockage ratio, b/w (Sharify et al., 2013).

The influence of upstream Froude number, Fr_1, on the flow state and form of the drag force is an important consideration. For emergent buildings ($h/H_b \leq 1$), as Fr_1 increases, the downstream Fr_2 increases (but by a larger amount). This is because the drag on the flow causes the upstream water height to increase and the downstream water height to decrease. The velocity between the building and channel wall is increased and this ultimately generates a supercritical flow. For this flow regime, the drag force is shown by Qi et al. (2014) to scale as (2.1). A point is reached where Fr_1 cannot increase further. At that stage the loss in momentum flux reaches a maximum (and no more momentum can be removed without the flow being unsteady). The flow then adjusts downstream through a hydraulic jump tending to a supercritical downstream flow. Waves are emitted from the sharp trailing edges of the building. As discussed in Section 1.2, in this choked state (indicated by $_c$), Qi et al. (2014) demonstrated that the drag force scales as

$$F_{\mathrm{D}} \approx \lambda_c \rho b g^{1/3} u^{4/3} h^{4/3}, \tag{2.3}$$

which includes both a hydrodynamic and hydrostatic component as given by (1.28).

Despite the fact that the drag is largely dominated by form drag, the pressure p on each surface is determined by the hydrostatic component. This is because the inertia of the flow is converted to a rise in the water surface at the front of the building. At the rear of the building, the low pressure of the attached wakes generates a local decrease in the water height, which is also reflected in the hydrostatic component.

While the framework of Qi et al. (2014) can be used to predict forces from an independent numerical model, there is no means of feedback into the flow conditions if the model cannot account for the presence of a structure in the flow and the momentum it changes. The influence of a structure on the flow, changes the forces it attracts from the flow, and blocking effects alter the flow and its critical behaviour.

Hence, simply taking the Qi et al. (2014) equations and applying them to maximum velocity and water depth output from a bare-terrain numerical model is not sufficient to predict accurately forces. In order to better understand whether this framework can be used in a predictive sense, it is more useful to incorporate it into a dynamic numerical model so that not only the forces, but also the flow conditions may be tested against experimental values.

To verify this framework and to parameterise further results of this thesis, a set of experiments were carried out in the Department of Mechanical Engineering laboratories at UCL. The results are used to help devise a simple numerical model which better links flows to the forces on a structure. As such a simple 1D model is defined in Section 2.2. This chapter describes experiments carried out to verify the framework and parameterise the force closure based on a blockage ratio of 0.25. Results of the numerical model are subsequently presented using the empirical parameters derived from steady experiments, which dynamically predict the forces on structures in flow as well as the flow conditions due to the presence of a structure. To achieve this, full control is required over the procedure and parameters varied in the experiments, which is why the tests are carried out.

2.2 One-dimensional model

In this section it is argued that the force on a square cylinder can be adequately modelled through a distributed drag force and a blockage ratio. As demonstrated in Section 1.2, there are a number of ways that the equations of motion can be simplified through various approximations and assumptions. A starting point is chosen as the 2D non-linear shallow water equations described in Section 1.2.2 (1.10 - 1.12), which are appropriate for modelling long-period waves in shallow water where pressure distributions are close to hydrostatic. We can re-write (1.10 - 1.12) in the following form, ignoring advection, substituting $\eta = h + z_b$ and including a

distributed drag term;

$$\frac{\partial h}{\partial t} + \boldsymbol{\nabla\cdot}\left(h\boldsymbol{u}\right) = 0, \tag{2.4}$$

$$\frac{\partial (uh)}{\partial t} + \boldsymbol{\nabla\cdot}(hu\boldsymbol{u}) = -g\frac{1}{2}\frac{\partial h^2}{\partial x} - gh\frac{\partial z_b}{\partial x} - \frac{\tau_{bx}}{\rho} - f_{Dx}h, \tag{2.5}$$

$$\frac{\partial (vh)}{\partial t} + \boldsymbol{\nabla\cdot}(hv\boldsymbol{u}) = -g\frac{1}{2}\frac{\partial h^2}{\partial y} - gh\frac{\partial z_b}{\partial y} - \frac{\tau_{by}}{\rho} - f_{Dy}h, \tag{2.6}$$

where the system is expressed in a flux conserving form. On the right hand side, the contribution due to bottom shear stresses $\boldsymbol{\tau}_b = (\tau_{bx}, \tau_{by})$ and a depth-averaged resistive force per unit mass, $\boldsymbol{f}_D = (f_{Dx}, f_{Dy})$ are included. A roughness model is applicable when the water depth is an order of magnitude larger than the height of the roughness elements, which in turn may also require the introduction of a roughness height of the flow above. These roughness models are only applicable when the roughness changes smoothly and so rapid changes due to localised groups of buildings may require additional closures.

In order to test rapidly the importance of various assumptions, it is helpful to simplify the problem further. Where blockage ratios are small, the transverse velocities are many times smaller than the inline velocities, so it makes sense to focus on the important behaviour. Hence, the general model can be described in one-dimension by averaging the flow in the y- direction. Across the flume a local blocking fraction is defined to be $\phi = \int_{-w/2}^{w/2} S_b dy$. When $\phi = 0$, there is no blocking; usually $\phi = b/w$, meaning the void fraction available for flow and mass to occupy is $1 - \phi$. The flow model is modified by multiplying all terms by ϕ to provide a reduction to the available conveyance in the region of the block in the following way;

$$\frac{\partial}{\partial t}((1-\phi)h) + \frac{\partial}{\partial x}\left((1-\phi)uh\right) = 0, \tag{2.7}$$

$$\begin{aligned}\frac{\partial}{\partial t}((1-\phi)uh) + \frac{\partial}{\partial x}\left((1-\phi)u^2h\right) = &-\frac{1}{2}g\frac{\partial}{\partial x}(1-\phi)h^2 \\ &- g(1-\phi)h\frac{\partial z_b}{\partial x} \\ &- gn^2(1-\phi)\frac{u^2}{h^{4/3}} - (1-\phi)f_D h.\end{aligned} \tag{2.8}$$

Bed shear stresses are modelled through a Manning roughness parameterisation as (1.13). The flow equations (2.7) and (2.8) can be thought of as average quantities

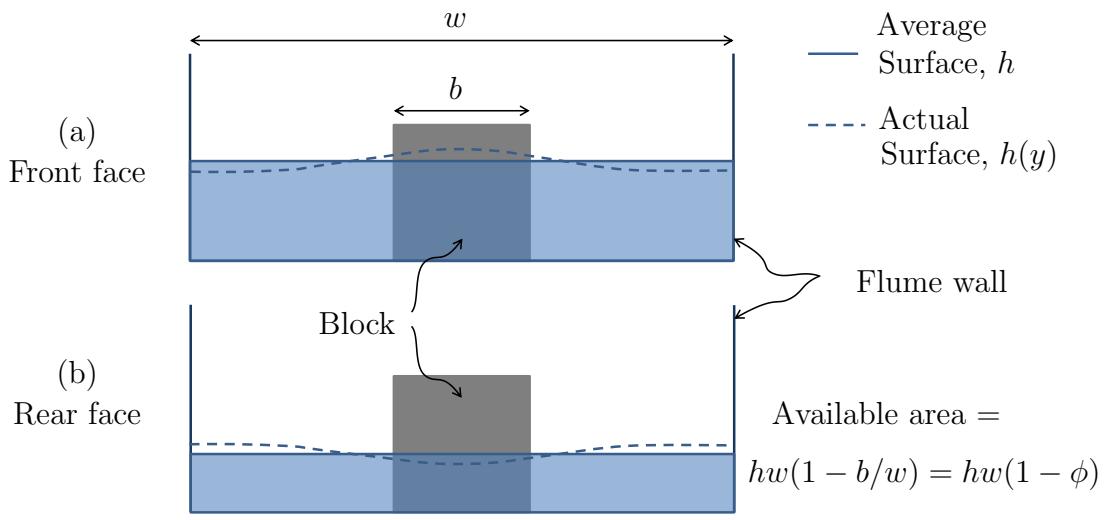

Figure 2.2: *Average flow conditions and reduction of cross-sectional area due to blocking. (a) View of channel cross-section at the upstream face of the block from upstream to downstream (b) View of channel cross-section at the downstream face of the block from downstream to upstream.*

per unit width, so ϕ can be applied to locally vary the average channel conveyance by multiplying all the terms by ϕ as shown in Figure 2.2. By the product rule, $\frac{\partial(1-\phi)h}{\partial t} = (1-\phi)\frac{\partial h}{\partial t} + h\frac{\partial(1-\phi)}{\partial t}$. The $(1-\phi)$ term here is invariant in time, so $\frac{\partial(1-\phi)}{\partial t} = 0$. Similarly as we are discussing a block of constant b with its front-face perpendicular to the flow, across the domain ϕ is zero in the regions without a block, and b/w in the regions with a block, so in these regions $\frac{\partial(1-\phi)}{\partial x} = 0$. It is therefore possible to simplify (2.7) and (2.8) by moving the $(1-\phi)$ terms outside the partial differentials. This gives a 1D flow model with blocking and drag as;

$$(1-\phi)\frac{\partial h}{\partial t} + (1-\phi)\frac{\partial}{\partial x}(uh) = 0, \tag{2.9}$$

$$\begin{aligned}(1-\phi)\frac{\partial(uh)}{\partial t} + (1-\phi)\frac{\partial}{\partial x}\left(u^2 h\right) &= -(1-\phi)\frac{1}{2}g\frac{\partial}{\partial x}h^2 \\ &\quad - g(1-\phi)h\frac{\partial z_b}{\partial x} \\ &\quad - gn^2(1-\phi)\frac{u^2}{h^{4/3}} - (1-\phi)f_D h.\end{aligned} \tag{2.10}$$

The form of these equations are very similar to those used to described bubbly two-phase flow, using the so-called two fluid model (Drew and Passman, 2006). Note that here ϕ is defined to be constant and uniform with its gradients zero. It is possible to explore the link between change in momentum flux and drag force for steady flows by integrating (2.10) over the whole domain to give

$$\left[u^2 h + \frac{1}{2} g h^2\right]_1^2 = -(1-\phi)\int_{-L/2}^{L/2} h f_D \mathrm{d}x \tag{2.11}$$

For steady flows, a drag coefficient can be identified:

$$C_D = \frac{F_\mathrm{D}}{(1/2)\rho b h_1 u_1^2}. \tag{2.12}$$

The drag is related to the change in the momentum flux and hydrostatic force between the upstream and downstream:

$$M_2 - M_1 = \frac{F_D}{\rho w} \tag{2.13}$$

where

$$M_i = h_i u_i^2 + \frac{1}{2} g h_i^2.$$

Defining $M = hu^2 + \frac{1}{2}\rho g h^2$, the decrease in M is related to the action of the body force on the flow, i.e.

$$\frac{M_2 - M_1}{w} = (1-\phi)\int_{-L/2}^{L/2} h f_D \mathrm{d}x, \tag{2.14}$$

and rearranging (2.13)

$$\rho(M_2 - M_1) w = F_\mathrm{D}, \tag{2.15}$$

then

$$F_\mathrm{D} = \rho(M_2 - M_1) w = \rho w (1-\phi)\int_{-L/2}^{L/2} h f_D \mathrm{d}x. \tag{2.16}$$

The closure used by Qi et al. (2014), was formed from a combination of form drag and hydrostatic force, (1.28). It was found that even for choked flows where large differences in water depth exist between the front and rear of a block, the dominant

contribution comes from the hydrodynamic drag component for lower values of ϕ. As such the hydrostatic component is firstly ignored. For low Fr it is expected that;

$$\rho(1-\phi)wf_D h_1 L = \frac{1}{2}\rho C_D b h_1 |u_1| u_1 \tag{2.17}$$

so that

$$f_D = \frac{C_D}{2L}\frac{\phi}{(1-\phi)}|u_1|u_1. \tag{2.18}$$

The form of this closure bears a similarity with (1.17). It is expected that it should provide reasonable results for subcritical flows, and because for low ϕ the hydrostatic component is small it is likely to be sufficient for choked flow also. The next section describes a set of experiments carried out to verify this behaviour and parameterise it for a different $\phi = 0.25$. The tests of Qi et al. (2014) were conducted on a tall cylinder where the building height, $H_b > h$ at all times. The experiments described in this these allow for flow conditions to occur where $H_b < h$, so that it is possible to observe over-topping.

For higher blockage ratios ($b/w \gtrsim 0.4$), transverse velocities are more significant and a two- or three-dimensional approach would therefore be more appropriate. A-two dimensional approach forms part of future work and is outside the scope of this thesis. Additional current work within the group at UCL is also examining higher blockage ratios while looking at three-dimensional effects and over-topping (Bahmanpour et al., 2015). As such higher blockage ratios are outside the scope of this thesis and do not feature in any of the experiments conducted and described as part of this work.

2.3 Experimental set-up and methodology

In these experiments, a steady-flow transparent acrylic flume is used in the Department of Mechanical Engineering laboratories at UCL. The flume is of width 0.50m, depth 0.20m and length 3.00m with a tapered inlet to reduce upstream perturbations in the flow. It is fed by a constant flow loop driven by a pump at the side of the flume, the frequency of which is digitally controllable. The total flow or volume flux, Q through the flume is correlated with the frequency of the pump. The test

set-up shown in Figures 2.3 and 2.4 are used to investigate relationships between the velocity, volume flux, elevation of the water surface, and the resulting forces on an emergent body. Free-surface profiles are measured using two optical methods, hence the water used is dyed blue for this purpose. This is preferred to other measurement techniques because the flume is sealed from the top making access difficult. Applied moments to a suspended block are measured via two cantilevered load cells fixed to a rig above the flume which is bolted in place.

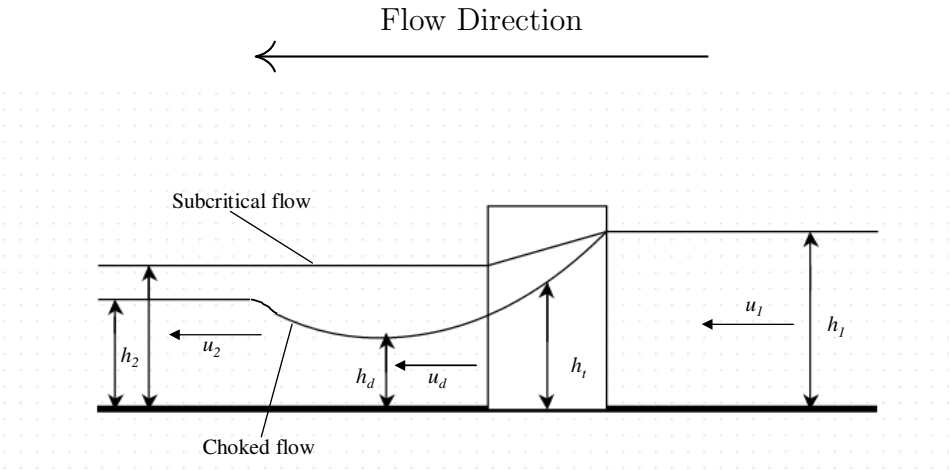

Figure 2.3: *Schematic diagram indicating the quantities described by this framework. Note, flow here depicted unconventionally positive from right to left in order to correspond to images of the flume used in the experiments of this chapter (the access to the flume is from one side only).*

Throughout this thesis the subscript $_1$ indicates upstream (i.e. Fr_1,h_1, etc.), and subscript $_2$ indicates downstream quantities away from the block (Fr_2,h_2, etc.). Subscript $_d$ indicates the immediate region downstream of the block (Fr_d,h_d, etc.), important for the choked flow regime, and where subscript $_t$ is mentioned, it relates to the throat of the blockage. Schematically we can think of the experimental set-up as shown in Figure 2.3. Much of the mathematical framework of Qi et al. (2014) is applicable. To begin with, a constant flow is introduced through our system. The flow or volume flux, Q, in a rectangular channel, is characterised by a depth, h, and velocity, u. The channel width is w and the obstacle breadth is b. The flow is constricted in the region of the obstacle to a width of $w-b$. Importantly, during the

steady experiments upstream and downstream of the constriction, Q is constant.

$$Q = uwh \tag{2.19}$$

Locally, the specific energy, H, sum of specific momentum flux and hydrostatic force on a vertical plane, M and Froude number, Fr are defined as;

$$H = \frac{u^2}{2g} + h, \qquad M = \left(u^2 h + \frac{1}{2} g h^2\right) w, \qquad Fr = \frac{u}{\sqrt{gh}}. \tag{2.20}$$

With invariant volume flux, Q; h, M and H can be expressed in terms of Q and Fr;

$$h = \frac{Q^{\frac{2}{3}}}{w^{\frac{2}{3}} Fr^{\frac{2}{3}} g^{\frac{1}{3}}}, \quad H = \frac{Q^{\frac{2}{3}}}{w^{\frac{2}{3}} Fr^{\frac{2}{3}} g^{\frac{1}{3}}} \left(1 + \frac{1}{2} Fr^2\right), \quad M = \frac{g^{\frac{1}{3}} Q^{\frac{4}{3}}}{w^{\frac{1}{3}} Fr^{\frac{4}{3}}} \left(\frac{1}{2} + Fr^2\right) \tag{2.21}$$

(2.19) and (2.21) can be non-dimensionalised using the specific energy upstream, H_1, which is chosen because it can be easily measured experimentally;

$$\hat{h}_1 = \frac{h_1}{H_1}, \quad \hat{h}_2 = \frac{h_2}{H_1}, \quad \hat{Q} = \frac{Q}{w g^{\frac{1}{2}} H_1^{\frac{3}{2}}} \tag{2.22}$$

which are expressed in terms of Fr in (2.23);

$$\hat{h}_1 = \frac{1}{1 + \frac{1}{2} Fr_1^2}, \quad \hat{h}_2 = \hat{h}_1 \left(\frac{Fr_1}{Fr_2}\right)^{\frac{2}{3}}, \quad \hat{Q} = Fr \hat{h}^{\frac{3}{2}} \tag{2.23}$$

The test procedure incrementally varies a steady flow in the flume past a fixed block, for different initial water levels. Two dimensional forces on the block can be inferred from moments measured by two (Transverse and Drag) load cells, by which the block is freely supported. The block protrudes into the flow leaving a $\sim$ 1mm clearance between it and the flume base, allowing free movement with negligible under-flow.

Flows are calibrated to the pump frequency, for a given initial water depth, h_i (as this influences the pump performance), before the tests are conducted by measurement of velocities across the flume with a miniature propeller-meter. An estimate of $\bar{u}$ is used to infer the flows, for given pump frequencies and h_i. The zones either end of the flume for flow relaxation can be considered approximately 0.4m from each end

with the inlet tapered to minimise upstream disturbances.

Images of the set-up can be found in Figures 2.4 and 2.5. Above the test specimen, a light box containing two fluorescent bulbs hangs, with a translucent perspex diffuser to produce homogeneous light. Beneath the flume, a 45% mirror is fixed, so that a tripod mounted camera can capture images of the underside of the specimen and the fluid around it, from the side. The camera (AVT black and white Dolphin F145B) is attached to a PC running control software, via a cable. The flume contains methylene blue dye (0.5g added when flume completely full). Water was only removed from the flume during course of the experiments, not added. As such the initial dye concentration remained constant throughout the testing because the water level was systematically dropped from the highest to lowest h_i during the course of testing.

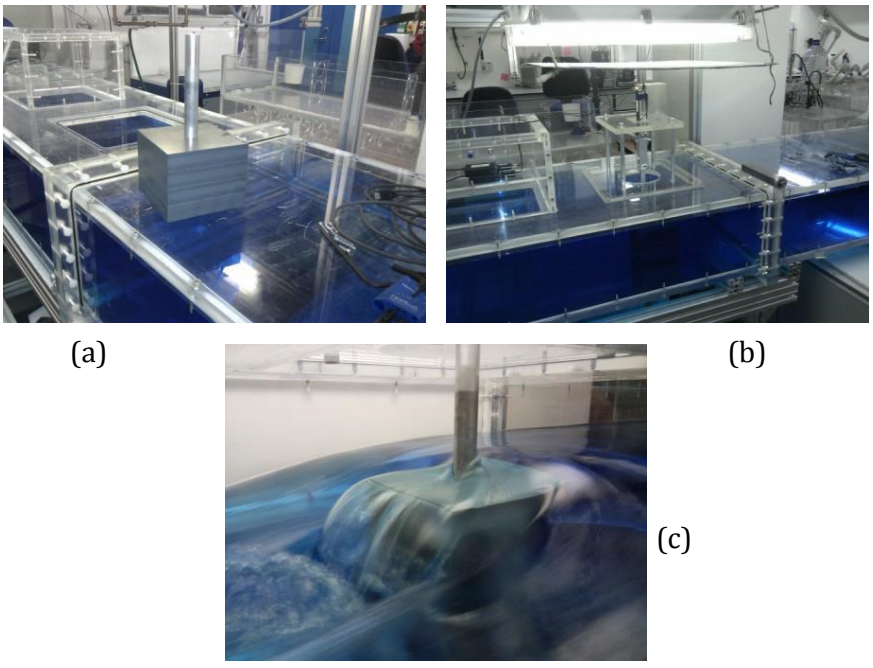

Figure 2.4: *(a) Test specimen, (b) wide image of set up, including the light box above the flume, (c) an image of the test specimen insitu undergoing an over-topping test.*

The measured quantities and their associated uncertainties can be found in Table E.1.

2.3.1 Flume

The flume is located in the lower basement floor of the building in a separate room, which allows for light levels to be controlled. The flume is sealed on the top with a further sheet of transparent perspex, save for two access panels. These panels are recessed and drilled so that test rigs can be secured and specimens suspended into the flow below. During these tests, the water level never reached this top perspex sheet, so open-channel flow is observed throughout the investigation. The pump is housed alongside the flume and a control panel is mounted on the wall. The flume is 3m long, 0.5m wide and 0.2m deep.

2.3.2 Load cell rig

Extensive details of the design and manufacture of the test rig used in these experiments can be found in Mandal (2011), but the equipment will be described here briefly and is shown in Figure 2.5. Key components of the rig are two, 3.0kg capacity, OBUG series, single point load cells from Applied Measurements Limited. The rig is designed in such a way that the two load cells can be joined end to end, rotated 90 degrees from each other (capturing displacements in perpendicular directions), and be suspended vertically, cantilevering from a rigid support. The distance from the support to the end of the second load cell is 235mm, used to define the moment in calibration.

The load cells are connected to two USB digitisers, also supplied by Applied Measurement Limited. Together with the acquisition software installed on a laptop, the package is capable of simultaneously recording voltages from the two load cells at frequencies up to 500 Hz. For these steady tests a sample frequency of 25 Hz was chosen.

2.3.3 Obstructive body

The block chosen for these experiments has dimensions, breadth, $b = 0.125$m, length $L = 0.125$m and depth $H_b = 0.100$m (Figure 2.4 (a)) to provide a blockage ratio of $b/w = 0.25$ in the flume. It is machined from acrylic and mounted via a threaded

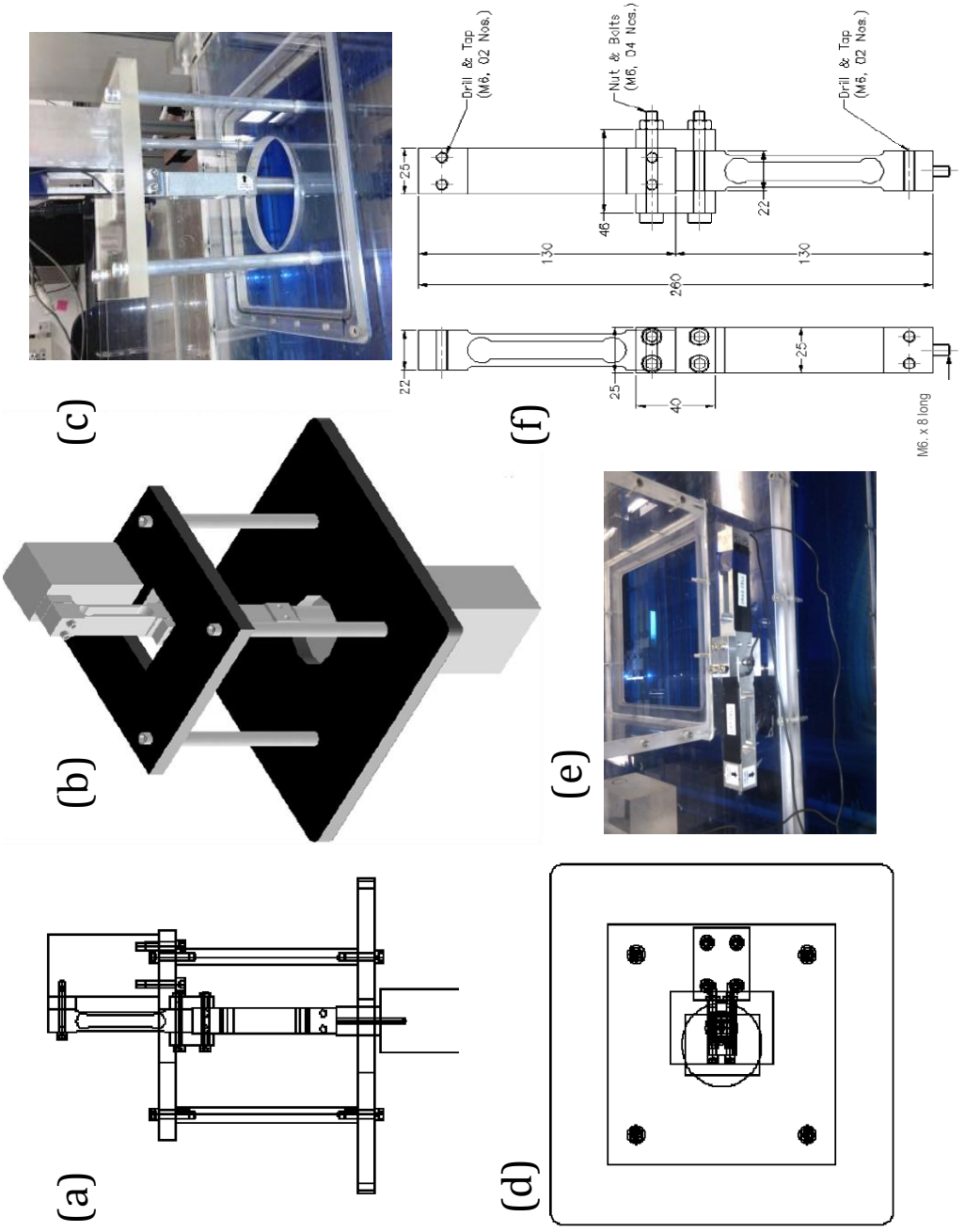

Figure 2.5: *Set-up of the steady experiments. (a) side elevation of the load cell rig, (b) isometric rendered AutoCAD Image of the load cell rig (adapted from Mandal (2011)), (c) image of load cell rig insitu in the flume, (d) plan view of the test rig, (e) image of the load cells removed from the rig, (f) detail of the load cell arrangement.*

recess onto a rigid aluminium connecting rod, and connected to the end of the two load cells described above. Once installed, the block sits approximately 1 mm from the bottom of the flume, so that no point of the body comes into contact with the flume (even under loading). The front face is approximately 1.3m from the inlet.

The key variables examined during these experiments are flow (or volume flux), the water depth, and the force on an emergent body. These variables cannot be measured directly. Hence, the processes to infer their values are described.

2.3.4 Force measurement

The forces on the emergent body are determined using the test rig described earlier and shown in Figure 2.5. Voltage outputs from the local Wheatstone bridges are logged with two USB digitisers to the hard drive of a laptop. This voltage varies linearly with applied moment and is measured to an accuracy of 0.03%. Due to the serially mounted nature of the test rig, a small degree of coupling is observed between the two load cells, and so a calibration was conducted taking account of both orthogonal load cell output voltages when calculating an applied moment in one direction.

The calibration procedure involves fixing the test rig to a bench, as it would be mounted in the flume, and incrementally applying weights via a pulley system and cable attached to the end of the second load cell. This applies a known moment to the measuring system and the process was repeated and recorded for the transverse and drag directions in both positive, and negative senses. The pulley system ensures minimal frictional losses are experienced. Each of the individual masses are weighed with a precision electronic scale to an accuracy $\pm 10^{-5}$ kg. The calibration equation 2.25 is given as

$$\mathbf{M}_{\mathrm{n\times p}} = \mathbf{V}_{\mathrm{n\times q}}\boldsymbol{\beta}_{\mathrm{q\times p}} + \boldsymbol{\varepsilon}_{\mathrm{n\times p}} \tag{2.24}$$

$$\begin{bmatrix} M_{\mathrm{D}1} & M_{\mathrm{L}1} \\ M_{\mathrm{D}2} & M_{\mathrm{L}2} \\ \vdots & \vdots \\ M_{\mathrm{D}n} & M_{\mathrm{L}n} \end{bmatrix} = \begin{bmatrix} 1 & V_{\mathrm{D}1} & V_{\mathrm{L}1} & V_{\mathrm{D}1}V_{\mathrm{L}1} \\ 1 & V_{\mathrm{D}2} & V_{\mathrm{L}2} & V_{\mathrm{D}2}V_{\mathrm{L}2} \\ 1 & \vdots & \vdots & \vdots \\ 1 & V_{\mathrm{D}n} & V_{\mathrm{L}n} & V_{\mathrm{D}n}V_{\mathrm{L}n} \end{bmatrix} \begin{bmatrix} \beta_{1,1} & \beta_{2,1} \\ \beta_{1,2} & \beta_{2,2} \\ \beta_{1,3} & \beta_{2,3} \\ \beta_{1,4} & \beta_{2,4} \end{bmatrix} + \boldsymbol{\varepsilon}$$

$$\boldsymbol{\beta} \;=\; (\mathbf{V}^{\mathrm{T}}\mathbf{V})^{-1}\mathbf{V}^{\mathrm{T}}\mathbf{M} \tag{2.25}$$

Here, n is the number of observations, p is the number of response variables in the regression and q is the number of predictor variables. $\mathbf{M}$ is the response matrix of applied moment pairs, and $\mathbf{V}$ is the design matrix of predictors. The first column of the design matrix is made of ones (to provide an intercept term), the second and third columns correspond to pairs of observed voltages corresponding to the pairs of observations in the response matrix, and the fourth column is a interaction term as the pairs of voltage measurements are correlated. This correlation between terms in the design matrix can cause an issue with some forms of multivariate regression, where $(\mathbf{V}^{\mathrm{T}}\mathbf{V})^{-1}$ can become close to singular and yield large variances. However, this was assessed and a suitable multivariate regression technique was used. The residuals term, $\boldsymbol{\varepsilon}$ is used to assess the suitability of the model.

In order to solve for the parameter matrix, β, a multivariate general linear model was used in MATLAB, utilising the `mvregress` function. For loads between ±10.26 N, (Moments between ±2.41 Nm) in both drag and transverse directions, the calibration matrix, $\boldsymbol{\beta}$, along with the corresponding standard errors for the parameters is given below;

$$\beta = \begin{bmatrix} 0.01361 & -0.01358 \\ -0.2421 & -0.0173 \\ 0.1080 & -3.5676 \\ 0.0626 & 0.1224 \end{bmatrix}, \quad S.E. = \begin{bmatrix} 0.0017 & 0.0014 \\ 0.0004 & 0.0003 \\ 0.0060 & 0.0048 \\ 0.0089 & 0.0072 \end{bmatrix} \tag{2.26}$$

The calibration produces a very good fit to the data as seen in Figure 2.6. The standardised residuals show homoscedasticity, indicating that the assumption of normally distributed residuals from the maximum likelihood regression algorithm is reasonable (Berry and Feldman, 1985), and the regression can be considered as valid. The same process was repeated for the calibration data without the correlation term included as a test. In this case (not plotted here) the regression produced a calibration which showed obvious hetroscedasticity in the equivalent residuals plot, and caused the predicted zero moments to shift to a positive value under increasing positive orthogonal load. This problem is not present when the correlation term is

included in the regression (as in Figure 2.6). The calibration essentially defines two separate surfaces for the transverse and drag moment pairs based on the two corresponding measured voltages, and the product of the voltage pair. These surfaces are used to convert the voltages into moments via a lever arm.

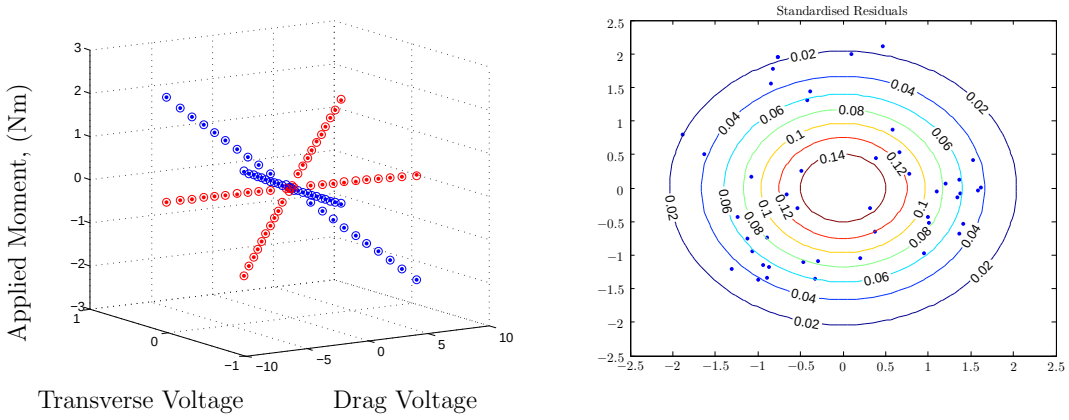

(a) (b)

Figure 2.6: *(a) Three dimensional representation of the moment calibration surfaces, Drag moment measurements ●, Drag moment predictions ○ circles, transverse moment measurements ● dots, transverse moment predictions ○ circles. (b) Standardised residuals from the regression.*

Moment time series are captured for each test in the drag direction and transverse direction, usually for a duration around 200 seconds. This is done to ensure that the full flow conditions had sufficient time to develop between each change in pump frequency. Once the conditions had stabilised, an image sequence was captured for the light attenuation technique, and a still image of the side profile was taken. Due to the steady nature of this set of tests, it is possible to time-average the moments in the following ways.

$$\overline{M_D} = \frac{1}{T}\int_0^T M_D dt, \qquad \overline{M_{L,RMS}} = \left(\frac{1}{T}\int_0^T {M_L}^2 dt\right)^{\frac{1}{2}} \tag{2.27}$$

A simple arithmetic mean is sufficient for the drag load cell as in (2.27). However, the transverse load cell records fluctuating moments in both positive and negative

directions, and so a simple mean over time produces an average moment of zero. For this reason the root-mean-square (RMS) moment is used for the transverse load cell. In order to convert these moments into a full-body force they must be divided by the lever arm, L_A, from the fixed support, to the centre of applied force on the body. This lever arm varies for every measurement of force on the body, as the position of the centre of force application depends on relative contributions of the components of fluid pressure exerted on the surfaces, and consequently on the water level and the velocity of the flow. In order to determine the lever arm, and therefore calculate the body forces, the latter quantities are required. As an approximation the point of application is assumed to be located at $h_1/2$, the centre of the ideal hydrodynamic pressure distribution on the front face. At higher Fr when there is a marked drop in water level at the rear causing an an additional hydrostatic pressure component, so in this case the point of application is changed. However, due to the large hydrodynamic component of pressure, the point of application remains close to $h_1/2$ throughout, so this is the quantity used to compute the lever arm.

2.3.5 Velocity measurement

Flows in the flume were related to the pump frequency in a separate calibration process. This involves measuring the velocity at three positions across the flume, at two depth positions. By symmetry, this provides ten velocity readings per pump measurement, per water depth set-up. The measurements are repeated over three initial still water depths, and eleven pump frequencies.

Due to the relatively shallow conditions in the flume necessary for these experiments, the Vectrino Doppler velocimeter made available to the author could not be used. Probes of this type require a minimum depth of water sufficient to define a control volume below the probe. Due to this restriction the Vectrino probe is inappropriate, so a miniature propeller-meter is used with a digital tachometer instead. Miniature propeller-meters are described in Section 3.3.6. The ten velocity points for each pump and depth configuration were interpolated to a 1 cm grid to provide a velocity field, and the mean velocity was calculated from this.

Clearly, the water level in the flume does not stay at the reference water level once the pump is switched on, but increases with higher pump frequency, and so a calibration

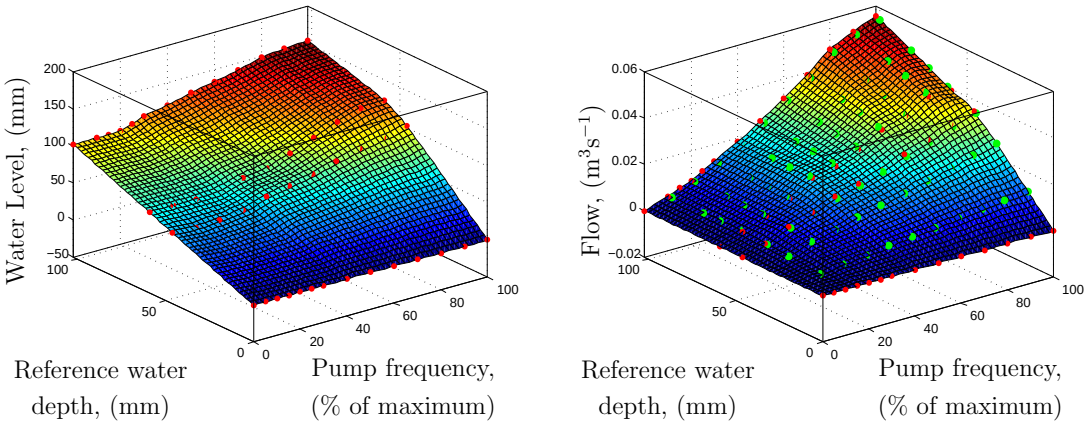

(a) (b)

Figure 2.7: *Pump calibration with flow for different reference water levels. (a) Relationship between water level in flume and pump frequency (as a percentage of the maximum frequency) for different h_i. (b) Relationship between flow and pump frequency for given h_i. Cubic spline surfaces fitted to data (red markers). Green markers indicate flows and levels used in the tests inferred from this calibration.*

is carried out to determine this relationship (Figure 2.7 (a)). This first calibration is used to calculate actual water levels, which allows the flow to be calculated using the velocity measurements. A further calibration is carried out (Figure 2.7 (b)) to relate the calculated flows back to the reference water level and the pump frequency, and this calibration is eventually used in the tests. Cubic spline interpolation is used to fit the two dimensional surfaces to the data in Figure 2.7, and this visibly represents the behaviour of the flow well.

2.3.6 Free-surface measurement

Two independent approaches are used to determine the free-surface elevations in the tests. Both adopt image processing, but in different ways. The first technique uses a light attenuation methodology relating the absorbance of light through water containing a fixed concentration of dye with depth, whereas the second uses orthorectification and digitisation to define the free-surface relative to known measured control points. Capacitance type wave gauges were rejected as an option due to restrictions of the flume access (the top is sealed).

2.3.6.1 Light attenuation measurement

The physical law relating absorbance of light through a transmissive medium to distance travelled through it, is commonly referred to as the Beer-Lambert law (Lambert, 1760; Beer, 1852). More specifically, here the derivation by Lambert (1760) is referred to. This relationship states that there is a logarithmic dependence between the transmissivity of a medium, to the distance light travels through it. Transmissivity can be described by the intensity ratio of light measured at depth z, $I(z)$, with that where no absorbent medium is present (at depth zero in this case), I_0. The ratio, $\frac{I(z)}{I_0}$, follows the relationship (2.28) through an ideal medium.

$$\frac{I(z)}{I_0} = e^{-\beta z} \tag{2.28}$$

$\frac{I(z)}{I_0}$ can be obtained by taking images (with a digital camera fixed on a tripod) of light passing through a medium at depth z, and at depth zero. By dividing the pixel values for the image at depth z, by the corresponding pixels at depth zero, the transmissivity is obtained for each pixel location. A coordinate system based on known points can be defined, so that the 'normalised' pixel values ($\frac{I(z)}{I_0}$) can be referenced spatially. By taking images at known water depths, a plot of $\ln(\frac{I(z)}{I_0})$ and water depth should yield a straight line, of gradient β, the absorbance coefficient. The camera is focussed on a mirror positioned at 45° directly below the flume (Figure 2.8 (a)). The regions where the depths based on average light intensity are determined are indicated in Figure 2.8 (b).

The result of these depth measurements is that the region immediately surrounding the obstacle could be determined to a good accuracy for flows which do not perturb the free-surface to a great extent. When there are large deviations from a horizontal free-surface, light is refracted and scattered, reducing the effectiveness of the approach.

Fundamental requirements for (2.28) to be true are that monochromatic light is used and that no scattering occurs. The set-up adopted violates these assumptions as the light source used was not monochromatic. This results in the data being

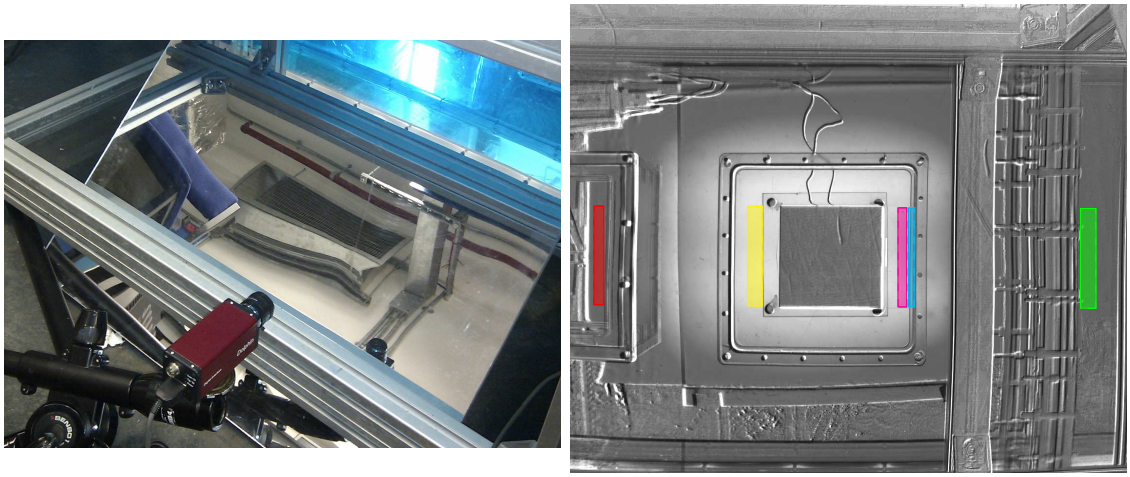

(a) (b)

Figure 2.8: *(a) Camera used to capture intensity of light passing through dyed water focussed on 45° mirror (b)* $\frac{I(90\text{mm})}{I_0}$ *normalised image showing regions where pixel values were used for intensity - depth calibrations. Flow from right to left during tests.*

observed to fall onto a curve in log $\frac{I(z)}{I_0}$ space, rather than on a straight line. For the purpose of this study, it is not necessary to investigate these deviations, but to fit an appropriate curve to the data in order to produce a working calibration. The curve chosen for this purpose, is a Gaussian function, due to its similar functional form to Equation (2.28). This also produces a better fit to the data than is achieved by fitting (2.28), as can be seen in Figure 2.9. The functional form of the second order Gaussian model used is

$$\frac{I(z)}{I_0} = \sum_{i=1}^{2} a_i e^{(\frac{z-b_i}{c_i})^2} = a_1 e^{(\frac{z-b_1}{c_1})^2} + a_2 e^{(\frac{z-b_2}{c_2})^2}. \tag{2.29}$$

A limitation of this technique, is the region over which it can be applied. The technique requires that a stationary camera be positioned throughout the testing period, and in order to achieve good resolution, this must be focussed on a relatively small region. However, it gives good depth measurements in the vicinity of the block, which is the purpose. A different measurement technique is required to quantify water depths at distances further away from the obstacle.

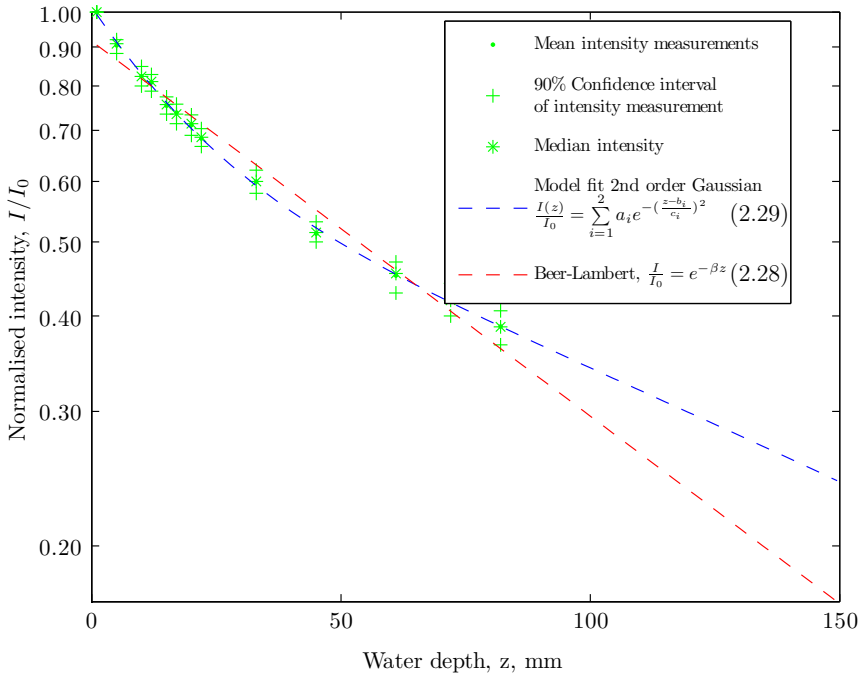

Figure 2.9: *Intensity-Depth calibration on a logarithmic scale for the green region in Figure 2.8 (b).*

2.3.6.2 Ortho-rectification and digitisation.

Knowing the limitations of the previously described technique and its very focussed region of interest, a simpler method is used to capture the side water surface profile for each test, as quantities are also required far from the block. As the free-surface away from the block is relatively flat across the flume, the side water profile is a reasonable estimate of the mean depth across the flume, and as such has uses for characterising the overall behaviour of the flow. This procedure is similar to the water surface capture techniques which are described in Appendix B, and indeed much of the processing is the same. Further detail may be found there.

As a transparent flume is used, the dyed water surface interface is clearly visible from the side. By measuring four fixed control points in the plane of the transparent side (the minimum necessary to define a projective transform), the position of the water surface against this plane can be measured. A standard five mega pixel colour digital camera was used to take photographs of every test from approximately the same location, making sure the same control points were visible in each photograph.

By applying a projective coordinate transform to the pixel location of each control point, the same transform allows the edge of the water surface to be converted from pixel space, into orthorectified real world coordinates based on the control point positions. As the coordinate system is defined on the plane of the flume side any known point visible to the camera can be used as a control point and measured. It is found that the addition of extra control points to the transform does little to increase the accuracy (possibly because the four control points on the flat flume side are very easily identified), and in some cases can degrade it. Distortions within the face of the defined coordinate system are at a minimum. In the unsteady experiments of Chapter 3 the coordinate system is defined on the face of a block (a representative model building fitted with pressure transducers). An exercise was carried out with this set up comparing the known positions of transducer centroids on the building sides with those measured in a rectified image with a coordinate system defined. In this case, measurements are within one millimetre, or approximately the size of a pixel when the photograph is taken fairly orthogonally to the face of the block. Similar accuracy is achieved in these steady tests.

The free-surface is manually captured for each test by digitising the orthorectified images (Figure 2.10 (b)) and the process is repeated for each test so that profiles can be determined (Figure 2.10 (c)). A key point is that the free-surface varies little across the width of the flume overall in the region upstream and downstream of the block and so this technique provides a robust measurement over the full length of the flume. In particular the values of h_2 and h_1 are very consistent across the flume with the greater variations seen in h_d, immediately behind the block, which was checked manually with a rule and with the light attenuation method. The pixel position of the control points changed for every test as the camera was hand held, so the coordinate system was defined separately for each test. The projective transform ensured that the profile was captured consistently from different camera angles. Accuracy was limited to the order of one pixel width. As in the case for the unsteady experiments, for most tests this represented approximately 2mm, so the precision of this technique can be considered to be around $\pm$1.0mm.

When combined with the light attenuation method for capturing water heights in the vicinity of the building all the necessary quantities can be captured.

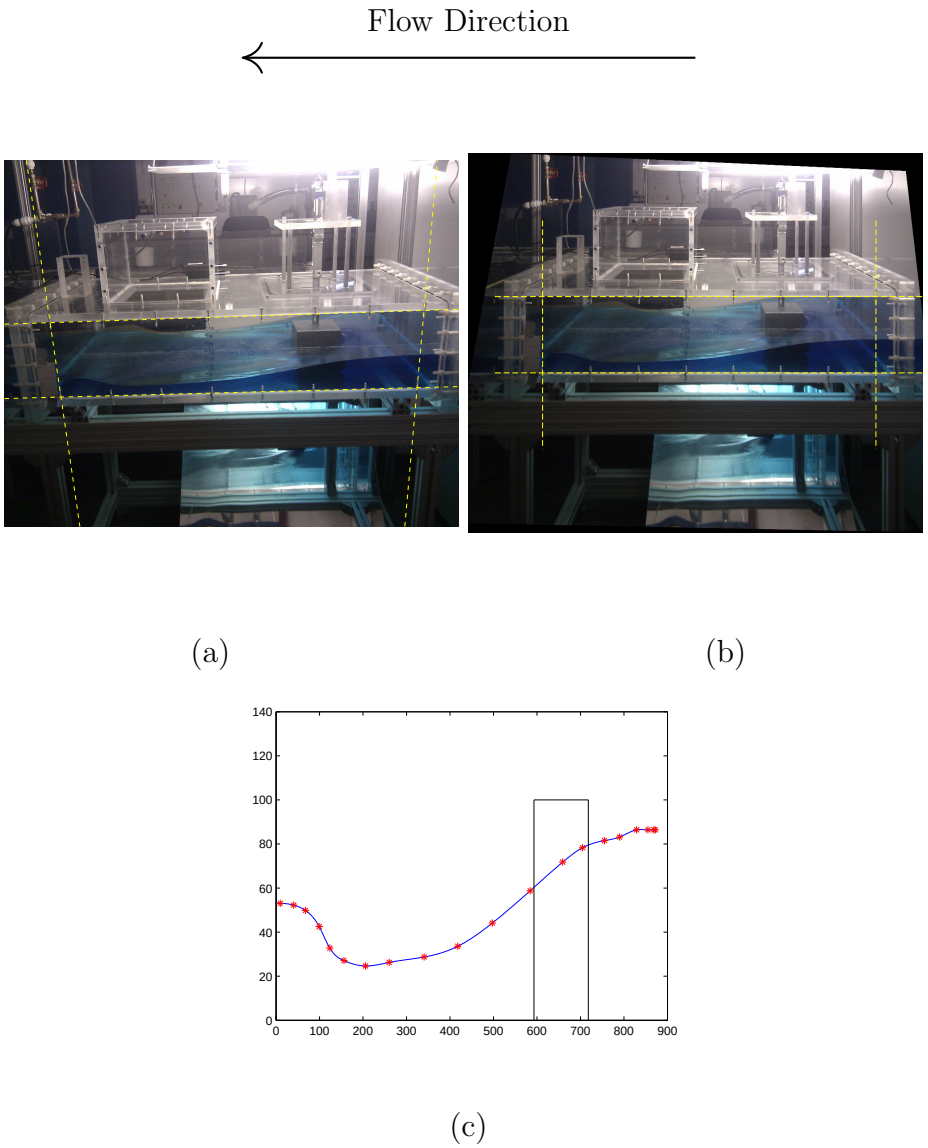

Figure 2.10: *(a) Side profile before orthorectification showing orthogonal lines of known measured points used as a basis for a coordinate sytem. (b) Side profile after orthorectification showing same gridlines. (c) Profile (in milimetres) digitised from orthorectified side image (b). Note, Y-axis is stretched, flow from right to left in all images and plots. X-axis defined in the negative X-direction because of flume access.*

2.4 Experimental results

Following the necessary calibrations described in the previous sections, a set of experiments are conducted using the set up described in Section 2.3, varying both the flow past a fixed block ($b/w = 25\%$) and the initial water depth, h_i, (effectively correlated to the total volume of water within the closed system). The aim of these experiments is to determine how the force on an emergent body varies with upstream steady flow conditions, u_1, h_1, verify the framework of Qi et al. (2014) and provide values for the necessary parameterisations in a one-dimensional model.

2.4.1 Observations

At rest, the water level is constant throughout the flume at an initial depth h_i. This depth is dropped between each set of tests by removal of water through the flume drain, to provide the range of h_i. The concentration of dye in the flume remains constant throughout. The pump is increased in power at regular intervals of 10% of the pump's maximum speed from 0% to 100%.

Figure 2.11 illustrates the four main phases observed in these experiments. All images and corresponding profiles are for constant flows some time after the pump frequency is changed. When the pump is activated, water in the flume accelerates until it reaches equilibrium with a constant flow. At this point the measurements are made, and the images in Figure 2.11 captured. For slower flows (Figure 2.11 (a)), changes in water level are barely perceivable between the front and rear of the obstruction and if left undisturbed, a regular vortex street forms in the wake for some Q, h_i combinations. This only occurs for slower flows where the downstream flow remains subcritical (the wake remains attached, $h_1 \approx h_d$).

For each h_i, the pump is incrementally increased in power, and the flows in the flume are allowed to increase in line with the calibrations, and settle into a steady state (Figure 2.11 (b)). At a critical point, the flow conditions around the structure change, and a large drop in water level between the front and the rear of the structure is observed (Figure 2.11 (c)). The vortex street has disappeared by this point and the wake is turbulent. Further downstream of the structure a hydraulic jump is observed, beyond which the water levels recover and the velocities reduce.

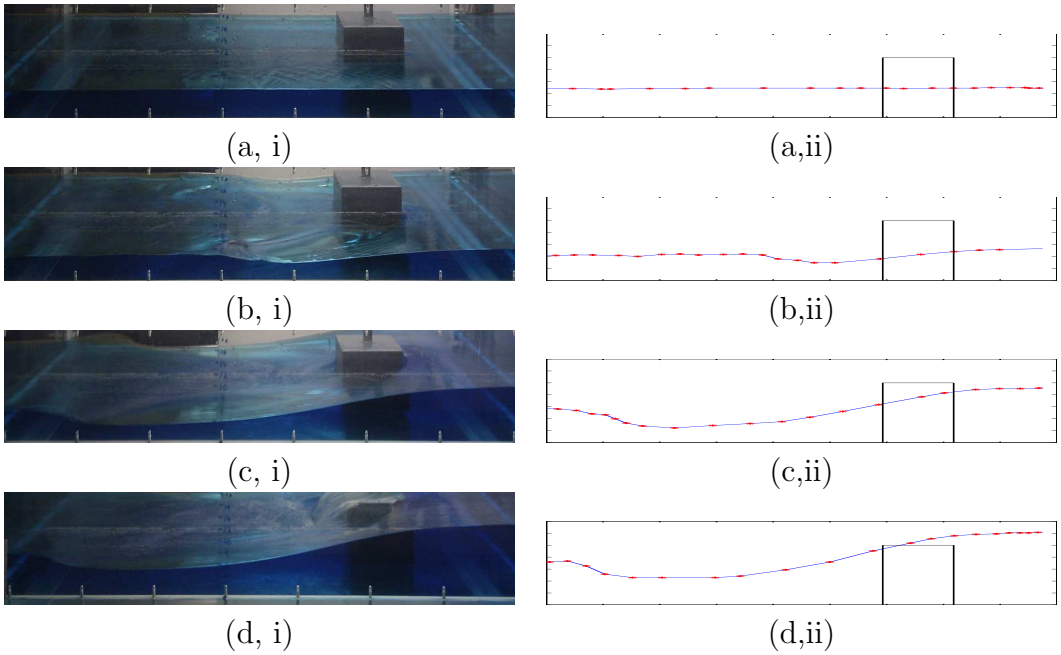

Figure 2.11: *Steady free-surface profiles for* $h_i = 45mm$*, (a),* $Fr_1 = 0.180$*,* $Fr_d = 0.184$*, (b),* $Fr_1 = 0.418$*,* $Fr_d = 0.693$*, (c),* $Fr_1 = 0.411$*,* $Fr_d = 0.881$ *and (d),* $Fr_1 = 0.421$*,* $Fr_d = 0.931$*. Flow direction right to left for all.*

In Figure 2.11 (d), the flow over-tops the structure, and the behaviour remains similar to the previous state.

2.4.2 Water height

A summary of the water heights for all of the steady tests can be found in Figure 2.12. Here two distinct regimes can be seen in the data directly. A regime, where the flows are subcritical, and the water levels are similar between the front and rear of the block (close to the dashed blue line), and a choked regime, where the free-surface deforms and produces a reduction in water level downstream of the block. For an increase in h_1 in the subcritical regime, there is an equal increase in h_d. This is characterised by the upper trend line in Figure 2.12 around the dashed blue line. Flows are increased to produce an increase in h_1. Beyond a critical point, an increase in flow (and therefore increased h_1) will not result in a significantly larger downstream h_d. Where this occurs the flow is said to be "choked". The transfer from subcritical to choked states, occurs rapidly, as is shown by the data in Figure

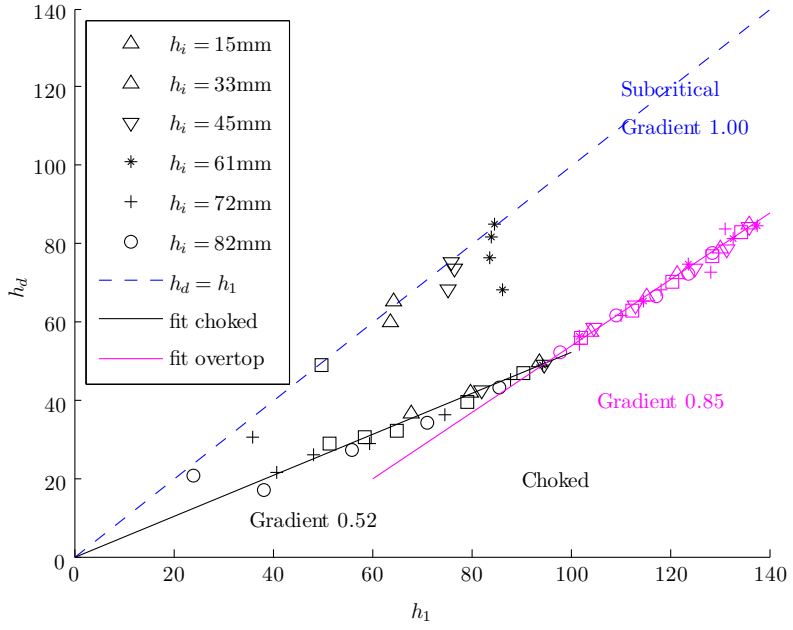

Figure 2.12: *Upstream, h_1, and downstream, h_d, water depth. Magenta indicates over-topping of the structure occurred in the test.*

2.12. Very few data fall in the intermediate states.

Another feature that can be determined from Figure 2.12 is the effect of over-topping. To represent buildings of a finite height, the height of the test specimen is limited to $H_b = 100$mm. The result of this is clearly highlighted by the magenta data. Though all tests were choked by the point of over-topping, there is a change in the gradient of the choked regime once over-topping can occur ($h_1 > 100$mm). The gradient switches so that it becomes closer to the subcritical gradient of 1.

In order to confirm the critical depth and this transition between the two regimes, we need to examine the specific energy. For a constant flow, Q, a plot of specific energy versus depth will yield a "C" shaped curve. Where the specific energy is at a minimum (to the far left of the curve), the flow is said to be critical. Below this critical depth, the flow is choked, and above it the flow is subcritical. In order to perform this particular comparison for our tests (which did not all share common flows), the specific energy and water depth are transformed into dimensionless quantities. The principle of the relationship between downstream specific energy,

H_d, and water depth, h_d, are found in Figure 2.13.

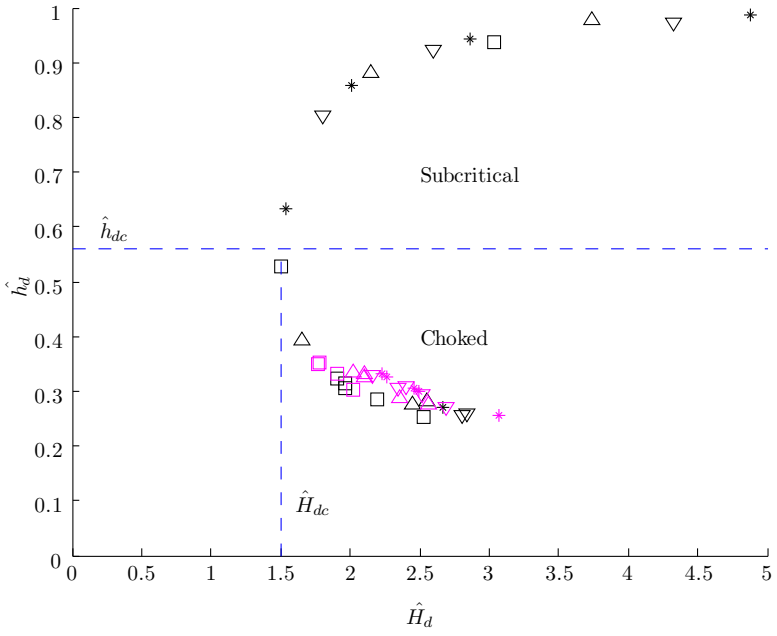

Figure 2.13: *Downstream dimensionless specific energy, $\hat{H}_d$, and downstream dimensionless water depth , $\hat{h}_d$. Magenta indicates over-topping of the structure occurred in the test. $\hat{h}_d = h_d/H_1$ and $\hat{H}_d = H_d/H_1$, where $H_1 = \frac{u_1^2}{2g} + h_1$.*

There is a clear transition between the subcritical and choked regimes in Figure 2.13, marked by the minimum specific energy. The data points in each regime correspond to those found in Figure 2.12 to be in the subcritical or choked regimes. Choosing the location where to measure various water depths is fairly straight forward for h_1 and h_2, as the surface in these regions is usually fairly calm and level. However, some judgement is required for the determination of h_d. This is perhaps best illustrated by Figure 2.14. Flow direction is shown as right to left for consistency with the images captured (flume is only accessible from one side).

The green location (•) for h_d is chosen for consistency (100mm from the rear of the block). This is because choosing a fixed location further back (say at 400mm •) means the position of the hydraulic jump when it occurred is sometimes beyond the measurement point, and sometimes before. The distance 100mm from the block, always falls upstream of any hydraulic jump present. The minimum point (•) pro-

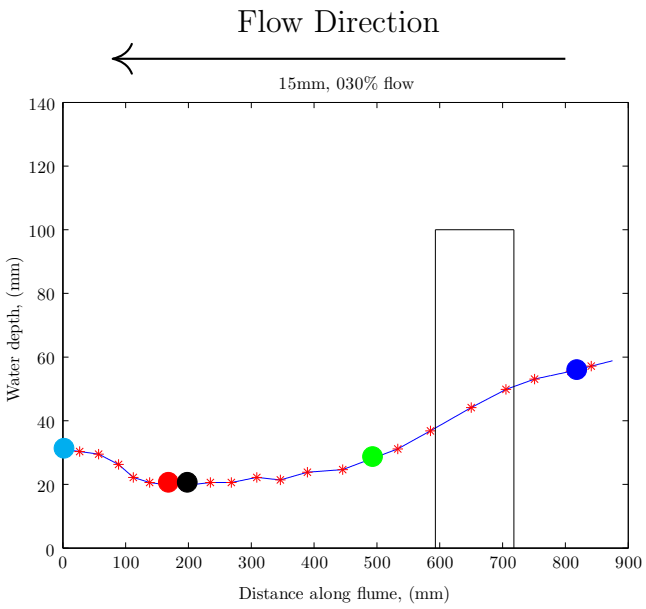

Figure 2.14: *Example profile showing location (relative to the coordinate system used in the tests) chosen for h_d (●) at 100mm behind the block, and an alternative (●) at the point of minimum water depth, as well as (●) at 400mm back from the block. (●) and (●) are the locations of h_1 and h_2 measurements respectively. Flow right to left.*

duces good results, and highlights the difference in the regime post over-topping well. However, as it does not occur at a fixed location the results are inconsistent. The point of minimum depth is also affected by instabilities in the vicinity of the hydraulic jump.

Examining the results for the up and downstream dimensionless water depths, with dimensionless flow reveals a clear trend. Figure 2.15 shows that up to certain flows (corresponding with the critical depth in Figure 2.13), the difference in water level is small between the front and rear of the obstacle, but at higher flows we see a larger difference. The position of the free-surface in the vicinity of the block will impact on whether the force contribution from hydrostatic loading is significant as we expect to see greater hydrostatic components for large differences in depth between the front and rear of the structure.

The results show similar behaviour to those of Qi et al. (2014) as expected. However, there are key differences between Qi et al. (2014) and these experiments. Due to the height of the test specimen being limited to that of a representative scaled structure

(rather than continuing to the top of the flume in Qi et al. (2014)), the range of water depths with which the equipment could be operated without over-topping occurring was limited. Qi et al. (2014) rejected the data for the lowest initial water depth, h_i, as these appeared to be governed by frictional effects. For the same reason, Qi et al. (2014) removed tests corresponding to the three lowest pump frequencies. These limitations and frictional observations were also true of the experiments described here and they are treated similarly.

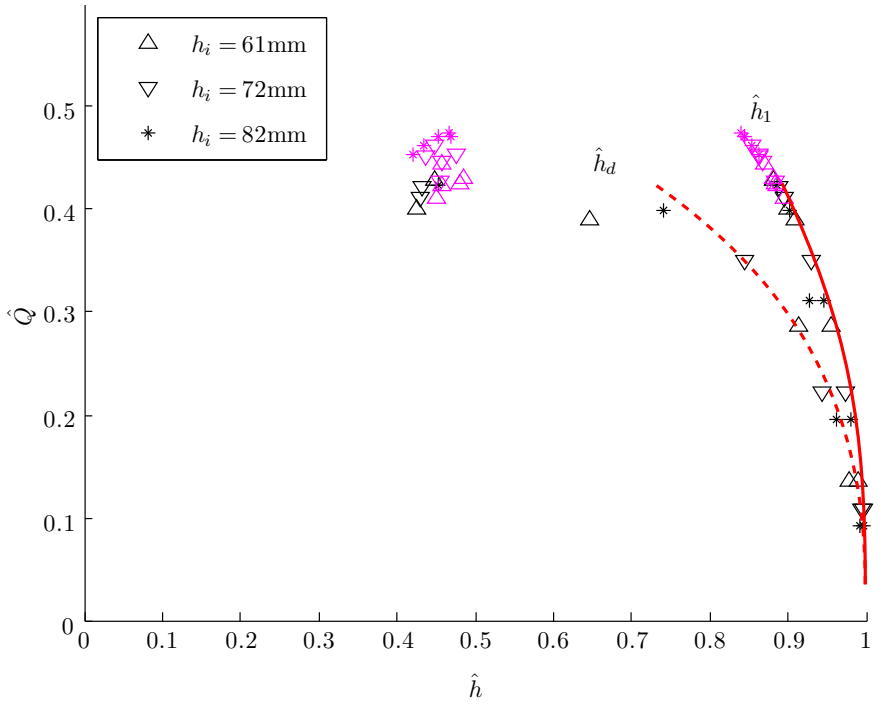

Figure 2.15: *Variation of upstream and downstream dimensionless water levels, $\hat{h}_1$ and $\hat{h}_d$, with dimensionless flow, $\hat{Q}$. Data points in magenta indicate over-topping of the structure occurred. In all $\hat{h}_1$ (solid), $\hat{h}_d$ (dashed) pairs, $\hat{h}_1 > \hat{h}_d$, the separation is indicated by the two theoretical red lines. h_i is the initial water level.*

Due to the depth restriction, faster flows tended to over-top the structure, as we saw in Figure 2.11 (d). For all flows where this occurred the flow was choked so there are no significant changes to the critical behaviour compared to the observations of Qi et al. (2014). However, it does serve to limit the top-end measurements which could be recorded reliably using this set-up. Faster flows without over-topping can be achieved using a lower initial water depth, but this causes the frictional effects seen by Qi et al. (2014) to dominate. By observing the over-topping behaviour it

is possible to assess whether the inclusion of over-topping would be of benefit. For $H_b < h$ the framework of Qi et al. (2014) works well and these tests seem to support that assertion.

2.4.3 In-line forces

As in the work of Qi et al. (2014); by solving (1.29) for Fr_d as a function of Fr_1, a maximum or choked value of Fr_1 is determined, which is noted as Fr_{1c}. Note that the solution to (1.29) is multivalued, but the solutions that produce an increase in specific energy between the throat and the downstream position Fr_d are not physically feasible, so the solution becomes single-valued. In order to solve this and (1.30), assumed values are required for C_D and C_H. C_D has been determined from (1.23) and values from literature, which is confirmed to be reasonable from the subcritical portion of Figure 2.16 (a). However, the higher hydrostatic force present in the choked regime will still contain a component of form drag, so it is not possible to measure C_H directly and this therefore must be inferred.

To achieve this Qi et al. (2014) use a new coefficient, C_K, which is defined by normalising the measured average drag force, ($\overline{F_D} = \overline{M_D}/L_A$), by $\frac{1}{2}\rho bg(h_1^2 - h_2^2)$. In particular, C_K can be written as (2.30).

$$C_K = \frac{2\overline{F_{\mathrm{D}}}}{\rho bg(h_1^2 - h_2^2)} = C_D \frac{Fr_1^{\frac{2}{3}}}{Fr_1^{-\frac{4}{3}} - Fr_2^{-\frac{4}{3}}} + C_H \frac{Fr_1^{-\frac{4}{3}} - Fr_d^{-\frac{4}{3}}}{Fr_1^{-\frac{4}{3}} - Fr_2^{-\frac{4}{3}}} \tag{2.30}$$

The framework applied so far takes the analysis up to and including the critical point, $Fr_1 \leq Fr_{1c}$. For the missing part, choked flows, we need to consider the effect of the hydraulic jump. Across a hydraulic jump, energy is not conserved, but momentum is. In order to relate the transition between S_d and S_2, momentum flux is conserved as in (2.31)

$$\begin{aligned} \hat{M}_d &= \hat{M}_2 \\ \frac{1}{Fr_d^{\frac{4}{3}}}\left(\frac{1}{2} + Fr_d^2\right) &= \frac{1}{Fr_2^{\frac{4}{3}}}\left(\frac{1}{2} + Fr_2^2\right). \end{aligned} \tag{2.31}$$

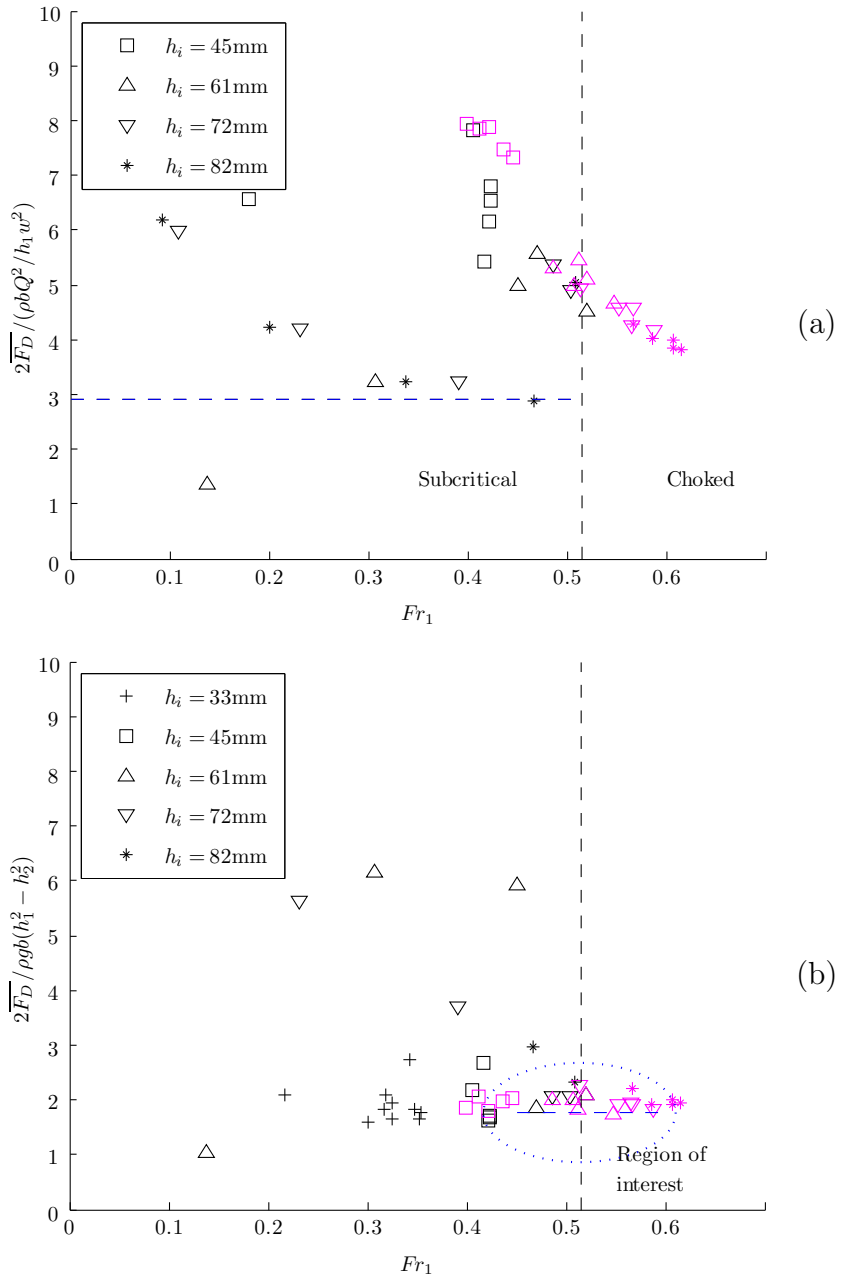

Figure 2.16: *Force coefficients, with varying upstream Froude number. (a) Drag coefficient, C_D, ($2F_D/(\rho b Q^2/h_1 w^2)$) with varying upstream Froude number, Fr_1. For subcritical flows, C_D approximately follows a constant value above very low upstream Fr_1, in line with predicted $C_D \approx 2.91$. (b) Coefficient C_K ($2\overline{F_D}/(\rho g b(h_1^2 - h_2^2))$). C_K converges to a single value in the choked regime. In both plots, magenta indicates over-topping of the structure occurred in the test. h_i is the initial water level.*

Fr_{2c} is obtained by the solution of (2.31), using Fr_{dc} from (1.30) and a value of C_H.

Focusing only on the region of choked Fr_1, Figure 2.16 (b), shows that the value of C_K can be estimated as ≈ 1.77. By substituting initial estimates of the choked values $Fr_{1c}, Fr_{dc}, Fr_{2c}$ into (2.30), and solving for C_H, the value can be returned to (1.29) and (1.30) to converge iteratively on the critical values of Fr, and the implied value of C_H. Following this double-iterative procedure, a value of 0.67 can be assumed for C_H, providing the solution of (1.29) in the process. The iterative procedure converges quickly from initial estimates of $Fr_{1c} = 0.5$, $Fr_{dc} = 1$ and $Fr_{2c} = 1$ to give a value of $C_H = 0.67$ and shown in Table 2.1.

Table 2.1: *Estimation of C_H by iteration.*

Iteration	Fr_{1c}	Fr_{dc}	Fr_{2c}	Estimated C_H	Change in C_H
0	0.5	1.0	1.0	0.5638	
1	0.5229	0.9268	1.0804	0.6549	0.0911
2	0.5189	0.9145	1.0955	0.6707	0.0158
3	0.5149	0.9123	1.0982	0.6718	0.0011
4	0.5149	0.9122	1.0984	0.6720	0.0002
5	0.5149	0.9121	1.0984	0.6721	0.0001
6	0.5149	0.9121	1.0984	0.6721	0.0000

Now that C_D and C_H are known, a general expression for force can be determined based only on the conditions of the flow which Qi et al. (2014) expressed as (1.31).

Using (1.29), (1.31) and (1.32) which can now be parameterised with the empirical values found in the experiments, gives us the ability to infer the force on an obstruction based only on the upstream flow condition. This is characterised by the upstream Froude number, Fr_1 (as we can also calculate Fr_d by solving (1.29)). This is an important result and allows us to use the model in a predictive sense for the forces on a block (with a ratio of 25%) in the experiments using only the upstream conditions. By doing so it provides an alternative method to parameterise f_D in (2.10), and provide further insight for extending to unsteady situations. Figure 2.17 shows similar information as Figure 2.15, but plotted in a different way. Again, the low initial water depth data displays different behaviour and the lowest ($h_i = 15$mm and 33mm) are not plotted here, but $h_i = 45$mm is shown this time to demonstrate the tendency for the lower h_i tests (some frictional behaviour is seen in these tests). For $h_i > 45$mm, the data appear to follow the line $\hat{h}_1 \approx \hat{h}_d$ up to a critical point,

where the downstream dimensionless water depth $\hat{h}_2$ drops away abruptly. Here we are seeing the start of a change in flow regime, which we would like to understand further. The framework described by Qi et al. (2014) is represented by the red line and its accompanying choked red value. As is clear by the close alignment of the data with the red line, the framework appears to be capturing the behaviour of the water surface well, for the up and downstream water surfaces in these tests.

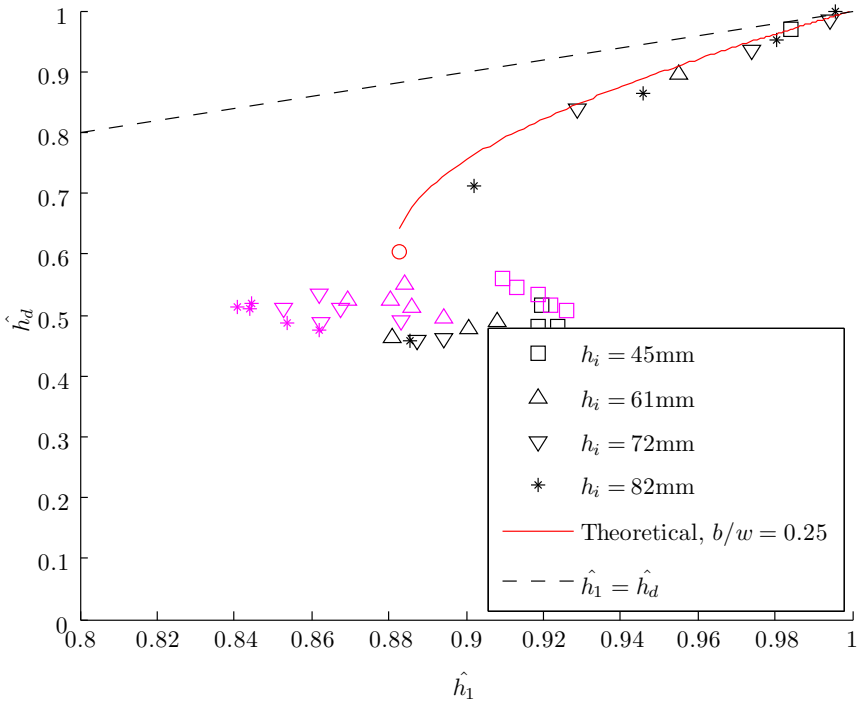

Figure 2.17: *Dimensionless water depth upstream, $\hat{h}_1$, and downstream, $\hat{h}_d$. Magenta indicates over-topping of the structure occurred in the test. Red lines correspond to the theoretical predictions given by the framework (solutions to (1.29)), where ∘ is the choked value.*

Similar behaviour is exhibited in Figure 2.18, where above a threshold upstream Froude number, ($Fr_1 \sim 0.2$), the downstream Froude number, Fr_d, increases and moves away from the line $Fr_1 = Fr_d$. Again, the lower h_i data show this too, but serve to blur the definition of this transition; i.e, they increase at an earlier Fr_1. The low h_i data show an increase in downstream Fr_d at much lower Fr_1. For the data where $h_i > 45$mm, the upstream Froude number where this transition appears to occur is $Fr_1 \approx 0.45 - 0.50$. As before, the data appear to follow the theoretical line derived by solving (1.29), with good agreement. The collapse of the data is very

good, particularly for the deeper h_i, which are less influenced by viscous effects.

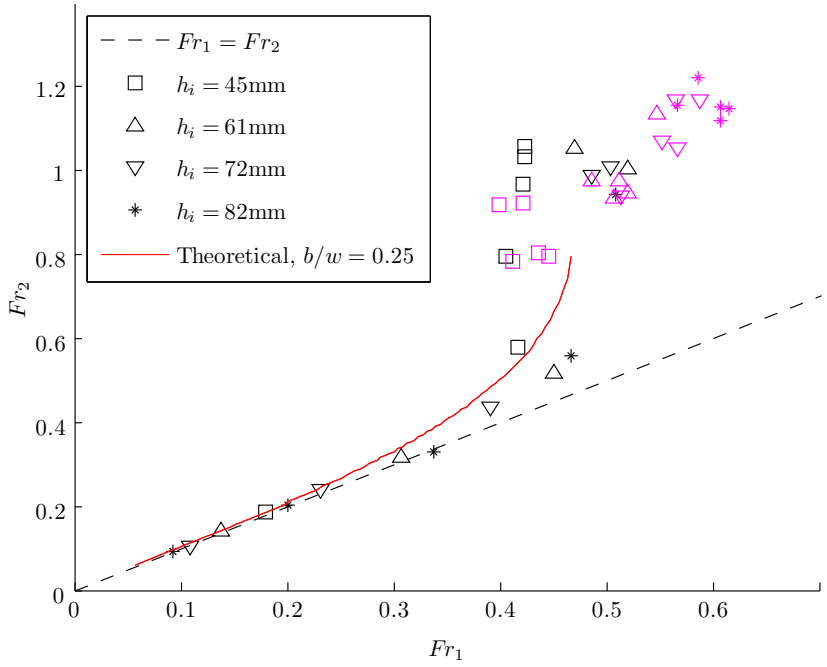

Figure 2.18: *Froude number upstream, Fr_1, and downstream, Fr_2. Magenta indicates over-topping of the structure occurred in the test. Red lines correspond to the theoretical predictions given by the framework (solutions to (1.29)), where ∘ is the choked value.*

The plot in Figure 2.19 shows the relationship between upstream Fr, and drag force normalised as $\overline{F_{\mathrm{D}}}/\rho g^{1/3} h_1^{4/3} u_1^{4/3}$, which is λ from (1.32). While the agreement with the theoretical curve shows some scatter due to few suitable tests of high h_i, that do not over-top, there is a reasonable collapse of the data particularly in the choked regime. In particular, the overall behaviour of λ can be seen in this figure, and the importance of taking account of the flow state in estimation of structural forces at a given instance. There is a clearly defined change in the behaviour as Fr_1 approaches Fr_{1c} which is captured by the λ parameter well.

The contribution between hydrostatic and form drag force components cannot be measured directly, but the percentage contributions can be inferred using this framework. The force components can be identified from the right hand side of (1.32) with the first term, $\frac{1}{2} C_D Fr_1^{2/3}$, hydrodynamic, and the second term, $\frac{1}{2} C_H (\frac{1}{Fr_1^{4/3}} - \frac{1}{Fr_d^{4/3}})$, hydrostatic. At critical flow for the blockage ratio in these experiments, $Fr_1 = 0.51$ and $Fr_d = 1.01$. Using these numbers, as percentage contribution of the hydrostatic

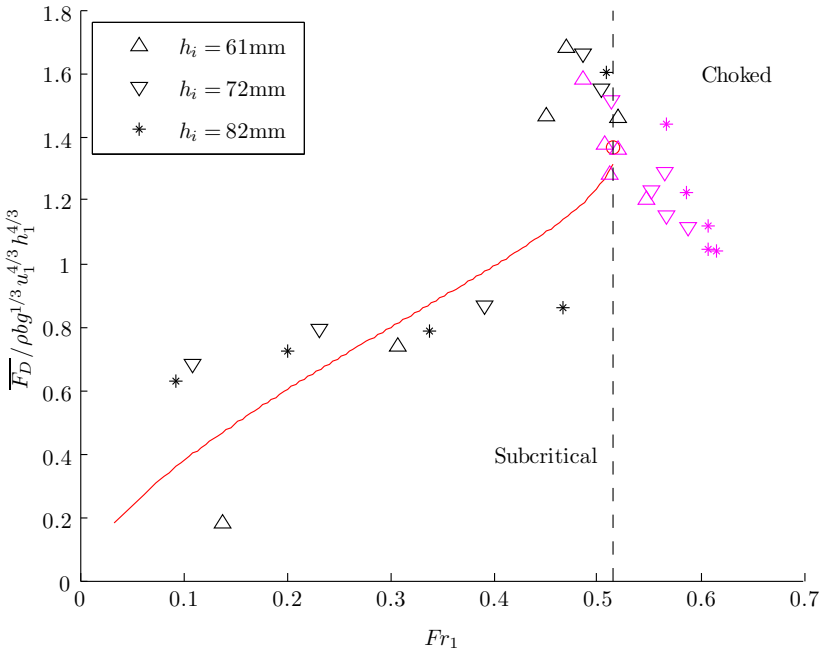

Figure 2.19: *Force normalised as* $\overline{F_D}/\rho g^{1/3} h_1^{4/3} u_1^{4/3}$, *(λ). magenta indicates over-topping of the structure occurred in the test. The red line is a theoretical curve.*

component with respect to the total force, this accounts for 36%. The percentage contribution varies with Fr_1, and the percentage hydrostatic contribution drops to around 17% at lower Fr_1. Figure 2.20 shows how this percentage varies with upstream Froude number.

In a slightly counter-intuitive result, it is clear that although a large difference in water depth is observed between the front and rear of a block at higher Fr_1, a larger contribution is still seen from the hydrodynamic drag compared to the hydrostatic force. This is likely to be due to the u^2 dependency. For larger b/w Qi et al. (2014) saw higher hydrostatic contributions which is intuitive because as b/w increases the behaviour will tend to $b/w = 1$, as in a wall. As b/w is increased towards 1 the flow is further restricted and so a build-up of water on the upstream side is expected.

This framework allows prediction of forces, based only on (1.32) throughout both subcritical and choked regimes. Once the water over-tops a structure, assumptions made regarding the blockage ratio are no longer correct, and the flow around the block alters accordingly. The obstacle now provides a blockage to the flow up to

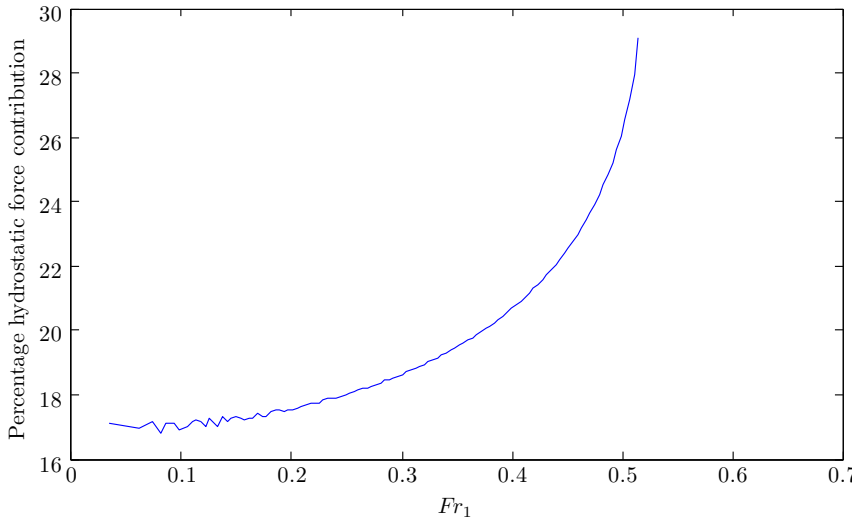

Figure 2.20: *Inferred percentage hydrostatic force component for given* Fr_1.

the top of the obstacle, and zero blockage ratio above this height. The additional resistance to the flow now only comes from frictional drag on the top surface, which we know is much smaller than the pressure drag. As the pressure drag at depths above the height of the obstacle is effectively zero, we see an overestimation of the predicted force once the water over-tops. The tests presented here do not push far beyond the onset of over-topping and as such can only give comment on the regime where flows spill off the back of the block in a nappe. At this point the situation of weir flow provides a reasonable insight (Chadwick and Morfett, 1993), and it is likely that the height of the block, H_b, controls the amount of force it attracts. As flows increase further another regime where $h_1 \approx h_d$ can occur, but at this point the block is submerged. However, the influence of blocking is still likely to be considerable at this stage. Other parallels may be drawn with spillways and stilling basins with baffle blocks (Chanson, 2004). However, in the latter examples, the oncoming flow is always supercritical with $Fr >> 1$ in many cases, so the similarities are somewhat limited.

From a damage to structures perspective, once the water over-tops a building, it is unlikely that any building designed to normal specifications is expected to survive, i.e. the probability that the damage state for collapse is reached tends to one. Structures that may have survived up to this stage are likely to lose their roof, and

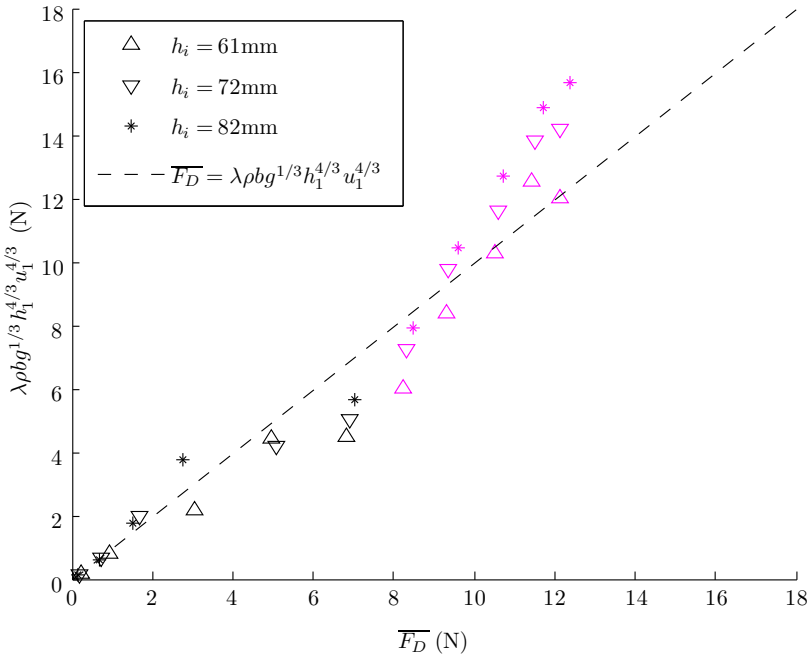

Figure 2.21: *Force versus predicted force (using measured upstream Fr_1, u_1 and h_1, and calculated Fr_d), assumed coefficients in λ calculation, $C_D = 2.91$, $C_H = 0.67$. magenta indicates over-topping of the structure occurred in the test.*

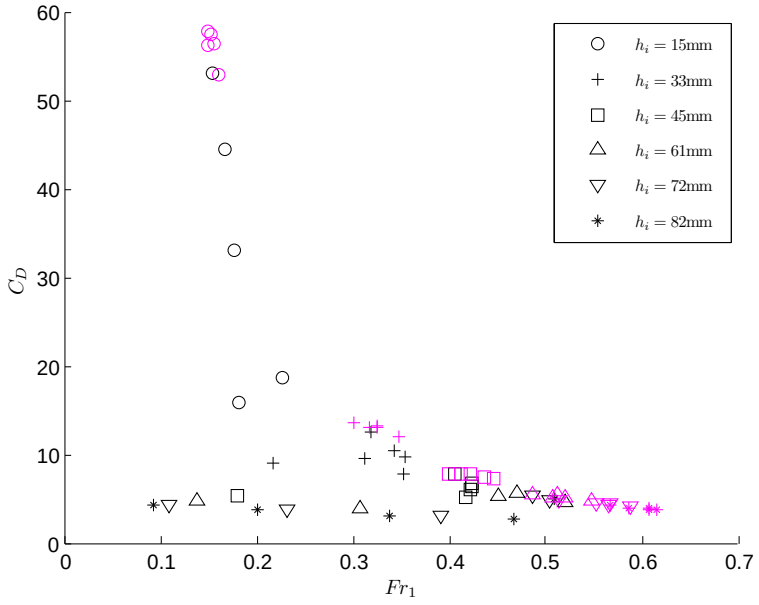

Figure 2.22: *Upstream Froude number, Fr_1 and Drag coefficient, $C_D = 2\overline{F_D}/\frac{\rho b Q^2}{h_1 w^2}$.*

compromise structural stability of the rest of the structure. For the majority of cases this $h_1/H_b < 1$ framework is therefore very relevant.

Figure 2.21 is effectively a plot of observed force versus predicted force. The 45° dashed line represents perfect correlation, and the data collapses onto this line up to the over-topping state. As expected, the predicted force over-predicts the measured force once over-topping occurs as blocking on the part of the flow above the height of the building is removed.

To give some context to the rest of the data which is excluded from the derivation of these force coefficients, the full set of C_D drag coefficient values are plotted in Figure 2.22 for all initial water depths, h_i. This illustrates some of the frictional effects of low initial water depths, and the reasons why these data are excluded from the analysis. The measured drag coefficients are much higher than expected for $h_i = 15$mm and 33mm and this is due to dominance of viscous effects.

2.4.4 Transverse forces

Finally, the influence of other potential forces on the body is checked. Another component which has been ignored up to now in the analysis, is the transverse forces in the direction perpendicular to the oncoming flow. When transverse forces are discussed in this context, this is not the same mechanism as generates transverse for an aerofoil i.e. lift. The dominant source of transverse force, F_L comes from the oscillatory separation of vortices from the trailing edge corners of the obstacle. Some rudimentary analyses are shown here, mainly to rule out its significance to these experiments, but also to the case of tsunami interactions with buildings at full-scale. As detailed in Section 2.3.4, transverse moments are time-averaged using (2.27) for the duration of the experimental measurements (approximately 2 minutes) and divided by the lever arm to determine a mean transverse force, $\overline{F_L} = \overline{M_{L,RMS}}/L_A$. The averaging process will return a quantity slightly lower than the peak transverse force, but it is more consistent in time.

Figures 2.22 and 2.23 presents the force coefficients, for the drag and transverse force. Visually it is clear that the transverse force coefficient C_L is significantly lower than C_D at high Fr_1. However, there are several instances at low Fr_1 where the contribution of transverse forces is significant. Taking a C_L in the experiments corresponding to $h_i = 61mm$ and $Fr_1 = 0.1380$ it can be seen in Figure 2.23, to be of comparable magnitude to the corresponding C_D point in Figure 2.22. Due to the requirements for vortex streets to occur, this behaviour is limited to low Fr_1. In order for a coherent vortex street to form, the wake needs to remain attached, meaning vortex shedding is only observed in these experiments when the flow is subcritical.

Using the highest C_L point for $h_i = 61mm$ (indicated by the red elipse in Figure 2.23) as an example, the times series of the transverse and drag forces can be examined in more detail. This point corresponds to $h_i = 61$mm, pump =10% ($Fr_1 = 0.1380$). By calculating the periodograms in Figure 2.24, significant periodic C_L components can be detected in several of the low Fr_1 tests (red trace), in line with the observation of a regular vortex street in the wake. Measured periods for these wake oscillations where they occur never drop below 1 second, though some periods were higher. The example plotted in Figure 2.24 has a period of roughly 1.43s. For some tests, $h_i = 45$mm $Fr_1 = 0.1800$ for example, C_L was very large, and the oscillations could

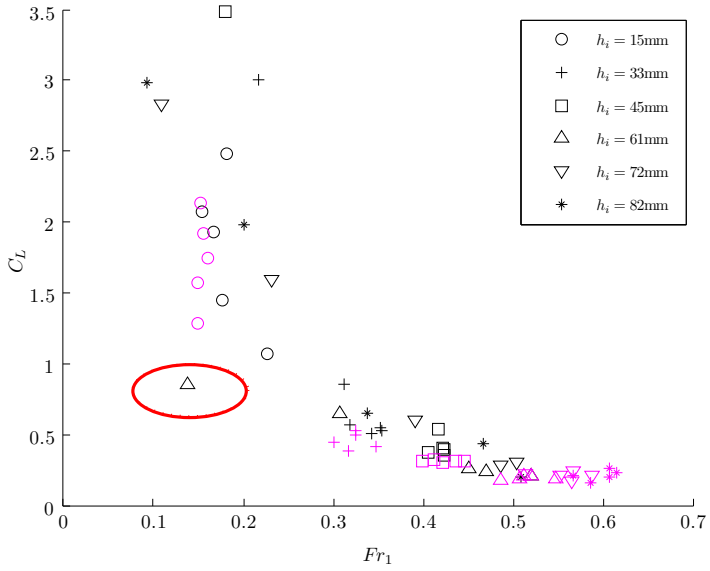

Figure 2.23: *Upstream Froude number, Fr_1, and Transverse coefficients, $C_L = 2\overline{F_L}/\frac{\rho b Q^2}{h_1 w^2}$.*

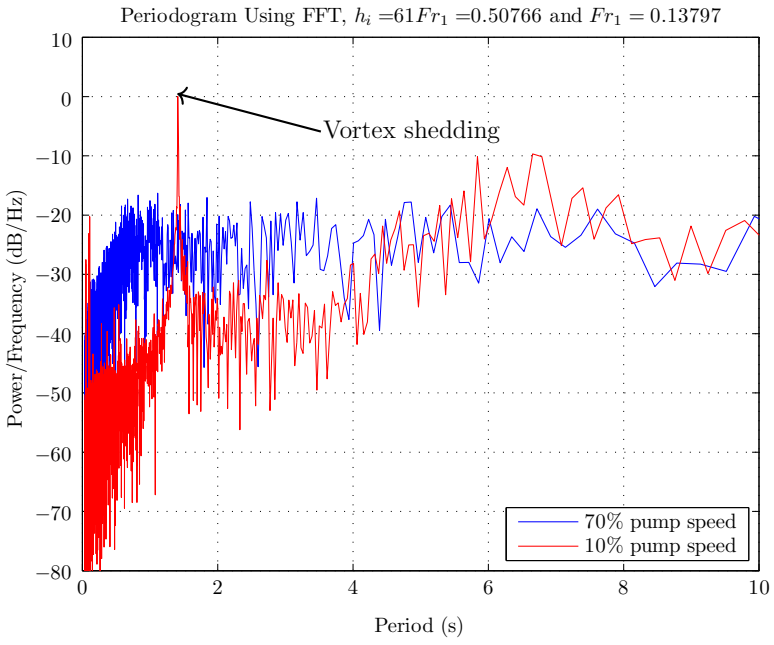

Figure 2.24: *Periodograms for F_L for Initial Water Level, $h_i = 61mm$, 10% pump speed and 70% pump speed.*

be easily detected in the time series. The shedding period for this test was higher than for our previous example at 4.23s. As can be seen, when the upstream Froude number is increased (as the blue trace in Figure2.24), the periodic nature of the transverse force disappears (blue trace).

The large scale tests described in Chapter 3 are designed with a length scaling factor of between 1:50 and 1:100, and these steady test specimens are $125/300 = 5/12$ the scale of the unsteady structures. This puts the length scale for these tests between 1:120 and 1:240. Assuming Froude scaling is used, this means the period scales between $1{:}120^{1/2}$ and $1{:}240^{1/2}$, so an expected prototype scale period would be greater than 10 seconds. The types of structure which are susceptible to tsunami loads (low - mid-rise buildings), have natural periods far beneath this level and generally lower than 1 second and so the oscillations we would see would be highly unlikely to excite the structure dynamically. Coupled with the low magnitude of the oscillatory forces involved, (vortex shedding only occurs at low Fr_1), and the low centre of force application it is very unlikely that vortex shedding will be a significant component of tsunami loading. For taller structures with higher natural periods that could potentially be excited by dynamic forces from transverse wake oscillations, the force is applied at a very low level compared to the overall structure height, hence generating a comparatively small moment. As such, most forces on the structure globally will be quasi-static forces due to the hydrodynamic and hydrostatic components, so the dynamic response of the building is unlikely to be important.

2.5 Application of a steady one-dimensional model

Now that results are available which allow f_D to be parameterised, it is possible to repeat the tests described, as well as those of Qi et al. (2014) in a numerical model in order to verify and extend this model to other applications. The distributed drag term may be applied to many different types of numerical models but as can be observed in the experiments, blocking appears to be very important and must be included. As a proof of concept, firstly (2.9) and (2.10) are discretised in a numerical scheme. A Lax-Wendroff (Lax and Wendroff, 1960) finite difference method is chosen as a simple and well known numerical scheme for solving the shallow water equations

(SWE). To fill up h and uh arrays, we start with an initial condition, and take repeated time-steps. The program outline is briefly given as:

- initialise dt, h and (uh) arrays, define constants like dx, $(1-\phi)$, C_D
- set solution at time-step 0 by initial conditions and begin time loop for nt steps
- estimate h and (uh) at midpoints, and a half time-step
- evaluate derivative at half time-step, take full step
- apply the boundary conditions and end of time loop

The half-step, $n+1/2$, is evaluated at the spatial mid-point between two nodes, here denoted by subscript $i+1/2$. At the mid point, $h_i+1/2$ can be estimated by the average of its neighbours on the left, i, and right, $i+1$. Time-steps are indicated by superscripts in this notation.

$$(1-\phi)h^n_{i+1/2} \approx \frac{(1-\phi)h^n_i + (1-\phi)h^n_{i+1}}{2} \tag{2.32}$$

The flux in (uh) can be estimated by the difference in values in the nodes to the right and left.

$$\frac{(1-\phi)\partial(uh)^n_{i+1/2}}{\partial x} \approx \frac{(1-\phi)(uh)^n_{i+1} - (1-\phi)(uh)^n_i}{dx}. \tag{2.33}$$

(2.9) means the time derivative of h plus the flux of uh, sums to zero. At $n+1/2$

$$\frac{(1-\phi)h^{n+1/2}_{i+1/2} - (1-\phi)h^n_{i+1/2}}{dt/2} + \frac{(1-\phi)(uh)^n_{i+1} - (1-\phi)(uh)^n_i}{dx} = 0. \tag{2.34}$$

Rearranging and substituting the expression for $(1-\phi)h^n_{i+1/2}$, (2.32),

$$h^{n+1/2}_{i+1/2} = \left[\frac{(1-\phi)h^n_i + (1-\phi)h^n_{i+1}}{2} - \left(\frac{dt}{2dx}\right)\left((1-\phi)(uh)^n_{i+1} - (1-\phi)(uh)^n_i\right)\right] /(1-\phi). \tag{2.35}$$

Similarly, a related scheme is set up for $(uh)_{i+1/2}^{n+1/2}$

$$(uh)_{i+1/2}^{n+1/2} = \left[\frac{(1-\phi)(uh)_{i+1}^{n} - (1-\phi)(uh)_{i}^{n}}{2} - dtf_D(1-\phi)h_i^n - dtgn^2(1-\phi)\frac{\left((uh)_i^n\right)^2}{h_i^n}\left(h_i^n\right)^{-4/3}\right.$$
$$-\left(\frac{dt}{2dx}\right)\left(\frac{(1-\phi)\left((uh)_i^n\right)^2}{h_i^n} + \frac{1}{2}g(1-\phi)(h_i^n)^2 + \frac{1}{2}g(1-\phi)h_i^n z_{bi}^n\right.$$
$$\left.\left.-\frac{(1-\phi)\left((uh)_{i+1}^n\right)^2}{h_{i+1}^n} - \frac{1}{2}g(1-\phi)(h_{i+1}^n)^2 - g(1-\phi)h_{i+1}^n z_{bi+1}^n\right)\right]/(1-\phi). \tag{2.36}$$

The scheme can now progress a full time-step, $n+1$, and evaluate h^{n+1} and $(uh)^{n+1}$. h^{n+1} is evaluated as follows.

$$h_{i+1}^{n+1} = \left[(1-\phi)h^n - \left(\frac{dt}{dx}\right)\left((1-\phi)(uh)_{i+1}^{n+1/2} - (1-\phi)(uh)_i^{n+1/2}\right)\right]/(1-\phi) \tag{2.37}$$

The $(uh)_{i+1}^{n+1}$ term is calculated as

$$(uh)_{i+1}^{n+1} = \left[(1-\phi)(uh)_{i+1}^n - dtf_D(1-\phi)h_{i+1}^{n+1/2} - dtgn^2(1-\phi)\frac{\left((uh)_{i+1}^{n+1/2}\right)^2}{h_{i+1}^{n+1/2}}\left(h_{i+1}^{n+1/2}\right)^{-4/3}\right.$$
$$-\left(\frac{dt}{dx}\right)\left(\frac{(1-\phi)\left((uh)_i^{n+1/2}\right)^2}{h_i^{n+1/2}} + \frac{1}{2}g(1-\phi)(h_i^{n+1/2})^2 + g(1-\phi)h_i^{n+1/2}{z_{bi}}^{n+1/2}\right.$$
$$\left.\left.-\frac{(1-\phi)\left((uh)_{i+1}^{n+1/2}\right)^2}{h_{i+1}^{n+1/2}} - \frac{1}{2}g(1-\phi)(h_{i+1}^{n+1/2})^2 - g(1-\phi)h_{i+1}^{n+1/2}{z_{bi+1}}^{n+1/2}\right)\right]/(1-\phi). \tag{2.38}$$

In the first instance the simple distributed drag closure (2.18) is applied as f_D. To parameterise it C_{D0} is chosen to be 2.1 as in the experiments. As discussed and justified in Section 1.2.5.2, for a 5% I_t this is lowered to 1.9. The simple code for the above numerical scheme is written in MATLAB. The flume dimensions as described in Section 2.3 are used and initially a constant dx is chosen for the entire domain. dt varies for stability based on the maximum value of $dx/((uh)/h)$ in the domain, in

line with a Courant number (Courant et al., 1967) defined as $Co = udx/dt$, a ratio of physical wave velocity to computational signal transmission velocity (Lai, 1993). Physically this means that for stability in the model the time-step chosen must be less than the time a wave of velocity u takes to move between computational cells in the model. A summary of parameters is given in Table 2.2.

Table 2.2: *Summary of model parameters for steady model runs.*

dx (m)	n ($\mathrm{sm}^{-1/3}$)	f_D formulation	ϕ
0.0025	-	-	-
0.0025	-	-	0.1 - 0.4
0.0025	-	(2.18)	-
0.0025	-	(2.18)	0.1 - 0.4
0.0025	0.005 - 0.5	(2.18)	0.1 - 0.4
0.0025	0.005 - 0.5	(2.39)	0.1 - 0.4

The domain was preliminarily created using progressively smaller grids, and each was run in turn using the first model in Table 2.2. While this was not a formal grid convergence study (Roache, 1994), it served to determine a suitable resolution for the models. The grid size was decreased until the flow results remained stable and in this case stability was achieved at 0.0025m. Below this size run-times increase dramatically, with no major change in flow results.

As boundary conditions a constant (uh) is introduced to the upstream end and a free boundary condition at the far end allowing the water level to adjust to the flow. This is essentially what was seen in the experiments. The flume used in the experiments has a length of 3m, which is used here. Firstly the model is run without friction, for a constant bathymetry and without blocking or drag (so the last three terms of (2.10) are all zero, and $\phi = 0$) to check the stability. Upstream the boundary condition is a constant volume flux on the first node, which is increased incrementally. Between each increment h and uh are allowed to stabilise until the differences in each quantity between time-steps are small (the tolerance can be varied in the code). As expected, without blocking or drag a linear 1:1 relationship between Fr_1 and Fr_2 is observed. A variable convergence criteria based on small dh/dt and $d(uh)/dt$ between time-steps is introduced to determine when a "steady solution" has been reached. This is set at 10^{-6} for both quantities, with a separate cap on total number of time-steps; if either threshold is met the code exits the simulation.

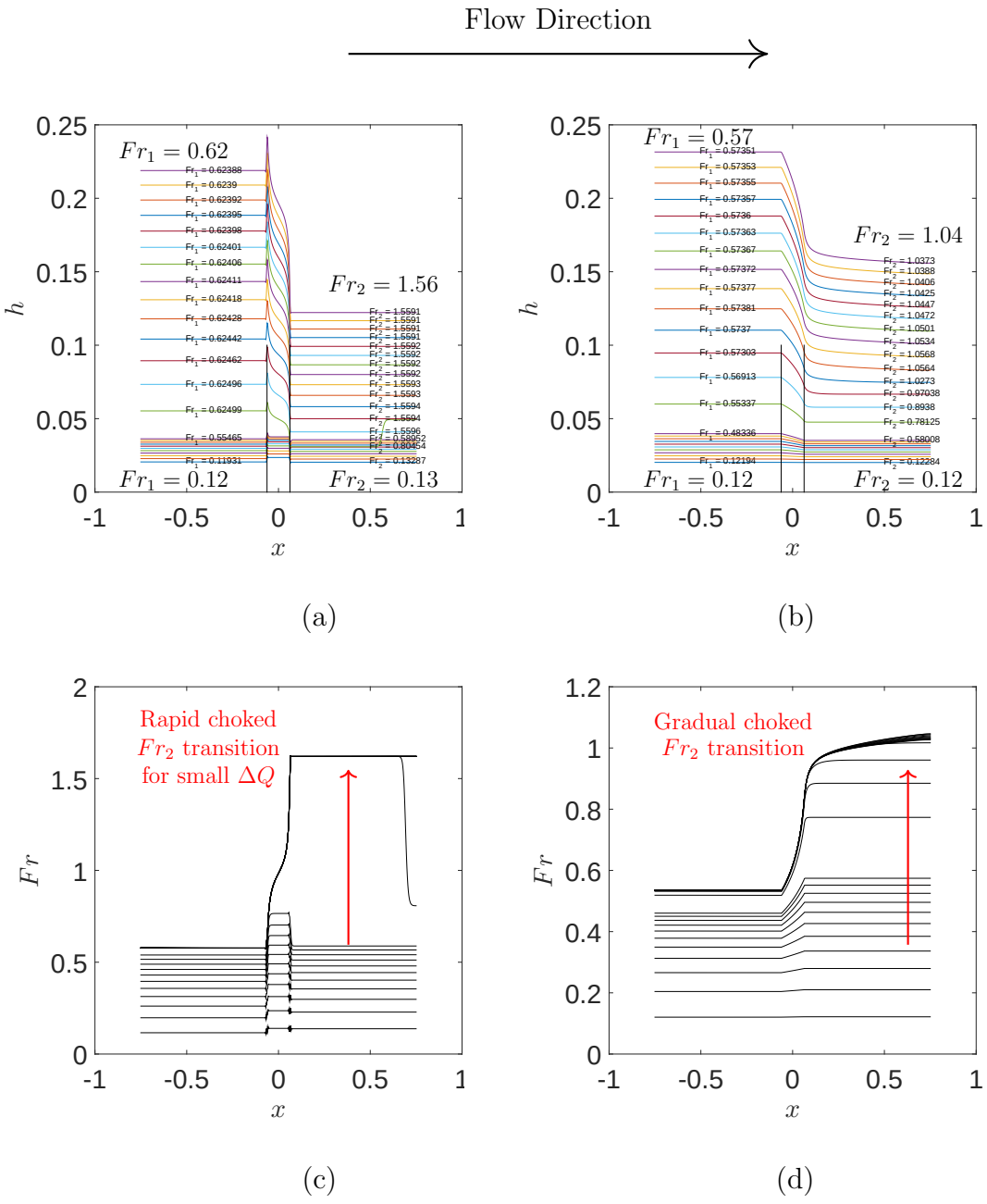

Figure 2.25: *Steady blocking only and drag only model comparison with incrementally increasing Q. (a) Blocking only water surface profile, (b), drag only water surface profile, (c) blocking only local Fr, (d) drag only local Fr. $b/w = 0.25$.* **Flow direction is from left to right in all sub-figures**. *Each coloured line in (a) and (b), and each black line in (c) and (d) represents one converged steady-model run for a single increment of Q. In (a) and (b) the corresponding values of Fr_1 and Fr_2 from (c) and (d) respectively are indicated on the free-surface plots.*

Blocking is added to the model via a $(1 - \phi)$ term. This is applied both to the continuity equation and the momentum equation. Immediately a difference in behaviour is observed and for higher Fr_1, $Fr_2 > Fr_1$. Upon changing the upstream boundary volume flux, a wave propagates down the flume. Once it interacts with the region of blocking the water level adjusts as the wave continues past the block and a smaller reflected wave travels upstream. Above certain Fr_1 a drop in water level is seen behind the block which is recovered almost immediately downstream and can be attributed to a hydraulic jump. At a certain choked Fr_1, the standing wave associated with the jump moves downstream and out of the domain. At this point a maximum value of Fr_1 is obtained, above which Fr_2 can increase without an increase in Fr_1. As we can see in Figure 2.25 (a) and (c), the critical behaviour is represented quite well by just including a blocking effect although the transition is very abrupt.

If instead blocking is not explicitly included ($1 - \phi = 1$ over the blocked region), but a distributed drag based on the blockage ratio is, then different behaviour is observed. A drop in water level between the front and rear of the structure is seen immediately even at low Fr, although the profile is smoother than before. With increasing flow the smooth surface drop across the region containing the building increases and Fr_2 eventually becomes supercritical, although only slightly greater than 1. However, unlike the case with blocking only, there is no rapid transition to choked flow and it is not as sensitive to very small changes in flow. At no point is a recovery in downstream water level observed, and the onset of critical flow is not marked by a moving hydraulic jump to the outlet. Figure 2.26 (b) and (d) shows the corresponding profiles for drag only.

To examine the effect of blocking and drag further, a plot of Fr_1 versus Fr_2 can be directly compared with Figure 2.18 as well as the data of Qi et al. (2014). In Figure 2.26 (a) and (b) the plots corresponding to the blocking only and drag only model are shown respectively. When both of these effects are included, the resultant curves are different again. In Figure 2.26 (c), the results of a model with blocking and drag are shown. Again friction is neglected here in order to focus on the important physics. The data of Qi et al. (2014) are shown in Figure 2.26 (d) along with the data from Figure 2.18 of this experimental study.

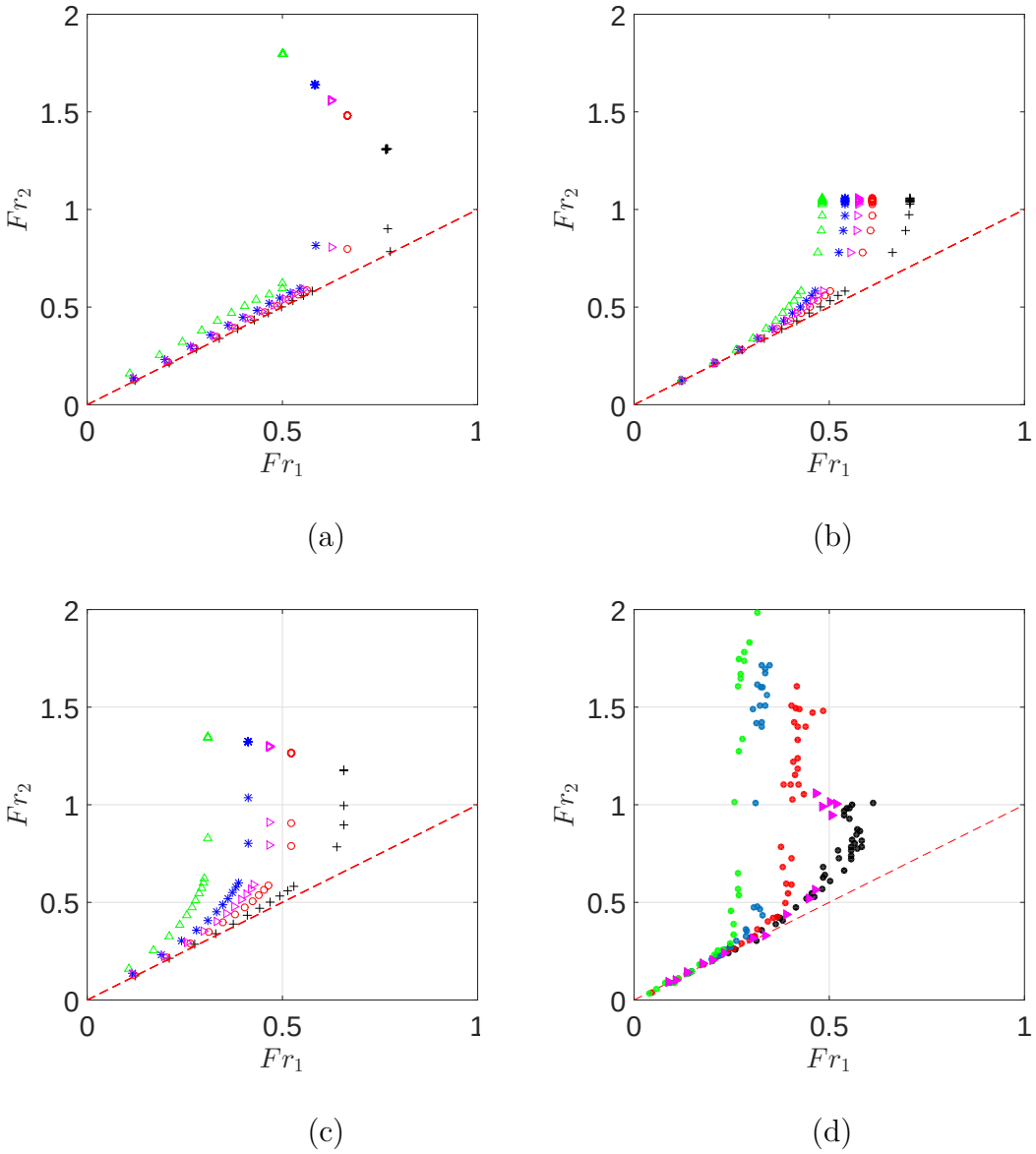

Figure 2.26: *Upstream and downstream Froude number results from 1D model including different terms. (a) No Friction, no drag, blocking only, (b), no friction, no blocking, drag only, (c) blocking & drag included, no friction.* $+$ $b/w = 0.1$, $\circ$ $b/w = 0.2$, $\triangleright$ $b/w = 0.25$, $*$ $b/w = 0.3$, $\triangle$ $b/w = 0.4$. *Each point represents a separate steady-state simulation. In (d), experimental results are presented from Qi et al. (2014), where* b/w $\bullet = 0.1$, $\bullet = 0.2$, $\bullet = 0.3$, $\bullet = 0.4$ *and the non- over-topping data for* $h_i > 0.45mm$ *from this experimental study,* $b/w = 0.25$, $\blacktriangleright$.

Looking at the profiles from the model with blocking and drag there is a noticeable difference between these and the individual blocking only and drag only plots in Figure 2.25. The Fr and h profiles for the full frictionless model are given in Figures 2.27 (a) and (c). The resulting plot of Fr_1 vs Fr_2 shows a strong resemblance to the experimental data. However the experimental results of Qi et al. (2014) seem to show critical behaviour at a lower Fr_1 than predicted by the numerical model, and actually by the theory of Qi et al. (2014). The experimental results of this thesis for $b/w = 0.25$ however are very close to the numerical results, and the theory of Qi et al. (2014).

As a last step, friction is added to the model. The effect of friction inclusion is discussed further in the next Chapter, but it is briefly investigated here for $b/w = 0.25$. The model including both blocking and drag is parameterised with a Manning's coefficient varying between 0.0005 and $0.05sm^{-1/3}$, and run up to steady convergence for various inflows. The resulting behaviour is summarised in Figure 2.28.

In terms of the effect on flow conditions, the value of Fr_1 generated for a given volume flux at the inlet is reduced with increasing n. For high friction, i.e., where $n > 0.005sm^{-1/3}$, this reduction is significant. The choked Fr_{1c} appears to remain largely the same between analyses, but Fr_{1c} becomes more difficult to achieve. This is reflected in Figure, 2.28 (a). In this plot, the dashed black lines indicate constant volume flux inflow boundary conditions in the model. Manning's n is varied between sets of model simulations (each n model set is plotted vertically). The transition in behaviour occurs where Fr_2 jumps from sub-critical to a choked state, which is indicated with a red line at $Fr_2 = 1$. For $n < 0.0025sm^{-1/3}$ the transition to a critical state occurs between the same two volume fluxes. The dashed equal volume flux lines here are relatively flat, indicating flow conditions are not affected dramatically by low n, as expected. For $0.0025 \geq n \leq 0.003sm^{-1/3}$ an additional volume flux is needed to achieve critical flow. At progressively higher friction coefficients the number of volume flux intervals required to achieve critical flow increases dramatically. At $n = 0.01sm^{-1/3}$ the highest volume flux tested used does not induce critical flow. Increasing the flow in the model would not give useful further insight.

As expected, in Figure 2.28 (b), friction does not tend to affect the dimensionless critical behaviour and all of the the data fall onto the same $b/w = 0.25$ curve, but

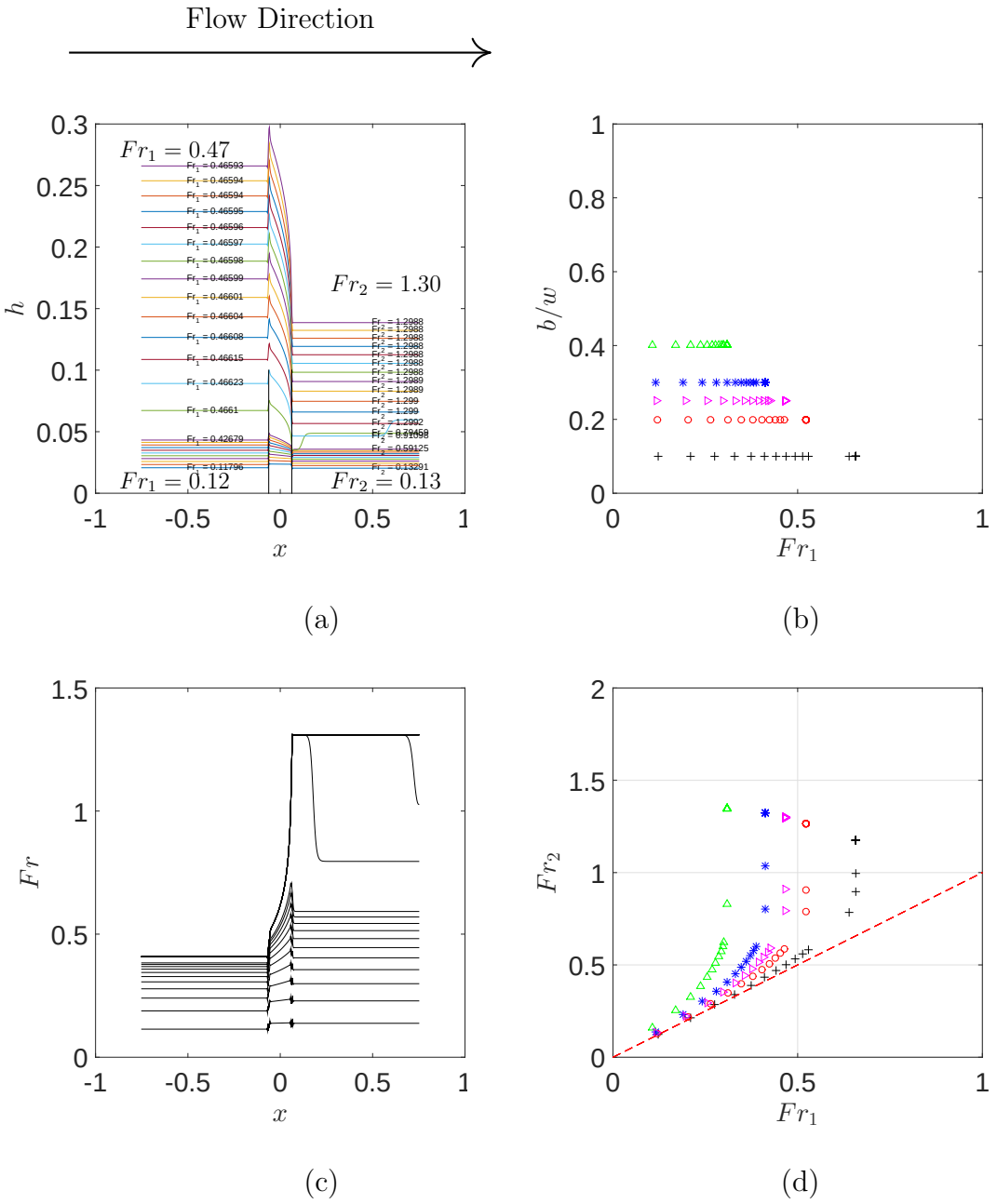

Figure 2.27: *Steady blocking and drag model comparison, no friction. (a) Blocking and drag water surface profile, (b), blocking and drag regime diagram, (c) blocking and drag local Fr, (d) blocking and drag Fr_1 vs Fr_2. $b/w = 0.25$*

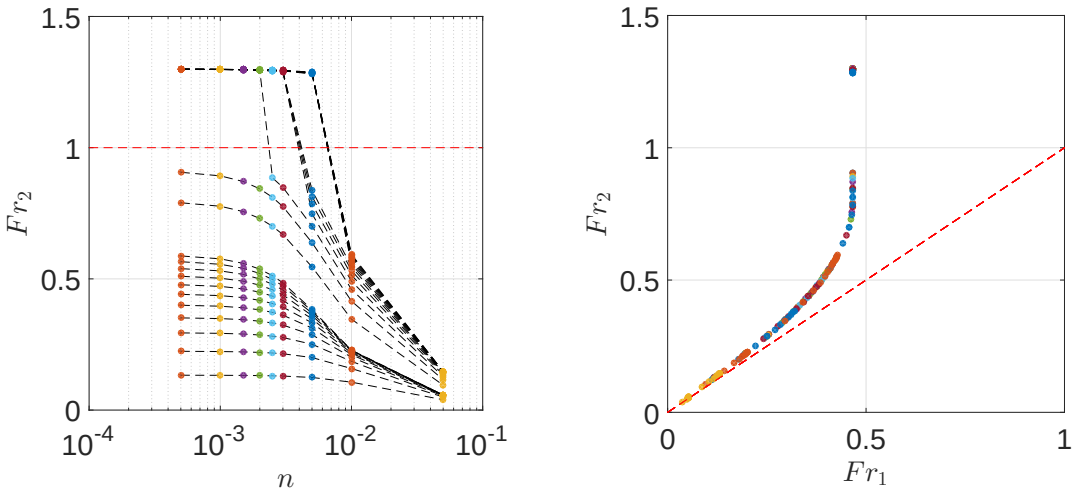

Figure 2.28: *(a) Blocking and drag model Fr_2 variation with n, (b), corresponding Fr_1 vs Fr_2. $b/w = 0.25$.*

the water levels and velocities that produce the Fr values are affected. In fact the onset of over-topping in the experiments can be used to help us rule out some high friction values. From the experiments, which used a blockage with $H_b = 0.1m$, taking $h_i > 0.45$mm, over-topping begins at $Fr_1 \approx 0.47$. Only Manning's n of $< 0.0015sm^{-1/3}$ produces $h_1 < H_b$, where $Fr_1(h_1 = H_b) \approx 0.466$. In Figure 2.27 (a), the onset of over-topping occurs at $Fr_1 \approx 0.466$, so it is clear that choosing any $n < 0.0015sm^{-1/3}$ in this case should not affect the water level results dramatically. The sensitivity to friction with respect to this particular behaviour is therefore fairly low, unless very large n are chosen which are orders of magnitude different.

For a final comparison, the full model with friction, blocking and drag is compared to an equivalent model where f_D is parameterised as per the descriptions in Qi et al. (2014). In order to do so, F_D in (2.16) is replaced by (1.31) to give

$$f_D = \frac{\phi}{(1-\phi)} \frac{\lambda g^{1/3} u_1^{4/3} h^{1/3}}{L} \tag{2.39}$$

where λ is (1.32). Evaluating λ requires the additional quantities Fr_1 and Fr_d to be computed on the fly, which is trivial in a steady model. As Fr_d can be determined at each time-step there is no requirement to solve (1.29).

It is possible to reproduce equivalent figures showing the effect of (2.39).

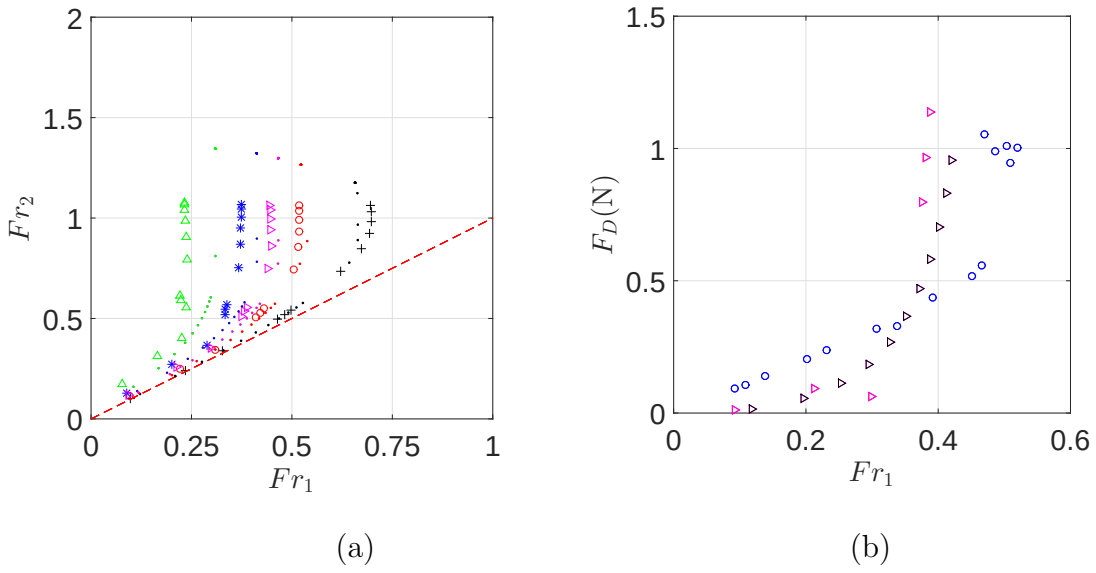

Figure 2.29: *Comparison between simple distributed drag and using the description of Qi et al. (2014). (a)* + $b/w = 0.1$, ○ $b/w = 0.2$, ▷ $b/w = 0.25$, ∗ $b/w = 0.3$, △ $b/w = 0.4$, $f_D = (2.39)$, ... $f_D = (2.18)$ *from Figure 2.27. (b)* $b/w = 0.25$ *for all,* ▷ $f_D = (2.39)$, ▷ $f_D = (2.18)$, ○ *Experimental,* $h_1 < H_b$, $h_i > 0.06m$. $n = 0.001sm^{-1/3}$.

Here we can see that the two models are comparable for $b/w < 0.25$. At higher b/w differences between the behaviour becomes significant. In Figure 2.29 (b) the force is compared to the experimental values obtained in this study. While the plots are similar, there are differences seen between both models and the measured drag force. The experimental results of Figure 2.26 (d) and numerical results of 2.29 (a) show very close resemblance for $b/w = 0.25$. The comparison is made between the non-over-topping tests as both models in their current forms are not capable of accounting for over-topping.

Once the flow over-tops, the blockage ratio for the portion of fluid above the structure becomes zero. In addition, the drag on this portion of the fluid changes from generating vertical vorticity as it was while $h_1 < H_b$, to horizontal vorticity associated with the top of the structure, which is more in line with friction modelling. As such it is expected that the force will scale differently for over-topping flows Other complexities due to spilling off the rear top edge also come into play until the rear water level h_d exceeds H_b, and the building can be considered submerged.

2.6 Conclusions

A set of tests have been conducted to examine the full-body force on a square block in a flume. The flow past the block was varied for a series of initial water depths. The results show two regimes; one where the downstream flow conditions are sub-critical, and the other where they are choked. The sub-critical regime is dominated by hydrodynamic drag forces, and in the choked regime a large difference in water level develops between the front and rear of the structure. This difference in water level produces a net hydrostatic force on the front face. Downstream, the wake becomes detached and further downstream a hydraulic jump forms where water levels recover.

In order to describe the transition between the two regimes and predict the downstream conditions given upstream conditions and the blockage ratio, a framework is validated based on a semi- empirical drag force closure. The framework is valid for steady flow, past a blockage ratio of 25%. Following work of Qi et al. (2014), extending the applicability of the framework to other blockage ratios, it is possible to be confident that the framework holds for other blockage ratios. Providing the flow conditions are not varied quickly, unsteady added mass forces should not be an important factor. Similarly, limiting the conditions to quasi-steady (small accelerations), the differences between upstream and downstream pressure distributions will be due only to the flow blockage, and not to the variation in the flow and the propagation time between the front and rear of a block.

For these reasons it is proposed that the framework that has been verified to describe the steady experiments in this chapter will potentially be valid for application to a set of unsteady experiments where first time derivatives are small. Intuitively, this makes sense for describing long-period wave inundations from tsunamis, where other than the initial wetting stage, time derivatives in the flow are generally small. In the next chapter results from the large-scale unsteady tests are described using the steady framework as a context, and investigated further using the same numerical modelling approach as presented here.

Chapter 3

Unsteady Flow Loading on an Obstacle in HR Wallingford Large Facility

3.1 Introduction

As a natural progression of the steady experiments, the results of a large-scale set of unsteady experiments carried out at HR Wallingford (HRW) are presented here. The purpose of the experiments is two-fold. Firstly to fill the gap in the literature on experimental testing of wave forces on buildings to wave periods never before possible, and at a scale such that they are comparable to tsunami and other long-period waves at prototype. Secondly to examine how the loading pattern varies as the wave period is increased, and as such whether changes to the loading pattern mean its primary characteristics can be predicted using a simple model.

The work of Qi et al. (2014) shows that the force on a block in a steady flow can be found by evaluating downstream flow conditions from given upstream steady conditions. There is therefore potential to apply this directly to output from numerical shallow water equation tsunami codes which cannot explicitly account for buildings. These "bare-earth" numerical models however, would be agnostic to the presence of the building, and remain independent. However, turning this basic flow output

into something relevant to engineering design or vulnerability analysis (estimating proportions of structures which will be damaged) is non trivial because as is demonstrated in Chapter 2, the flow is drastically altered by the building. If knowing the blockage ratio, and the upstream flow conditions are all that is required to estimate the force on a structure, the output from a bare-earth numerical model has potential to be used more effectively.

Stronger links between the steady experiments and these unsteady tests are however found through use of the numerical model presented in Chapter 2. The numerical model of Chapter 2 shows that for steady flows the force and critical flow behaviour can be determined through a simple drag closure. As such there is a possibility of fully integrating the forces on buildings and the effect they have on the flow into SWE models, and potentially even existing codes in widespread use. However, the methodology described thus far is derived to describe steady flows, so an assessment of the applicability to unsteady conditions is necessary. Initially the method is applied to published unsteady experiments.

The large-scale unsteady experimental results presented in this chapter demonstrate that the methodology holds and produces useful results for the quasi-steady flow conditions found in long-period waves. They also demonstrate that experimental studies using short-period waves are not equivalent to those from long waves and in particular that the loading patterns are very different. The following sections describe the observations and apply the steady methodology to these large-scale quasi-steady results. Firstly the simple 1D description is applied to published experimental data in order to investigate whether the developed code is able to capture the main features of unsteady experiments which could be adopted in the calibration of tsunami inundation numerical models.

3.2 Unsteady one-dimensional model comparison to published experimental studies

In order to extend the applicability of the one dimensional model to the unsteady case, it makes sense to firstly run the 1D model unsteady for some published scenarios in order to demonstrate and verify that the major effects are still captured.

Several studies are highlighted in the section 1.2 but as previously discussed many of these are short-period wave experiments of limited comparative use for a study focussed on the interactions of long-period waves. However, one method of generating moderate-period interactions is by the sudden release of impounded water from a reservoir in the form of a dam-break.

Two such published studies are considered here due to their completeness of published geometry information as well as containing detailed time-history measurements of forces and water levels. These form ideal comparisons for extending the steady numerical model presented in Section 2.2 without over-complicating the situation (the bathymetry remains flat, the blockage ratios are similar to the tests described in this thesis). Additionally, the two experimental studies have subsequently been used to validate published sophisticated 3D numerical modelling studies. As such a further comparison can be made and there is an opportunity to test how much of the important physics can be captured by a comparatively very simple model. As the raw laboratory or numerical data from these studies are not available to the author, the results for these studies are digitally transcribed from the publications in which they appear. It is recognised that this process inevitably introduces some errors, although any comparisons made here are purely visual so there are no further calculations derived from these data which could be affected.

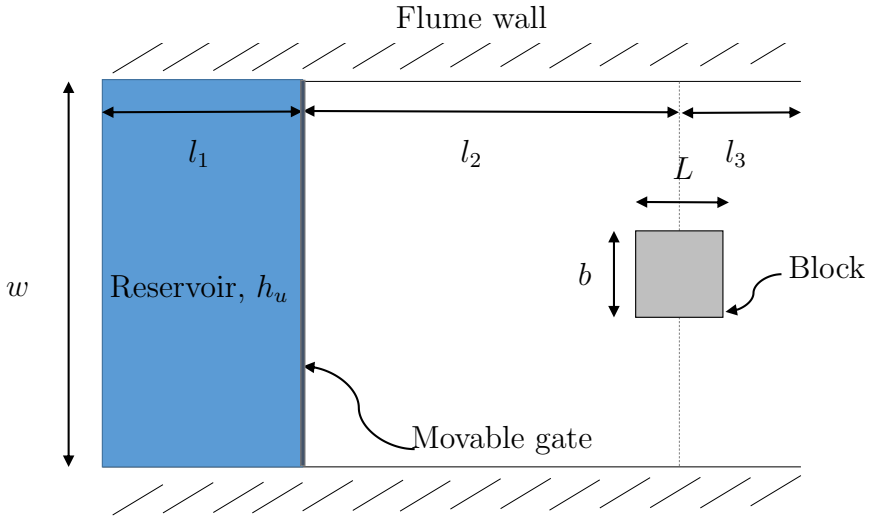

Figure 3.1: *Schematic of published dam-break experimental set-ups. Parameters for individual experiments and subsequent numerical models can be found in Table 3.1.*

Table 3.1: *Summary of model parameters for dam-break model runs using experimental set-up of (a), Al-Faesly et al. (2012) and (b), Árnason et al. (2009).*

Ref	dx(m)	n(sm$^{-1/3}$)	ϕ	w(m)	b(m)	L(m)	l_1(m)	l_2(m)	l_3(m)	h_u(m)
(a)	0.0069	0.0025	0.23	1.3	0.3	0.3	11.63*	4.92	2.65	1.15
(a)	0.0069	0.0025	0.23	1.3	0.3	0.3	11.63*	4.92	2.65	0.85
(a)	0.0069	0.0025	0.23	1.3	0.3	0.3	11.63*	4.92	2.65	0.55
(b)	0.0027	0.0025	0.20	0.6	0.12	0.12	5.9	5.2	5.5	0.1
(b)	0.0027	0.0025	0.20	0.6	0.12	0.12	5.9	5.2	5.5	0.15
(b)	0.0027	0.0025	0.20	0.6	0.12	0.12	5.9	5.2	5.5	0.2
(b)	0.0027	0.0025	0.20	0.6	0.12	0.12	5.9	5.2	5.5	0.25

* is an effective length

As discussed in Section 1.2.5.5, Al-Faesly et al. (2012) examined the interaction between a square column and a dam-break flow produced by the rapid opening of a gate releasing water at a range of impoundment depths. The results were used by St-Germain et al. (2012) and Douglas and Nistor (2015) for comparison with SPH and RANS models respectively. The bathymetry in these tests is flat and sensitivity tests are carried out by Douglas and Nistor (2015) by varying the initial water level downstream of the dam gate in the model domain. The results, dimensions and boundary conditions from the square cylinder study (where ϕ = 0.3m/1.3m = 0.23) are taken for comparative purposes. In Douglas and Nistor (2015), the physical tests were compared to a two-phase (water-air) RANS 3D model in OpenFOAM, which showed good agreement to the experimental measurements. The numerical simulations show similar peak pressures as found in the experiments but with initially far higher splash height and fast relaxation of the free-surface height near the obstacle. It is postulated that this could be an issue due to surface roughness parameterisation.

The boundary conditions and dimensions from these tests are applied to the 1D model with blocking and drag, which is run initially with a constant dx, but with a dynamic time-step based on $Co < 1$. Friction is neglected at first. A good agreement is found between the proposed 1D model and the published data for both cases (with or without a block) but a small difference in arrival time is seen. As such the model was re-run with friction by setting $n = 0.0025sm^{-1/3}$. The results of the experiments and numerical model of Douglas and Nistor (2015) for an impoundment depth of 1.15m are compared to the 1D case and presented in Figure 3.2. No formal

grid convergence study of the type described by Roache (1994) was carried out, but the final resolution chosen was based on a balance between increased run-times for higher spatial resolution (i.e. $dx/2$), and differences in the velocity, water depth and force results (which if small, the coarser grid was chosen).

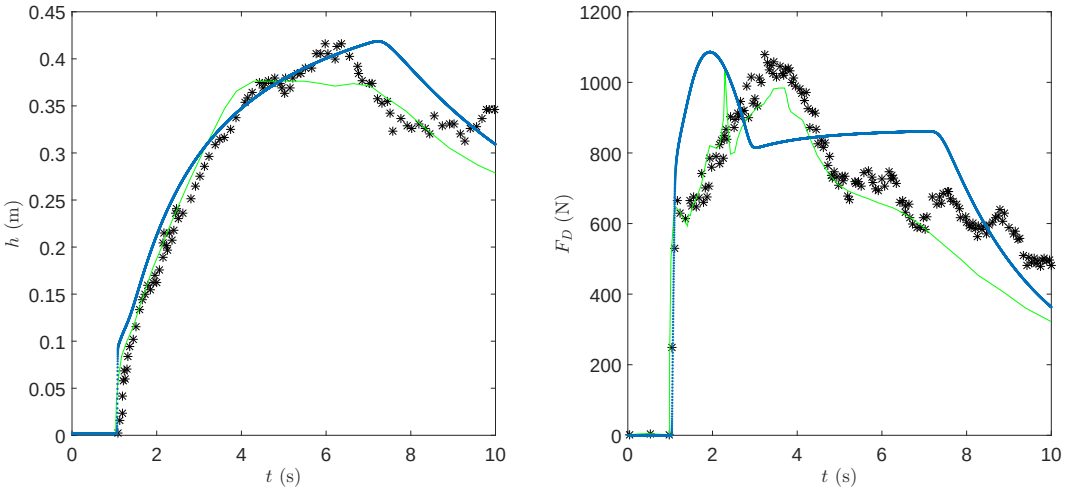

(a) (b)

Figure 3.2: *Published experiments compared to 1D model. (a) h at the location of the square cylinder, with the cylinder removed. (b) force on a square cylinder as in the experiments of Al-Faesly et al. (2012). Green Douglas and Nistor (2015) numerical, $*$ Al-Faesly et al. (2012) Experimental. In (a) and (b) the results of the 1D numerical model are presented as ●.*

Numerical studies of St-Germain et al. (2012, 2013) used SPH to model the same experiments of Al-Faesly et al. (2012) and their numerical results produced a far higher peak in the impact pressures as the dam-break wave hit the cylinder. As the forces are produced by an integration of the pressure distribution, this translates to an over-predicted peak force. Douglas and Nistor (2015) attribute this to a single phase only being accounted for in the SPH model, and compressibility of air entrained in the bore front in reality. The peak forces were better captured by the two-phase RANS model of Douglas and Nistor (2015). As can be appreciated from examining Figure 3.2 (a) and (c), the behaviour found in this example is not perfectly captured by a distributed drag closure, but the model is far simpler than both the RANS and SPH models used by Douglas and Nistor (2015) and St-Germain et al. (2012) respectively, and it reproduces comparable peak forces, water

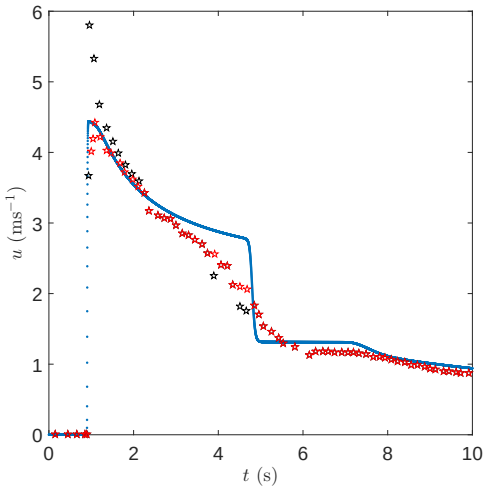

Figure 3.3: *Depth-averaged velocity from our 1D model (with h_i = 5mm)* • *and comparison with numerical results of Douglas and Nistor (2015);* ★ *dry bed,* ★ *h_i=5mm.*

levels and velocities at far lower computational expense. Good matches with the ID model were also obtained for the experiments of Al-Faesly et al. (2012) with impoundment depths of 0.55m and 0.85m, although fewer data were available in the literature for the comparison. A numerical depth-averaged velocity trace is provided for the 1.15m impoundment depth measurement in Douglas and Nistor (2015) with different initial downstream water depths, and a further comparison with the 1D description is made in Figure 3.3. Here it is clear that the velocity is very similar in the 3D models of Douglas and Nistor (2015), and the 1D model of this thesis.

A similar set of tests were undertaken by Árnason et al. (2009) of bore interactions with a square column. A corresponding numerical study was carried out by Wei et al. (2015) based on the Árnason et al. (2009) tests using a SPH method. The Árnason et al. (2009) tests are again run in the 1D model and the results presented in Figure 3.4, together with the numerical predictions of Wei et al. (2015). It is observed that the time of initial bore impact is captured well by the 1D model and the reflected wave from the back wall for Árnason's experiments is also perfectly timed. The water levels (again only provided in the paper without the column present) are replicated well.

Forces are remarkably well captured for both cases, especially considering the current incomplete force description and the un-tuned nature of the drag coefficient used

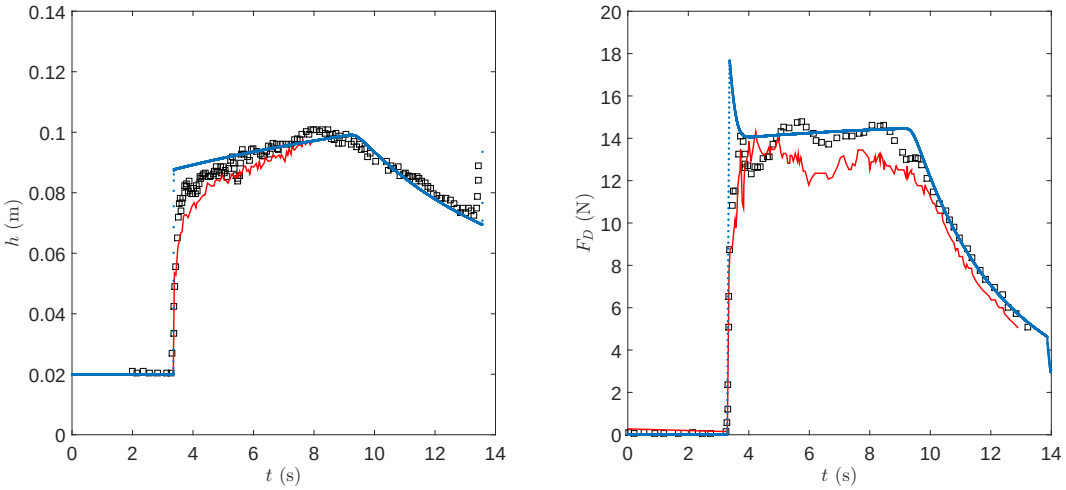

(a) (b)

Figure 3.4: *Published experiments compared to 1D model. (a) h at the location of the square cylinder, with the cylinder removed. (b) force on a square cylinder as in the experiments of Árnason et al. (2009). Red Wei et al. (2015) numerical, □ Árnason et al. (2009) experimental. In (a) and (b) the results of thr 1D numerical model are presented as ●.*

within the 1D model ($C_D = 2$). These two examples provide some confidence that applying the 1D model to an unsteady case, without an explicit unsteady force component is likely to generate reasonable results. The application of this framework to describe large-scale tests of long-period waves is therefore justified and can be expected to give a reasonable approximation. Although these experiments are for dam-break waves that are usually related to a long or sometimes infinite period, in reality due to finite reservoir volumes these inundations correspond to those which are seen during short-period wave inundations. The fact that the quasi-steady model appears to give very reasonable results for force is very encouraging from this perspective and the comparison to less peaky, longer-period inundations is expected to improve.

3.3 Experimental set-up and methodology

Much of the design of the equipment underpinning these experiments was carried out prior to the start of this project in October 2008, as it required a relatively long lead-time for manufacture. The design of the new wave generator is detailed in Bazin (2008) and its capabilities and operation are described by Charvet (2012). In relation to the experiments described here, the design of the experimental procedures carried out, the testing schedule and the running of the flume experiments are entirely the responsibility of the author. However, the data acquisition for the work of Charvet (2012) and for this thesis are necessarily carried out jointly (as the machinery and site requires a minimum of two personnel to operate safely and effectively). The transfer, backup, storage on-site processing of data responsibilities and all post-processing presented here are also carried out by the author.

The measured quantities and their associated uncertainties can be found in Table E.2.

3.3.1 Wave generator

The new wave generator is inspired by a pneumatic tide generator used by HR Wallingford (HRW) (Wilkie and Young, 1952) which is capable of producing a prototype tide of 12.5 hours in 7.5 minutes (Bazin, 2008). In order to achieve this, the generator draws a controlled volume of water from a wave basin into a tank, and releases it over time. An air pump linked to the tank provides a constant suction, and a separate motor controlled valve regulates the air pressure within the tank. Tides, being of longer period than tsunami require a slower exchange of water between the basin and the tank. So in order to produce waves of similar scaled period to tsunami a faster control mechanism was necessary. The new generator is also required to produce waves in a flume, rather than a wave basin, and so the necessary dimensions and geometry are totally re-designed. Aside from these alterations, the principles behind the new generator are essentially the same as that of Wilkie and Young (1952).

The tsunami generator is operated by varying the pressure inside the tank, by actuation of a computer-controlled and motorised valve. A constant suction is supplied

by the air pump. When the control valve (CV) is closed, water is drawn up into the tank from the flume, and released back to the flume when the valve is opened. A second security valve (SV) is present to prevent the water level from reaching the top of the tank and being drawn into the air pump. This scenario would damage the pump, and as such the SV is always set slightly open to allow regulation of the internal vacuum and prevent water being drawn up too far inside the tank. It is occasionally necessary to alter the SV position, particularly if varying the water depth in the flume greatly, but on the whole and for the duration of these tests the SV remained in the same position throughout. This is clearly desirable as the SV position alters the performance of the generator. The released water forms the positive part of the wave, and the draw-up stage produces the negative trough in the flume. The experimental set-up can be seen in Figure 3.5.

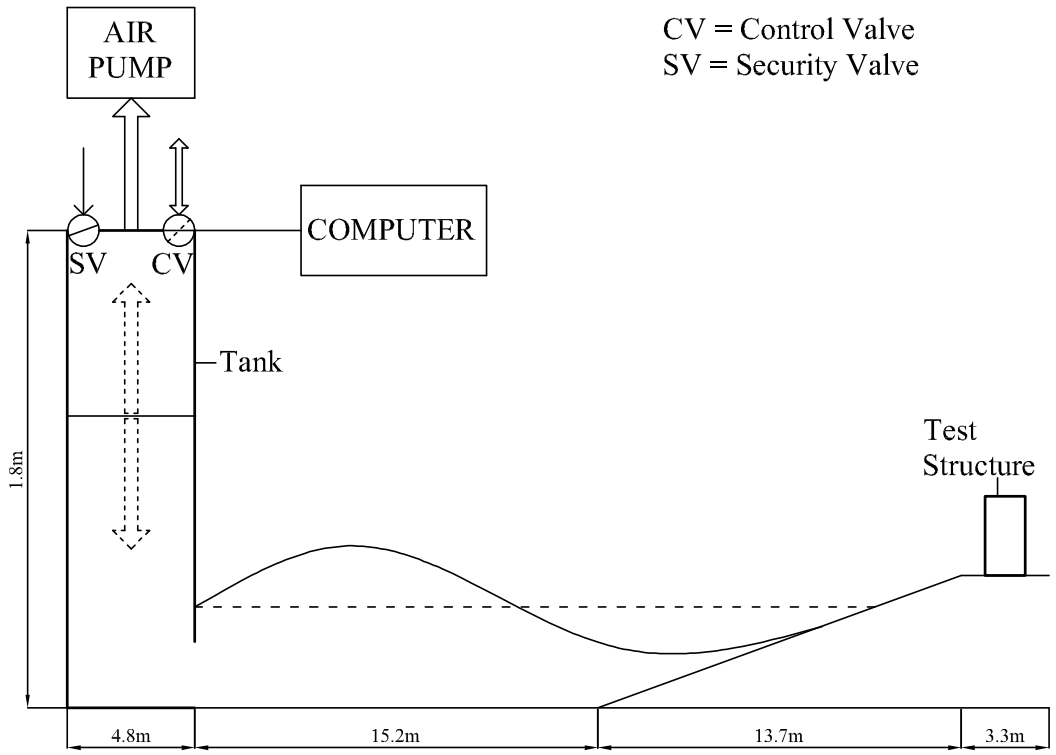

Figure 3.5: *Schematic diagram of the flume at HRW and new pneumatic wave generator system. Vertical scale emphasised. Not to scale.*

The operation of the motorised valve is controlled in a user interface based in Lab-

View software, which has been developed by HRW staff. The valve is able to open between zero and 42° and this can be varied manually, or from a pre-defined time-series loaded onto the control computer. A summary of the design process and calculations which were done prior to the manufacture of this generator can be found in Rossetto et al. (2011) and Charvet (2012). The generator tank is 1.15m wide, 1.8m high and 4.8m long and fully removable from the wave flume so that normal paddle generators can be reinstated when the generator is not in use.

3.3.2 Flume

The flume used for the experiments described by this chapter is shown in Figure 3.6. It is located in the Froude Modelling Hall at HR Wallingford, Oxfordshire, UK. The length of the flume is 45 metres by 1.2 metres wide and it is constructed of reinforced concrete with two viewing windows (3.3 by 1.7m). The effective length of the flume is further reduced by some 12.2 meters by the pneumatic generator installed in front of the insitu paddle generators and a sump created behind a 13.7m stretch of 1:20 fixed bathymetry. A flat area of beach for conducting structural tests provides a constant depth propagation region of 15.2m, with some 28 metres in total for propagation. The beach area is chosen to coincide with the location of one of the viewing windows so that video data can be collected.

The flume is filled with fresh water which at the time of the experiments (Autumn/Winter 2008) is on average 8° Celsius. This water is filtered, but contained traces of organic debris and other non organic particles originating from its source in the adjacent River Thames. Though generally invisible to the eye, this debris can affect some instruments. In particular the velocity readings are found to be particularly susceptible, as the probes are frequently contaminated with fine algae fibres which clog the mechanisms periodically.

The control room can be seen in Figure 3.6 spanning between the adapted flume and that adjacent to it and the view is looking towards the beach inundation area. At the far end of the flume is a sump, where inundating water is collected and measured. The water is returned to the main flume via a sump pump, which is used between tests to retain fluid volumes in the system.

Figure 3.6: *45m wave flume in Froude Modelling Hall at HW Wallingford, photographed from the top of the wave generator.*

Throughout this work, various quantities are measured. As stated earlier, the experimental work was undertaken in conjunction with that of Charvet (2012) and as such many of the measurements made in that study are highly relevant to this thesis. The different types of data observed are described separately. Most of the data are captured using a 64 channel data acquisition system enabling simultaneous recordings of all quantities to a single file on a computer. Other measurements, in particular the video recording require a separate recording system located away from the main control office, or manual measurements in the case of sump volumes.

3.3.3 Test structures

There are two structures used in these tests which are instrumented with six pressure transducers. The structures are shown in Figure 3.7 with the full dimensions given. Importantly to the framework used to describe these tests, these two structures were 300mm and 150mm wide respectively, giving blockage ratios of 0.25 and 0.125.

The outer casing of the structures is fabricated from 10mm marine ply, which has a varnished finish to aid with water-proofing. The joints are sealed with a waterproof beading and screwed secure. The six pressure transducers are installed from the inside of the casing into a threaded hole so that they are flush-mounted with the

outer surface. The whole structure is fastened to a hardwood base with ten 40mm screws. The base fits flush with the concrete bathymetry onto a set of recessed wooden rails running longitudinally along the centre of the flume. These rails are fixed to the base of a shallow conduit formed in the "dry land" section of the concrete bathymetry. The hardwood base is secured to these rails. Waterproof cables for the transducers passed through the base via a hole in the centre, along the conduit to the back of the flume and out to the control office.

The two different shaped structures are interchangeable and their orientation and position could be varied by securing the structure to a different position on the base.

3.3.4 Pressure measurement

Six TRAFAG pressure transducers are used to measure the normal pressures exerted by the fluid on the surfaces of the structure inundated by our waves. The sensing element consists of a micro-machined silicon diaphragm with piezo-resistive strain gauges diffused into the surface. The sensing element is mounted behind a thin diaphragm to produce a rugged assembly. The combined linearity and hysteresis errors are less than 0.25% of full scale range (HR Wallingford, 2012). The probes are fully immersible and can be mounted flush to a surface using their threaded outer casing which screw into the tapped holes on the test structures, as seen in Figure 3.8.

The transducers are plugged directly into a multichannel data acquisition rack and energised to 10V through this system. The output voltage is recorded in synchronisation with velocity and wave height measurements.

Separate calibrations are carried out by HRW technicians for each pressure transducer and this was provided prior to testing. The calibration involved immersing the transducer under known depths (0 to 1000mm, at 200mm intervals) of fresh water and observing the resulting linear relationship (Equation 3.1) between water depth, h (mm), and voltage, V, recorded by the acquisition system. Here A is the slope of the linear regression and B is the intercept (generally the intercept was ignored as

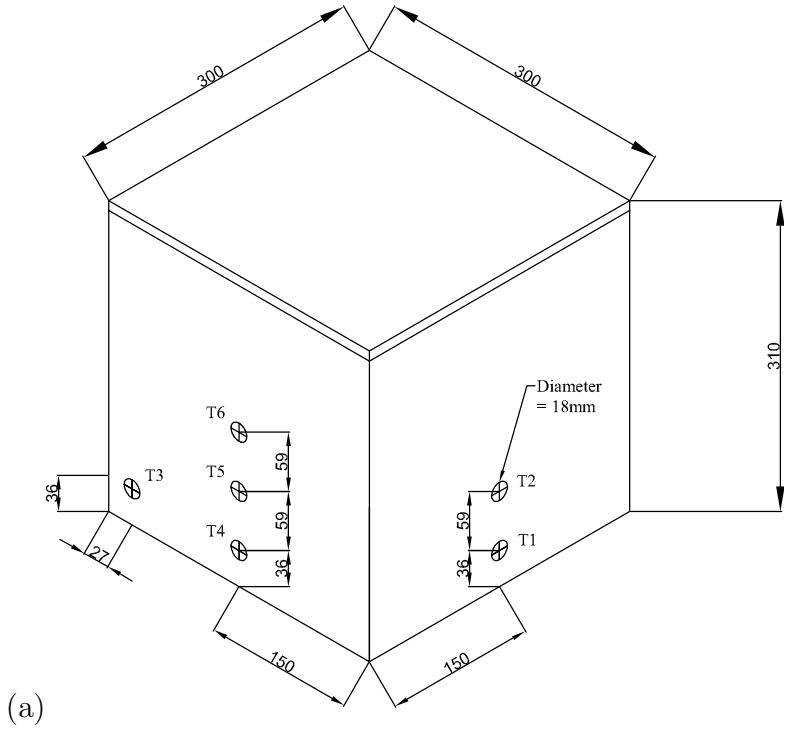

(a)

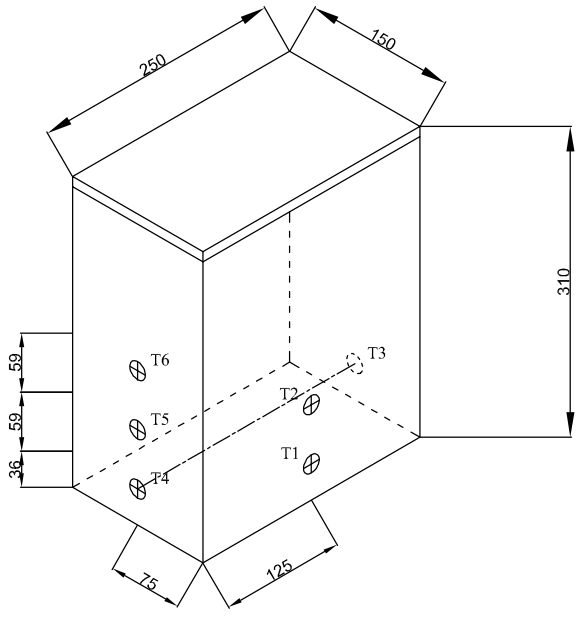

(b)

Figure 3.7: *Isometric drawing of both types of pressure transducer instrumented buildings used in these tests. All dimensions in millimetres.* (a) *Broad (300mm) building* ($b/w = 0.25$). (b) *Narrow (150mm) building* ($b/w = 0.125$).

(a) (b)

Figure 3.8: *Front,* (a) *and side,* (b)*, of square test structure used to house the six pressure transducers.*

the pressures were zeroed based on the average voltage before wave impact).

$$h_{(\mathrm{mm})} = AV + B \tag{3.1}$$

Clearly, the conversion between mm of water and pressure is trivial assuming a known density of water and acceleration due to gravity. The water used in the labs is cold (around 8°C) and at this temperature, fresh water has a density of 999.849 kgm^{-3} which is approximately 1000 kgm^{-3}. The figure of $\rho = 1000\mathrm{kgm}^{-3}$ is widely quoted and used in the literature and is assumed here. The conversion from water depth (mm) to pressure in Pascals (Pa, Nm^{-2}, $\mathrm{kgm}^{-1}\mathrm{s}^{-2}$) is given by equation 3.2.

$$p_{(\mathrm{Pa})} = \rho g \left(\frac{h_{(\mathrm{mm})}}{1000} \right) = \rho g \left(\frac{AV + B}{1000} \right) \tag{3.2}$$

$$p_{(\mathrm{Pa})} = \frac{\rho g A}{1000} \left(V - V_{\mathrm{zero}} \right) \tag{3.3}$$

However, due to electrical drifts in the voltages over time, (3.2) is modified to account for the drifts with (3.3), which is found to be more robust. The drift manifests as a change in intercept, whereas the gradient remains constant. (3.3) is therefore the preferred form, as the determination of V_{zero} means that any electrical drifts can be removed for each test. V_{zero} is chosen as the average voltage measured for the first 200 data (where no water was present). Regardless, these drifts are seen to be very small in the case of the pressure transducers.

3.3.4.1 Pressure transducer processing

The pressure transducers are an integral part of the data collected in this study. The raw voltage signals of the pressure transducers are reasonably free from interference and require little de-noising. The calibration (3.3) is used directly on the signals based on the slopes given by the individual pressure calibrations carried out by HRW technicians. The pressure data are ultimately combined with the free-surface information described next in order to add additional points of known pressure to the solid fluid interface. At the free-surface boundary, the pressure is atmospheric, so there is no force from the water exerted on the building along the free-surface. With the spatially discrete points measured by the pressure transducers, a reasonable estimate for the pressure distribution on the face of the structure can be interpolated onto a regular grid for each time sample, for each face.

Alderson and Allsop (2007) give justification for this approach, and demonstrate good corroboration between forces estimated from integrated pressure distributions and full-body forces from load cell set-ups. A similar exhibit is presented by Shafiei et al. (2016) who use five Honeywell 26PC series differential pressure sensors arranged vertically up the face of their 300 x 300 x 600mm test column (the same dimensions as one of the experiments described in this thesis) as well as a multi-axis waterproof load cell. Using this equipment, Shafiei et al. (2016) also note the excellent agreement between the load cell measurements and integrated pressure distributions in their sudden release bore tests described in their paper.

In order to verify this result further, a small dataset was collected during subsequent preliminary experiments at HRW using a larger updated version of the pneumatic wave generator used for the tests in this thesis. Crucially, the test rig used in this case is able to simultaneously capture full-body force measurements from load cells, and pressure measurements at discrete points on the structure faces. Example force profile measurements are given in Figure 3.9.

The reason for this close match between the two approaches is largely because we are looking at long-period waves where impulsive forces are minimised and pressure distributions are close to hydrostatic in shape. More care is necessary when short-period interactions are the focus of interest, and it is likely that both pressure transducers and load cells would be necessary to capture the full and correct be-

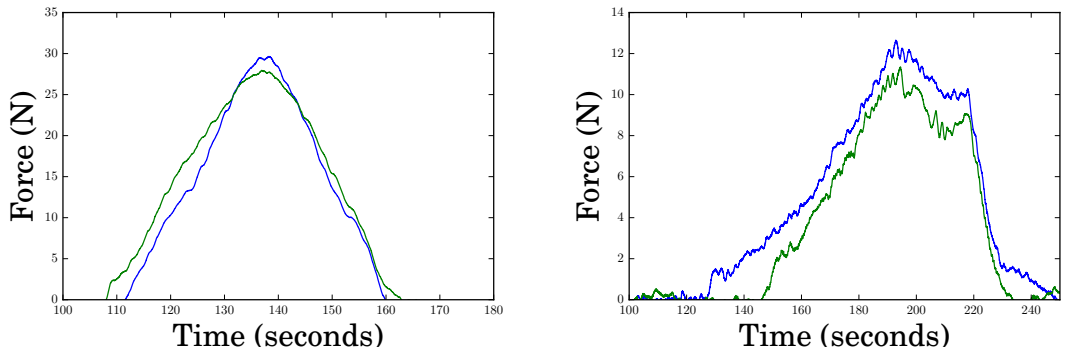

(a) (b)

Figure 3.9: *Full-body load cell measurements (blue) and integrated pressure measurements (green). Data from recent tests at HRW (a) $T = 80s$ (b) $T = 160s$.*

haviour. For the purpose of these tests, a reasonable estimation of the force can be expected, particularly as the free surface is also captured at the face of the structure. This provides crucial additional data points for an interpolation which estimates the pressure distribution. From this, reliable estimates of the force can be integrated.

Recalling Figure 3.7, six pressure transducers are available for the 300 x 300 x 310mm structure, four on the front face and two on the side. Additionally, the time-dependent free-surface profile at the side of the structure is known from image processing of the high speed video. On the 150 x 250 x 310mm structure, three transducers are installed on the front, two on the side and one on the rear. By assuming a water profile at the front face to match the front measurements of the side profile (for simplicity this is assumed to be flat, which is later discussed in Section 3.4.4), an interpolation of the pressure measurements, and the zero pressure assumption at the free-surface is performed.

With the discrete pressure distribution known, the total force on each face can be estimated using (1.20), where $\boldsymbol{\tau}$ is neglected because the structure is bluff. As the pressure distribution in this case is discrete, (1.20) is modified to evaluate numerically the double integral as a Riemann sum. The force in direction of the flow, F_x, is therefore;

$$F_x \approx \sum_{j=1}^{b/dy} \sum_{k=1}^{H_b/dz} p(y_j, z_k) s_{jk}, \tag{3.4}$$

where b/dy is the number of intervals across the building face, H_b/dz is the number of elements up the face, and s_{jk} is the surface area of each element $dydz$.

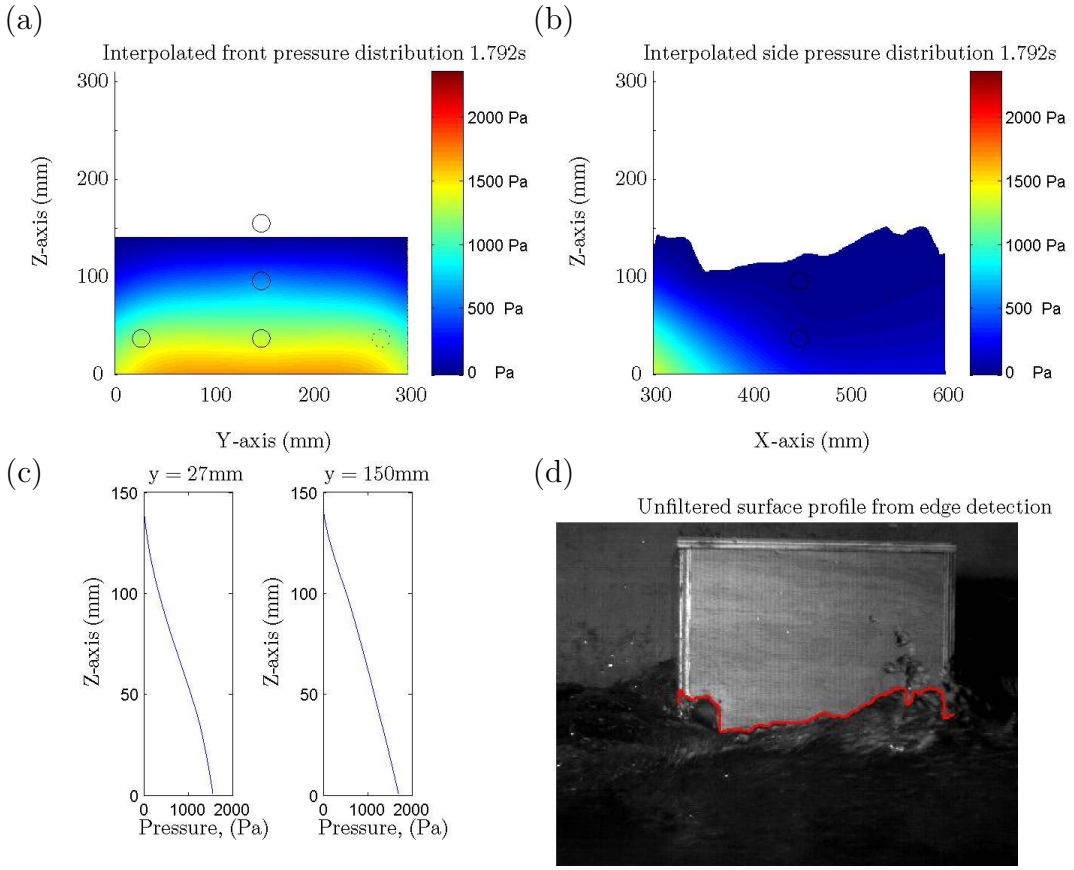

Figure 3.10: *Interpolated pressure distribution based on six pressure transducers and the measured and implied free-surface at a single time sample. (a) front face pressure distribution, (b) side face pressure distribution, (c) vertical pressure distribution at the side of the front face and at the centre of the front face, (d) corresponding image of side face at the same time frame showing captured surface from image processing.*

An example interpolation at a particular time interval for a particular wave is visualised in Figure 3.10. The wave in this example is wave ID 135, a short-period elevated profile wave. The pressures on the front face are interpolated together with the pressures on the right side, and an assumption of symmetry for the left side. Similarly, for purpose of the interpolation the pressure transducer on the bottom left of the front face is assumed to capture the same measurements as if it were placed in the bottom right. With the free-surface boundary providing a zero pressure measurement, the interpolation is carried out using Biharmonic spline in-

terpolation (Sandwell, 1987), a non-triangulation Green's function based approach. Other interpolation methods were investigated such as "cubic spline" and 'linear" interpolation, but for the particular locations of pressure transducers, the biharmonic spline gives the most consistent distributions in line with expectations. The results of this are shown in Figure 3.10 which are discrete pressure distributions on a $1mm^2$ grid.

Knowing the interpolated pressure at each $1mm^2$ grid on the front surface, it is possible to make an assessment of the total force due to fluid pressure acting on the front face. An integration of the pressure distribution over the area would give the total force, and so (3.4) is applied to the discrete pressure field.

3.3.5 Free-surface measurement

The offshore and nearshore elevation of the water surface are measured using a series of electrical resistance probes. These wave gauges measure the voltage from a current flowing between two stainless steel conductors immersed in water. As the fluid is conductive, the current passes via the shortest path (through the water at the free-surface), and so the resistance of the circuit increases for shallower measurements and decreases for deeper water. A linear output is captured in the form of voltage, which is proportional to the immersion depth. Calibration is simply achieved by raising or lowering the wave gauge by a set distance (dictated by pre-drilled holes in the tube of the attachment device). A minimum of three measurements are necessary to achieve a linear calibration. When water is added to the system, a recalibration is necessary due to changes in the electrical conductivity associated with the new concentration of ions. Any large change in water temperature would also change the conductivity and require a re-calibration.

A maximum of twelve such probes are used during the course of the experiments, mostly during the period for validation of the generator mechanism. The voltages are recorded using a multichannel data acquisition rack and logged to a binary file on a computer running the HRW acquisition software. The calibration files are kept with the other data and a note of which calibration corresponded to which data timespan was logged. During the loading tests discussed in this thesis, two key wave probes are in operation; "Offshore 1" and "Toe" as described in Charvet (2012),

located 1.3 and 15.2m from the opening of the wave generator respectively.

For an in-depth analysis of the offshore wave data related to these tests Charvet (2012) provides an excellent summary. The wave probes used for the tests described here are a subset of those used in Charvet (2012), but the best performing probes were selected (minimal interference from transverse vortex loading and strong linear relationship between Voltage and depth).

In the flume, reflections occasionally interfere with the free-surface expected from a given valve input signal, which are sometimes constructive and sometimes parasitic. Charvet (2012) identified a consistent peak in the energy spectra at a period around 26s, which does not vary due to the input wave. This can be attributed to the flume geometry, and so can be attributed to natural resonance of the system. The characteristic length of the flume can be estimated by this period. Assuming the period found corresponds to the first mode, the well known Merian's formula (Merian, 1828) can be used to estimate the characteristic length as $\frac{T_n(gh)^{1/2}}{2}$. For a depth of 0.665, and a natural period, $T_n = 26$s, the characteristic length of the flume (assuming it is rectangular and rectangular) is ~ 33.2m. In reality the flume is not a completely regular rectangular shape, but the total longitudinal dimensions of the flume (including the tank 4.8m, flat region 15.2m, and sloping bathymetry 13.7m) are of similar order to this number (33.7m). It is therefore very likely these interferences are due to natural basin resonance.

3.3.5.1 High speed digital photography

Water elevations in the vicinity of the test structures are captured using a high speed camera and image processing. High speed digital imagery was captured of the side on view of the interactions between the waves and the structure. A Photron FASTCAM Digital Video Recorder was used to capture images at 125 frames per second (fps). The camera wrote the images directly to a hard drive on an attached computer in Tagged Image File Format (TIFF) format. The camera capures images directly to its inbuilt hard drive, due to data exchange speed issues with capturing high speed imagery. The scene was lit using overhead spotlights such that a good contrast in brightness could be clearly detected between a water surface, and the structure. 125 fps was chosen because it provided high time-resolution, without

reducing the quality of images captured - an important consideration for processing the images later. It also means that the camera hard drive is not filled too quickly during a full day of testing, and can be downloaded and cleared over night.

The purpose of the imagery is to capture the free-surface elevation in the vicinity of the structure, and obtain an estimate for the velocity of the wave front. The side-view was chosen primarily due to the window location on the flume, but also because it provided the most information in one shot - side face (full distribution), and also an indication of the front, and rear elevations.

The images are taken as far as possible, pointing directly at the side of the test structure to give as close to an orthogonal image as could be achieved of the side plane of the building. Later, the distortions are rectified using a projective transform. A full description of the image processing techniques used in this thesis is found in Appendix B.

3.3.6 Velocity measurement

Four STREAMFLO miniature velocity probes were used throughout the tests in a wide range of configurations. They are designed to measure flow velocities between 5cms^{-1} and 150cms^{-1} in open channels and in perfect operation can deliver accuracy of $\pm 2\%$.

(a) (b)

Figure 3.11: *Front,* (a) *and side,* (b)*, of STREAMFLO miniature velocity propellermeter.*

The probe head has a five bladed PVC propeller mounted on a hardened stainless steel shaft. This runs in jewelled bearings that are mounted in a protective cage. The cage is joined to a long thin tube inside which is an insulated gold wire that projects to within 0.1mm of the tips of the blades. When the propeller rotates in a conductive liquid, the movement of the blades past the end of the wire varies the impedance between the wire and the tube (HR Wallingford, 2010). This variation in impedance is used to modulate the carrier signal, and after amplification and filtering a square wave signal is obtained (Charvet, 2012). The pulses from this signal are counted over time using a tachometer to obtain a digital reading in volts which is linearly proportional to the of the frequency of the propeller (except at very low speeds).

Calibrations are carried out at HR Wallingford for each of the velocity probes to firstly produce a relationship between flow velocity and number of counts. There is an additional calibration for each tachometer used to relate number of counts to a voltage output, which is ultimately written to a file by the data acquisition system. The two calibrations combined, produced a relationship between flow velocity and voltage, which was captured simultaneously with the other data in the experiments. The voltages were recorded on four channels of the data acquisition rack.

The responsiveness of the propeller to rapid changes in flow or wetting/drying can cause issues. When rapidly wetted by a moving wave front for instance, a lag is expected while the propeller firstly becomes immersed, and then spins up from stationary towards a rate associated with the steady calibration. If the flow acceleration is great, the propeller will not reach the steady calibration frequency before the flow changes, and a reduced rate is reported by the probe as an increased lag. However, the inertia of the propeller is relatively small, so spin-up lag issues are unlikely to be of major concern. Before the propeller is immersed completely, there will be air entrainment from the slightly deformed free-surface as the propeller blades pass close to it, which will reduce the conductivity of the fluid in the vicinity of the probe. However, under quasi-steady conditions, the velocities recorded are accurate so the issue is mainly confined to the arrival of a wave front.

3.3.6.1 Velocity processing

The propeller meters when running in clear and clean water are good indicators of flow velocity. Unfortunately the water in the flume contained fine particulate matter as well as fine fibrous debris. It is the fibrous debris which causes issues with the velocity measurements. The delicate blades of the probes tend to trap the fibrous material and spin it into the bearings of the probe. This in itself rarely stopped the probes from recording and rather just returned a lower count rate to the tachometer. This is undetectable at the time of testing and the probes needed to be checked before each test for functionality. This becomes a particular problem when the probes are placed in the inundation region around buildings and probes require constant maintenance in this case.

While the probes are functioning correctly, the signal to noise ratio was high, and they enabled good capture of data in the difficult shallow flow region. The propeller meters can detect and measure flows in just a few centimetres of water, which is why they are preferred to alternative methodologies such as Doppler velocimeter which require a significant control volume below the probe. One major limitation with the propeller meters was that there was no means of distinguishing between positive and negative flows directly. However, most of the time this could be easily inferred and due to the sump behind the buildings catching the full over-topping volume for all but a few waves, return flow was not generally an issue in the inundation zone.

Charvet (2012) used a power spectrum technique to identify probes which were malfunctioning. This same process is expanded on and used here. The energy spectrum method uses results from a review of Kolmogorov's contribution to the understanding of small scale turbulence (Hunt and Vassilicos, 1991). By selecting a sample of reliable, repeatable velocity data for each probe, a trusted reference energy spectra can be taken and compared to the power spectra from readings that are of unknown reliability. When the probes are functioning correctly, a constant decay in energy can be seen for angular frequencies above $\omega_m = 1\text{rad}s^{-1}$. Hunt and Vassilicos (1991) state that signals such as velocity time-series containing discontinuities, exhibit an energy spectra of the form $E(\omega) \propto \omega^{-2p}$ as $\omega \to \infty$, where $p = 1$ for sharp discontinuities and $p = 2$ for other discontinuities. The following relationship (3.5) is used

to compare with the energy spectra from the velocity probes for $\omega > 1$.

$$Y(\omega) = Y(\omega_m)\omega^{-N} \tag{3.5}$$

Data which fall broadly within the $2 < N < 4$ region are retained otherwise the probe is rejected on the basis that it is not following the profile of a normally functioning energy spectra. An example of this is shown in figures 3.12 and 3.13.

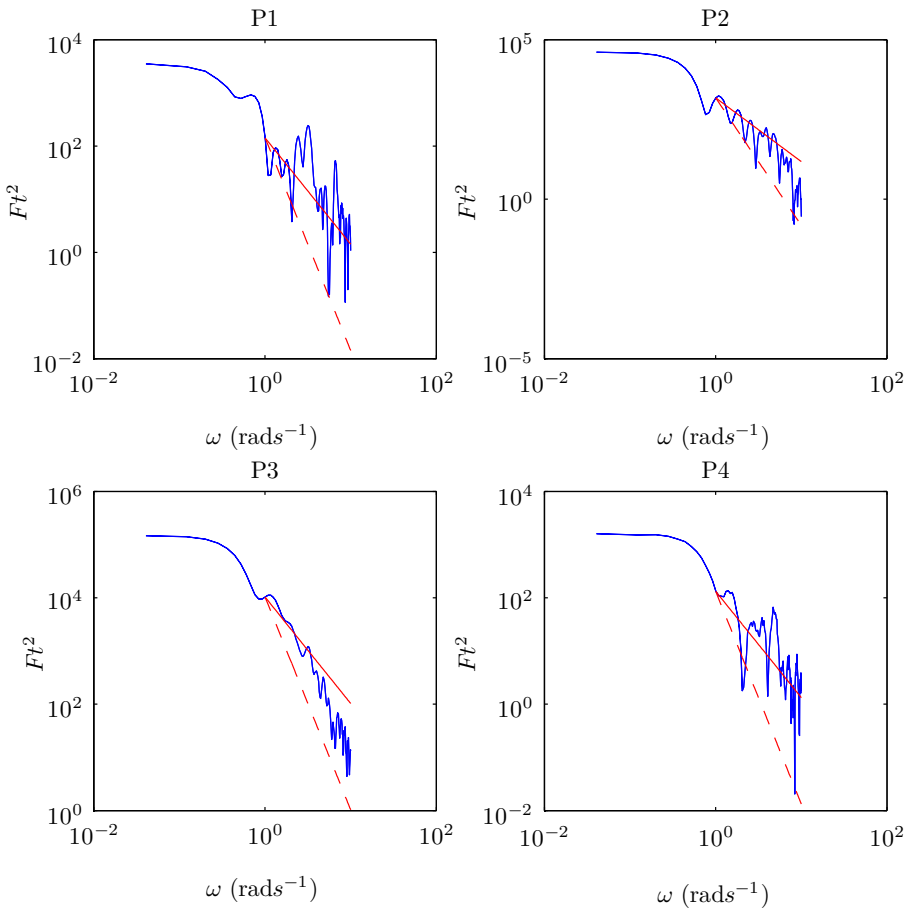

Figure 3.12: *Velocity spectra for wave 307 - all probes functioning correctly. Solid red, $N = 2$, dashed red $N = 4$, energy decay roughly follows this bounds. "P" refers to the probe number.*

The data in figure 3.12 are retained for all four probes, though the time-series for probe 1 and 4 were re-examined more closely and showed no obvious low peak velocities in comparison to the previous identical test. Figure 3.13 shows two clear

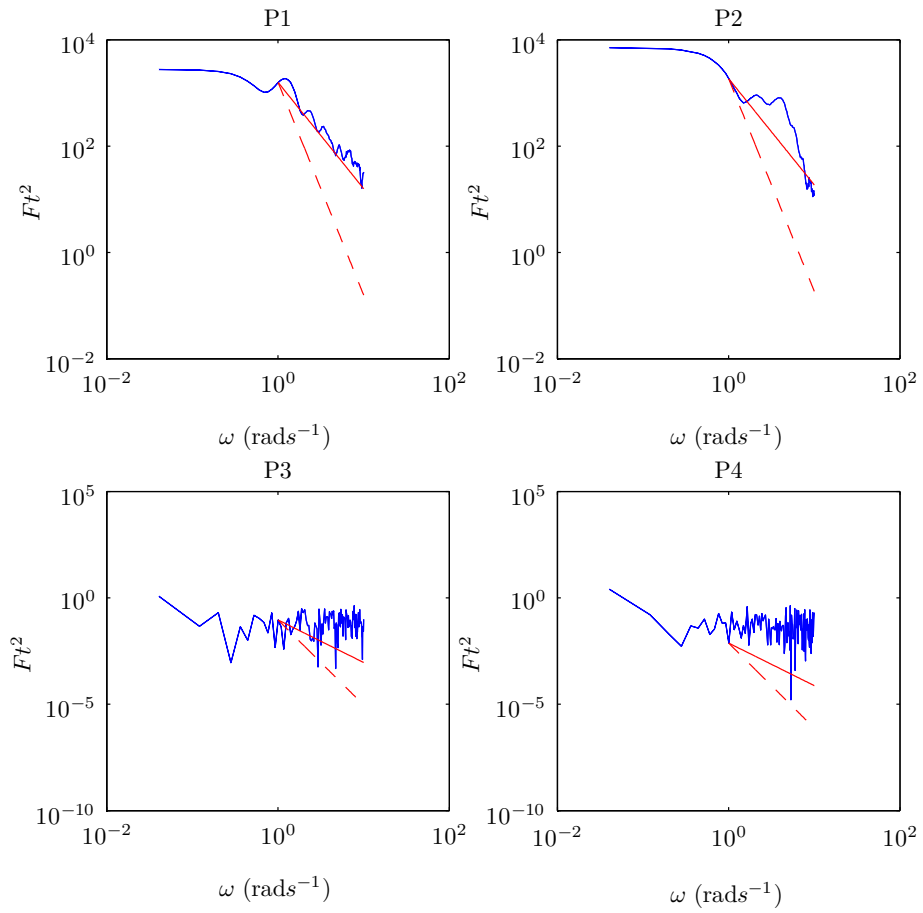

Figure 3.13: *Velocity spectra for wave 133 - probes 3 and 4 malfunctioning. Solid red, $N = 2$, dashed red $N = 4$, energy decay roughly follows the bounds for probes 1 and 2, but clearly deviates for probes 3 and 4. "P" refers to the probe number.*

exhibits where the data are rejected (probe 3 and 4). Referencing this particular test a note entered in the lab book revealed that a fibre was removed from probe 3 and that probe 4 required cleaning following this test. This information is reassuring and provides evidence that the methodology provides a robust and clear means of testing the quality of velocity readings. The same analysis was applied to the remaining velocity data so that confidence in the results used in further analysis could be assured.

The four velocity probe results for each test are processed in this way and a matrix constructed with a 1 if the probe was functioning correctly and a 0 if it was malfunctioning. This reliability matrix is carried forward and used in the subsequent further analysis conducted with the velocity data to allow for elimination where appropriate.

3.3.7 Scaling and dimensional analysis

The experiments described thus far in the thesis are scaled physical models designed to capture the characteristic processes of long wave inundations. In order to use the results and infer representative prototype (full-scale) forces and flow conditions, the scaling has to be thought about carefully.

When carrying out scale experiments it is important to ensure that distortions are kept to a minimum and the easiest way of avoiding this is to test at large-scale. The unsteady tests that were carried out were in a 45m long wave flume for this very purpose. Even so, due to the size constraints it was only feasible to test waves at scales between 1:50 and 1:100. Instrumented buildings that are used also have this scale range in mind, with the building height equivalent to a 15-30m high structure depending on the scale. By assuming the same prototype building the UCL-based steady tests the equivalent scales were between 1:120 and 1:240. It is essential to consider the most important parameters, fluid properties, flow properties and geometries and use scalings that minimise distortions to those quantities. The most common way of doing this, is by choosing a dimensionless quantity involving these properties and ensuring this remains constant between model (subscript m) and prototype (subscript p) scale. Dimensionless groups can be found using Buckingham's Π-theorem (Buckingham, 1915).

Froude scaling, where similarity is preserved between Froude numbers assumes that viscous forces are insignificant in comparison to inertial forces. Scaling by preserving the Froude number, maintains the inertial force scaling. If flows are dominated by viscous forces (i.e. at low Reynolds numbers), the scaling of the Reynolds number needs to be maintained.

Froude scaling is specifically stating that $Fr^2 = \frac{u_m^2}{gL_m} = \frac{u_p^2}{gL_p}$. This is a requirement if the results of this thesis are to be scaled up to prototype scale. Maintaining Fr at model and prototype scales produces the following scale factors relative to the length scale, λ_{sf}, in Table 3.2:

Table 3.2: *Froude scaling factors for various quantities.*

Quantity	Scaling factor
Length, L	λ_{sf}
Time, T	$\sqrt{\lambda_{sf}}$
Force, F	λ_{sf}^3
Moment, M	λ_{sf}^4
Pressure, P	λ_{sf}
Flow, Q	$\lambda_{sf}^{5/2}$

Scaling in relation to impulsive pressures associated with wave impacts is discussed in Cuomo et al. (2010), where the application of Froude scaling is justified for quasi-static pressures after the impact has finished. However, the unsteady and short-duration impulsive pressures during the initial impact of a wave are influenced by the presence of air in the water and as such the application of Froude scaling under these conditions will yield incorrect prototype pressures (generally over-predicted). Bullock et al. (2001) investigate the effect of entrained air and note that this causes particular issues due to differences in the way bubbles form and times they persist in salt water compared to freshwater, and so scaling small-scale freshwater tests up to prototype-scale in sea water is difficult because of the complexities of compressibility. Bullock et al. (2001) find that using a Cauchy scaling law (maintaining ratios of inertial to elastic forces) for the compressible flows instead of Froude scaling gives an under-prediction of pressures. Bredmose et al. (2015) also confirm that there is an under-prediction of impact pressures by Froude scaling at high impact pressures with trapped air pockets. In this case Bredmose et al. (2015) find the values follow more closely a Bagnold-Mitsuyasu scaling law (Bagnold, 1939; Mitsuyasu, 1966).

The investigation of impulsive impact pressures on the building is not a focus of this thesis. As is discussed further in the thesis, the predominant loading that is of concern in this study is that of quasi-steady flows where the resultant loading is quasi-static. The dynamic impacts of tsunami bore fronts on buildings is of some interest, as it can be associated with sudden failure of individual structural elements, but it is beyond the scope here. As such, Froude scaling is applicable to all quantities described in this work.

3.3.8 Phase synchronisation between tests

For a host of diagnostics and in order to produce the results later in this chapter, zeroing and synchronisation of repeated tests was required. Repeated tests need to be synchronised in order that they can be compared, and in some cases, averaged to account for some of the uncertainty between tests. Other areas which require synchronisation are where data are captured at the same time, but from a separate acquisition system.

It can be quickly noticed by the reader when comparing two repeated time-series from experimental data, that variations due to several sources of uncertainty mean that they are not identical. This causes problems when attempting to synchronise two signals based on say, the time of peak. Unless there is a very sharp step-like signal with an instantaneous peak, when noise is introduced to a fairly flat underlying peak, the time of local maximum will vary between signals. Similarly, when using a maxima (or minima) in the time-derivative, similar problems are encountered. Using combinations of these values and searching for several constraining points in the time signal can improve the performance, but results were unsatisfactory.

An alternative to looking at only single points in the time-domain is to utilise the entire signal. A technique for doing this is known as *Cross Correlation*. Cross correlation essentially compares one function with another by shifting one along by a lag, and testing the correlation between the two functions. A cross correlation is very similar to a convolution (see Kreyszig (1999) for example), a technique widely used in probability theory and signal processing. The difference being in a convolution, one signal is reversed during the process, which does not occur during a cross-correlation. For two functions, $f(t)$ and $g(t)$, the cross correlation (denoted by the $\star$ symbol) is

defined in (3.6).

$$(f \star g)(t) = \int_{-\infty}^{\infty} f^*(\tau) g(t+\tau) \mathrm{d}\tau \tag{3.6}$$

where f^* indicates complex conjugate of f, where τ is the phase shift. For discrete data, as required for our purpose, a different form is used (3.7);

$$(y_1 \star y_2)[n] = \sum_{n=-\infty}^{\infty} y_1^*[\delta] y_2[n+\delta] \tag{3.7}$$

where y_1 and y_2 are time-series (sampled at the same rate), δ is the lag and n is the data point. When the cross-correlation is plotted against the lags, a peak in the correlation function corresponds to a maximum likelihood estimate of the phase shift between the two signals. The time lag can be identified in this way and the performance is found to be very good, even for signals with moderate levels of noise.

In order to compare signals from different tests and synchronise them in this manner, at least one reference signal is required that is present in all tests to be synchronised to. Within the data collected for the unsteady tests, three channels are common to all data throughout the test duration without any variation (movement of probes etc). Two wave probes, ("Offshore 1", located just away from the mouth of the generator and "Toe", which is located at the toe of the bathymetry where the flat propagation region finished) were common to all tests. In addition to this, a time-series is captured which logs the wave generator's valve position, and this was also present across all tests.

An example set of profiles that has been synchronised to the time of the first test is shown in Figure 3.14. The profiles are for the wave probe at the toe of the bathymetry, but by synchronising this profile, the entire set of data for those waves are also synchronised that were captured using the same data acquisition board. This enables velocity, pressures, load signals and other wave probes to be viewed for a given wave type; particularly useful as the velocity probes are moved around between different tests to cover other regions. One remaining data set that cannot be

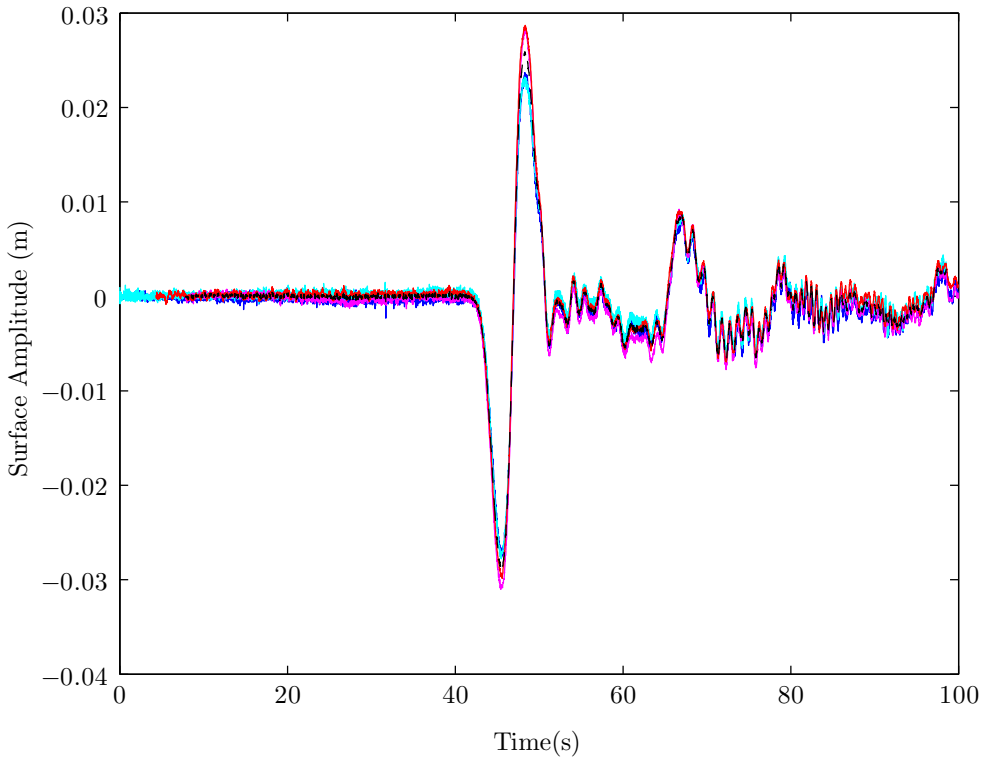

Figure 3.14: *Free-surface elevation time series measurements of the wave probe located at the toe of the bathymetry. Plot shows four repeated tests, and the average of all four (black dashed line).*

captured on the same acquisition board is the water elevation data around the structures. This is instead captured using image processing of high speed photography and so is not synchronised with the rest of the data in its raw form. However, the pressure transducer tests with the pressures left in units of mm of water ($p/\rho g$) are compared to the surface elevation at the front of the structure in mm. The height of the lowest transducer (36mm) is added to the pressure, and water depths lower than this were set to 36mm in the surface profile. In this way, the same cross-correlation technique could be used to calculate the necessary phase shift. For tests without pressure measurements, the water profile could be shifted by comparing to other tests with pressure measurements. In this way, all data regardless of the logging system are synchronised for each test along with any repeated tests. The data for subsequent repeated tests are synchronised to the timing of the first test.

By performing these analyses, it is possible to combine quantities like velocity and water height, an essential step in the following sections which rely heavily on the ability to do this with confidence.

3.4 Experimental results

3.4.1 Observations

Initially water levels in the flume are still and at a level close to the top of the sloping bathymetry at an offshore still water depth (SWD) of between 640 and 670mm, depending on the wave and valve position and wave being generated. SWD is achieved with the pump activated and control valve closed for our elevated wave tests, and with the valve open for the N-wave tests. This is because the elevated waves are created only by positive discharge from the wave generator, whereas for the N-waves the generator removes water from the flume firstly in the negative portion of the wave. To therefore maintain the required constant SWD, a different volume of water is required in the flume system for the different types of waves.

Once the generator control valve is actuated, water is either released or taken in to the tank through the gate, and a positive / negative fronted wave propagates along the flume towards the bathymetry. The waves in this portion of the flume

propagate with a constant profile shape, at a constant velocity which approximately corresponds to the shallow water wave celerity $(gh)^{1/2}$. When this wave interacts with the bathymetry, the free-surface profile changes. The amplitude increases, and the velocity reduces in line with the effects of shoaling. As the wave approaches the shoreline, the water depth initially increases for elevated waves causing the shoreline to advance, and reduces for the N-waves causing the shore to initially retreat. Once the positive portion of the N-waves arrives, the water depths increase and the shore advances back up the bathymetry. At this point for both elevated and N-waves, the shore advances up to the flat portion, over-topping at the point where the bathymetry slope becomes zero, and velocities increase. Longer period waves tend to advance more slowly and act like a slowly rising flood. Water inundates the shore, propagating across the flat region of the flume and onto the instrumented buildings.

When the water reaches the instrumented test structures, the depth increases slightly upstream of the block, and water flows around the structure. Short-period waves (here $T \lesssim 10$s) tend to make an impulsive impact on the front of the structure and water splashes upwards to heights occasionally in excess of the building height (300mm). For low flow rates, the upstream and downstream depths (h_1, h_d) are similar, but as the wave approaches its peak and flows increase, the free-surface profile around the structure changes. Levels drop away towards the rear of the structure, before the inundating water spills into the sump at the rear of the flume. This is the same choked flow behaviour as observed for the incremental steady-flow tests of Chapter 2. For long-period waves, as would be expected for a tsunami, the transition between these states occurs within one time-series of the same wave.

3.4.2 Data collected

A wide range of parameters are tested by sets of specific tests. These tests are summarised in Table 3.3 and the various variables used are discussed in isolation. There are some overlaps in the data collection between this project and that of (Charvet, 2012), whose primary dataset was the run-up/run-down tests. A subset of the waves described in Charvet (2012) have been used throughout this thesis.

Description	Key variables	Data collected
Run-up/-down tests	Wave profile, position of sensors	Run-up/-down distance and elevations, velocity profile up the beach, over-topping volumes
Pressure tests	Aspect ratio of structure, distance from the shore, wave profile	Pressures, velocities, high speed imagery

Table 3.3: *Summary of experiments carried out at HRW as part of this study. All tests additionally included capture of the offshore wave surface behaviour*

3.4.3 Offshore surface height

A subset of waves used in Charvet (2012) is chosen for the building experiments. Broadly speaking, the waves are of two varieties; leading elevation and leading trough, with a range between short and long periods.

Six leading elevation waves and seven leading depression waves are selected for use in these tests. They are chosen because of their variations in profile shape and period, their repeatability and their ability to propagate inland. Table 3.4 gives some selected characteristics of each of these waves. Each wave is referred to by its wave ID for the remainder of this thesis. The N-wave with ID 307 is the attempted scale recreation of the now famous "Mercator time-series" (Siffer, 2005) which came from Belgian yacht Mercator which was anchored about 1.6 km off the Phuket coast (07.715N; 98.28E) during the Indian Ocean tsunami 2004. The yacht happened to have its "fishfinder" depth gauge switched on and so provides one of the only offshore recordings of the 2004 tsunami. In the tests the height of the free-surface is captured at two capacitance type wave gauges.

The mean time-series of water surface amplitude at the toe of the bathymetry is plotted in Figure 3.15, for elevated waves (a) and N-waves (b). Periods, T, and wavelengths, λ_w, are calculated using the first half of the positive wave, assuming symmetry, consistent with Charvet (2012):

$$T = 2(t_{\eta_{\max}} - t_0), \tag{3.8}$$

Wave ID	Type	Typical Period (s)	Typical Wave-length (m)
138	Leading elevation	6.90	14.50
136	Leading elevation	7.10	14.92
135	Leading elevation	8.70	18.48
441	Leading elevation	23.08	67.68
415	Leading elevation	52.40	161.60
442	Leading elevation	98.20	282.02
130	Leading depression	7.10	17.93
133	Leading depression	8.50	21.95
113	Leading depression	9.00	22.73
439	Leading depression	16.69	45.85
435	Leading depression	37.91	102.10
434	Leading depression	76.92	202.50
307	Leading depression	114.85	280.46

Table 3.4: *Subset of wave profiles used in this study.*

where $t_{\eta_{\max}}$ is the time of the peak wave surface elevation, η and t_0 is the time when the value of η is 1% of the peak.

3.4.4 Water surface height around structure

The measurement of water surface heights around the structure is crucial to constrain the interpolation of a pressure distribution. An example is presented here where the free-surface has been captured on the front of a test specimen. The structure used in this example is the 150mm wide building and the wave is ID 415 (Elevated, $T \approx 52s$). The building is positioned at D3, so 1400mm back from D1 where the wider structure is positioned throughout the experiments. In this position it is possible to see the front directly, and observe the free-surface position (Figure 3.16 (a)). This front part of the image can be orthorectified based on the known dimensions of the building (Figure 3.16 (b)), to allow image processing methods for extraction of the free-surface to be applied. Details of the processes applied to obtain the water surface profile time-series from high speed imagery are given in Appendix B.

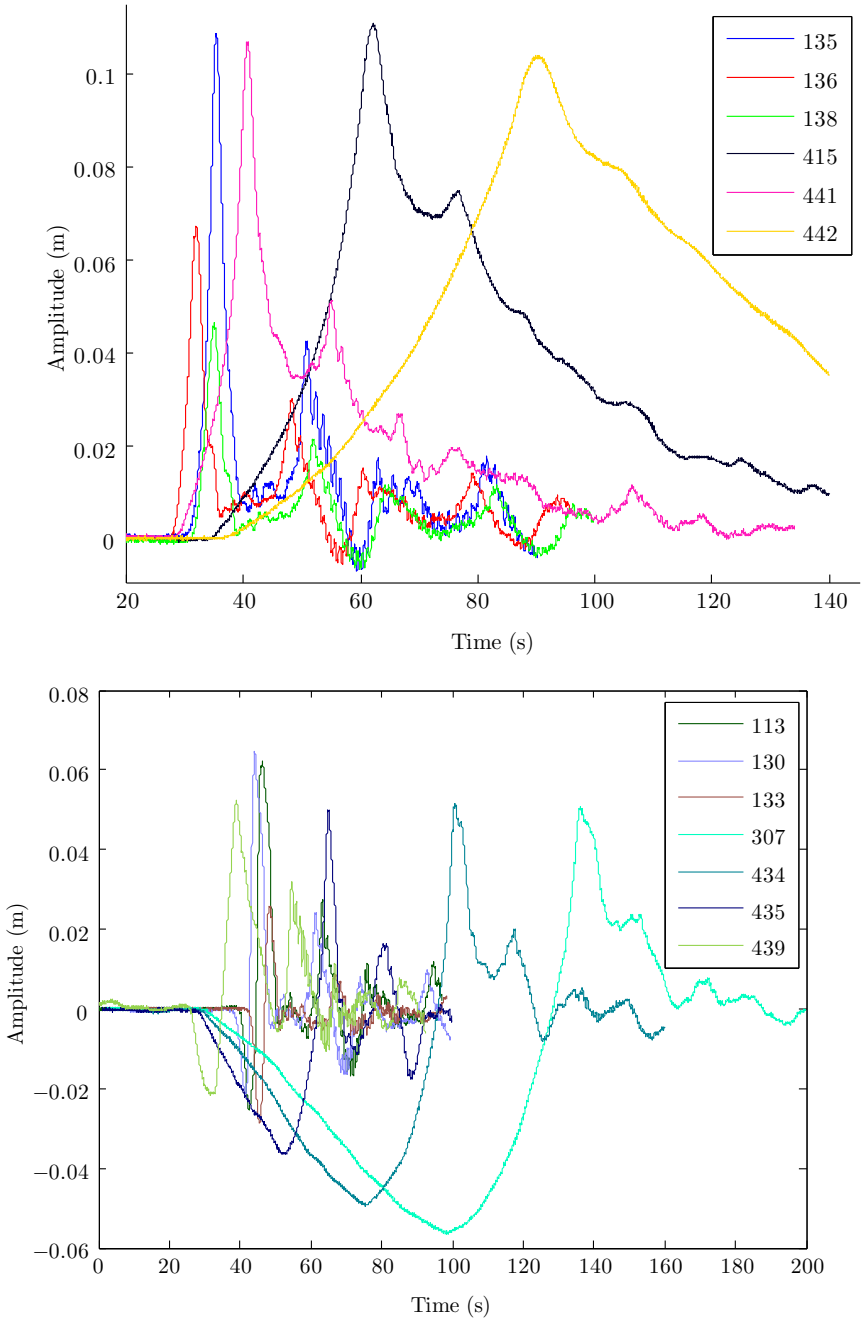

Figure 3.15: *(a) Mean elevated wave profiles at the toe of the bathymetry. (b) Mean N-wave profiles at the toe of the bathymetry. Legend refers to Wave ID number, each trace based on four repeated waves.*

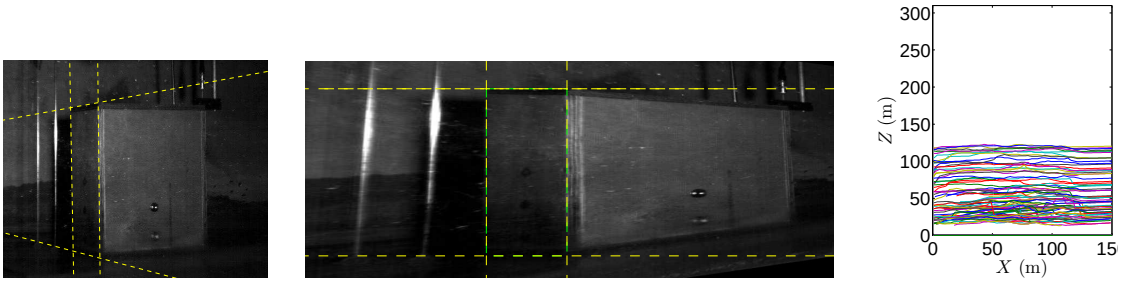

(a) (b) (c)

Figure 3.16: *Procedure for water surface extraction. Wave 415 at D3. (a) Raw image with coordinate system. (b) undistorted transformed area where coordinate system is valid, distortions outside this range. (c) extracted front free-surface profile plotted at 0.2s intervals (available at 125Hz) to demonstrate the shape is relatively horizontal.*

As can be observed in Figure 3.16 (c), the water profile across the front of the structure is largely horizontal, with some higher levels recorded at the centre of the front face. Some of these increased water levels are high and exceed $1.5h_1$, as measured at the side. However these are due to splashing as the wave front hits the face, and generally occur at low h_1. At most the increase in central water height on the face during the quasi-steady flow part of the inundations is $\sim 1.2h_1$. On average, the variation in height across the front for the majority of waves is small, and while the highest force is applied (usually while the water level is at its highest) the variation is at its lowest.

A similar procedure is carried out on the side face, so that the free-surface is known for the front face, and one side. By symmetry the opposite side will have a similar pressure distribution (ignoring any effects due to vortex shedding), and so the pressure distributions should cancel out in terms of global forces on the building. The greatest variation in water surface height across the face is found in the side profile. The front face gives a flat profile such that once the pressure distributions are calculated, the difference between using the actual measured profile and using an equal level across the front based on the front side value is negligible (discussed in the next section). As such in order to capture the most information, the side profile only is focussed on at position D1 and D2.

In terms of the water level at the rear of the structure, the levels are not measured

during the tests because for all but a few individual tests it is observed to be very low. The velocity past the structure to the sides was high, with limited transverse component, and as such very limited potential for flowing immediately behind the structure. Additionally, with the sump at the back of the flume, the volume overflowing is effectively removed from the system, so no form of upstream restriction existed. For the majority of cases in reality, this would clearly not be the same due to buildings, topography and other forms of loss to the momentum.

3.4.5 Pressures on the face of the structure

The individual pressures from six transducers are presented here for one wave (ID 135) for the building at position D1 (see Appendix C.1).

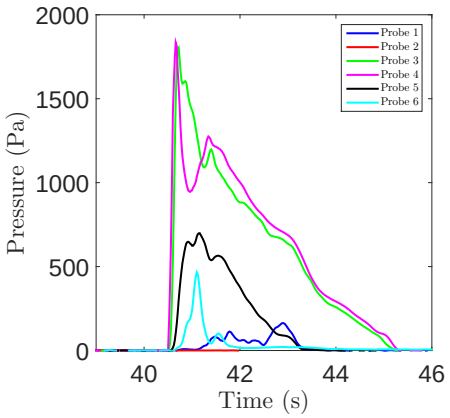

Figure 3.17: *Pressure transducer plots from the 300mm wide building. Wave 135.*

As discussed in Section 3.3.4.1, a simple summation is carried out by firstly Interpolating the point pressures onto a regular surface and converting the pressure (in Nm^{-2}) to force per mm^2. For every time interval, the process is repeated, so that a new time-series is generated for the integrated force. This avoids the issues found by Fujima et al. (2009), where simply integrating the maximum pressure envelope overestimated peak forces significantly. The average (from two individual tests) front-face force for the 300mm wide building at position D1 is shown for each of the 13 different waves used in this thesis in Figure 3.18 (a).

A sensitivity test assuming a parabolic shaped free-surface variation across the front

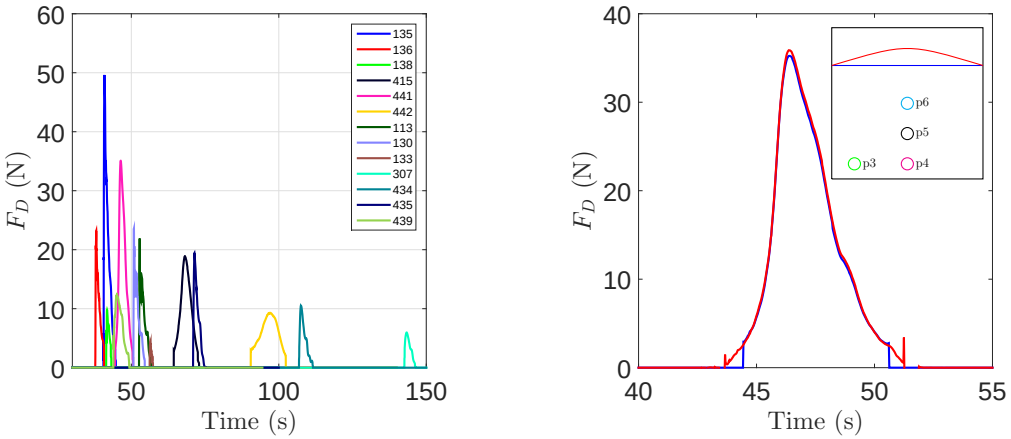

(a) (b)

Figure 3.18: *Average (from two individual tests) integrated pressure distributions to produce total force on the building for all waves and the effect of accounting for a parabolic front surface profile with a 30% increase in h_1 at the centre. (a) All waves integrated pressure distribution (full-body force). Wave IDs as given in legend. (b) Wave 441 integrated pressure distribution with flat front and with 30% increase to h_1 at the centre line of face (150mm from the side). – horizontal free-surface assumed, – parabolic free-surface assumed. Inset image in (b) shows pressure transducer locations and front surface shape assumptions corresponding to the force estimates shown.*

of the structure shows the difference in computed full-body force to be negligible. This alternative assumption is achieved by substituting a parabolic free-surface at the front of the building instead of using the front value from the side profile across the whole face. By assuming a large free-surface increase in the centre of the front face (30% higher than at the side), the interpolation and summation is carried out for wave 441 in Figure 3.18 (b), where it is compared to the horizontal front surface assumption.

As may be appreciated, the integrated force when the parabolic front free-surface shape is assumed is larger than that from a horizontal front free-surface, but the differences seen are negligible. Due to this result the assumption of a flat front free-surface profile is applied to all integrated pressure distributions used in determining full-body forces.

3.4.6 Onshore velocity

Once the probes are filtered for suitability using the techniques of Section 3.3.6.1, they are available to estimate the overground velocities of waves which inundate the shore. The locations for the probes while test structures are in position are given by Figures C.1 to C.2 in Appendix C.

Onshore velocities are also captured without buildings present. In this case the probes are located at; p1 = 13.80m, p2 = 14.30m, p3 = 14.80m, p4 = 15.30m, which are all positions on the flat portion of the beach. All distances are relative to the toe of the bathymetry. An example set of onshore velocity data is presented in Figure 3.19, which is for wave ID 307 (the scaled "Mercator time-series"). As discussed in Section 3.3.6, the propeller meters only operate reliably under water depths above $\sim$ 15mm, so the initial parts of the profiles in Figure 3.19 are unreliable. As the probes can not distinguish between positive and negative velocities, the absolute velocity, $|u|$ is presented.

For comparative purposes, the absolute depth-averaged velocities predicted by the 1D numerical model of Chapter 2 are also shown in Figure 3.19. It is clear that the simple model predicts the overground velocities well. As the wave for the initially dry positions gave positive onshore velocities, the transition between positive and

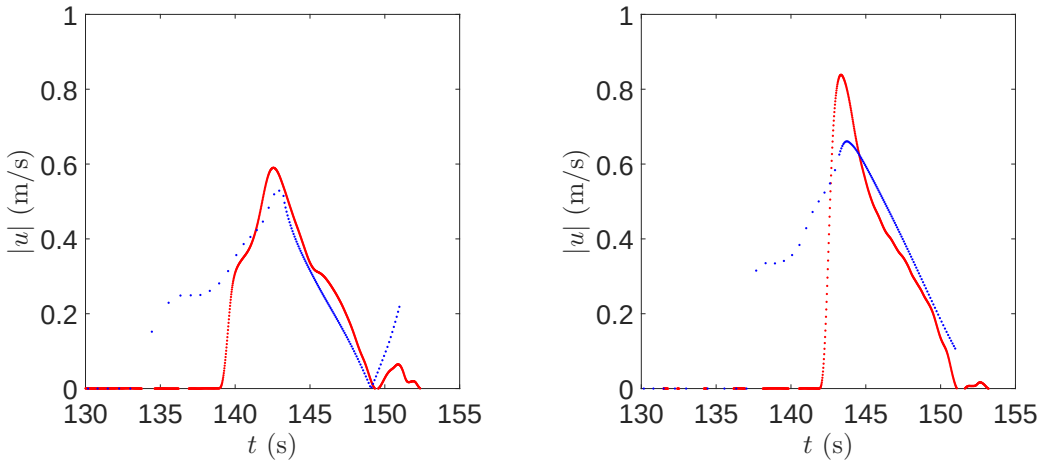

Figure 3.19: *Absolute onshore velocities from long- N-wave, 307 ("the Mercator", $T \approx 114s$), (a) at 13.8m, (b) at 14.8m from the toe of the bathymetry.* ●*, 1D numerical,* ●*, large-scale experimental velocity from propeller meters. No building present during these tests.*

negative (reverse flow) is indicated by a "V" shaped portion of the profiles which touches zero. This occurs in Figure 3.19 (a), although it should be made clear that the reverse flow is associated with very low water heights, $h \lesssim 20$mm. This is likely to be why the magnitude of the measured reverse flow at the end of the test in Figure 3.19 (a) is lower than the model. As expected, the model provides velocities at low water depths, but the probes are unable to detect velocities until $h > 0.015$m.

3.4.7 Nearshore velocity

For some of the tests the velocity probes are placed in the nearshore region. The performance of the devices actually improves as they appear not to experience the same level of clogging from fibrous debris discussed in Section 3.3.6 as when located in the wetting and drying zone on the shore. Additionally they are always in deep water, and so do not experience the same wetting and drying issues found when the flows are low. In this case the probes are located at p1 = 9.50m, p2 = 10.50m, p3 = 11.50m, p4 = 12.50m from the toe of the bathymetry. The probes are located approximately 10mm from the bottom, so the velocities measured relate to this

depth. As with all measurements from the propeller meters, the reported velocities are absolute, as there is no way to distinguish positive and negative counts with this equipment set-up. However, with wider information about the wave, their sign can be inferred.

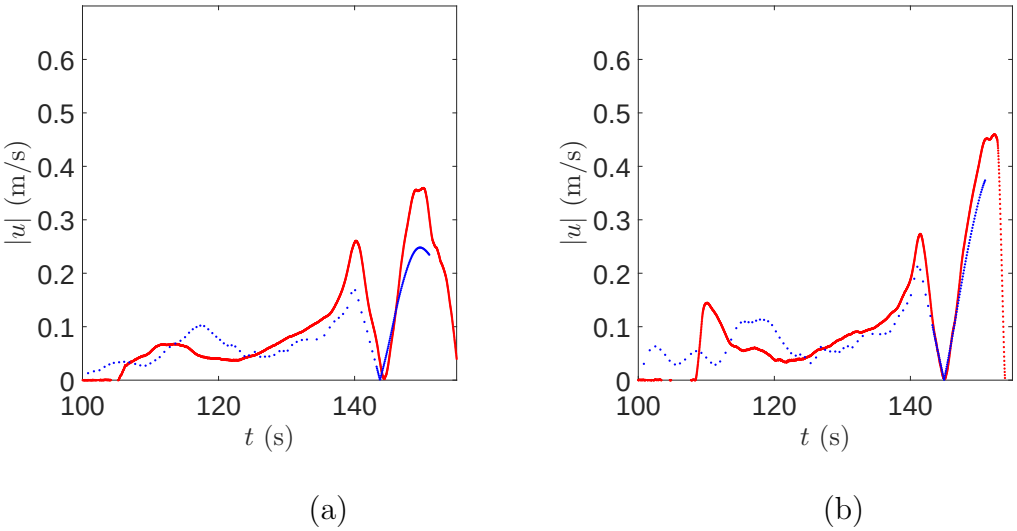

Figure 3.20: *Absolute nearshore velocities from long- N-wave, 307 ("the Mercator", $T \approx 114s$), (a) at 9.5m, (b) at 11.5m from the toe of the bathymetry.* •, *1D numerical,* •, *large-scale experimental velocity from propeller meters.*

The example data in Figure 3.20, and the full set in Appendix D.2 are used for validation purposes. The collection of velocity information in the near-shore region allows an assessment of the performance of the depth-averaged velocity calculated by the one-dimensional model. The blue trace is the absolute velocity, $|u|$, which matches the measurements well.

3.5 Application of quasi-steady framework

In many ways, parallels may be drawn between the experiments discussed in Chapter 2. There is a clear transition between the sub-critical and choked flow regimes (later demonstrated in Figure 3.22), within the same wave. The key difference between the steady tests and these unsteady tests, other than the complexity of the

equipment and scale, is that flows and depths vary instantaneously, so the conditions are unsteady.

However, for many of the waves and certainly those with a longer period, flow conditions are what we would describe as quasi-steady, which means first-order time derivatives are generally small. Longer period waves are more representative of tsunami inundations than shorter period waves which sometimes exhibit significant unsteady behaviour, and so it is reasonable to propose that the steady-based methods discussed in Chapter 2 could give a good approximation for the quasi-steady conditions observed in these tests.

In particular, to apply the steady framework to the unsteady experiments it is important that accelerations in the flow are small. The model described in Chapter 2 is based on the assumption of a constant flow, Q, and the steady Navier-Stokes equations. The force closure used considers only a hydrodynamic drag component, which can be extended by Qi et al. (2014) to include hydrostatic and drag, whereas to fully consider unsteady conditions an inertial term would be needed to account for "added mass" forces, which are a result of accelerations in the flow. With small accelerations, these terms would become insignificant and with this caveat, a range of waves; from short to long period, and covering both negatively (N-wave) and positively (Elevated) led waves were used in this study (see Table 3.4).

A complete set of results is available for the thirteen different waves that were used, with up to four repeats for some measured quantities. The sets of waves can be split into Elevated waves (6 profiles), and N-waves (7 profiles). A plot of these 13 waves at the Toe of the bathymetry is found in Figure 3.15.

Firstly attention focusses on those results from the square shaped building (300 x 300 x 310mm), and at distance D1, which is closest to the shoreline. Results are restricted to this particular set up because it is the most complete of all datasets, and most representative of the complementary steady experiments that were carried out. The flume width is 1200mm, so the blockage ratio (b/w) for this set up is 0.25, identical to the steady tests.

A key assumption of using the framework from steady tests, is the assumption that forces due to accelerations represent a small contribution to the overall force on a structure. In order to test this assumption, we need information about the

accelerations in the flow around the structure. Velocity recordings are made in the vicinity of the building to capture this information using miniature propeller meters. By taking the difference in velocity between samples and dividing by the time interval as (3.10), a proxy for the first time derivative can be determined. Using this pseudo acceleration, an estimation of the contribution to overall forces on the test structure can be made using the inertia term of (1.33), which is repeated below.

$$\rho V C_{\mathrm{m}} \dot{u} \tag{3.9}$$

For the 300mm test structure, the plan area was $0.3 \times 0.3 = 0.09\mathrm{m}^2$. The instantaneous volume displaced can be estimated knowing the front and rear water level from the side profile as $\frac{0.3^2}{2}(h_f + h_r)$. C_{m} for a square based prism is given as 2.19 and for a cube 1.67 (see Table 1.2). Given that the bottom and top faces of the structure are not in contact with the water, the inertia coefficient is likely to be lower than these C_{m} values for our case. Using a coefficient of 2, the average time-varying inertial contribution to the force for all 13 waves tested in these experiments is given in Figure 3.21.

The velocity propeller meter used to provide the accelerations to calculate inertial forces in Figure 3.21 is placed 4cm in front and 4cm to the left of the structure. This ensured the velocity of the incoming wave is captured rather than a measurement which could be highly influenced by the presence of the structure. Towards the rear the flow exhibited more more turbulent behaviour at certain phases of the inundation, and as such made the accelerations more difficult to analyse.

However, the accelerations derived from the propeller meter measurements are very noisy as taking a difference between samples is fairly unstable. The accelerations are calculated as

$$\left.\frac{du}{dt}\right|^{n_s+1/2} \approx \frac{\Delta u}{\Delta t} \approx \frac{u^{n_s+1} - u^{n_s}}{1/f_s}, \tag{3.10}$$

where f_s is the sample frequency and n_s is the sample number. As such the resultant accelerations require filtering with a moving average in order to produce meaningful signals which are used to produce Figure 3.21. As is clear, based on this analysis the total forces are two orders of magnitude larger than the highest calculated unsteady contribution. It can be seen in Figure 3.21 that the contribution from inertial forces

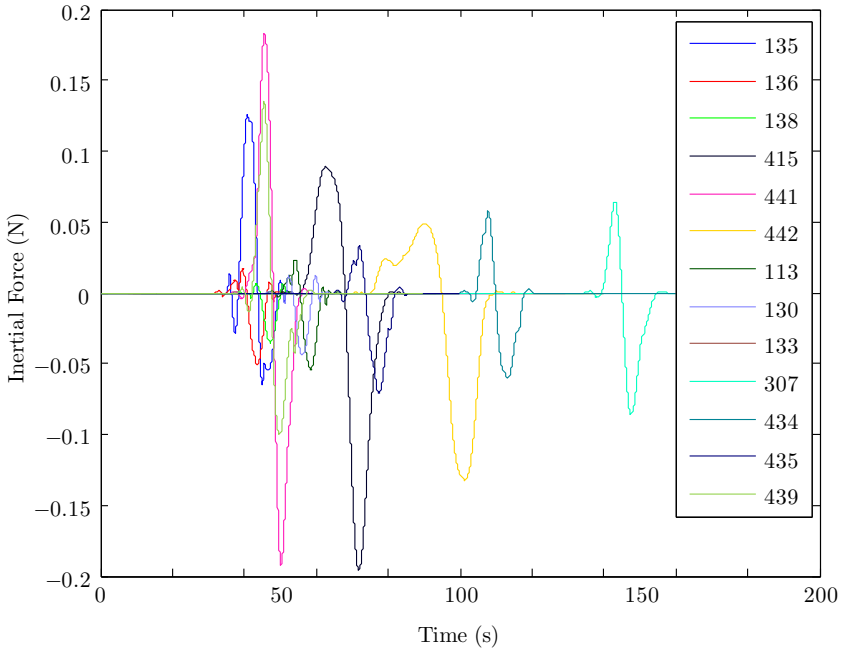

Figure 3.21: *Inertial force contribution for all waves $\rho V C_m \dot{u}$. Numbers in legend correspond to the Wave IDs in Table 3.4.*

for all waves tested in this project does not exceed 0.2N.

With this result in mind, the unsteady force appears to be low, and it is expected that the steady framework of Chapter 2 is a reasonable representation of the unsteady or "quasi-steady" case for all 13 waves. Having calculated the integrated forces from only the pressure and water level measurements, it is possible to perform a comparison between the results of the large-scale tests, and the predicted forces based only on the measured upstream velocity and depth information.

The first thing to check is that the relationship between upstream and downstream Froude number derived in (1.29) holds for the quasi-steady case. Measurements of upstream and downstream Froude number (from the velocity and depth data) are available, but plotting Fr_1 and Fr_2 for each sample is not sufficient. As we have seen in the calculation of accelerations, and in Section 3.3.6.1, the velocity data has significant uncertainty associated with it (see Appendix E). Basing calculations (which are very sensitive to velocity and water levels) on these data means that

the subsequent quantities are also affected by uncertainty. In addition to this, due to the unsteady nature of the wave interactions, there is a delay between a change in velocity and depth at the front of the structure, and the subsequent change at the rear. To compare the upstream and downstream Froude numbers, this phase shift needs to be accounted for in some way if the experimental data are to be used directly. A simple constant shift can be employed as an approximation.

For rapidly-varying flows, the results of this constant phase-shift are not accurate. The necessary phase shift should vary with time as the velocity changes (faster velocities affect the downstream conditions quicker). An average phase shift can be determined using cross-correlation. This gives a reasonable approximation to an equivalent steady flow case. In order to make this assumption, accelerations must be minimised. In Figure 3.22 the data are plotted for the unsteady tests where the accelerations are below 0.2ms^{-2} and Fr_2 is a shifted value. Data are also excluded where the depth does not exceed 15mm in an attempt to avoid some of the frictional effects observed in the steady tests of Chapter 2.

Although not strictly a like-for-like comparison, Figure 3.22 is included as an illustration of the applicability of the framework of Qi et al. (2014) and to compare directly with Figure 2.18. Whilst the data do not collapse onto the theoretical line, similar patterns of scatter are seen in the steady tests, particularly for the low h_i tests where data tended to detach from the theoretical curve at much lower Fr_1 than Fr_{1c}. In general the inundation depths in the unsteady tests were not deep and when data below 45mm (around the threshold of frictional effects observed in the steady tests) was excluded there were insufficient points to determine a reasonable trend. Only at the peak of some tests did the water exceed 100mm, and often for brief times. As such, this kind of frictional behaviour is expected, particularly as every wave produces a range of depths for the duration of the inundation. Add to this the uncertainty from the accurate measurement of u, and the phasing issue comparing between the front and back of the structure in an unsteady test, scatter is certainly expected. Fundamentally, we are looking at the instantaneous force on the front face, so this serves as a check that the rear conditions are broadly in line with expectations, and following similar patterns that are observed in Chapter 2, i.e. a critical detachment from the line $Fr_1 = Fr_2$. Whilst far from perfect, this appears to be the case.

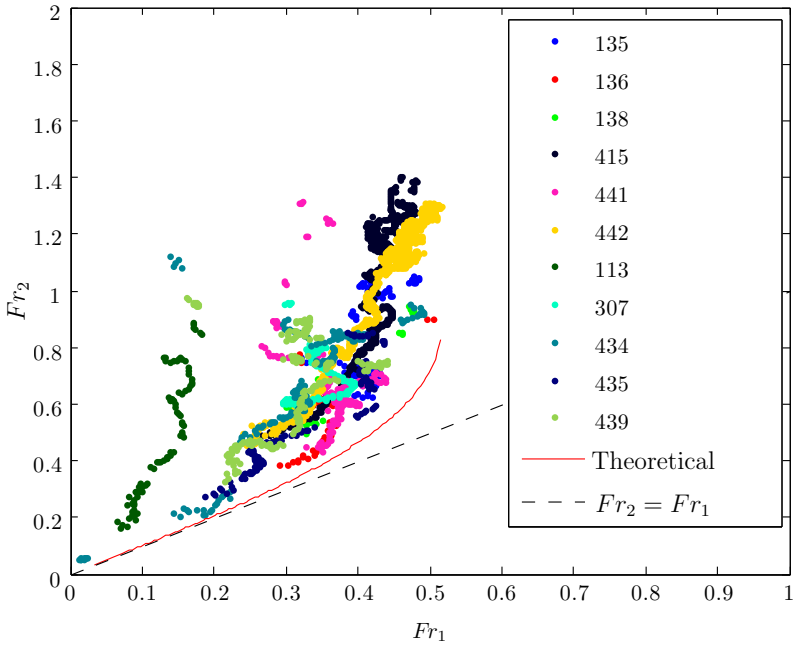

Figure 3.22: *Unsteady upstream and downstream Froude number from the 300mm wide structure ($b/w = 0.25$) and the theoretical curve. Upstream Froude numbers lagged based on cross-correlation between the upstream and downstream velocity profiles. Data with corresponding upstream or downstream acceleration exceeding $0.2ms^{-2}$ or depths below 15mm were excluded. Numbers in legend correspond to the Wave IDs in Table 3.4.*

Satisfied that the model developed in Chapter 2 captures the instantaneous behaviour of the flow, and that unsteady forces would be minimal, it is possible to look at the forces we calculated for the front face, and compare them to predicted forces from our model. Before doing so, it makes sense to check the simpler direct application of (1.31) for estimating forces directly from measured Fr estimates. Having already calculated a relationship between Fr_1 and Fr_2 for the b/w ratio of 0.25 to describe the unsteady tests (shown in Figure 3.22), instantaneous λ can be calculated using (1.32) and $C_D = 2.9$ and $C_H = 0.67$ for each sample of the 13 waves. Following the calculation of λ, the predicted force can be calculated using (1.31).

The force observed in Figure 3.18 is calculated in detail for the front face only, so an estimation of the rear force is necessary. Velocities immediately behind the block are generally small in magnitude, but act in several directions and are turbulent.

There is no net direction to the velocity and the primary component to the force is hydrostatic and small (only a handful of tests on the 150mm building produce a rear water level sufficient to register a pressure on the rear transducer at 36mm from the bed). The net force on the rear face therefore opposes the force acting on the front face so the full-body force will generally slightly lower than that measured by the front pressure transducers. In order to compare the front-face force with the full-body force predicted by the framework, this rear hydrostatic force needs to be calculated and added to the full-body force. An assumption about the rear water surface profile is therefore required.

The unsteady tests are different from the steady tests for all the reasons that have been discussed already, but also because the test specimen is located on a dry beach. The steady tests are wetted throughout the set of experiments whereas the unsteady tests are dry initially, become wet, and then dry again. This means when the wave inundates initially and exerts a force on the front of the structure, there is no fluid behind it to counter. This is important, as the steady framework is predicting full-body forces. The rear water profile therefore takes some time to develop as the inundation progresses, and for shorter period waves, the difference between the water behind the structure for the same flow conditions could vary greatly between the start of the test, and when the flow is fully developed. Generally, the assumption made about the level water surface on the front face is not appropriate for the rear face as the surface begins at zero and fills up gradually to a height below the depth measurements captured at the rear of the side profile. This rear hydrostatic pressure distribution is relatively small in comparison to the front initially, but when the velocities are slow and the period of the wave is longer, this can be a large opposing force to the overall full-body force. Due to observed low rear water depths, the rear water profile was not captured by measurements, so in the centre it is assumed to be an average of half the side depth at the rear of the structure, based on the assumption of a "meniscus" shaped profile.

At very low or zero measured front forces (particulaly when the water has not reached the transducers at 36mm), the implementation of this assumption means that the observed full-body forces can be slightly negative (which is incorrect and an artefact of the assumption), but as the front force increases, it becomes a measurable additional component. By adding this small rear hydrostatic component to the forces predicted by (1.31), a reasonable comparison is made between observed front-face

forces and the prediction of the steady framework. A plot of this for a subset of samples chosen by the same depth and acceleration criteria as in Figure 3.22, is shown in Figure 3.23.

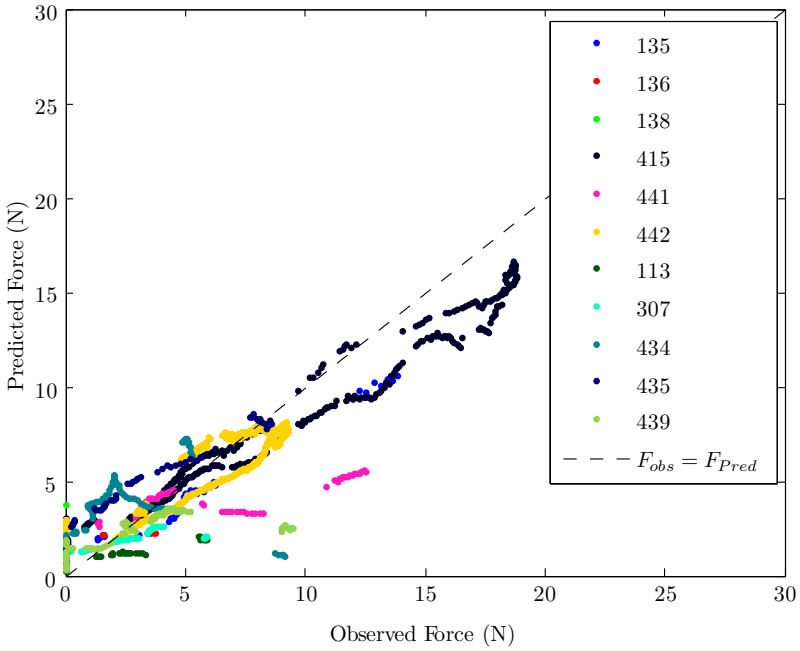

Figure 3.23: *Observed integrated front force versus predicted full-body force + assumed rear hydrostatic force. Numbers in legend correspond to the Wave IDs in Table 3.4.*

The data in Figure 3.23 show a reasonable collapse onto a 45 degree line between observed and predicted. However, it is far from ideal and much of the data is excluded on grounds of poor correlation between measured up and downstream flow conditions, low water levels and high accelerations. Forces can only be determined accurately with the set up once the water level reaches the pressure transducers, the lowest of which are centred at a height of 36mm. This is why there are several points at zero measured force, but with a non-zero predicted force. There also was a time delay between the front and rear of the structure, so there is a rear hydrostatic force calculated under the simplified time-shift assumption employed. The scatter in Figure 3.23 can largely be accounted for by the simplification of the assumptions used to define the rear pressure distribution for these tests. Another source of variance comes from the viscous effects observed in Figure 3.22. At prototype scale,

this frictional behaviour would not be as prominent, and the data would be expected to fall more closely with the red line in Figure 3.22. Additionally, the longer periods of full-scale inundations from tsunamis, means that accelerations would be lower for the majority of the inundation period. For these reasons the force is better approximated by (1.31). Due to the formulation of full-body force with an assumed rear hydrostatic force in order to show this comparison, it is expected that an under-prediction in the front force would be seen while the wave is under deep slow moving conditions. With the addition of a better rear surface profile assumption, the trend would show less of a loop characteristic around the 45 degree line and show more of a collapse on to it.

As can be appreciated, whilst the analysis presented here shows some similarities to the real force behaviour, it is a far from perfect comparison. It is perhaps better to approach the problem more holistically than choosing point velocity measurements from propeller meters (with their uncertainty) and height measurements from image processing, shifting them, and hoping that the force results derived correspond to those measured. In Section 3.6, forces from the unsteady wave tests described here are compared to the output of a numerical model which includes a distributed drag term.

3.6 Application of unsteady one-dimensional model

The simple one-dimensional model described in Chapter 2 appears to capture much of the behaviour seen in the steady experiments. Additionally, similar patterns are seen between the model, and tests carried out by Qi et al. (2014). The key component missing from the current model for applying it to the unsteady situation, is the inclusion of unsteady forces which arise because of flow accelerations. The additional effect of an unsteady flow is the introduction of a new force component that arises from the unsteady pressure field caused by the flow accelerating or decelerating in time. The major problem in estimating the influence of unsteadiness on the force acting on the building arises because the free-surface in front of the building will necessarily rise as the flow velocity increases. However, despite these concerns the model shows promising results when compared to published unsteady experimental data in Section 3.2.

As demonstrated by the low forces estimated in Figure 3.21, there is a strong argument for ignoring these unsteady components where inundations from tsunamis are of concern. This argument is further justified when considering that periods of tsunami waves (and therefore the periods of inundating flows) are so large that the flow is essentially quasi-steady, i.e. the accelerations are small. This is confirmed by the good performance of the model without any unsteady force components included during the comparison with published experimental and numerical studies in Section 3.2.

In order to apply the 1D model to the unsteady experiments described in this chapter, the bathymetry term, or bed-slope, $\frac{\partial z_b}{\partial x}$ must be included. Additionally some mechanism for allowing the shoreline boundary to move both up, and down the beach, as well as across the flat portion hosting the instrumented structures. As a simple implementation the shoreline is tracked via wetted nodes. A node becomes wetted (i.e. simply added to the computational domain with a minimum water level h_{min}) if the free-surface slope between the adjacent two nodes exceeds a threshold. Similarly, the node becomes "dry" if the water height, h drops below h_{min}, or the free-surface slope exceeds a negative threshold. While the author acknowledges the lack of sophistication in this approach, numerical wetting/drying boundaries is not the focus of this thesis, and the simple algorithm described here performs admirably for this purpose. Douglas and Nistor (2015) showed that although differences are seen between a surge over a dry bed and a bore propagating over an initial water depth (50mm), the difference over a very shallow layer (5mm) of standing water became very small. As such when the wave in the one-dimensional model begins to inundate the flat portion of the beach, the values for h are set to $h_{min} = 0.5$mm. A close match with the behaviour of a dry bed is therefore expected.

To allow for more refined results around the block the resolution is increased, so in order to reduce computing times the model is modified to allow for a variable spatial resolution - high resolution on the beach and around the building and lower resolution offshore. For the examples provided in this thesis, the spatial resolution on the beach is set at 4.4mm, and 21mm offshore. Roughness is included by setting $n = 0.0025\text{sm}^{-1/3}$, and the model is driven by a boundary condition using the free-surface at the probe "Offshore 1" to vary the water height here.

At the other end of the flume and downstream of the buildings, the bathymetry

ends abruptly to overfall into a sump, essentially designed to prevent return flow occurring and complicating the experiments, which is unfortunately a troublesome condition to model correctly. For a free overspill like a waterfall which forms a nappe, there is an upstream critical depth, h_c which usually occurs $3h_c$ - $4h_c$ from the end (Chow, 1959). Beyond this point h is reduced to h_e, as some texts describe which is the height at the point of the overspill where $h_e < h_c$. Here the pressure distribution is no longer hydrostatic due to the bottom of the nappe being open and at atmospheric pressure. The upstream surface water profile for steady sub-critical flow approaching a free overfall is known as a backwater curve (Chadwick and Morfett, 1993), in this case an "H2" profile because of the horizontal bed slope and "2" because it is a drawdown curve $h > h_c$ (Chanson, 2004). However, as the flows in the experiments are unsteady and often with supercritical flow in the wake of the building, there are no major backwater effects seen to develop upstream. Various boundary conditions are investigated for capturing the behaviour at the end, including setting a critical depth boundary and the overall effect on flows in and around the building is found to be relatively limited regardless of which is chosen. However, the most representative condition found was to enforce a condition such that $(uh)_{end} = (uh)_{end-1}$ and set the end node in the model to be 20cm from the overfall location. Flow depths at the end of the flume are rarely more than 5cm and if supercritical h either are at or below h_c, so moving the boundary slightly away from the overspill gave good results.

The results for the broad building are firstly presented and the interaction between three elevated waves are discussed within this chapter. The three waves chosen are ID 135 (T $\approx$ 8.7s), 415 (T $\approx$ 52.4s) and 442 (T $\approx$ 98.2s), so a short-period wave (comparable to paddle generated periods), medium- and long-period wave respectively. The simulations complete once the interaction with the building is finished (low water levels) as this is the focus of the study, so the offshore model is curtailed. Results for all these interaction wave experiments discussed in this thesis, along with the results from corresponding 1D descriptions are systematically presented in Appendix D for those interested readers.

Figure 3.24 presents upstream water levels, integrated full-body force (from pressure transducers), up and downstream velocity and the water height at the toe of the bathymetry observed for Wave 135. As this is one of the shorter period waves tested it is expected that the shape of the force time-series is front weighted as

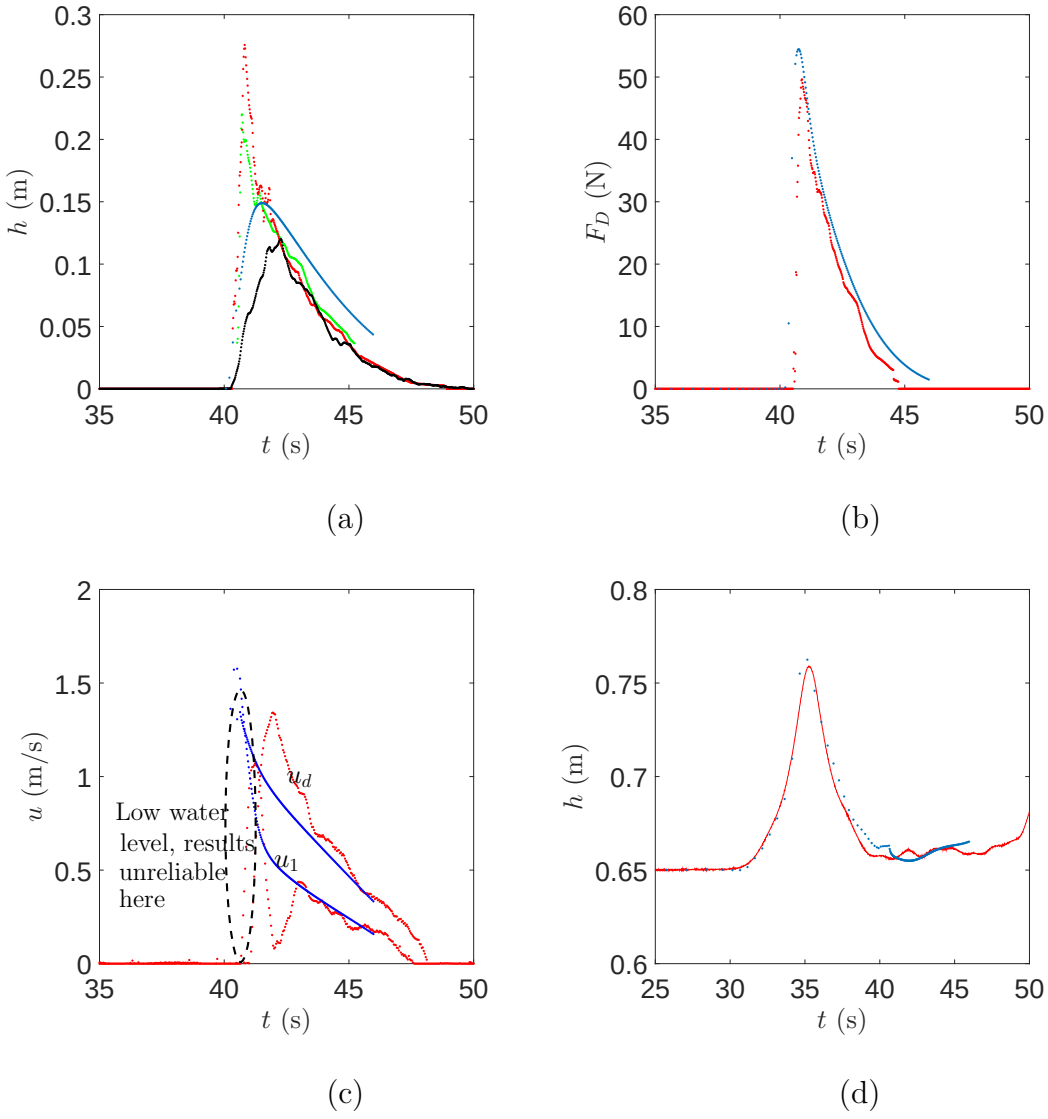

Figure 3.24: *Results from a short-period wave, 135, ($T \approx 8.7s$), (a) Water height at the front face, (b), Full-body force on the building, (c) upstream, u_1 and downstream velocity, u_d, (d) Wave height at toe of bathymetry. ●, 1D numerical, ●, large-scale experimental front height from image processing, ●, height from images 10cm in front of building, ●, front face pressure transducer measurement (36mm off the bed). In (c), the early velocity data (dashed black ellipse) are captured at water depths below 10mm, meaning a reasonable comparison is not possible.*

this interaction is characterised by a leading surge front. Acquiring the free-surface interface for these short period interactions is difficult in the first few seconds due to significant splashing. However, although this splashing is dramatic and catches attention, other than the high frequency impact force associated with the front hitting the face of the building, the overall effect on the force is minimal.

In Figure 3.24 it can be seen that the measured hydrodynamic effects (velocities and water heights) are not reflected perfectly by the results of the 1D model. However, it is worth remembering what the SWE results represent. The SWE model provides a depth-averaged view of the velocity, and furthermore, due to the 1D simplification, it averages velocities and water depths across the flume. In most cases this is perfectly reasonable but as such, a comparison between the measured velocities ($\sim 10-15$mm above the bathymetry) and a depth- (and width-) averaged flow velocity is not expected to be perfect match. Additionally as reported in Section 3.3.6 there are serious issues measuring the flow velocity in thin layers which transition between dry and wet, then back to dry again. The ingress of material which can foul the propeller meters is also common in this environment where material may have been floating on the surface of the water or on the dry bed before being picked up by an incoming wave. Despite these challenges, while the flow is of a reasonable depth and after the initial peak, the depth-averaged velocities from the model eventually settle down and match the observed values well.

In terms of the modelled water height, the initial splash is not captured by the 1D model, which is to be expected because it does not contain the necessary physics to do so. The modelled water height is lower than the measured splash/actual water height initially and later over-predicts the position of the free-surface.

However, despite this and somewhat surprisingly the full-body force derived from an element-wise summation of an interpolation of the pressure transducers and the free-surface at the front and rear of the structure appears to match the distributed drag term, i.e. the momentum removed from the flow by the model. This particular model uses f_D parameterised as (2.16), so that $F_{\mathrm{D}} = \rho(1-\phi)wf_Dh_1L$. The free-surface at the toe is captured reasonably well by the model. Every 100 data points is plotted here to reduce file size, and also to show when the model required a smaller time-step. Offshore the lower resolution does not require small time-steps, but as the wave climbs the beach and inundates the building a combination of higher resolution

and higher flow velocities causes the required time-steps to become smaller for the whole domain.

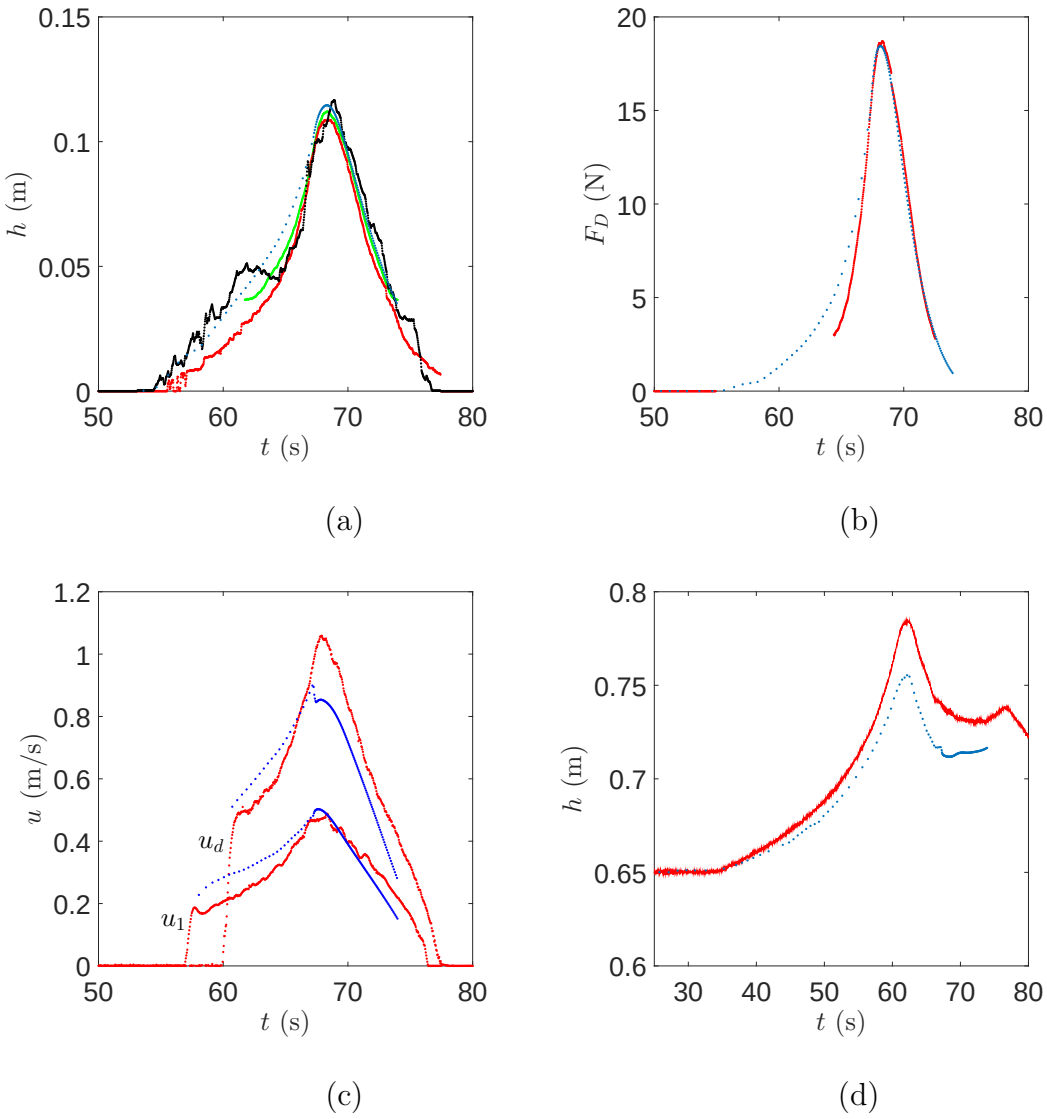

Figure 3.25: *Results from a medium-period wave, 415, ($T \approx 52.4s$), (a) Water height at the front face, (b), Full-body force on the building, (c) upstream, u_1 and downstream velocity, u_d, (d) Wave height at toe of bathymetry.* •, *1D numerical,* •, *large-scale experimental front height from image processing,* •, *height from images 10cm in front of building,* •, *front face pressure transducer measurement (36mm off the bed).*

In Figure 3.25 the corresponding results for a much longer period wave ($\sim$ 52s) are presented, and the difference is immediately clear when looking at (a) the water height and (c) the upstream and downstream velocity. Here a much closer match

can be seen between the water height as measured by image processing the side images (red line), as well as a manual estimate of the water level 10cm in front (black line). For interest, the equivalent water height as measured by the lower (36mm off the bed) middle pressure transducer is plotted (green line), which shows that the majority of the pressure can be explained by a hydrostatic description. Due to the probe location depths below this cannot be measured. The velocities u_1 and u_d from the propeller meters are given in red and the model results (where $h > 15mm$) are plotted in blue. The reason for not plotting the u for lower h is that the propeller meters are unable to capture velocities at heights lower than this. Both upstream and downstream depth-averaged velocities match the observations with a slight overestimation on the rising limb and underestimation on the falling limb. u_d is under-predicted at the peak.

In terms of the force in Figure 3.25 (b), once again a good match is observed between the model and the estimated full-body force. The initial rising limb appears to overestimate the force, but for much of the early part of the test the trace for the measured force is missing. This is because the flow depths are lower than the pressure transducer locations, so the pressure distribution used to derive the force cannot be reliably estimated under these flow conditions. In (d) the water height at the toe is not as well captured for this test, despite other parameters matching well (see Appendix D for more data from wave 415). The overall shape of the wave trace is a close match with the observations but the water levels are seen to be higher than the model predicts. There could be an issue with the performance of the wave probe on this particular test or there could also have been an error in the still water level measurement. Figure D.12 shows that the near-shore velocities matched observations well, other than a period between 45 and 55 seconds when propeller meter 2 appears to clog, and later becomes free again (Figure D.12 (b)).

Finally, selected results from a long-period wave ($\sim$ 98s) are presented in Figure 3.26. At prototype scale, based on the experiments being between 1:50 and 1:100 length scales, this period would correspond to between 690s (11min 30s) and 980s (16min 20s), which is certainly of the order expected for tsunamis. A close match can be seen between the water depths and velocities and a very good agreement is achieved with the force profile for the portion of the time-series where water covers the transducers. A slight over-prediction of the force is seen at the peak, but it is certainly within a few percent of the measured value. Water levels offshore match

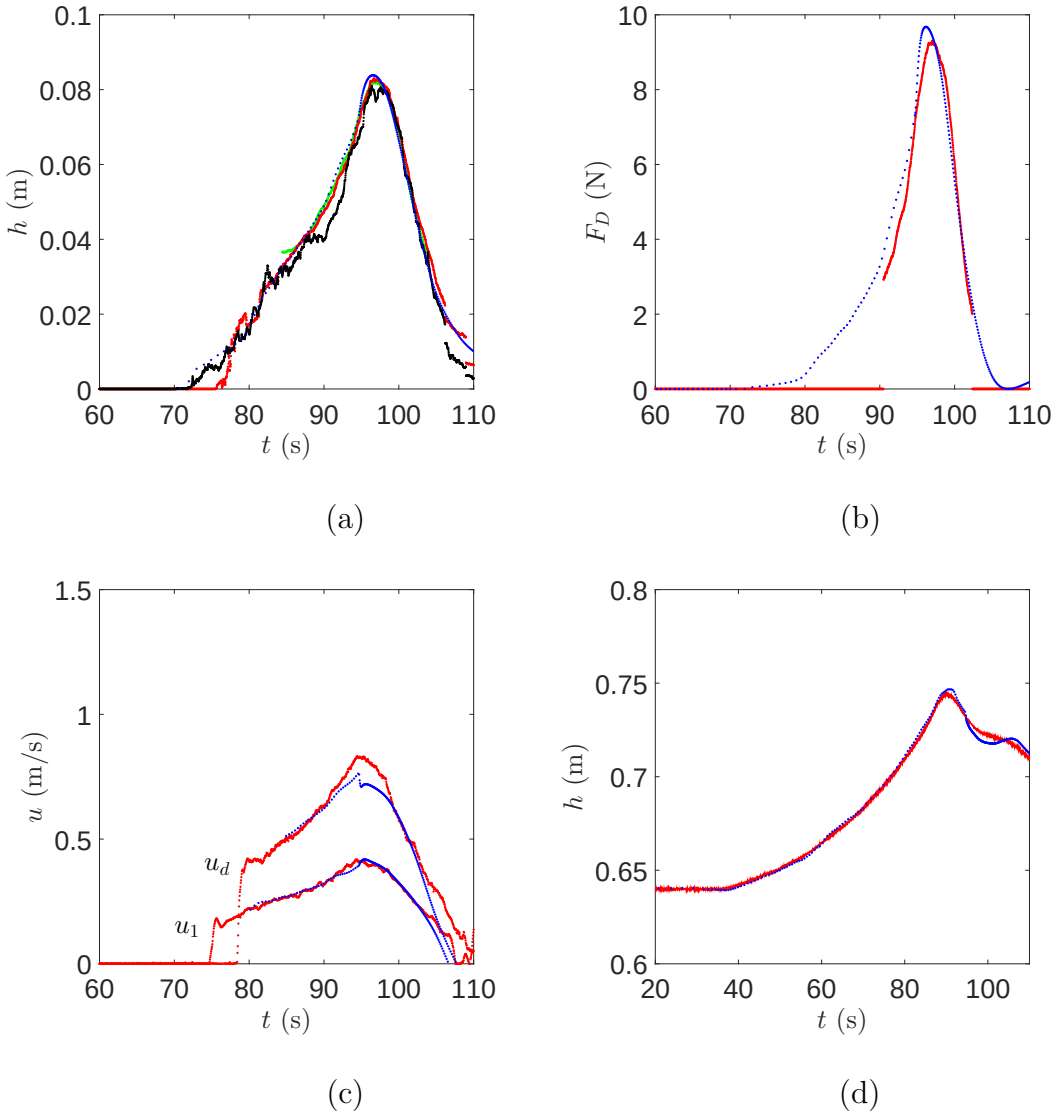

Figure 3.26: *Results from a long-period wave, 442, ($T \approx 98.2s$), (a) Water height at the front face, (b), Full-body force on the building, (c) upstream, u_1 and downstream velocity, u_d, (d) Water height at toe of bathymetry. ●, 1D numerical, ●, large-scale experimental. In (a) ●, front height from image processing, ●, height from images 10cm in front of building, ●, front face pressure transducer measurement (36mm off the bed).*

closely with the observed and near-shore velocities in Figure D.13 again match very well, with the exception of probe 2 in (b), which was clogged for the duration of the test.

The period of the wave fundamentally alters the shape of the loading profile observed. With shorter period waves the front of the force-time curve is steeper, and the duration of inundation is shorter. As the period of the wave increases, the time of the peak moves closer to the centre of the force-time profile, which becomes more symmetrical. With increasing period, flow conditions onshore are steadier and there is a closer match between observed velocities, water heights and forces to those depth-averaged values predicted by the 1D model, indicating that the shallow water approximation remains reasonable for inundation.

To test the more complete force closure provided by Qi et al. (2014), the version of the model which uses (2.39) to parameterise the distributed drag was run. For the same wave IDs as discussed here, the equivalent results are discussed. As the steady closure provided by (2.39) requires the downstream flow conditions characterised by Fr_d, there is an issue with unsteady flows because the rear flow conditions are lagged behind the front flow conditions by approximately $2L/(u_1 + u_d)$ based on the average velocity between the front and rear. This lag clearly changes as the wave passes, which gives further issues as found in Section 3.5. As such the downstream conditions are estimated from the upstream conditions, Fr_1, and b/w using (1.29). For this model, (1.29) is solved for Fr_d for a range of Fr_1 and $b/w = 0.25$ prior to running the model, so that Fr_d can simply be interpolated on the fly based on a given Fr_1. This interpolation adds some computational expense to the procedure (up to 50% increase in run-times), but with the run-times for a long-period wave interaction around six minutes on a very modest laptop, this is not a major overhead. Alternatively, the actual Fr_d can be used from the model ignoring the unsteady time lag issue, but this results in discontinuities in the estimated force as the wave front passes the building. For longer period waves the forces predicted in this way are reasonable, but model which interpolates the pre-solved Fr_1, Fr_d relationship is presented instead.

Figure 3.27 shows a comparison between predicted forces using the simple drag closure of (2.16) and the results using (2.39). Both formulations appear to predict the force to a reasonable accuracy which is encouraging.

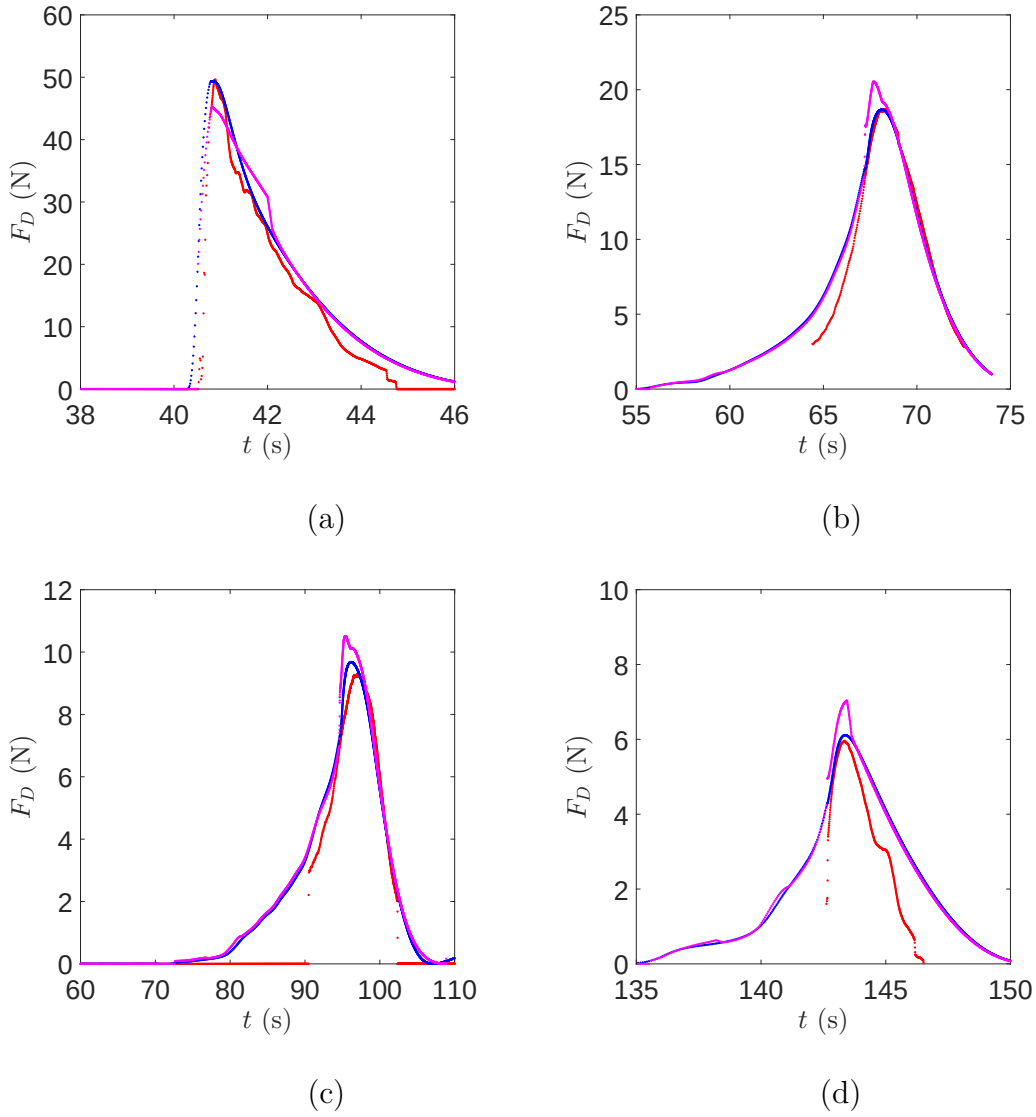

Figure 3.27: *Comparison between forces from a simple drag closure and Qi et al. (2014). (a) Wave 135 (b), Wave 415, (c) Wave 442, (d) Wave 307 (Mercator).* • *1D numerical* $f_d = (2.18)$, • *1D numerical* $f_d = (2.39)$, • *large-scale experimental integrated force from measured pressure and water levels.*

When plotted as measured versus predicted force the pattern is very clear. This is presented in Figure 3.28 (a) and (b) for the 1D model with f_D as (2.16). The trend is visibly stronger than seen in Figure 3.23 and appears to be equally valid for elevated and N-wave profile shapes. Additionally the version of the model which uses a distributed drag based on the work of Qi et al. (2014) (2.39) gives similar results as seen in Figure 3.28 (c) and (d). In fact for the examples seen in these tests the simple drag model seems to predict the measured forces more accurately.

Another parameter which is varied in the unsteady tests is the blockage ratio. The building with dimensions 150 x 250 x 310mm is subjected to the same waves as the larger structure. Broadly speaking the results are as may be expected, the lower $b/w = 0.125$ produces different results to the building with $b/w = 0.25$, and lower forces as expected. The flow conditions are also different in the case of the $b/w = 0.125$ with velocities at the side lower than the $b/w = 0.25$ experiments.

From the comparisons in Figure 3.29 it is clear that the model captures the behaviour of blocking well for $b/w = 0.125$ and there is therefore potential for the model to be extended to other b/w.

Experiments are also carried out with the $b/w = 0.125$ at different distances D1, D2, D3. However, the forces which are measured on the buildings are generally all within a few percent (i.e. within the tolerance of repeated waves) and sometimes the structure located further away recorded the highest forces. As such it appears that the distance from the shore at least in these tests is not a major factor. This in fact makes intuitive sense when it is considered that the distances between the test structure positions is only 700mm (35-70m prototype distance). Additionally, the only form of resistance acting on the flow is bed friction, as the bathymetry at this point is perfectly flat. Over a distance of 1.4m which covers the the range of the building positions it is unlikely that friction from the smooth finished concrete of the flume would created major differences in applied force. Potentially the major factor is the varnished marine ply panels which the structures attach to recessed and fixed flush to the flume floor directly in front of the structures providing very low friction. This appears to be the case and the profiles at D2 and D3 are therefore omitted from this thesis. Over larger distances, there is potential for the force to be reduced, but it is more likely that bathymetry effects have a more important role. It is however an interesting result that the forces at least in this nearshore regions

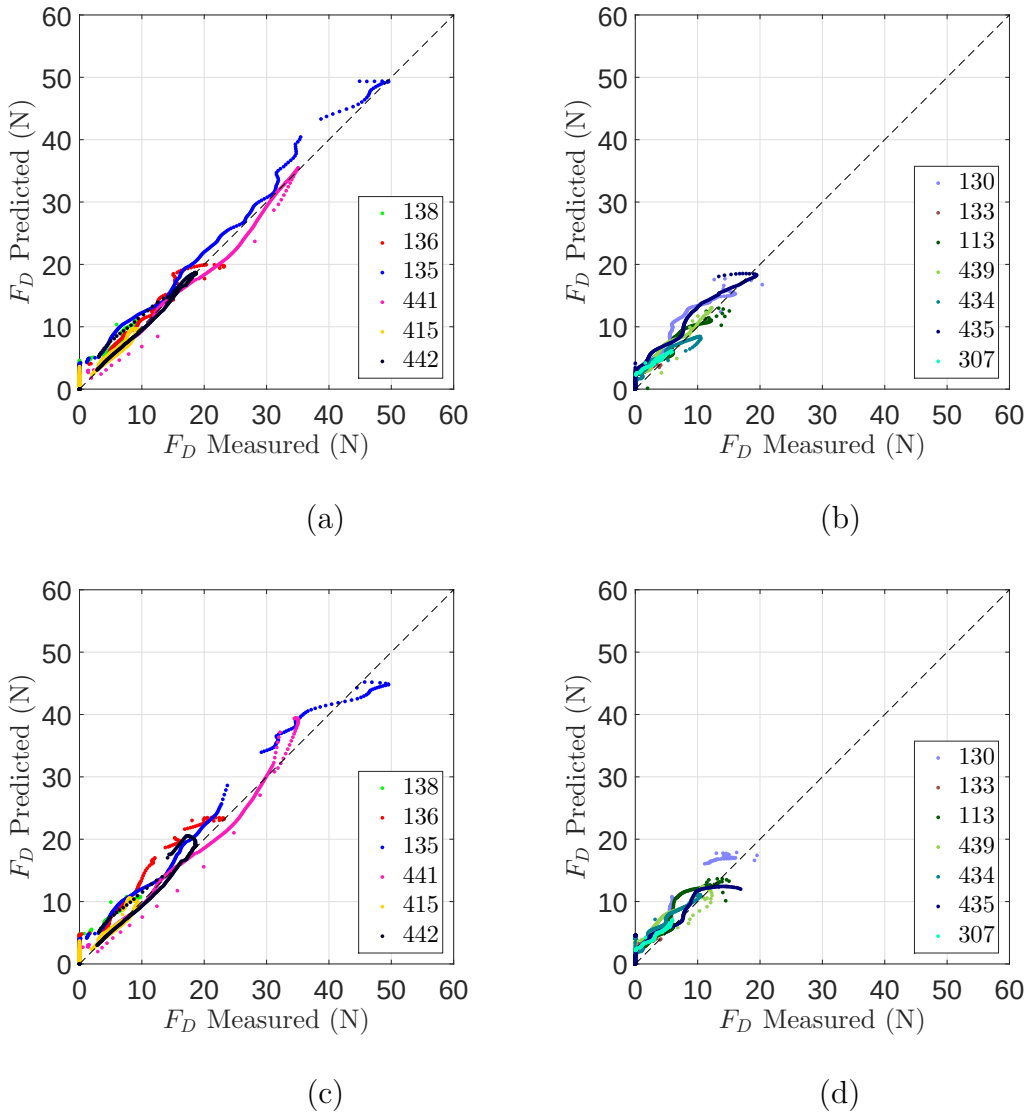

Figure 3.28: *Force predictions. (a) Elevated waves with f_D as* (2.16)*, (b) N-waves with f_D as* (2.16)*, (c) Elevated waves with f_D as* (2.39)*, (d) N-waves with f_D as* (2.39)*. Wave IDs are given in legends.*

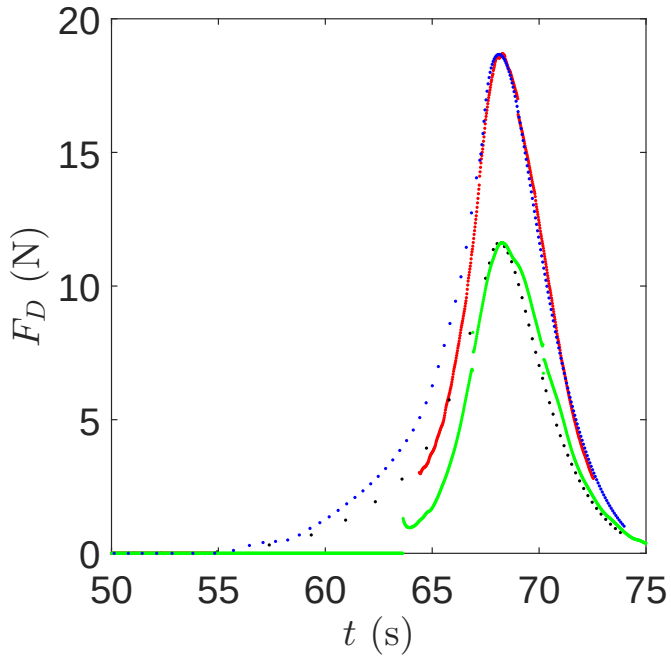

Figure 3.29: *Force measurements for Wave 415 of different b/w at position D1.* • $b/w = 0.25$ *experimental,* • $b/w = 0.25$ *numerical,* • $b/w = 0.125$ *experimental,* • $b/w = 0.125$ *numerical.*

seem to be independent of distance to coast, despite the possible causes.

As a final comparison, some of the most common equations given in the design guidelines presented in Appendix A are compared to the numerical model. The velocity and height output from a bare-earth version of the numerical model are used to estimate forces on a 300mm test structure using the recommendations of FEMA (2012). The hydrodynamic force and hydrostatic force are plotted against the measured force, and the result from the 1D model, including the presence of the building.

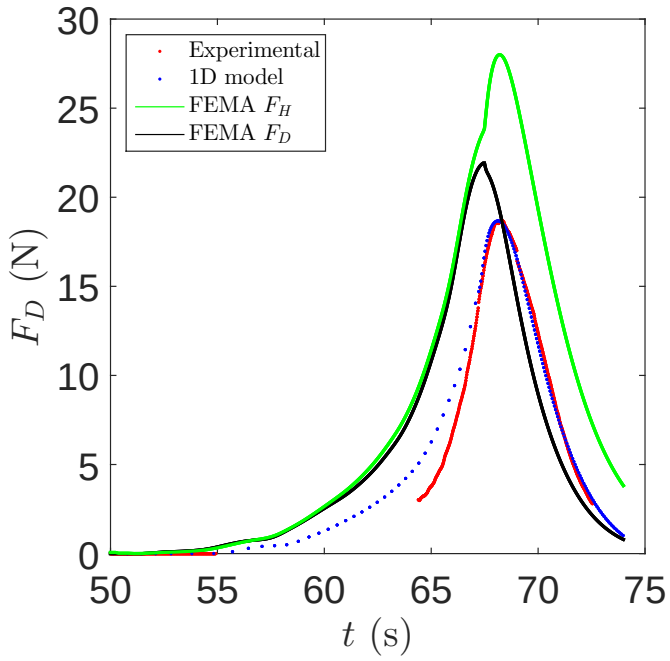

Figure 3.30: *Force comparison with FEMA (2012). Wave 415 force as measured, calculated from a 1D model with distributed drag and blocking, as estimated from a bare-earth model using FEMA (2012) hydrodynamic and hydrostatic force recommendations (F_H as* (1.21) *and F_D as* (1.22)*).*

As is expected, the 1D model predicts the force very well, because the building's influence on the flow conditions is accounted for. The hydrodynamic force in FEMA (2012) and many other guidelines is essentially the same as (1.22). It is calculated here based on the outcome of a bare-earth numerical model and actually performs fairly well. The peak force is 16% higher than the measured force and the 1D model, which is not necessarily a bad thing for a design equation. However, because of the

use of a bare-earth model, there is a problem with the timing of the force profile where it is shifted forwards in time due to the lack of flow resistance in the model. This means the force is vastly over-predicted initially, and towards the end of the inundation it under-predicts the force. From a practical design perspective this is unlikely to be an important point, but it is worth noting from the perspective of load duration.

The other design profile shown is the hydrostatic force. Clearly in the bare-earth model, h_2 is essentially the same as h_1, which would produce a zero resultant force from the opposite force on the rear of the structure. However it is important if the inside of the building remains dry, as the loads on the walls can become very high. An interesting point is that the hydrostatic profile appears to envelope both the observed forces, as well as the hydrodynamic estimate.

3.7 Conclusions

A set of tests have been conducted examining the unsteady interaction between waves and a sloping beach, with and without instrumented buildings. Water heights offshore, velocities near-shore and onshore are recorded, as well as the water surface profile and velocities around the buildings, and pressure measurements on the face of the building. The pressure distribution for all wave interactions is found to be close to hydrostatic (triangular in shape) for much of the interaction duration, with an additional hydrodynamic component present during spells of high velocity, as expected.

Using the pressure measurements from six transducers, as well as the free-surface height profile around the structure measured from high speed imagery, a surface pressure distribution is interpolated at every time interval (50Hz). Justification for doing this comes from the consistent measurements between pressure probes width-wise across the front face (indicating very little horizontal variation), the close to hydrostatic behaviour vertically, and the availability of a high resolution free-surface measurement (where $p = p_{atm}$ at the free-surface). All of available pressure measures are used where possible and this discrete estimate of the pressure distribution is numerically integrated in order to provide an estimate of the force on each face.

The full-body force is estimated, assuming a hydrostatic distribution on the rear with a drop to close to zero at the centre of the rear face. This is confirmed by the rear pressure transducer in the 150mm building, and from visual observations while testing.

In Section 3.5 the framework of Qi et al. (2014) is compared using the measured upstream flow parameter Fr_1 and downstream Fr_2 to predict a full-body force, and broadly speaking a reasonable agreement is found with the integrated measured pressure distribution if the steady portions of the waves are isolated. However significant variation is present in the measured upstream-downstream flow relationships due in part to the unsteady nature of the tests, as well as significant uncertainty in the measured quantities, particularly u_1 and u_2 used to calculate Fr.

Finally, the waves are modelled in 1D by modifying the steady model from Chapter 2 to include non-flat bathymetry and a moving shoreline. Two methods of including an additional resistance are investigated and both appear to produce reasonable results. The simple hydrodynamic drag in the cases found in these experiments appears to perform as well as, potentially better than, the more complex framework of Qi et al. (2014). As such there is potential for further work to investigate using this method for inexpensively estimating the forces on buildings within widely used existing numerical codes. There is clearly the potential that this approach would be appropriate for application to shallow water equation models in 2D.

Chapter 4

Conclusions and Recommendations

4.1 Conclusions

The aims of this thesis were to provide better insight into the interaction between tsunami-like inundation flows and buildings, to develop an experimentally validated approach for evaluating the forces imparted by these flows on buildings and to provide a new set of published inundation tests for long-period unsteady waves at large-scale for other researchers to adopt in numerical model validation.

In the literature review it is shown that current published guidance on tsunami load determination focuses upon large numbers of short-period wave experiments, often at scales too small to be reliably compared to actual tsunami waves. In addition numerical models commonly used for modelling tsunamis generally have no means of determining forces on structures in the flow, and attempts to parameterise forces using output from bare-earth models can lead to inaccuracies. Design guidelines generally seem reasonable at recommending conservative estimates of the full-body force, but do not explicitly account for flow blocking, meaning there are potential situations where they could be underestimating the hydrodynamic forces in built-up areas. They are also often reliant upon bare-earth flow models to provide flow estimates in order to parameterise the force, which may be incorrect in terms of

magnitude and timing.

The flow past a block is experimentally examined using a highly controllable, small-scale steady flow set-up. The flow conditions for the case of $b/w = 0.25$ are parameterised, with the results compared to a previous study using different b/w. A simple 1D numerical model is devised and parameterised using the steady experiments. A distributed drag term of $f_D = \frac{C_D}{2L}\frac{\phi}{(1-\phi)}|u_1|u_1$ is included in the model with the drag force smeared over the region of the flow blockage. The model represents the flow conditions and crucially, the force on the blockage well. In itself the model is novel because it includes both flow blocking and a distributed drag term to remove momentum from the flow, which correlates to the total force on the structure. The steady model is extended to the unsteady case; firstly by comparing the model output to published studies of dam-break experiments in order to test the assumption that unsteady forces are a small component of the overall force, and secondly to a new set of unsteady long-period wave experiments, conducted at large-scale. The model performance is excellent in both cases. A separate version of the model with the drag instead parameterised as $f_D = \frac{\phi}{(1-\phi)}\frac{\lambda g^{1/3} u_1^{4/3} h^{1/3}}{L}$ produces similar results in terms of predicted force and flow conditions. The model performs better in terms of force prediction than current guidance based on bare-earth flow models which are agnostic to the building presence.

An important set of long-period wave experiments on a sloping beach interacting with instrumented buildings is detailed in this thesis. The research described has successfully characterised the forces due to long-period wave interactions with a fixed structure. The results are also used to validate a numerical model. The large-scale long-period wave experiments presented here are unique. To the author's knowledge the longest period waves that have been previously recreated in a laboratory and used to test structures are below 10 seconds with a few examples pushing 20 - 25 seconds using paddle generators at the limit of their stroke capabilities. These are well below the ∼30s period required to model tsunami like waves at scales of ∼1:100. As confirmed by the experiments in this thesis, the inundation tests in this lower range of wave periods are peaky, with highly unsteady initial flow conditions, splashing and other complexities to the flow pattern which mean that shallow water approximations cannot capture the flow behaviour well. However, after the initial impact has passed, the inundation and interaction can be reasonably well described by shallow water equations, but these short-period waves are still not comparable

to tsunamis. These new tests examine waves with periods of up to 114s (between 13 and 19 minutes prototype period depending on the scale factor chosen). Due to these longer periods, measured unsteady behaviour is minimal, and the flow is dominated by quasi-steady processes at all times. Loads from the inundating flows as such are quasi-static in nature and highly dependent on the deformation of the free surface around the building.

These experiments provide new insights into the loading pattern of inundating long-period waves, and clearly demonstrate that there are considerable differences when compared to short-period waves. The implication of this is that some of the guidelines which have been developed based solely on short-period wave experiments have the potential to be inappropriate. There is a possibility that design guidelines based on short-period waves could over predict forces at certain points in the inundation, but under predict at others. These experiments also provide a first published dataset of inundating long-period waves and interactions with instrumented buildings, which are of a comparable period to tsunamis ($T > 5$s) when scaled-up to prototype. As such the experiments are of value for validation of numerical modelling codes which are in use today. Numerical codes, which have until now only been validated against short-period wave experiments, sparse run-up data, and even sparser velocity data from recent tsunami events, may now be tested against a more complete dataset containing onshore velocities, water depths and integrated pressures on buildings.

4.2 Recommendations

It is firstly recommended that the effect of blocking from adjacent structures be accounted for in design codes. This can be achieved either by provision of recommended drag coefficients which vary with building b/w or through suitable factors of safety. Additionally design codes based on the outcome of short-period experimental studies should be reviewed. It is also recommended that future benchmark validation tests for numerical tsunami models are based on large-scale experimental long-period wave inundations.

Efforts to extend the 1D numerical model presented in this thesis to a 2D description are already ongoing within the EPICentre research group at UCL. Work is also under

way using outcomes of the quasi-steady framework of Qi et al. (2014) to derive analytical fragility functions. Early indications in Macabuag et al. (2016) show that the estimated force using the Qi et al. (2014) description provides a better correlation with damage than the more widely used u and h from a bare-earth hydrodynamic model. However, the flow parameters used by that study are still agnostic to the building presence. As such there is a clear avenue to explore by including the drag estimation within the flow model itself to produce more reliable estimates of force and the flow conditions.

As a result of this work, integration of a distributed drag term with blocking within existing models is being considered by sections of the insurance industry relating to catastrophe model development. Suitable models where the work of this thesis is of relevance include tsunami, storm surge or potentially inland flood models. It is of interest to catastrophe model developers who require an "intensity measure" which correlates well to building damage and does not significantly increase run-times of models, which typically number many thousands of unique simulations.

References

Aburaya, T., Imamura, F., 2002. The proposal of a tsunami run-up simulation using combined equivalent roughness. Annual Journal of Coastal Engineering [in Japanese] 49, 276–280.

Adriano, B., Mas, E., Koshimura, S., Fujii, Y., Yauri, S., Jimenez, C., Yanagisawa, H., 2013. Tsunami inundation mapping in Lima, for two tsunami source scenarios. Journal of Disaster Research 8 (2), 275.

AIR, 2013. Introducing the Indistry's First Fully Probabilistic Tsunami Model. AIR Worldwide, AIR Current, `http://www.air-worldwide.com/Print-Preview/23259/`.

Al-Faesly, T., Palermo, D., Nistor, I., Cornett, A., 2012. Experimental modeling of extreme hydrodynamic forces on structural models. International Journal of Protective Structures 3 (4), 477–506.

Alderson, J. S., Allsop, N., 2007. Comparison of observed pressure integrated and directly measured global force measurements on caisson breakwater models. In: Proc. 5th Int. Conf. Coastal Structures. pp. 249–258.

Arikawa, T., 2009. Structural Behavior Under Impulsive Tsunami Loading. Journal of Disaster Research 4 (6), 377–381.

Árnason, H., 2005. Interactions between an Incident Bore and a Free-Standing Coastal Structure. Ph.D. thesis, University of Washington.

Árnason, H., Petroff, C., Yeh, H. H., 2009. Tsunami Bore Impingement onto a Vertical Column. Journal of Disaster Research 4 (6), 391–403.

Arsen'ev, S. A., A, Z. O., Seliverstov, S. V., Sheikovnikov, N. K., 1998. Force Action of Tsunamis on Different Structures. Atomic Energy 85 (1), 69–72.

Asakura, R., Iwase, K., Ikeya, T., Takao, M., Kaneto, T., Fujii, N., Ohmori, M., Nov. 2002. The tsunami wave force acting on land structures. In: Proceedings of Coastal Engineering 2002. pp. 1191–1202.

ASCE, 2016. Minimum Design Loads for Buildings and Other Structures, asce/sei 7-16 Edition. American Society of Civil Engineers, Reston, VA.

Bagnold, R. A., 1939. Interim report on wave pressure research. Journal of the institution of Civil Engineers 12, 201–226.

Bahmanpour, A., Eames, I., Richardson, S., Rossetto, T., 2015. Computational study of the force and surface pressure on rectangular buildings in a steady free channel. Unpublished, in preparation.

Bassi, F., Rebay, S., 1997. A high-order accurate discontinuous finite element method for the numerical solution of the compressible navier–stokes equations. Journal of Computational Physics 131 (2), 267–279.

Batchelor, G., 1967. An Introduction to Fluid Dynamics. Cambridge University Press.

Bates, P. D., Horritt, M. S., Fewtrell, T. J., 2010. A simple inertial formulation of the shallow water equations for efficient two-dimensional flood inundation modelling. Journal of Hydrology 387 (1), 33–45.

Bazin, P. H., 2008. Tfe report: Development of hr wallingford's new tsunami generator. Internal Report, HR Wallingford.

Beer, A., 1852. Bestimmung der absorption des rothen lichts in farbigen flüssigkeiten. Ann. Phys. Chem 86 (2), 78–90.

Belcher, S., Jerram, N., Hunt, J., 2003. Adjustment of a turbulent boundary layer to a canopy of roughness elements. Journal of Fluid Mechanics 488, 369–398.

Benjamin, T. B., 1956. On the flow in channels when rigid obstacles are placed in the stream. Journal of Fluid Mechanics 1 (02), 227–248.

Bernard, E. N., Mofjeld, H. O., Titov, V. V., Synolakis, C. E., González, F. I., Aug. 2006. Tsunami: scientific frontiers, mitigation, forecasting and policy implications. Philosophical Transactions. Series A, Mathematical, Physical, and Engineering Sciences 364 (1845), 1989–2007.

Berry, W. D., Feldman, S., 1985. Multiple regression in practice. No. 50 in Quantitative Applications in the Social Sciences. Sage.

Borthwick, A., Ford, M., Weston, B., Taylor, P., Stansby, P., 2006. Solitary wave transformation, breaking and run-up at a beach. Proceedings of the Institution of Civil Engineers-Maritime Engineering 159 (3), 97–105.

Boussinesq, J. V., 1871. Théorie de l'intumescence liquide appelée onde solitaire ou de translation se propageant dans un canal rectangulaire. C. R. Acad. Sci. Paris 72, 755–759.

Boussinesq, J. V., 1872. Théorie des ondes et des remous qui se propagent le long d'un canal rectangulaire horizontal, en communiquant au liquide contenu dans ce canal des vitesses sensiblement pareilles de la surface au fond. Journal de Mathématique Pures et Appliquées, Deuxième Série 17, 55–108.

Bredmose, H., Bullock, G., Hogg, A., 2015. Violent breaking wave impacts. Part 3. Effects of scale and aeration. Journal of Fluid Mechanics 765, 82–113.

Bruwier, M., Archambeau, P., Erpicum, S., Pirotton, M., Dewals, B., 2015. A shallow-water model with depth-dependent porosity for urban flood modeling. In: E-proceedings of the 36th IAHR World Congress. pp. 1–10.

Buckingham, E., 1915. Model experiments and the forms of empirical equations. Transactions of the American Society of Mechanical Engineers 37, 263–296.

Bukreev, V. I., May 1999. Correlation between theoretical and experimental solitary waves. Journal of Applied Mechanics and Technical Physics 40 (3), 399–406.

Bullock, G., Crawford, A., Hewson, P., Walkden, M., Bird, P., 2001. The influence of air and scale on wave impact pressures. Coastal Engineering 42 (4), 291–312.

Camfield, F. E., 1980. Tsunami Engineering. Special Report No. 6. US Army Coastal Engineering Research Center, Fort Belvoir, Virgina.

Camfield, F. E., 1991. Wave Forces on Wall. journal of Waterway, Port, Coastal and Ocean Engineering 117 (1), 76–79.

Camfield, F. E., Street, R. L., 1969. Shoaling of solitary waves on small slopes. Journal of the Waterways and Harbors Division 1, 1–22.

Canny, J., Jul. 1986. A computational approach to edge detection. IEEE transactions on pattern analysis and machine intelligence 8 (6), 679–98.

CCH, 2000. City and County of Honolulu Building Code (CCH). Tech. Standard. Chapter 16, Article 11: Regulations Within Flood Hazard Districts and Developments Adjacent to Drainage Facilities, Department of Planning and Permitting of Honolulu, Hawaii, Honolulu, HI.

Chadwick, A., Morfett, J., 1993. Hydraulics in civil and environmental engineering. E & FN Spon.

Chanson, H., 2004. Hydraulics of open channel flow. Butterworth-Heinemann.

Charvet, I., 2012. Experimental modelling of long elevated and depressed waves using a new pneumatic wave generator. Ph.D. thesis, University College London, UK.

Charvet, I., Eames, I., Rossetto, T., 2013. New tsunami runup relationships based on long wave experiments. Ocean Modelling 69, 79–92.

Chen, A. S., Evans, B., Djordjević, S., Savić, D. A., 2012a. A coarse-grid approach to representing building blockage effects in 2d urban flood modelling. Journal of Hydrology 426427, 1 – 16.

Chen, A. S., Evans, B., Djordjević, S., Savić, D. A., 2012b. Multi-layered coarse grid modelling in 2d urban flood simulations. Journal of Hydrology 470, 1–11.

Chen, Q., Kirby, J. T., Dalrymple, R. A., Kennedy, A. B., Chawla, A., 2000. Boussinesq Modeling of Wave Transformation, Breaking, and Runup. II: 2D. Journal of Waterway, Port, Coastal, and Ocean Engineering 126 (1), 48.

Chian, S. C., Fraser, S., Goda, K., Macabuag, J., Offord, M., Pomonis, A., Raby, A., Saito, K., Salmonds, P., 2011. The Mw9.0 Tōhoku Earthquake and Tsunami of 11th March 2011. A field report by EEFIT, Institution of Structural Engineers, Earthquake Engineering Field Investigation Team, London.

Chock, G., Robertson, I. N., Riggs, H. R., 2011. Tsunami structural design provisions for a new update of building codes and performance-based engineering. Proceedings, Solutions to Coastal Disasters 2011.

Chow, V. T., 1959. Open-channel hydraulics. McGraw-Hill, New York.

Coceal, O., Belcher, S., 2005. Mean winds through an inhomogeneous urban canopy. Boundary-Layer Meteorology 115 (1), 47–68.

Constantin, A., Sep. 2009. On the relevance of soliton theory to tsunami modelling. Wave Motion 46 (6), 420–426.

Courant, R., Friedrichs, K., Lewy, H., 1967. On the partial difference equations of mathematical physics. IBM journal 11 (2), 215–234.

CRATER, 2006. Reduce Tsunami Risk - strategies for urban planning and guidelines for construction design. CRATER, Coastal Risk Analysis of Tsunamis and Environmental Remediation - The Italian Ministry for the Environment, Land and Sea & the Asian Disaster Preparedness Centre, Bangkok.

Cross, R. H., 1967. Tsunami surge forces. Journal of the Waterways and Harbors Division 93 (4), 201–231.

Cumberbatch, E., 1960. The impact of a water wedge on a wall. Journal of Fluid Mechanics 7 (03), 353–374.

Cuomo, G., Allsop, W., Takahashi, S., 2010. Scaling wave impact pressures on vertical walls. Coastal Engineering 57 (6), 604–609.

Davis, R., Moore, E., Purtell, L., 1984. A numerical-experimental study of confined flow around rectangular cylinders. Physics of Fluids (1958-1988) 27 (1), 46–59.

Deltares, 2014. Delft3D-FLOW, Simulation of multi-dimensional hydrodynamic flows and transport phenomena, including sediments User Manual. Delft, the Netherlands.

Douglas, J., Gasiorek, J., Swaffield, J., 1995. Fluid Mechanics. Longman Scientific & Technical.

Douglas, S., Nistor, I., 2015. On the effect of bed condition on the development of tsunami-induced loading on structures using openfoam. Natural Hazards 76 (2), 1335–1356.

Drew, D. A., Passman, S. L., 2006. Theory of multicomponent fluids. Vol. 135 of Applied Mathematical Sciences. Springer Science & Business Media.

Duda, R. O., Hart, P. E., Jan. 1972. Use of the Hough transformation to detect lines and curves in pictures. Communications of the ACM 15 (1), 11–15.

FEMA, 2000. Coastal Construction Manual. third edition FEMA 55, Federal Emergency Management Agency, Washington D.C.

FEMA, 2008. Guidelines for Design of Structures for Vertical Evacuation from Tsunamis. Tech. Rep. P-646, Federal Emergency Management Agency, Washington D.C.

FEMA, 2012. Guidelines for Design of Structures for Vertical Evacuation from Tsunamis. Tech. Rep. P-646, Federal Emergency Management Agency, Washington D.C., Second Edition.

Fenton, J. D., 2003. The effects of obstacles on surface levels and boundary resistance in open channels. In: Ganoulis, J., Prinos, P. (Eds.), Proc. 30th IAHR Congress, Thessaloniki 25-29 August. pp. C2 9–16.

Fenton, J. D., 2008. Obstacles in streams and their roles as hydraulic structures. In: Stefano, P. (Ed.), Hydraulic Structures - Proc. 2nd International Junior Researcher and Engineer Workshop on Hydraulic Structures, Pisa, Italy,30.7-1.8.2008. pp. 15–22.

Friedman, J. H., 1984. A Variable Span Smoother. Technical Report No. 5, Laboratory for Computational Statistics. Department of Statistics, Stanford University.

Fritz, H. M., Phillips, D. A., Okayasu, A., Shimozono, T., Liu, H., Mohammed, F., Skanavis, V., Synolakis, C. E., Takahashi, T., 2012. The 2011 japan tsunami current velocity measurements from survivor videos at kesennuma bay using lidar. Geophysical Research Letters 39 (7).

Fryer, G. J., Watts, P., Pratson, L. F., 2004. Source of the great tsunami of 1 april 1946: a landslide in the upper aleutian forearc. Marine Geology 203 (3-4), 201 – 218.

Fujima, K., Achmad, F., Shigihara, Y., Mizutani, N., 2009. Estimation of Tsunami Force Acting on Rectangular Structures. Journal of Disaster Research 4 (6), 404–409.

Fujima, K., Masamura, K., Goto, C., 2002. Development of the 2d/3d hybrid model for tsunami numerical simulation. Coastal Engineering Journal 44 (04), 373–397.

Fukui, Y., Nakamura, M., Shiraishi, H., Sasaki, Y., 1963. Hydraulic study on tsunami. Coastal Engineering in Japan 6, 67–82.

Gayer, G., Leschka, S., Nöhren, I., Larsen, O., Günther, H., 2010. Tsunami inundation modelling based on detailed roughness maps of densely populated areas. Natural Hazards and Earth System Sciences 10 (8), 1679–1687.

Gedik, N., Irtem, E., Kabdasli, S., Apr. 2005. Laboratory investigation on tsunami run-up. Ocean Engineering 32 (5-6), 513–528.

Geist, E. L., 1999. Local tsunamis and earthquake source parameters. Advances in Geophysics 39, 117–209.

Gingold, R. A., Monaghan, J. J., 1977. Smoothed particle hydrodynamics: theory and application to non-spherical stars. Monthly Notices of the Royal Astronomical Society 181 (3), 375–389.

Goda, K., Song, J., 2015. Uncertainty modeling and visualization for tsunami hazard and risk mapping: a case study for the 2011 Tohoku earthquake. Stochastic Environmental Research and Risk Assessment, 1–15.

Goring, D. G., 1979. Tsunamis- the Propagation of Long Waves onto a Shelf. Phd, California Institute of Technology.

Goseberg, N., Wurpts, A., Schlurmann, T., 2013. Laboratory-scale generation of tsunami and long waves. Coastal Engineering 79, 57–74.

Grilli, S. T., Ioualalen, M., Asavanant, J., Shi, F., Kirby, J. T., Watts, P., 2007. Source Constraints and Model Simulation of the December 26, 2004, Indian Ocean

Tsunami. Journal of Waterway, Port, Coastal, and Ocean Engineering 133 (6), 414.

Guinot, V., 2012. Multiple porosity shallow water models for macroscopic modelling of urban floods. Advances in Water Resources 37, 40–72.

Hall, J. V., Watts, J. W., 1953. Laboratory investigation of the vertical rise of solitary waves on impermeable slopes. Tech. Memo 33, Beach Erosion Board, USACE.

Hammack, J. L., 1972. Tsunamis - a model of their generation and propagation. Ph.D. thesis, California Institute of Technology.

Haralick, R. M., Jan. 1984. Digital step edges from zero crossing of second directional derivatives. IEEE Transactions on Pattern Analysis and Machine Intelligence 6 (1), 58–68.

HR Wallingford, 2010. Miniature propeller meters for physical models.

HR Wallingford, 2012. High performance pressure sensors for physical models.

Hsiao, S.-C., Lin, T.-C., 2010. Tsunami-like solitary waves impinging and overtopping an impermeable seawall: Experiment and rans modeling. Coastal Engineering 57 (1), 1–18.

Huang, C.-J., Hsu, M.-H., Teng, W.-H., Wang, Y.-H., 2014. The impact of building coverage in the metropolitan area on the flow calculation. Water 6 (8), 2449–2466.

Hubbard, M. E., Dodd, N., 2002. A 2D numerical model of wave run-up and overtopping. Coastal Engineering 47 (1), 1–26.

Hunt, J. C. R., Vassilicos, J. C., 1991. Kolmogorov's contributions to the physical and geometrical understanding of small-scale turbulence and recent developments. The Royal Society Proceedings: Mathematical and Physical Sciences 434 (1890), 183–210.

Hunter, N. M., Horritt, M. S., Bates, P. D., Wilson, M. D., Werner, M. G., 2005. An adaptive time step solution for raster-based storage cell modelling of floodplain inundation. Advances in Water Resources 28 (9), 975–991.

Imamura, F., Yalciner, A. C., Ozyurt, G., 2006. Tsunami modelling manual. UNESCO IOC international training course on Tsunami Numerical Modelling.

IMPW, 2009. Guidelines for Planning of Infrastructure and General Development in Regions Prone to Tsunami. (in Indonesian). No. 06/PRT/M/2009, Indonesian Ministry of Public Works (IMPW), Jakarta.

Kaiser, G., Scheele, L., Kortenhaus, A., Løvholt, F., Römer, H., Leschka, S., 2011. The influence of land cover roughness on the results of high resolution tsunami inundation modeling. Nat. Hazards Earth Syst. Sci 11, 2521–2540.

Kirby, J. T., Wei, G., Chen, Q., Kennedy, A. B., Dalrymple, R. A., 1998. Funwave 1.0: fully nonlinear boussinesq wave model-documentation and user's manual. Tech. rep., University of Delaware.

Korteweg, D. J., deVries, G., Feb. 1895. On the change of form of long waves advancing in a rectangular canal, and on a new type of long stationary waves. Philosophical Magazine Series 5 39, 422–443.

Koshimura, S., Oie, T., Yanagisawa, H., Imamura, F., 2009. Developing Fragility Functions for Tsunami Damage Estimation Using Numerical Model and Post-Tsunami Data From Banda Aceh, Indonesia. Coastal Engineering journal 51 (03), 243–273.

Kreyszig, E., 1999. Advanced Engineering Mathematics, eighth Edition. John Wiley & Sons, Inc.

Lai, C., 1993. Courant number and unsteady flow computation. In: Proceedings of the National Conference on Hydraulic Engineering. pp. 2196–2201.

Lambert, J.-H., 1760. Photometry, or, on the measure and gradations of light, colors, and shade: translation from the Latin of photometria, sive, de mensura et gradibus luminis, colorum et umbrae. sumptibus viduae E. Klett.
URL `http://imgbase-scd-ulp.u-strasbg.fr/displayimage.php?album=53&pos=1`

Lax, P., Wendroff, B., 1960. Systems of conservation laws. Communications on Pure and Applied Mathematics 13 (2), 217–237.

Lee, B. E., 1975. The effect of turbulence on the surface pressure field of a square prism. Journal of Fluid Mechanics 69 (02), 263–282.

Liang, D., Falconer, R. A., Lin, B., 2007. Coupling surface and subsurface flows in a depth averaged flood wave model. Journal of Hydrology 337 (1), 147–158.

Lloyd, T., Rossetto, T., 2012. A comparison between existing tsunami load guidance and large-scale experiments with long-waves. In: 15 World Conference on Earthquake Engineering. pp. 1–10.

Lubkowski, Z., D'Ayala, D., Crewe, A. J., Manafpour, A., Grant, D. N., Lloyd, T. O., Escribano Leiva, D., Novelli, V., 2010. The Mw 8.8 Maule Chile Earthquake of 27th February 2010: A Preliminary Field Report by EEFIT. Tech. rep., Institution of Stuctural Engineers, Earthquake Engineering Field Investigation Team (EEFIT), London.

Luettich, R. A., Westerink, J. J., 2004. Formulation and numerical implementation of the 2D/3D ADCIRC finite element model version 44. XX.

Lukkunaprasit, P., Ruangrassamee, A., Thanasisathit, N., 2009a. Tsunami loading on buildings with openings. Science of Tsunami Hazards 28 (5), 303–310.

Lukkunaprasit, P., Thanasisathit, N., Yeh, H. H., 2009b. Experimental Verification of FEMA P646 Tsunami Loading. Journal of Disaster Research 4 (6), 410–411.

Lynett, P. J., Wu, T.-R., Liu, P. L.-F., Jul. 2002. Modeling wave runup with depth-integrated equations. Coastal Engineering 46 (2), 89–107.

Macabuag, J., Rossetto, T., Ioannou, I., Suppasri, A., Sugawara, D., Adriano, B., Imamura, F., Eames, I., Koshimura, S., 2016. A proposed methodology for deriving tsunami fragility functions for buildings using optimum intensity measures. Natural Hazards, 1–29.

Macabuag, J., Rossetto, T., Lloyd, T., 2014a. Sensitivity analyses of a framed structure under several tsunami design-guidance loading regimes. In: 2nd European Conference on Earthquake Engineering and Seismology. pp. 1–12.

Macabuag, J., Rossetto, T., Lloyd, T., 2014b. Structural analysis for the generation of analytical tsunami fragility functions. In: 10th International Conference on Urban Earthquake Engineering. pp. 1–11.

Madsen, P. A., Fuhrman, D. R., Schäffer, H. A., Dec. 2008. On the solitary wave paradigm for tsunamis. Journal of Geophysical Research 113 (C12).

Madsen, P. A., Murray, R., Sørensen, O. R., 1991. A new form of the boussinesq equations with improved linear dispersion characteristics. Coastal Engineering 15 (4), 371–388.

Madsen, P. A., Sørensen, O. R., 1992. A new form of the boussinesq equations with improved linear dispersion characteristics. part 2. a slowly-varying bathymetry. Coastal Engineering 18 (3), 183–204.

Mallock, A., 1907. On the resistance of air. Proceedings of the Royal Society of London A: Mathematical, Physical and Engineering Sciences 79 (530), 262–273.

Mandal, D., 2011. Impact on obstacles in free surface channel flows. Master's thesis, Department of Mechanical Engineering , University College London.

Massey, B., 1970. Mechanics of fluids. Van Nostrand Reinhold Company Ltd.

MathWorks, 2010. MATLAB R2010b, Product Help. Tech. rep., MathWorks.

Matsutomi, H., Iizuka, H., 1998. Tsunami current velocity on land and its simple estimation method. In: Proc. of Coastal Eng., JSCE. Vol. 42. pp. 346–350.

Matsutomi, H., Okamoto, K., 2010. Inundation flow velocity of tsunami on land. Island Arc 19 (3), 443–457.

Maxworthy, T., Apr. 1976. Experiments on collisions between solitary waves. Journal of Fluid Mechanics 76 (01), 177–185.

Merian, J. R., 1828. Ueber die Bewegung tropfbarer Flüssigkeiten in Gefässen. Schweighauser.

Miles, J. W., Jan. 1980. Solitary Waves. Annual Review of Fluid Mechanics 12 (1), 11–43.

Mitsuyasu, H., 1966. Shock pressure of breaking wave. In: Proc. of 10th Int. Conf. Costal Eng. ASCE, p. pp. 268283.

Morison, J., O'Brien, M., Johnson, J., Schaaf, S., 1950. The Force Exerted by Surface Waves on Piles. Petroleum Transactions 189, 149–154.

Murty, T. S., et al., 1977. Seismic sea waves: tsunamis. Ottawa, Ont.(Canada) Dept. of Fisheries and the Environment, Fisheries and Marine Service.

Nakamura, S., Tsuchiya, Y., 1973. On the shock pressure of surge on a wall. Bulletin of the Disaster Prevention Research Institute 23 (3-4), 47–58.

Newcomb, K. R., McCann, W. R., 1987. Seismic history and seismotectonics of the Sunda Arc. Journal of Geophysical Research 92 (B1), 421–439.

Nomanbhoy, N., Satake, K., 1995. Generation mechanism of tsunamis from the 1883 krakatau eruption. Geophysical Research Letters 22 (4), 509–512.

Nouri, Y., Nistor, I., Palermo, D., Cornett, A., 2010. Experimental Investigation of Tsunami Impact on Free Standing Structures. Coastal Engineering Journal 52 (01), 43.

NTHMP, 2001. Designing for tsunamis - seven principles for planning and designing for tsunami hazards. Tech. rep., National Tsunami Hazard Mitigation Program, USA.

Nwogu, O., 1993. Alternative Form of Boussinesq Equations for Nearshore Wave Propagation. Journal of Waterway, Port, Coastal and Ocean Engineering 119 (6), 618.

OCDI, 2002. Technical Standards and Commentaries for Port and Harbour Facilities in Japan. Tech. rep., The Oversees Coastal Area Development Institute of Japan, Tokyo, Japan.

Ohmori, M., Fujii, N., Kyotani, O., 2000. The numerical computation of the water level, the flow velocity and the wave force of the tsunami which overflow the perpendicular revetments - (in Japanese). Proceedings of the Coastal Engineerings of JSCE 47, 376–380.

Okada, T., Sugano, T., Ishikawa, T., Ohgi, T., Takai, S., Hamabe, C., 2005. Structural design method of buildings for tsunami resistance (proposed). Draft tsunami design methodology, The Building Centre of Japan, Japan.

Okada, Y., 1985. Surface deformation due to shear and tensile faults in a half-space. Bulletin of the Seismological Society of America 75 (4), 1135–1154.

Otsuki, Y., Fujii, K., Washizu, K. t., Ohya, A., 1978. Wind tunnel experiments on aerodynamic forces and pressure distributions of rectangular cylinders in a uniform flow. In: Proceedings of the fifth symposium on wind effects on structures. pp. 169–176.

Pararas-Carayannis, G., 1992. The tsunami generated from the eruption of the volcano of Santorin in the Bronze Age. Natural Hazards 5 (2), 115–123.

Park, H., Cox, D. T., Lynett, P. J., Wiebe, D. M., Shin, S., 2013. Tsunami inundation modeling in constructed environments: a physical and numerical comparison of free-surface elevation, velocity, and momentum flux. Coastal Engineering 79, 9–21.

Park, H., Wiebe, D. M., Cox, D. T., Cox, K., 2014. Tsunami inundation modeling: Sensitivity of velocity and momentum flux to bottom friction with application to building damage at seaside, Oregon. Coastal Engineering Proceedings 1 (34), 1.

Patera, A. T., 1984. A spectral element method for fluid dynamics: laminar flow in a channel expansion. Journal of computational Physics 54 (3), 468–488.

Pedersen, G., Gjevik, B., 1983. Run-up of solitary waves. Journal of Fluid Mechanics 135, 283–299.

Peregrine, D. H., Mar. 1967. Long waves on a beach. Journal of Fluid Mechanics 27 (04), 815–827.

PIANC, 2010. Mitigation of tsunami disasters in ports. PIANC Report 112, PIANC, Bruxelles.

Qi, Z., Eames, I., Johnson, E., 2014. Force acting on a square cylinder fixed in a free-surface channel flow. Journal of Fluid Mechanics 756, 716–727.

Raby, A., Macabuag, J., Pomonis, A., Wilkinson, S., Rossetto, T., 2015. Implications of the 2011 Great East Japan Tsunami on sea defence design. International Journal of Disaster Risk Reduction 14, 332–346.

Ramsden, J. D., 1993. Tsunamis : Forces On A Vertical Wall Caused By Long Waves, Bores, And Surges On A Dry Bed. PhD Thesis, California Institute of Technology.

Ramsden, J. D., 1996. Forces on a Vertical Wall due to Long Waves, Bores, and Dry-Bed Surges. Journal of Waterway, Port, Coastal, and Ocean Engineering 122 (3), 134.

Ramsden, J. D., Raichlen, F., 1990. Forces on vertical wall caused by incident bores. Journal of Waterway, Port, Coastal, and Ocean Engineering 116 (5), 592–613.

Rayleigh, J. W. S., 1876. On Waves. Philosophical Magazine Series 5 1, 257–279.

Roache, P. J., 1994. Perspective: a method for uniform reporting of grid refinement studies. Journal of Fluids Engineering 116 (3), 405–413.

Roh, M., Tanaka, H., Aditaywan, M. B., Mano, A., Udo, K., 2012. Evaluation of celerity and velocity for tsunami propagation into rivers. Coastal Engineering Proceedings 1 (33), currents–12.

Rosman, J. H., Hench, J. L., 2011. A framework for understanding drag parameterizations for coral reefs. Journal of Geophysical Research: Oceans 116 (C8).

Rossetto, T., Allsop, W., Charvet, I., Robinson, D. I., Jun. 2011. Physical modelling of tsunami using a new pneumatic wave generator. Coastal Engineering 58 (6), 517–527.

Rossetto, T., Peiris, N. L. M., Pomonis, A., Wilkinson, S. M., Del Re, D., Koo, R., Gallocher, S., Nov. 2006. The Indian Ocean tsunami of December 26, 2004: observations in Sri Lanka and Thailand. Natural Hazards 42 (1), 105–124.

Russell, J. S., 1845. Report on Waves. In: Report of the 14th Meeting of the British Association for the Advancement of Science, York. John Murray, London, pp. 311–390.

Sandwell, D. T., 1987. Biharmonic Spline Interpolation of GEOS-3 and SEASAT Altimeter Data. Geophysical Research Letters 14 (02), 139–142.

Schimmels, S., Sriram, V., Didenkulova, I., 2016. Tsunami generation in a large scale experimental facility. Coastal Engineering 110, 32–41.

Shafiei, S., Melville, B. W., Shamseldin, A. Y., 2016. Experimental investigation of tsunami bore impact force and pressure on a square prism. Coastal Engineering 110, 1–16.

Sharify, E. M., Saito, H., Harasawa, H., Takahashi, S., Arai, N., 2013. Experimental and numerical study of blockage effects on flow characteristics around a square-section cylinder. Journal of the Japanese Society for Experimental Mechanics 13 (Special_Issue), s7–s12.

Shimamoto, T., Tsutsumi, A., Kawamoto, E., Miyawaki, M., Sato, H., 1995. Field survey report on tsunami disasters caused by the 1993 Southwest Hokkaido earthquake. Pure and Applied Geophysics PAGEOPH 144 (3-4), 665–691.

Siffer, T., 2005. Mercator depth gauge recording of 26 December 2004 tsunami. KNMI (Royal Netherlands Meteorological Institute).

Simamora, C., Shigihara, Y., Fujima, K., 2007. Experimental Study on Tsunami Forces Acting on Structures (in Japanese). Proceedings of Coastal Engineering, JSCE 54, 831–835.

Sitanggang, K., Lynett, P., 2010. Multi-scale simulation with a hybrid boussinesq-rans hydrodynamic model. International Journal for Numerical Methods in Fluids 62 (9), 1013–1046.

Sitanggang, K. I., 2008. Boussinesq-equation and rans hybrid wave model. Ph.D. thesis, Texas A&M University.

Smit, J., Roep, T. B., Alvarez, W., Montanari, A., Claeys, P., Grajales-Nishimura, J. M., Bermudez, J., 1996. Coarse-grained, classic sandstone complex at the K/T boundary around the Gulf of Mexico: Deposition by tsunami waves induced by the Chicxulub impact? In: The Cretaceous-Tertiary event and other catastrophes in earth history. The Geological Society of America, Inc, pp. 151–182.

St-Germain, P., Nistor, I., Townsend, R., 2012. Numerical modeling of the impact with structures of tsunami bores propagating on dry and wet beds using the SPH method. International Journal of Protective Structures 3 (2), 221–256.

St-Germain, P., Nistor, I., Townsend, R., Shibayama, T., 2013. Smoothed-particle hydrodynamics numerical modeling of structures impacted by tsunami bores. Journal of Waterway, Port, Coastal, and Ocean Engineering 140 (1), 66–81.

Suppasri, A., Koshimura, S., Imamura, F., 2011. Developing tsunami fragility curves based on the satellite remote sensing and the numerical modeling of the 2004

indian ocean tsunami in thailand. Natural Hazards and Earth System Science 11 (1), 173–189.

Swiss Re, 2012. Losses from recent major earthquakes. Swiss Reinsurance Company Ltd.

Synolakis, C., Bernard, E., Titov, V., Kanoglu, U., González, F., 2007. Oar pmel-135 standards, criteria, and procedures for noaa evaluation of tsunami numerical models. Report No. NOAA Tech. Memo. OAR PMEL-135, NOAA/Pacific Marine Environmental Laboratory, Seattle, WA.

Synolakis, C., Bernard, E., Titov, V., Kânoğlu, U., González, F., 2008. Validation and verification of tsunami numerical models. Pure and Applied Geophysics 165 (11-12), 2197–2228.

Synolakis, C. E., 1987. The runup of solitary waves. Journal of Fluid Mechanics 185, 523–545.

Synolakis, C. E., Bardet, J.-P., Borrero, J. C., Davies, H. L., Okal, E. A., Silver, E. A., Sweet, S., Tappin, D. R., Apr. 2002. The slump origin of the 1998 Papua New Guinea Tsunami. Proceedings of the Royal Society A: Mathematical, Physical and Engineering Sciences 458 (2020), 763–789.

Synolakis, C. E., Bernard, E. N., Aug. 2006. Tsunami science before and beyond Boxing Day 2004. Philosophical transactions. Series A, Mathematical, physical, and engineering sciences 364 (1845), 2231–2265.

Tadepalli, S., Synolakis, C. E., 1994. The run-up of n-waves on sloping beaches. Proceedings of the Royal Society of London A: Mathematical, Physical and Engineering Sciences 445 (1923), 99–112.

Tamura, T., Miyagi, T., 1999. The effect of turbulence on aerodynamic forces on a square cylinder with various corner shapes. Journal of Wind Engineering and Industrial Aerodynamics 83 (1), 135–145.

Tappin, D. R., Matsumoto, T., Watts, P., Satake, K., McMurtry, G. M., Matsuyama, M., Lafoy, Y., Tsuji, Y., Kanamatsu, T., Lus, W., et al., 1999. Sediment slump likely caused 1998 papua new guinea tsunami. Eos, Transactions American Geophysical Union 80 (30), 329–340.

Tavoularis, S., 2002. Flow past immersed objects. In: Saleh, J. M. (Ed.), Fluid Flow Handbook. McGraw-Hill, New York, pp. 20.l–20.44.

Thurairajah, A., 2005. Structural design loads for tsunami & floods. In: International Symposium Disaster Reduction on Coasts. pp. 1–11.

Thusyanthan, N. I., Madabhushi, G. S. P., Jan. 2008. Tsunami wave loading on coastal houses: a model approach. Proceedings of the ICE - Civil Engineering 161 (2), 77–86.

Titov, V. V., González, F. I., 1997. Implementation and testing of the Method of Splitting Tsunami (MOST) model. NOAA Technical Memorandum ERL PMEL-12, NOAA / Pacific Marine Environmental Laboratory, Seattle , WA.

Titov, V. V., Synolakis, C. E., 1998. Numerical modeling of tidal wave runup. Journal of Waterway, Port, Coastal, and Ocean Engineering 124 (4), 157–171.

USACE, 1988. Breaking Wave Forces on Walls. Coastal Engineering Technical Note CETN-III-38, U.S. Army Engineer Waterways Experiment Station, Coastal Engineering Research Centre, Vicksburg, Mississippi.

USACE, 1989. Water Levels and Wave Heights for Coastal Engineering Design. Engineer Manual EM 1110-2-1414, U.S. Army Corps of Engineers, Washington D.C.

USACE, 1990. Wave Forces on a Wall Shorewards of the Stil-Water Line. Coastal Engineering Technical Note CETN-III-29, U.S. Army Engineer Waterways Experiment Station, Coastal Engineering Research Centre, Vicksburg, Mississippi.

USACE, 1991. Broken Wave Forces. Coastal Engineering Technical Note CETN-I-50, U.S. Army Engineer Waterways Experiment Station, Coastal Engineering Research Centre, Vicksburg, Mississippi.

USACE, 1995. Flood Proofing. Engineer Pamphlet EP 1165-2-314, U.S. Army Corps of Engineers, Washington D.C.

USAEWES, 1984. Shore Protection Manual. (SPM) 4th ed., 2 Vol, U.S. Army Engineer Waterways Experiment Station, U.S.Government Printing Office, Washington D C.

USNRC, 2009. Tsunami hazard assessment at nuclear power plant sites in the united states of america. Tech. Rep. NUREG/CR-6966, United States Nuclear Regulatory Commission, USA.

van De Lindt, J. W., Gupta, R., Garcia, R. A., Wilson, J. S., Nov. 2009. Tsunami bore forces on a compliant residential building model. Engineering Structures 31 (11), 2534–2539.

Wakaba, L., Balachandar, S., 2007. On the added mass force at finite reynolds and acceleration numbers. Theoretical and Computational Fluid Dynamics 21 (2), 147–153.

Ward, S., May 2000. Asteroid Impact Tsunami: A Probabilistic Hazard Assessment. Icarus 145 (1), 64–78.

Watts, P., Grilli, S. T., Kirby, J. T., Fryer, G. J., Tappin, D. R., 2003. Landslide tsunami case studies using a Boussinesq model and a fully nonlinear tsunami generation model. Natural Hazards and Earth System Science 3 (5), 391–402.

Wei, G., Kirby, J. T., 1995. Time-dependent numerical code for extended Boussinesq equations. journal of Waterway, Port, Coastal, and Ocean Engineering 121 (5), 251–261.

Wei, Z., Dalrymple, R. A., Hérault, A., Bilotta, G., Rustico, E., Yeh, H., 2015. SPH modeling of dynamic impact of tsunami bore on bridge piers. Coastal Engineering 104, 26–42.

Wilkie, M. J., Young, G. A. J., 1952. Pneumatic Tide Generator. Report 10.EB1981, HR Wallingford.

Wilson, J., 2008. Behavior of a 1/6th scale, two-story, wood framed residential structure under surge wave loading. Ph.D. thesis, Oregon State University.

Wilson, J. S., Gupta, R., van de Lindt, J. W., Clauson, M., Garcia, R., 2009. Behavior of a one-sixth scale wood-framed residential structure under wave loading. Journal of Performance of Constructed Facilities 23 (5), 336–345.

Yeh, H., Barbosa, A. R., Ko, H., Cawley, J. G., 2014. Tsunami loadings on structures: review and analysis. Coastal Engineering Proceedings 1 (34), 4.

Yeh, H., Li, W., 2008. Tsunami scour and sedimentation. In: Fourth International Conference on Scour and Erosion 2008. pp. 95–106.

Yeh, H. H., 2006. Maximum Fluid Forces in the Tsunami Runup Zone. Journal of Waterway, Port, Coastal, and Ocean Engineering 132 (6), 496.

Yeh, H. H., 2007. Design Tsunami Forces for Onshore Structures. Journal of Disaster Research 2 (6), 531–536.

Appendix A

Force equations present in design codes

Table A.1: *Force equations present in design codes and other selected literature*

Year of publication	Reference	Velocity	Vertical hydrostatic	Lateral hydrostatic	Hydro- dynamic	Impulsive/ Surge	Inertia	Hydraulic gradient	Impact
1980	Camfield (1980)	$2\sqrt{gh}$	$\rho g V$	$\frac{1}{2}b\rho g h^2$	$\frac{1}{2}C_\mathrm{D}\rho bhu^2$	$4.5\rho gbh^2$			$m\frac{\Delta u_i}{\Delta t}$
1981	FEMA (2000)	$2\sqrt{gh}$	$\rho g V$	$\frac{1}{2}b\rho g h^2$	$\frac{1}{2}C_\mathrm{D}\rho bhu^2$				$m\frac{\Delta u_i}{\Delta t}$
1984	USAEWES (1984)								
1988	USACE (1988)				*Breaking wave forces on a sea wall using Goda's method*				
1989	USACE (1989)	$2\sqrt{gh}$							
1990	USACE (1990)			$\frac{1}{2}b\rho g h^2$		$4.5\rho gbh^2$			
1991	USACE (1991)		*Broken wave forces on a sea wall based on offshore wave height and broken wave decay* (Camfield, 1991)						
1995	USACE (1995)			$\frac{1}{2}b\rho g h^2$					
1998	Arsen'ev et al. (1998)				$\frac{1}{2}C_\mathrm{D}\rho dhu\lvert u\rvert$		$C_\mathrm{m}\rho\frac{\pi d}{4}\dot{u}h$	*(where d is the diameter of a cylinder)*	
2000	CCH (2000)	h		$\frac{1}{2}b\rho g\left(h+\frac{u^2}{2g}\right)^2$		$4.5\rho gbh^2$			
2000	Ohmori et al. (2000)				$\frac{1}{2}C_\mathrm{D}\rho bhu\lvert u\rvert$	$\frac{1}{2}C_\mathrm{s}(\theta)\rho bhu\lvert u\rvert$ *	$C_\mathrm{m}\rho bLh\dot{u}$	$\rho gbLh\frac{\mathrm{d}h}{\mathrm{d}x}$	
2001	NTHMP (2001)				*refers to FEMA (2000) for guidance*				
2002	Asakura et al. (2002)	$Fr\sqrt{gh}$		— "Tsunami force" $4.5\rho gbh^2$ —					
2002	OCDI (2002)								
2005	Okada et al. (2005)	$Fr\sqrt{gh}$	$\rho g V$	— "Tsunami force" $4.5\rho gbh^2$ —					
2005	Thurairajah (2005)	$\sqrt{1.67gh}$	$1.2\rho g V$	$\frac{1}{2}b\rho g h^2$	$\frac{1}{2}C_\mathrm{D}\rho bhu^2$	$\frac{1}{2}C_\mathrm{s}(\theta)\rho bhu^2$			
2006	CRATER (2006)	$2\sqrt{gh}$			$\frac{1}{2}C_\mathrm{D}\rho bhu^2$	$4.5\rho gbh^2$			$m\frac{\Delta u_i}{\Delta t}$
2007	Yeh (2007)	$2\sqrt{gh}$			$\frac{1}{2}C_\mathrm{D}\rho b(hu^2)_{max}$	$4.5\rho gbh^2$			Various
2008	FEMA (2008)	$2\sqrt{gh}$	$\rho g V$	$\frac{1}{2}b\rho g h^2$	$\frac{1}{2}C_\mathrm{D}\rho b(hu^2)_{max}$	$1.5\frac{1}{2}C_\mathrm{D}\rho b(hu^2)_{max}$			$C_\mathrm{m}u\sqrt{km}$

Continued on next page

*where $C_\mathrm{s}(\theta) = 3.6\tan\theta$ and θ is the angle of the wave

Table A.1 – continued from previous page

Year of publication	Reference	Velocity	Vertical hydrostatic	Lateral hydrostatic	Hydro- dynamic	Impulsive/ Surge	Inertia	Hydraulic gradient	Impact
2009	IMPW (2009)		$\rho g V$	$\frac{1}{2} b \rho g \left(h + \frac{u^2}{2g}\right)^2$	$\frac{1}{2} C_{\mathrm{D}} \rho b h u^2$	$4.5 \rho g b h^2$			
2009	USNRC (2009)			$\frac{1}{2} b \rho g \left(h + \frac{u^2}{2g}\right)^2$	$\frac{1}{2} C_{\mathrm{D}} \rho b h u^2$				$m \frac{\Delta u_i}{\Delta t}$
2010	PIANC (2010)	$2\sqrt{gh}$		$\frac{1}{2} b \rho g \left(h + \frac{u^2}{2g}\right)^2$	$\frac{1}{2} C_{\mathrm{D}} \rho b h u^2$				$m \frac{\Delta u_i}{\Delta t}$
2011	Chock et al. (2011)	various	$\rho g V$	$\frac{1}{2} b \rho g h^2$	$\frac{1}{2} C_{\mathrm{D}} \rho b (h u^2)$	$\frac{1}{2} C_{\mathrm{r}} \rho b (h u^2)$			$\pi u \frac{(m_{\mathrm{d}} + C_{\mathrm{m}} m_{\mathrm{f}}}{2 \Delta t}$
2012	FEMA (2012)	various	$\rho g V$	$\frac{1}{2} b \rho g h^2$	$\frac{1}{2} C_{\mathrm{D}} \rho b (h u^2)_{max}$	$1.5 \frac{1}{2} C_{\mathrm{D}} \rho b (h u^2)_{max}$			$1.3 u_{\max} (km(1+c))^{\frac{1}{2}}$

Appendix B

Image processing

Image processing is a very powerful tool for the acquisition of laboratory data. Imagery from high speed cameras allows measurement of variables remotely, without influencing the system being observed, and high precision is possible. Images were acquired during the testing period at HR Wallingford using a high speed camera pointed at our test structure through the observation window of the flume. From this position, and with careful lighting, it is possible to observe the wave profile on the side of the structure as the tests are carried out.

The camera was a Photron FASTCAM Digital Video Recorder which is capable of capturing images at frame rates of up to 2000 frames per second (fps), though the resolution capabilities drop off at this speed. For our purposes, the lower frame rate of 125fps was chosen for all tests to enable higher resolution, and images were stored in the "TIFF" format. MATLAB was used for the image processing.

A digital image is simply a matrix of numbers (or pixels) which relate to a colour map. Often a colour image is represented by three such matrices, for Red, Green and Blue (RGB) respectively. Each pixel is then represented by a certain proportion (intensity) of the Red, Green and Blue channels to make up the final image - the channel intensities typically take values between 0 and 255. As our tests did not require colour images, we captured in grayscale, i.e. the Red , Green and Blue values are all identical (in reality there are sometimes slight differences, but generally these are unnoticeable). In our case the spatial value of the pixels was more important and required higher precision than the intensity information.

B.1 Definition of a coordinate system

The overall aim of this image processing is to obtain accurate water surface profile time histories for each test that was filmed. The water profile we are interested in for the more simple case of a building face on to the flow, is the profile on the side. This profile will give us a good estimation of the water level across the front and backs of the structure, while also providing information about how the water levels change around the structure.

In order to extract the wave profile information from a series of digital photographs, there are a number of steps to be taken. Firstly a suitable basis for a coordinate system is necessary. The dimensions of the structure are known and as the flows in close proximity to the structure are of interest, the four corners of the structures side face can be used as a basis for defining the coordinate system. A clear image of the structure before any wave has come into view makes the best image to base a coordinate system on, and has other uses which will be discussed shortly.

A clearer image can be obtained by taking an time-average of several frames, and thereby reducing some of the noise present in one image. The first 200 frames in the video sequence were used for this purpose as follows:

$$[\mathbf{A}] = \frac{1}{200} \sum_{i=1}^{n=200} [\mathbf{I}_i] \tag{B.1}$$

The resulting averaged image, $[\mathbf{A}]$, can be seen in Figure B.1 (a). Although not very large differences can be detected between the first 200 images, there are small effects due to light flicker and other noise. The time averaged image is an improvement, and helps with the next stage.

The reason for requiring a clean initial image, is so that some degree of edge detection can be performed on it with greater ease. As can be seen in Figure B.1 (a), there are four strong straight lines present in the image and we wish to use those lines to define a coordinate system. Once we have the coordinate system, it is possible to measure movements with respect to it.

There are several methods for implementing edge detection, but generally they all

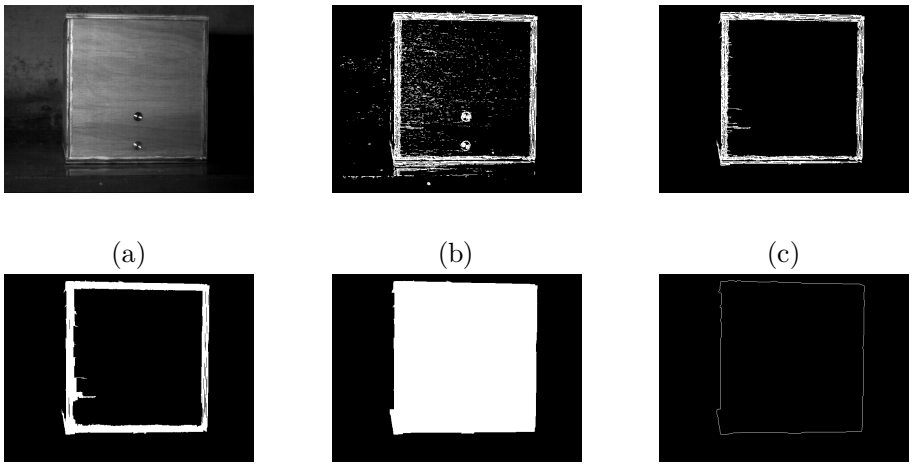

Figure B.1: *Sequence of pre-processing initial image. Average image of building from first 200 frames of image sequence.*

rely on thresholding the image, i.e. converting pixels with intensity below the threshold to zero (black) and those above to one (white). Several ways of detecting the sharp changes in intensity are possible in this state. Often the gradient magnitude is used to first find local maxima in an image before thresholding, but some algorithms use the second derivative such as Haralick (1984). However, few algorithms are more effective than the Canny edge detector (Canny, 1986). This assertion is based on the more robust methodology which uses the derivative of a Gaussian filter to find the gradient, and then uses two thresholds to detect both strong and weak edges. Weak edges are only retained if they are connected to strong edges, meaning it is less likely than other methods to be fooled by noise, and more likely to detect true weak edges (MathWorks, 2010).

Another type of edge detection uses the Sobel operator as an approximation to the intensity gradient, which works on a 3 by 3 region about each pixel. The Sobel operator then uses integer coefficients to weight the image intensities to derive the approximate gradient. Whilst not particularly accurate for some other applications of edge detection requiring greater intensity precision, it is well suited for our initial edge detection. Sobel edge detection is used for the first pass edge detection in Figure B.1 (b). It tends to give slightly rougher results than other methods as it is a less sophisticated algorithm, and from experience it does not tend to close

boundaries automatically as other more sophisticated methods do. Boundary closing is not something desired at this stage, which is why the Sobel edge detection is used for highlighting peaks in pixel intensity gradient magnitude. The pixel values from the Sobel operation have been thresholded at 20 percent of the maximum (255) to produce the black and white image. In Figure B.1 (c), only linked pixels of areas greater than 2000 pixels have been opened. Gaps are filled with a line structure element where they are less than ten pixels across in a vertical direction (Figure B.1 (d)), and then in a horizontal direction (not shown here). This is to ensure production of a closed shape based on the outermost edge when the image does not produce as sharp results as shown here.

The now closed shape is filled to produce a solid square shape (Figure B.1 (e)). The outer perimeter of this follows very closely the outline of the test structure, and finally, Canny edge detection is used to produce the outer boundary in Figure B.1 (f). This border fits the outline of the structure very well, but not exactly. In order to accurately capture this for use in a coordinate system we need to capture the corners of the building, and as can be seen, these are not indicated clearly. One benefit we can see in the resultant boundary, is that the lines on average are very straight. This feature can be exploited by another type of edge detection which utilises the Hough transform (Duda and Hart, 1972).

The Hough transform in its simplest form is a linear transform used for detecting straight lines. More complex implementations of the Hough transform are capable of detecting curves and shapes, as well as 3D objects like planes and cylinders, but this is not necessary for our purpose. For a simple explanation of how the Hough transform works, consider a straight line in image space, $y = mx + c$ where each pair of coordinates (x, y) can be plotted to draw the line. The line could just as easily be represented by using the other parameters, slope, m, and intercept, c. Unfortunately, when vertical lines are encountered the parameters m and c become unbounded with an infinite slope, and no intercept.

To overcome this problem the coordinates are converted to their polar representation for use in the Hough transform. The equation for a line now becomes; $y = (-\frac{\cos\theta}{\sin\theta})x + (\frac{\rho}{\sin\theta})$, which can be rearranged to $\rho = x\cos\theta + y\sin\theta$, where ρ is the perpendicular distance between the line, and the origin.

Every point from x, y space produces a sinusoid in (ρ, θ) space, based on every possible line that could go through it, and the resulting ρ value which would produce the line with that θ. The points which make a straight line will have a sinusoidal curve that cross in (ρ, θ) space. As the ρ and θ values for points connected by a line are equal, the sinusoids for all points on a line will cross at the value of ρ and θ corresponding to the straight line. In this way, the problem is altered from one of finding points on the same line, to one of intersecting curves making it vastly simpler.

In the Hough transform algorithm, an accumulator array is used to count and bin the number of points (and their near neighbours) in (ρ, θ) space that could contribute to there being a line. This accumulator space, is plotted in Figure B.2 for a Hough transform of Figure B.1 (f). The peaks of this accumulator space correspond to the bins which the algorithm has determined to have enough evidence for the presence of a line. ρ is used to indicate the distance values in the accumulator, a θ matrix stores the angles, and every element has a points per pixel value for each parameter (ρ, θ).

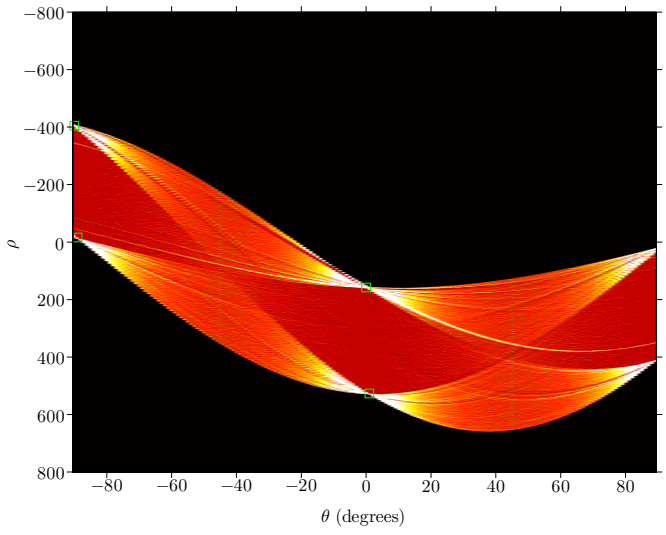

Figure B.2: *Visualisation of Hough transform accumulator array when performed on Figure B.1* (f)*. Four peaks identified (green squares) corresponding with the four strongest straight lines in Figure B.1* (f)*.*

As can be seen, the peaks have also been determined in Figure B.2 and are shown as green squares. MATLAB makes this process easier with its `hough`, and `houghpeaks`

functions. Peaks in this case were found with a threshold of 30% of the maximum accumulator value. The `houghpeaks` function also retains some of the position data of the points which contributed to the peaks, and this allows the length of the lines/edges to be determined. This information is usually lost in the Hough transform.

Figure B.3: *Edge detection based on peaks of Hough transform visualised in Figure B.2. Corners/coordinate control points (yellow squares) identified by extending the Hough lines to the image limits (red circles). The extended lines are shown in Figure B.4.*

After the edges have been determined, a visual check is necessary. The Hough method is generally very good, but occasionally will pick up the wrong edge. In this case, some functionality has been written into the script so that the user can manually enter two points on each of the four lines. Once, either way, four lines have been detected, they are extended to the boundaries of the image. The intersections between the four lines represent the four control points used to define the coordinate system. The detected edges are shown in Figure B.3 along with the determined control points/intersections.

The baselines of the coordinate system are shown in Figure B.4. It can be observed that the angles between the lines are not precisely 90°. In fact the line angles which come out of the Hough transform peaks are $89°, 0°, 1°$ and 90° respectively. There is a small degree of distortion in the image, which though not large, is enough to introduce an unnecessary extra degree of error to our measurements. This means the width/height of a pixel does not necessarily have a constant conversion to mm

Figure B.4: *Average image over-layed with the gridlines defined by edge detection in Figure B.3.*

across the image.

Projection distortions of this type are easily accounted for. As the four control points we selected from the edge detection have known real world coordinates (based on the building dimensions), they can be used to define a transform between the pixel based control points and the mm based - base points. A "projective" transform can be determined with this information using the spatial transform function `cp2tform` in MATLAB. This transform matrix can be applied to single points, lines or even whole images. The result of the transform being applied to the original time-averaged image of the structure (Figure B.1 (a)) can be seen in Figure B.5. The image has been ortho-rectified so that the side of the building is now square on to the viewer.

Figure B.5 is presented for demonstration purposes only; there is no need to ortho-rectify each image in the video sequence. Information subsequently derived from sequenced images can be ortho-rectified at far less computational expense by itself, without affecting the quality of the information. The transform (in the forward direction) converts pixel coordinates into millimetre based coordinates with an origin on the top left corner of the building and the positive direction is down. This was chosen to avoid problems with incompatibility, as this is the convention for pixel coordinates in images. It is also a position rarely obstructed by incoming waves.

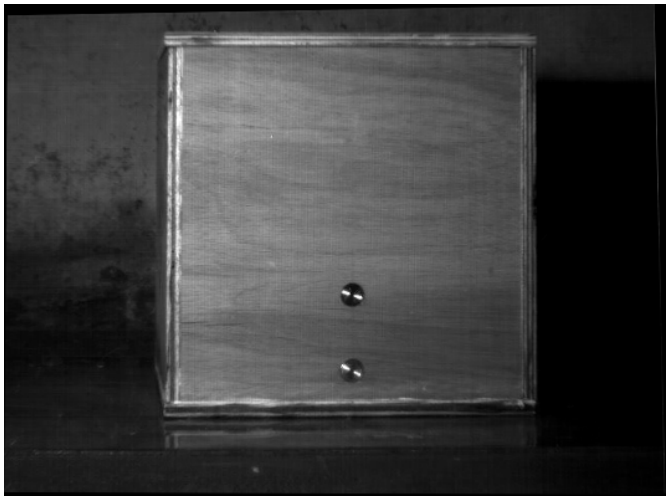

Figure B.5: *Ortho-rectified average image. The same transformation matrix applied to the average base-image as used to define the coordinate system.*

B.2 Measurement of wave surface profiles

The next stage of image processing concerns the automated detection of the wave profile as it travels past the side of the building. Edge detection again is the primary tool which is used for this, but there are a few other techniques which are useful.

Images are captured at a frame rate of 125 fps, meaning that a typical wave interaction period of say ten seconds, would produce 1250 digital images. Sequences are often captured for longer than this in order to ensure the interaction is observed. Due to this, sequences often contain large periods of motionless footage which add unnecessary computational time to the processing as well as difficulties with storage space. The first stage of this is manual editing and discarding of the surplus images, taking care to leave some lead in and out for capture of the initial average image.

The process described in the Section B.1 is applied to the resulting trimmed down sequence, and the coordinate system is determined. In the previous section a coordinate system, or more accurately a transform is defined to convert the distorted image pixels to a rectified Cartesian coordinate. This transform does not need to be applied until the final stage, but should be based on the average initial image.

In order to detect a water profile, there must be a noticeable change in image

intensity from one side of the edge, to the other. The unprocessed raw images, whilst well lit, sometimes gave only a small contrast between the two areas of interest. A far more robust method for detecting something such as this uses the change in an image with respect to the original. One method for doing this is by subtracting one image from another, which can work very well in binary images. However, it does not always yield good results with grayscale images. A far better method of detecting a difference or change in an image with respect to the original is by using normalisation as in (B.2).

$$[\mathbf{I}_{\text{norm}}] = \frac{[\mathbf{I}] + 1}{[\mathbf{A}] + 1} \tag{B.2}$$

in (B.2), the normalised intensity is $[\mathbf{I}_{\text{norm}}]$, $[\mathbf{I}]$ is the image in the sequence the information is extracted from and $[\mathbf{A}]$ is the average initial image (as defined by (B.1)). The division operation in equation (B.2) is the element by element division given by MATLAB's `./` operator. To enhance the contrast further, logarithms of the intensity given by $[\mathbf{I}_{\text{norm}}]$ are often taken. The +1 was simply added to every pixel to avoid division by zero and had the effect of uniformly increasing the brightness by 1/255, so was trivial. In our images, the logarithm of $1/[\mathbf{I}_{\text{norm}}]$ was actually found to yield the best results after some experimentation, and was used for the basis of our water profile detection. A comparison between edge detection capabilities when using $\log\left(1/[\mathbf{I}_{\text{norm}}]\right)$ and that given by equation (B.2) is demonstrated in Figure B.7.

The log-normalised grayscale images were further processed by thresholding the pixel values at 50% and converting them to binary images (Figure B.6, (d)). From this stage, the image processing is similar to that used to detect the edges for defining the coordinate system. The coordinate system is used to remove areas not of interest, i.e. not on the side of the building. This was achieved by setting pixel values to zero. Finally, holes were filled and areas of the binary image with pixel value of 1 were removed if their joined area was less than 2000 pixels. From the resulting image (Figure B.6, (f)) the boundaries could be extracted using the `bwboundaries` function in MATLAB.

In order to plot water surfaces, it is helpful to have arrays which are square so that the values are always sampled at the same positions. Edge detection does not always

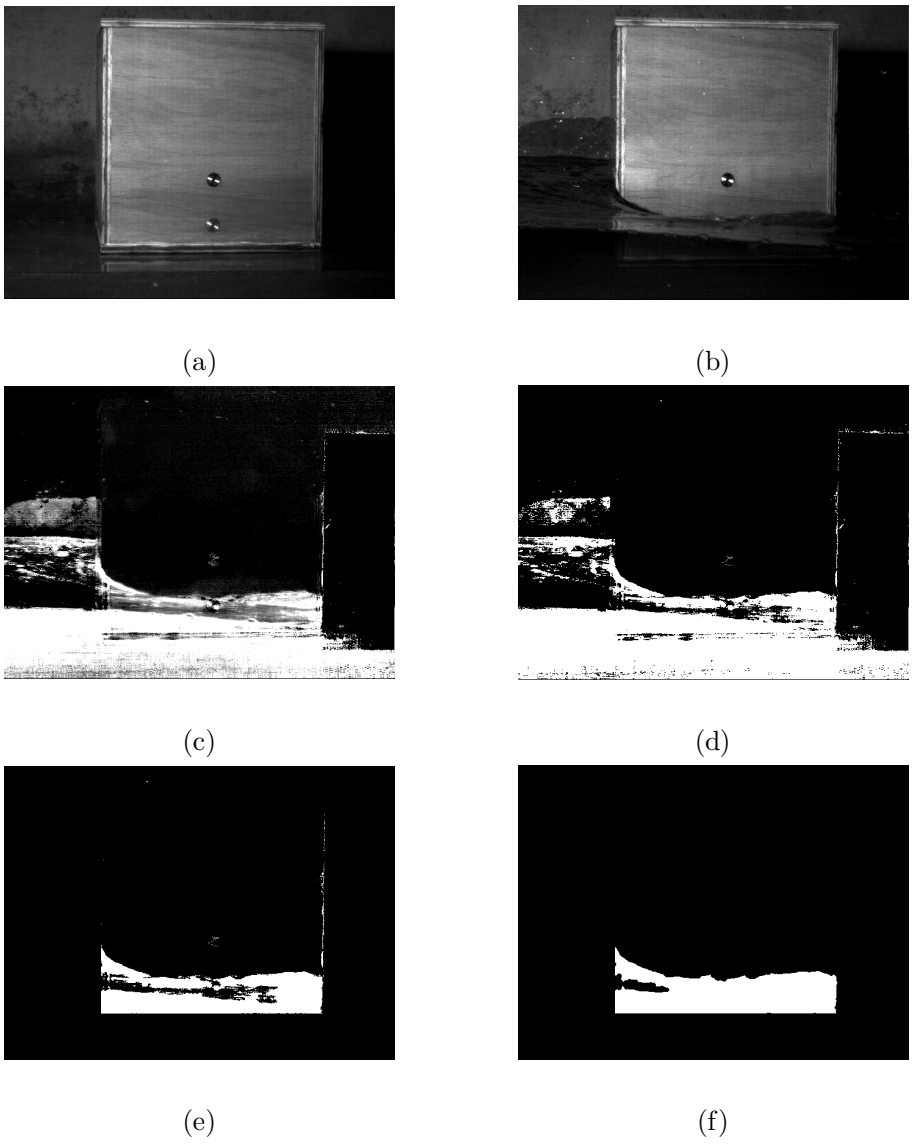

Figure B.6: *Steps taken in processing image to retrieve water profile information.* (a) *Average initial image,*[**A**], (b) *image from which to recover water profile,*[**I**], (c) $\log\left(\frac{[\mathbf{A}]+1}{[\mathbf{I}]+1}\right)$, (d) *black and white image produced by threshold at 50%* (e) *areas outside the coordinate system set to zero, black holes filled in,* (f) *white areas less than 2000 pixels removed.*

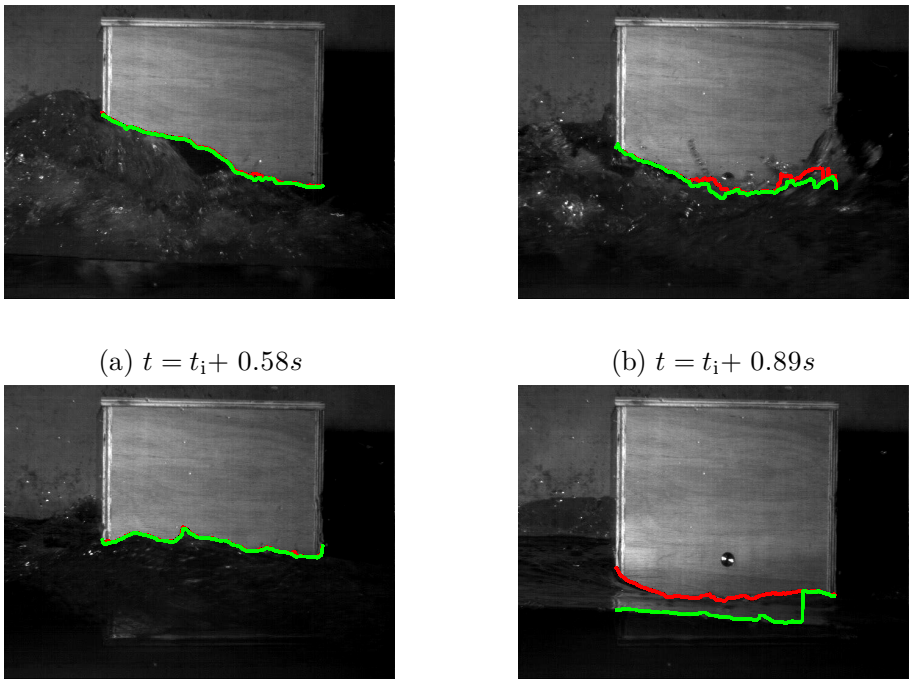

(a) $t = t_{\mathrm{i}} + 0.58s$ (b) $t = t_{\mathrm{i}} + 0.89s$

(c) $t = t_{\mathrm{i}} + 1.22s$ (d) $t = t_{\mathrm{i}} + 2.51s$

Figure B.7: *Detected water surface profiles. Test 081128-13. Red line* $\log(1/[\mathbf{I}_{\mathrm{norm}}])$ *edge detection methodology, Green line* $[\mathbf{I}_{\mathrm{norm}}]$ *methodology*

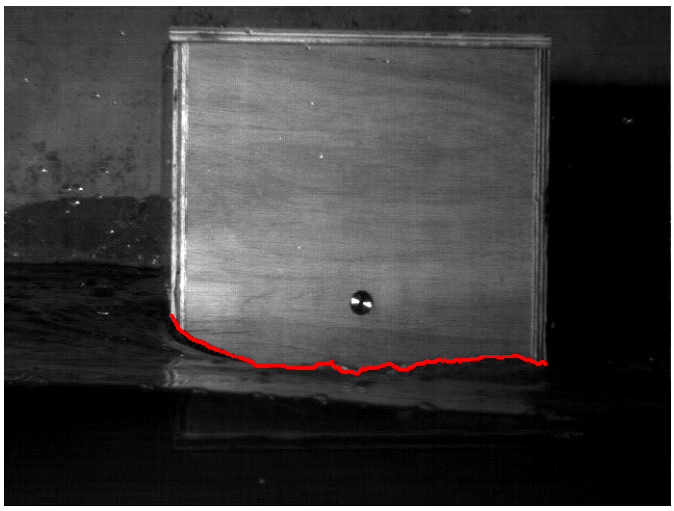

Figure B.8: *Detected water surface profile. Test 081128-13,* $t = t_{\mathrm{i}} + 2.51s$.

return a value for every position of x, and additionally distance per pixel varies with position, due to the projected view of the image and corrective transform performed on the data.

For this reason the boundary edge must be sampled at equally spaced values of x, and the corresponding z values interpolated from this. The water profile is sampled at 1mm intervals between $x = 1$mm and $x = 300$mm (for the 300mm wide building) to ensure regularity in the surface array and interpolated based upon this.

Figure B.7 shows the edge detection is fairly robust, but at times suffers from problems due to reflections of the building in the water, as well as the strong edge of the waterline on the glass occasionally preferred by the algorithm to the waterline of interest (shown in Figure B.7, (d)). These issues are usually momentary and occur as the water level recedes, so the edge transition is usually fairly stable with time. These anomalies happen more frequently using the $[\mathbf{I}_{\text{norm}}]$ detection methodology. For this reason the alternative $\log(1/[\mathbf{I}_{\text{norm}}])$ based detection was chosen and the superior profile in Figure B.7, (d), is shown clearer in Figure B.8. A filtering process has been applied in the time domain to detect and remove data corresponding to the obvious occasions when the wrong edge is detected, and these data are treated as outliers.

Difficulties with identification of the erroneous edge detection arise when automating the filtering process. The data points associated with the erroneous edge form clusters in the data, making them difficult to filter directly with say, a moving average type filter. This point is illustrated in Figures B.9 and B.10 where the outliers can be quite clearly seen with the naked eye. In order to filter the surface profile data in the time domain, these erroneous points must be detected and removed using non-standard techniques and a custom filter algorithm was written.

For standard outlier detection, the data can be assumed to be normally distributed about a mean value and an outlier can be classified based on being greater than a threshold number of standard deviations from the mean. For time series data, this mean is usually assumed to be the underlying function. The key point is that the data are assumed to be equally distributed above and below the mean underlying function. Robust time-domain filtering methods exist which assign a lower weighting to values which lie further from this mean and perform a regression based on

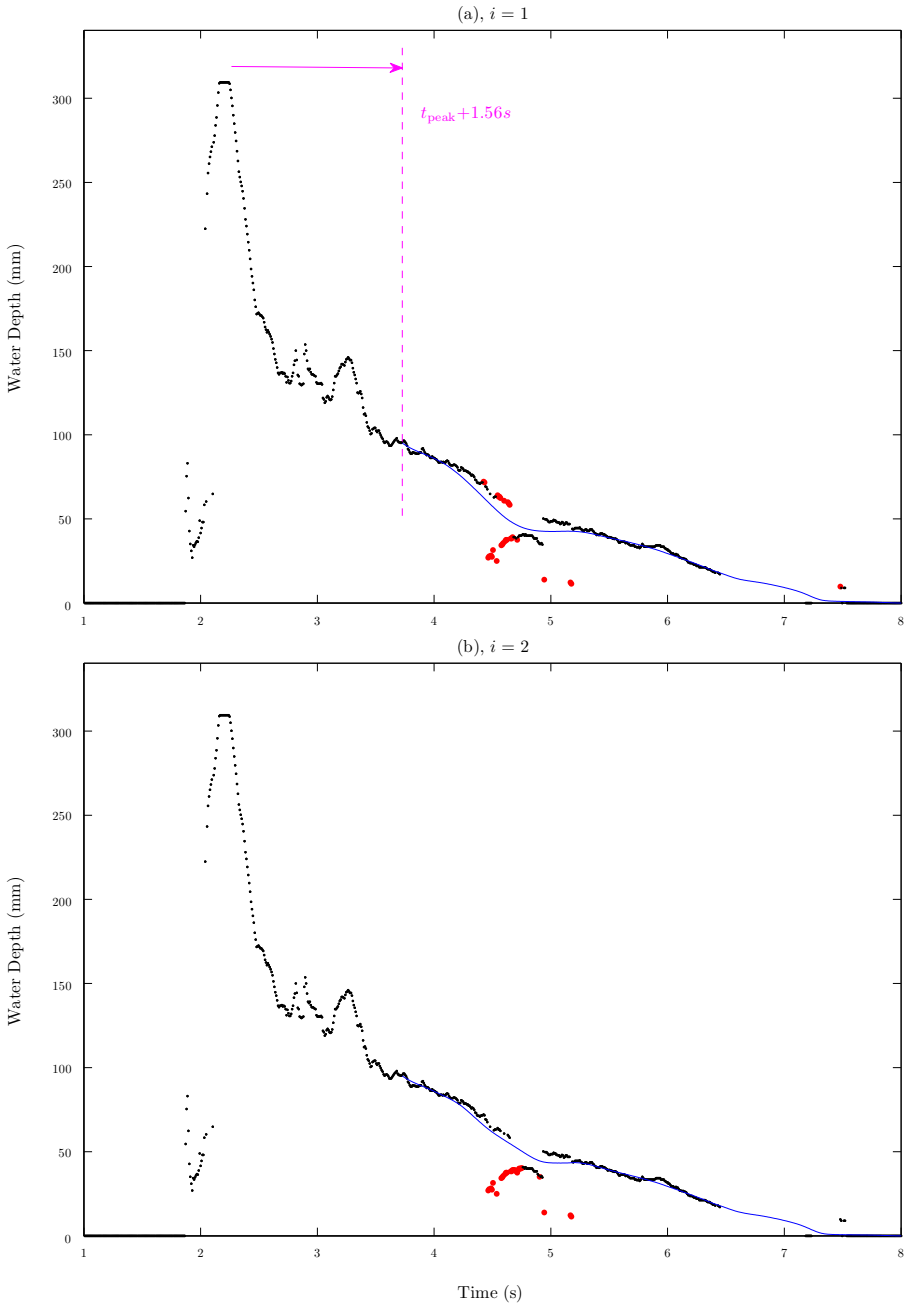

Figure B.9: *Outlier detection profile plots with time, test 081128-13 at position 15mm from the front face.* (a) *first iteration candidate outliers* (red) *and the cut off time* ($t_{peak} + 1.56s$) *below which outliers are not removed (magenta).* (b) *second iteration candidate outliers.*

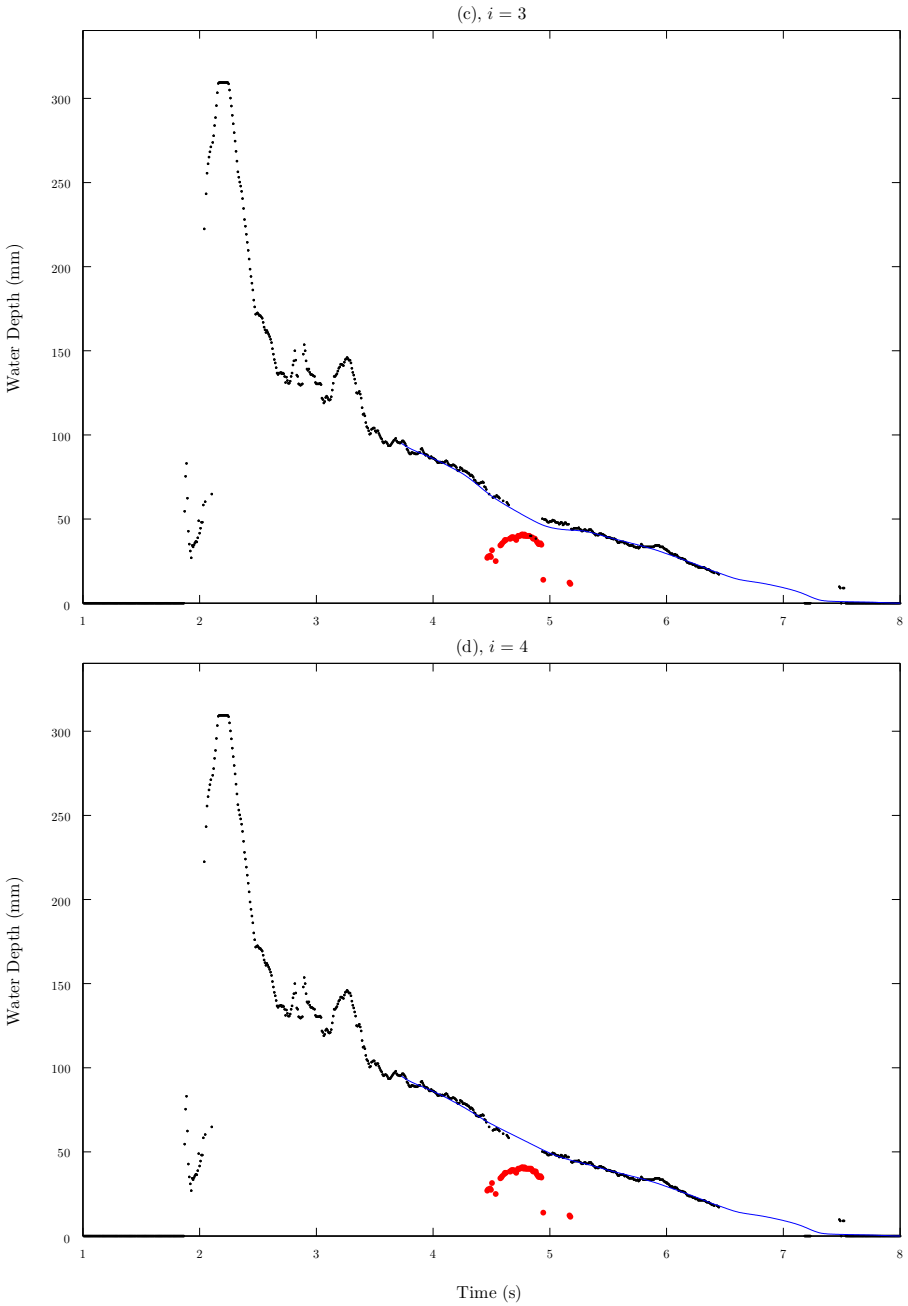

Figure B.10: *Outlier detection profile plots with time, test 081128-13 at position 15mm from the front face.* (c) *third iteration.* (d) *by the fourth iteration, all outliers detected.*

this. As seen in figure, B.9, (a), the data are not the same case, and the outliers are not equally distributed above and below. A cluster of data associated with the erroneous edge detection can be clearly seen, crucially lying below the mean underlying function. Another issue is the high variance of the data in the vicinity of the peak. In order to prevent points being detected as outliers in this region, data before the time of peak (t_{peak}) + 1.56 seconds are excluded from outlier detection and standard deviation calculation. This time increment is 15% of the data length. Applying a first order local weighted linear least squares regression (lowess) filter to the full data with a span equal to the 10% length of the data, produces the blue curve in Figure B.9, (a). It should be noted, that this is not used to fit the whole time series as the peak is not represented well. Its long span enables a good fit in the region of the outliers for use in their detection and correction.

The points coloured red in Figure B.9, (a), have been identified as candidate outliers based on their location being further than two standard deviations from the blue curve (95% of points are expected to be within 2σ), and with time greater than $t_{\text{peak}} + 1.56$s. The standard deviation is also calculated based on time greater than $t_{\text{peak}} + 1.56$s and is performed on the residuals. As expected, this curve is pulled towards the outliers and any direct evaluation of outliers based upon the standard deviation of the residuals will also classify some points which lie on the true curve as outliers. For this reason, the process has to be iterative. The next stage removes the candidate outliers detected in (a), and applies another lowess filter to the remaining data. This is the blue curve in Figure B.9, (b) and though still affected by some of the remaining outliers, it is appreciably closer to the true data than the curve in (a). The process is repeated and the whole data set (including the previously removed points) is analysed and points further than two standard deviations from the new curve are identified as red in (b). New outlier candidates are detected based on the new criterion and the process is repeated up to a maximum of ten iterations, or while there is a change in selected outliers. The final underlying curve, being a reasonably good fit in the later stages of the profiles, is then used to fill any gaps in the data produced by the removal of outliers and regions of poor edge detection. In this example, the fifth iteration of the sequence shown in Figure B.10 detects the same outliers as $i = 4$, and so the "while" criterion is invoked in the script and the outlier detector terminates before the maximum ten iterations are reached.

The algorithm converges because the standard deviation is recalculated each iter-

ation based on the original points and the new smoothed curve. The curve itself becomes closer to the unaffected data and so outliers become more pronounced (i.e., σ increases for each iteration until there is no change. It is relatively computationally expensive, but not prohibitively so. A single test (300 time profiles) usually computes in around a minute.

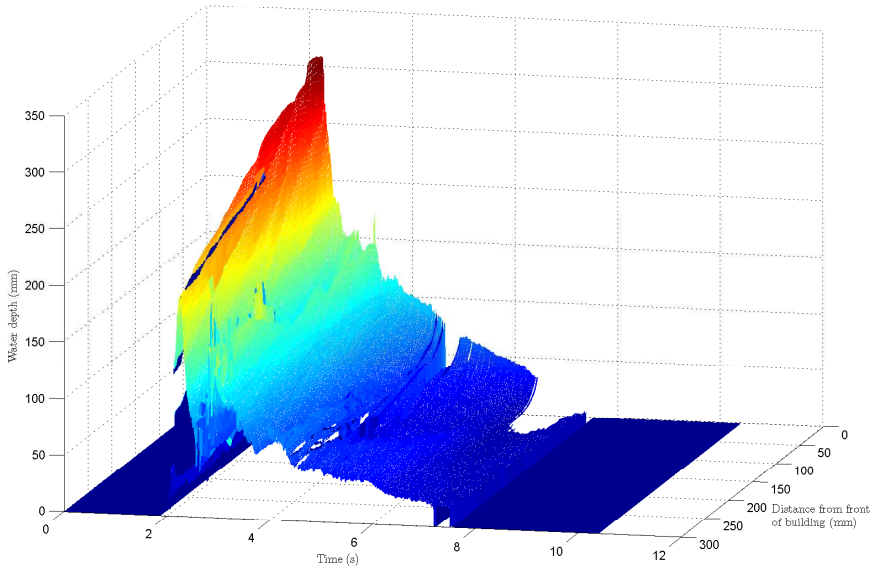

Figure B.11: *Unfiltered water profile plots with time. Test 081128-13.*

Once the erroneous points have been removed by outlier detection, a short-span (no more than five point) moving average-based filter can be applied to the data for each of the 300 x positions on the building front. The short-span is necessary so that the time response of the edge detection remains sharp. The results of the water profiles before outlier removal can be seen in Figure B.11 and the filtered water profiles with outlier removal and interpolation can be seen in Figure B.12 which used a version of Friedman's "Super Smoother" algorithm (modified by the author as an adaptive moving average smoother (Friedman, 1984)).

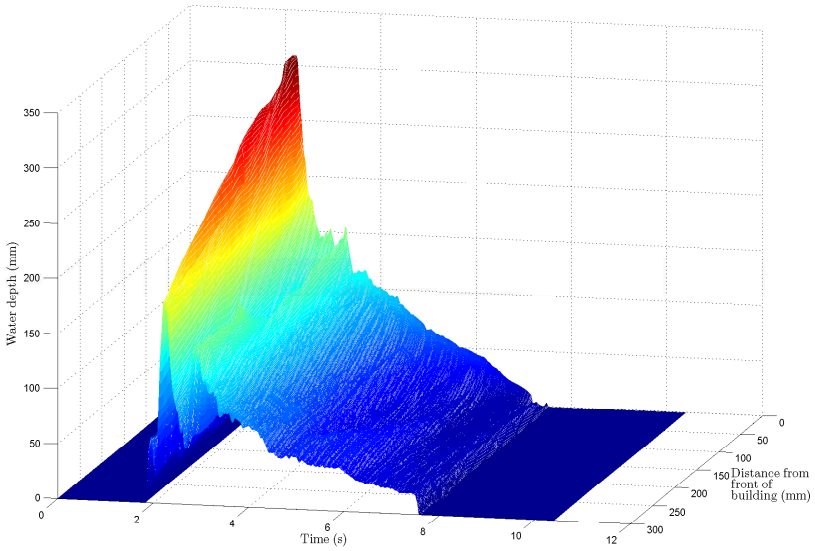

Figure B.12: *Filtered water profile plots with time. Test 081128-13.*

Appendix C

Experimental set-up drawings

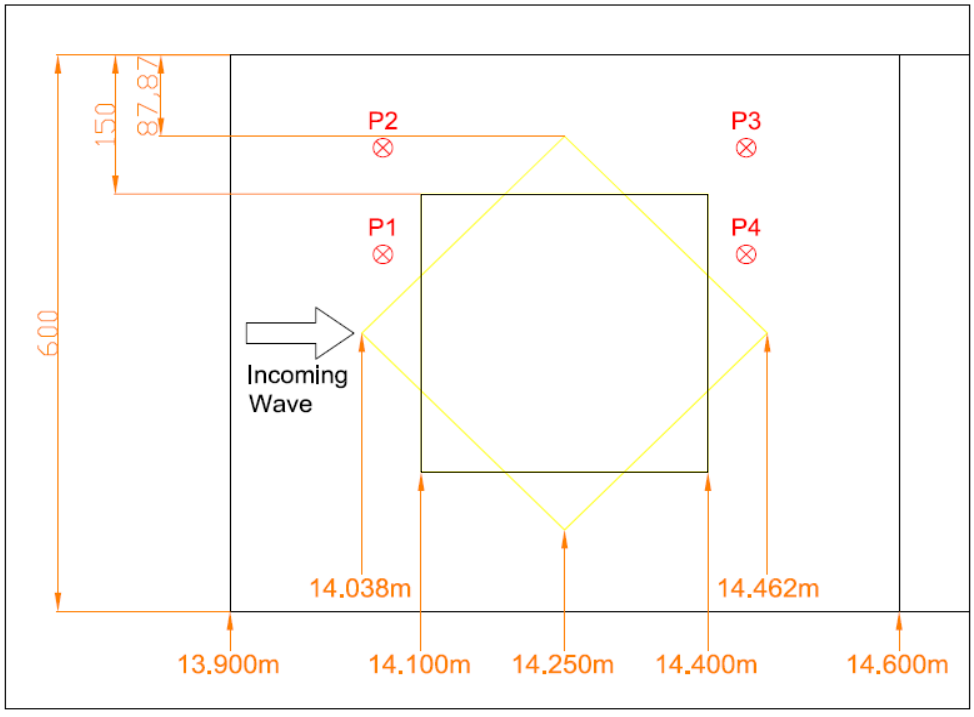

Figure C.1: *300mm wide pressure instrumented, location D1. Orientation = 90° and 45°. Showing location of velocity propeller meters.*

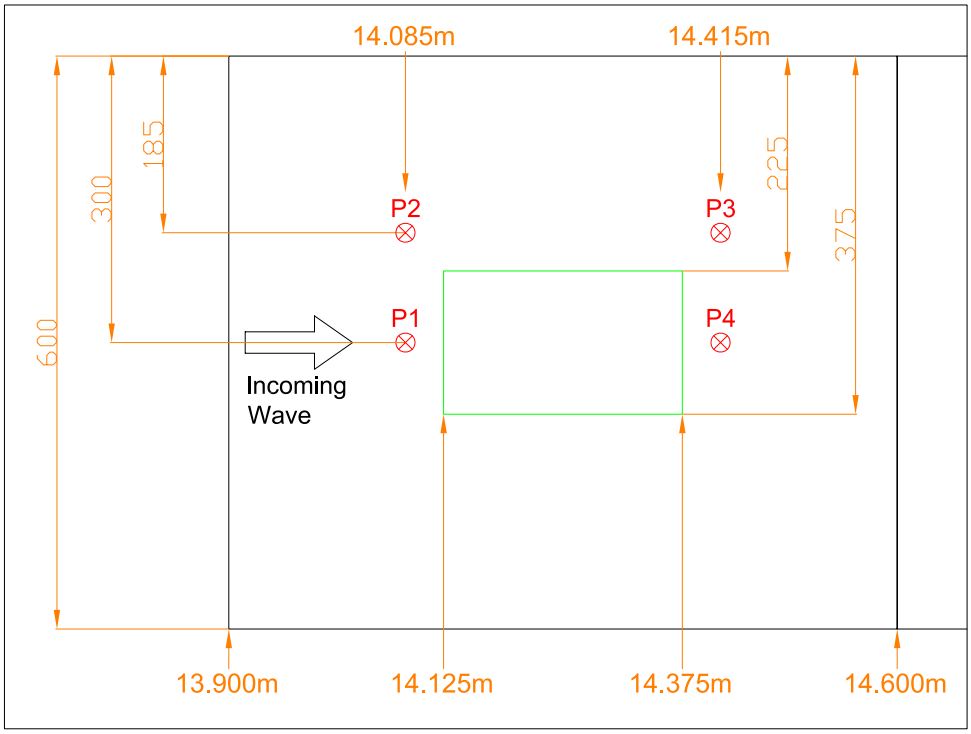

Figure C.2: *Narrow 150mm pressure instrumented structure, location D1. Orientation = 90°. Showing location of velocity propeller meters. D2 all x dimensions add 700mm. D3 all x dimensions add 1400mm*

Appendix D

Results from unsteady experiments

D.1 Offshore wave profile

D.1.1 Elevated waves

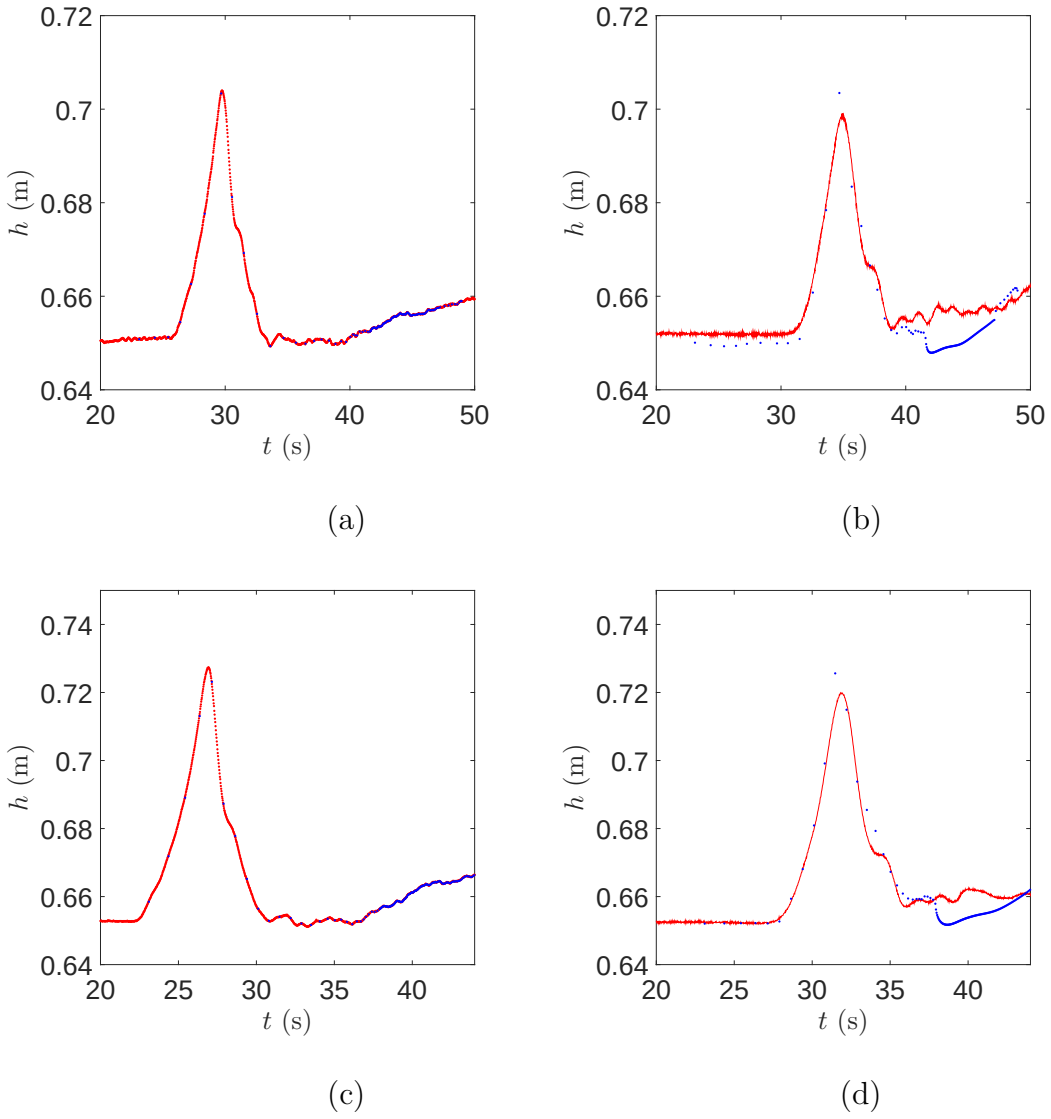

Figure D.1: *(a) Wave 138 water height at "Offshore 1" (1.3m from the tank), (b) Wave 138 water height at the "Toe" (15.2m from tank), (c) Wave 136 water height at "Offshore 1", (d) Wave 136 water height at the "Toe". ●, 1D numerical, ●, large-scale experimental.*

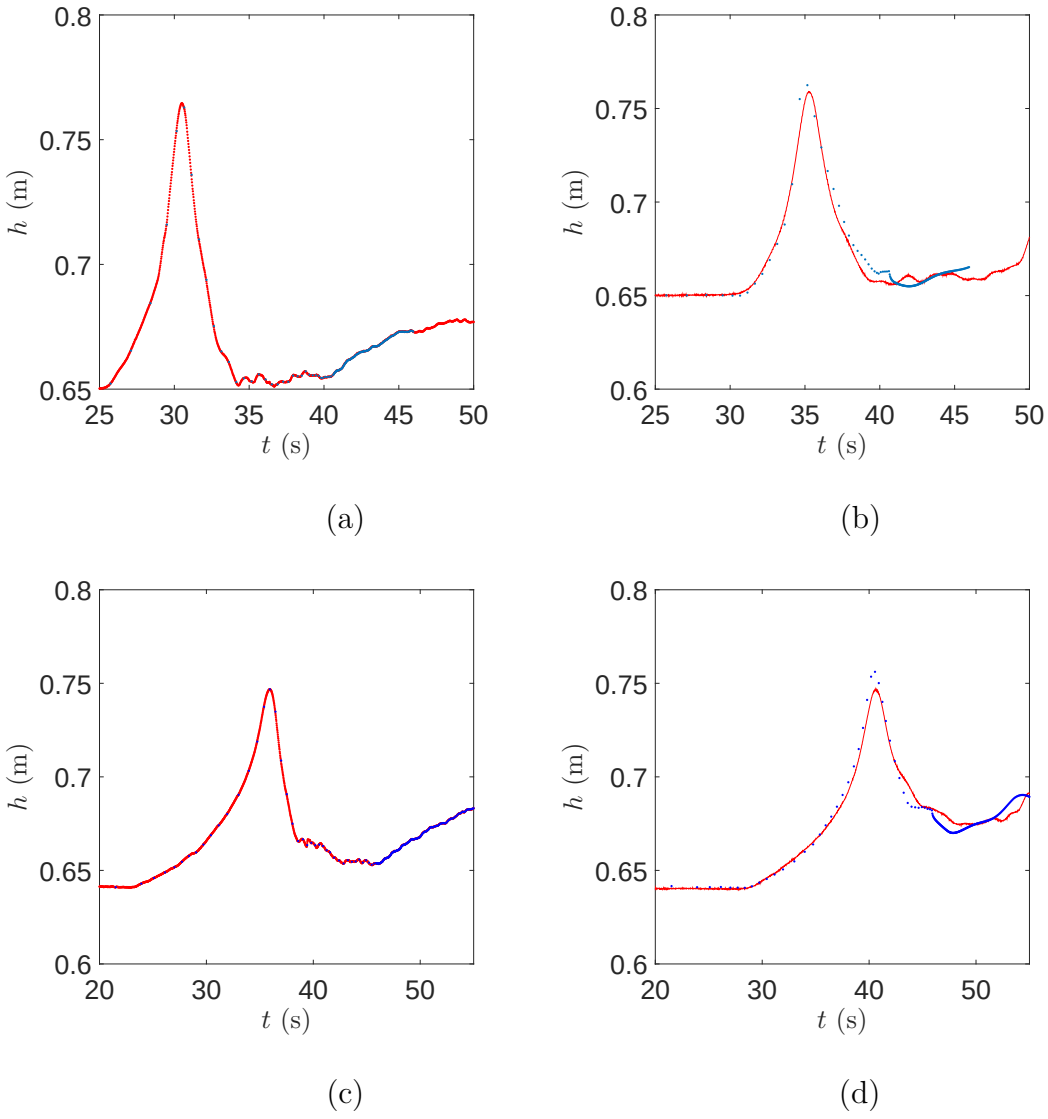

Figure D.2: *(a) Wave 135 water height at "Offshore 1" (1.3m from the tank), (b) Wave 135 water height at the "Toe" (15.2m from tank), (c) Wave 441 water height at "Offshore 1", (d) Wave 441 water height at the "Toe". ●, 1D numerical, ●, large-scale experimental.*

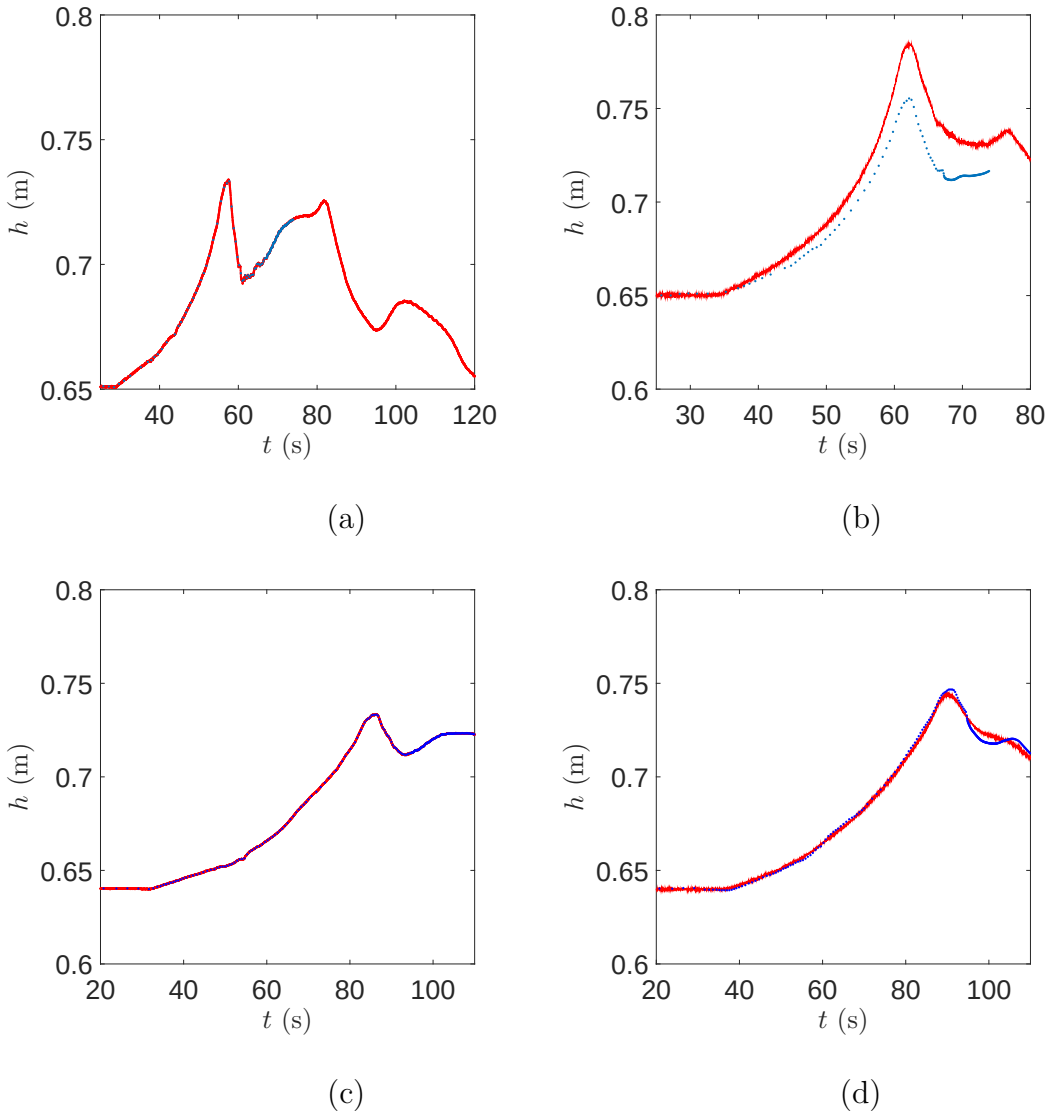

Figure D.3: *(a) Wave 415 water height at "Offshore 1" (1.3m from the tank), (b) Wave 415 water height at the "Toe" (15.2m from tank), (c) Wave 442 water height at "Offshore 1", (d) Wave 442 water height at the "Toe". ●, 1D numerical, ●, large-scale experimental.*

D.1.2 N-waves

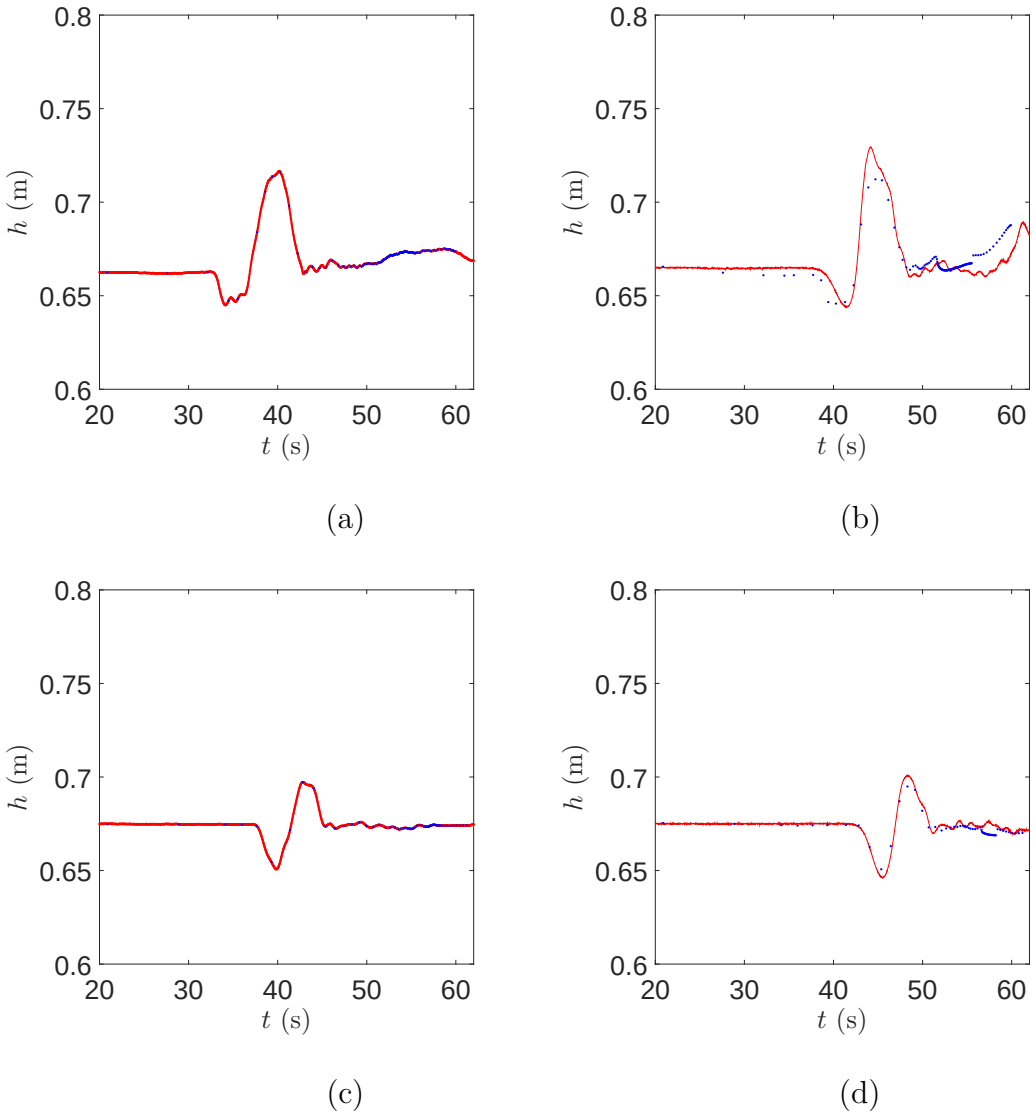

Figure D.4: *(a) Wave 130 water height at "Offshore 1" (1.3m from the tank), (b) Wave 130 water height at the "Toe" (15.2m from tank), (c) Wave 133 water height at "Offshore 1", (d) Wave 133 water height at the "Toe".* ●*, 1D numerical,* ●*, large-scale experimental.*

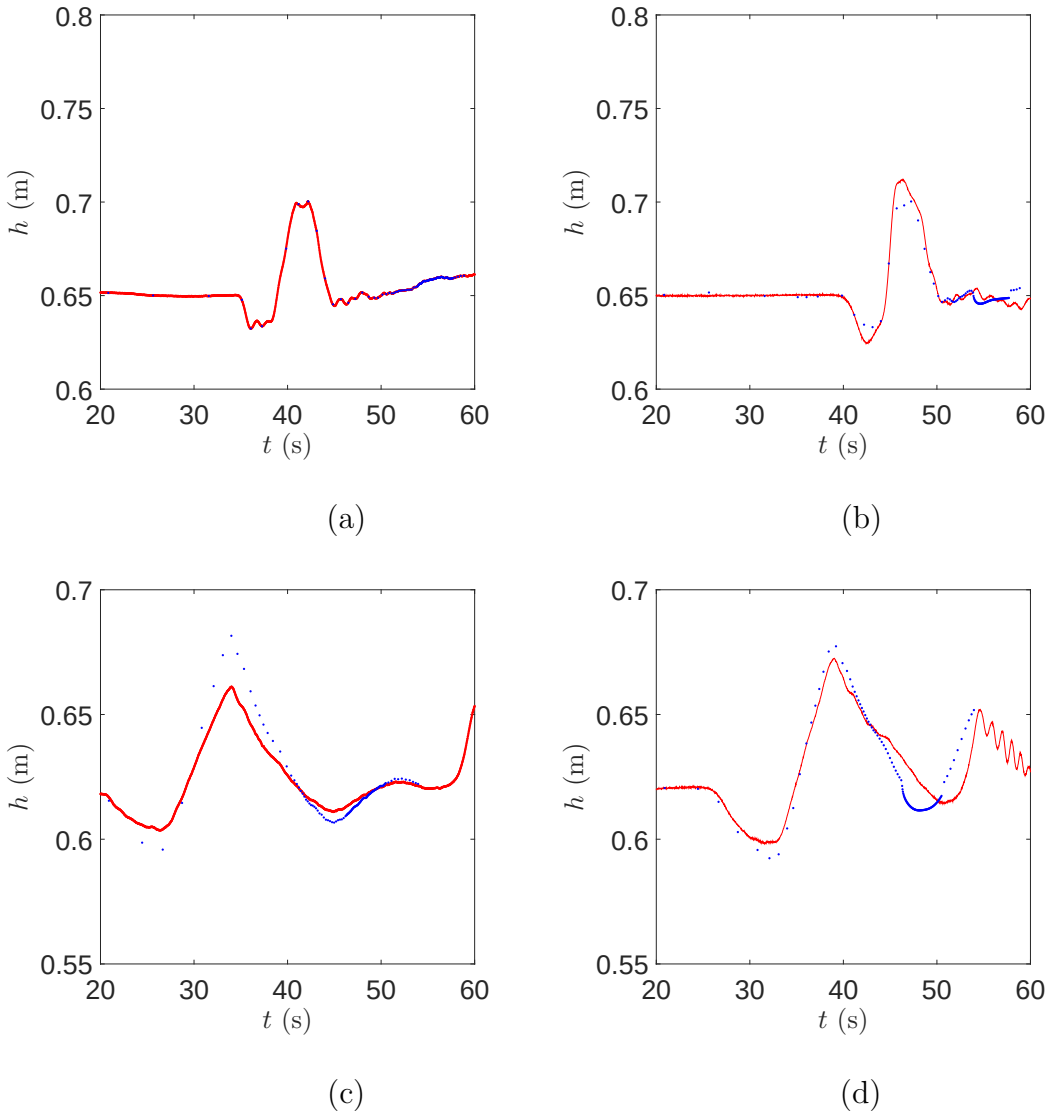

Figure D.5: *(a) Wave 113 water height at "Offshore 1" (1.3m from the tank), (b) Wave 113 water height at the "Toe" (15.2m from tank), (c) Wave 439 water height at "Offshore 1", (d) Wave 439 water height at the "Toe".* ●*, 1D numerical,* ●*, large-scale experimental.*

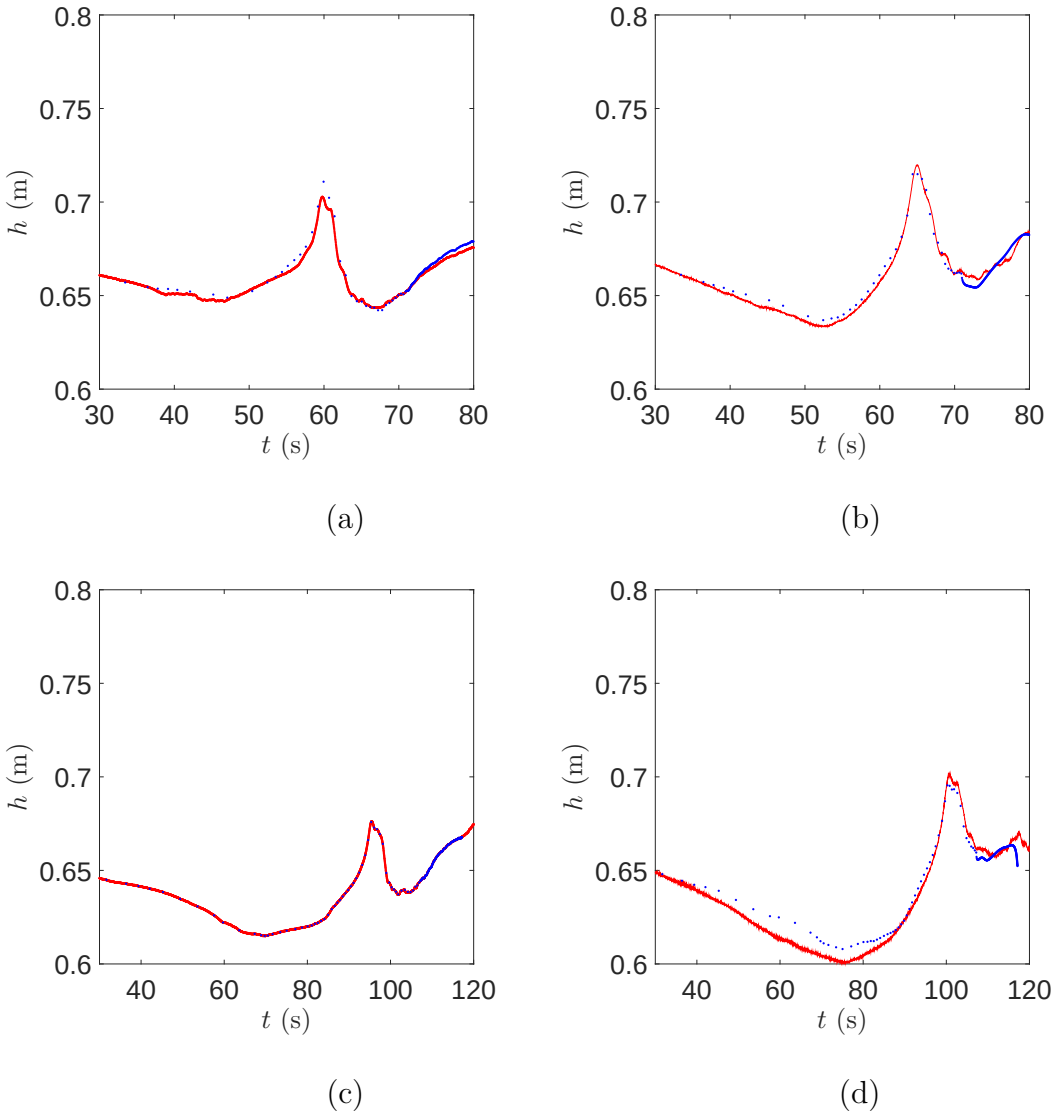

Figure D.6: *(a) Wave 435 water height at "Offshore 1" (1.3m from the tank), (b) Wave 435 water height at the "Toe" (15.2m from tank), (c) Wave 434 water height at "Offshore 1", (d) Wave 434 water height at the "Toe".* •*, 1D numerical,* •*, large-scale experimental.*

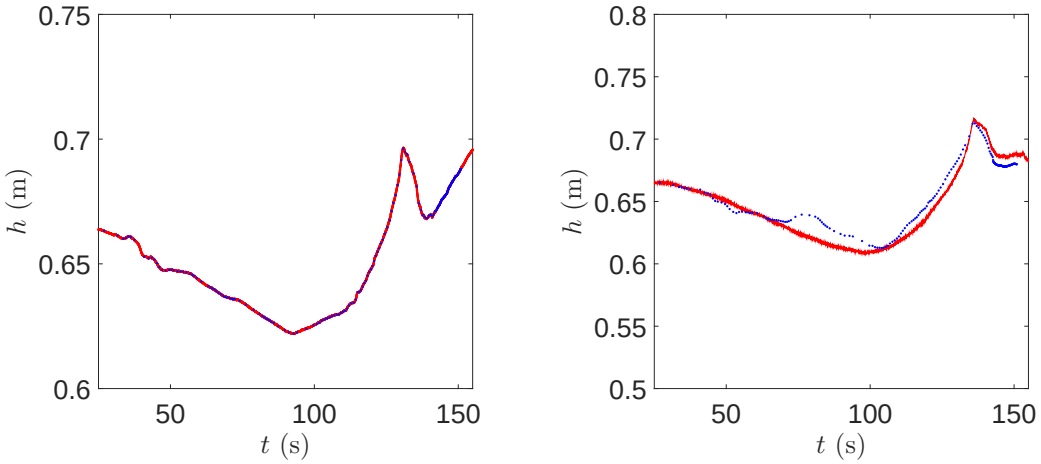

(a) (b)

Figure D.7: *(a) Wave 307 water height at "Offshore 1" (1.3m from the tank), (b) Wave 307 water height at the "Toe" (15.2m from tank).* •, *1D numerical,* •, *large-scale experimental.*

D.2 Nearshore velocities

D.2.1 Elevated waves

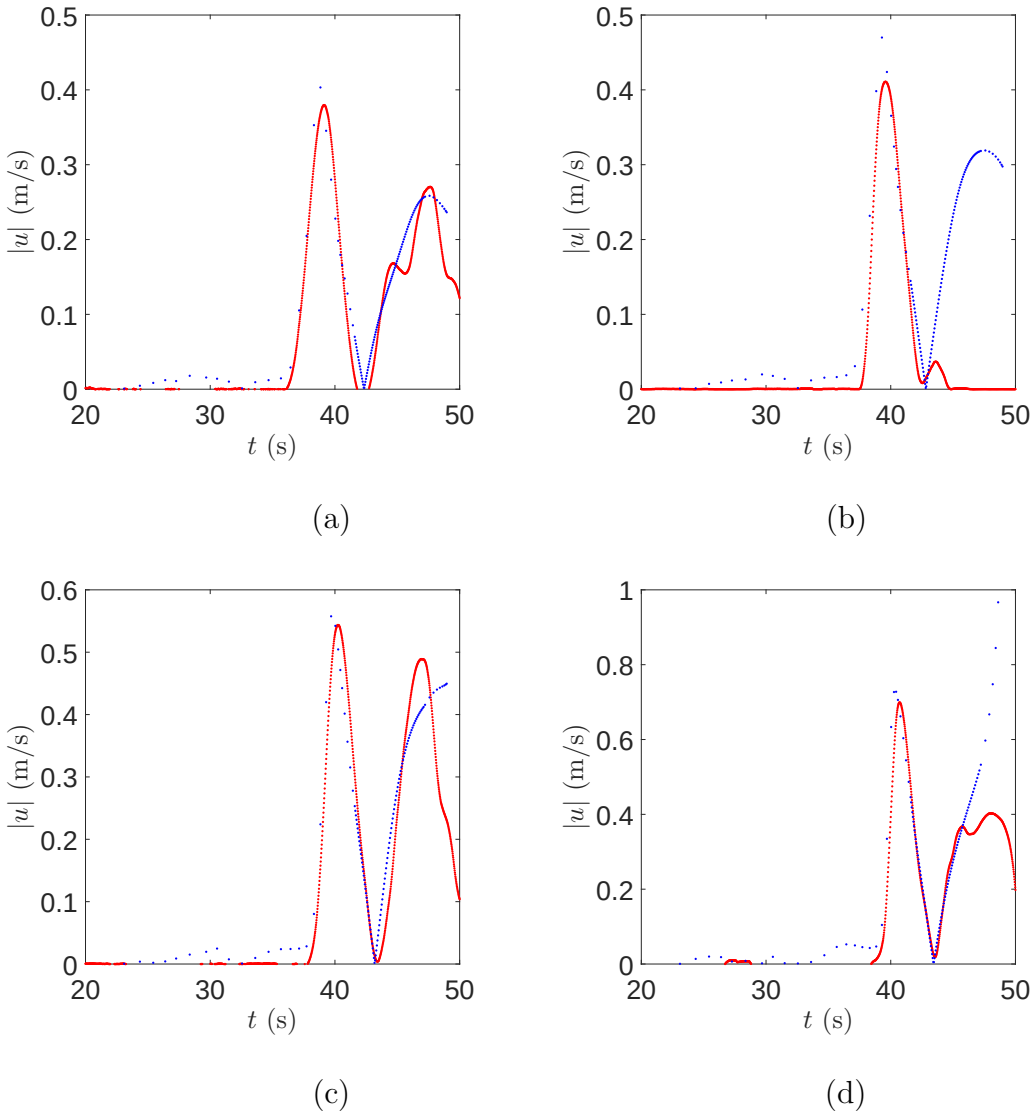

Figure D.8: *Wave 138. (a) Velocity at 9.50m, (b) 10.50m, (c) 11.50m, (d) 12.50m from the "Toe". ●, 1D numerical, ●, large-scale experimental.*

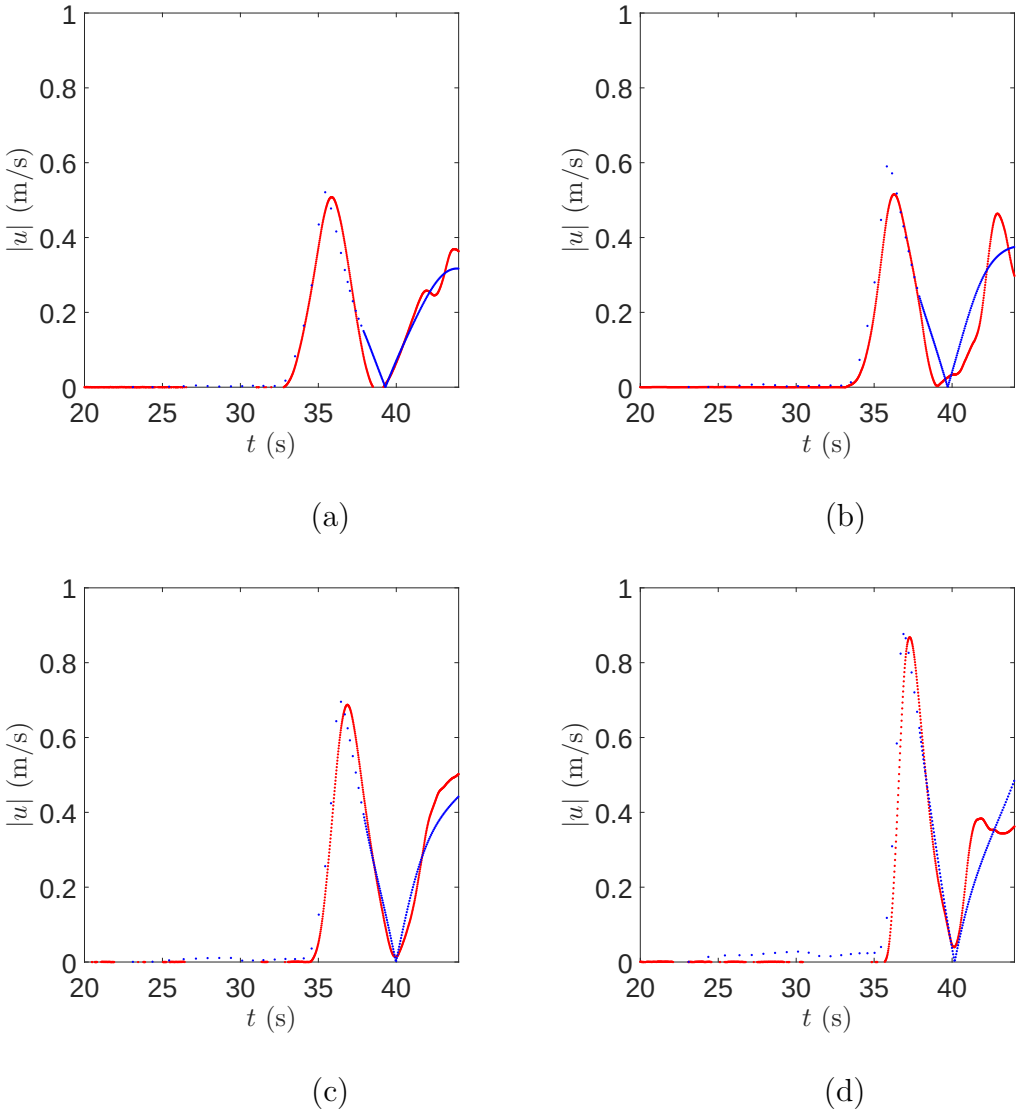

Figure D.9: *Wave 136. (a) Velocity at 9.50m, (b) 10.50m, (c) 11.50m, (d) 12.50m from the "Toe". ●, 1D numerical, ●, large-scale experimental.*

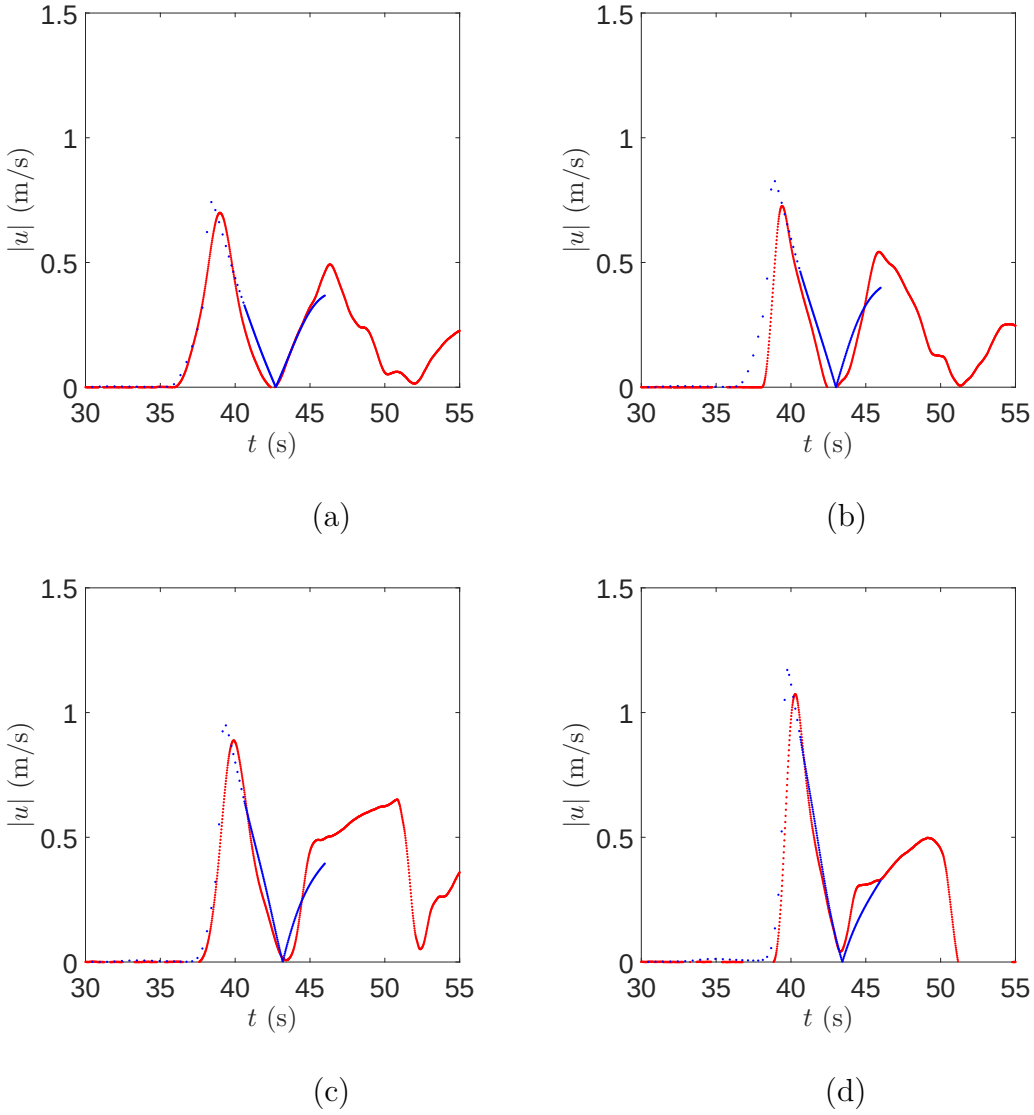

Figure D.10: *Wave 135. (a) Velocity at 9.50m, (b) 10.50m, (c) 11.50m, (d) 12.50m from the "Toe". ●, 1D numerical, ●, large-scale experimental.*

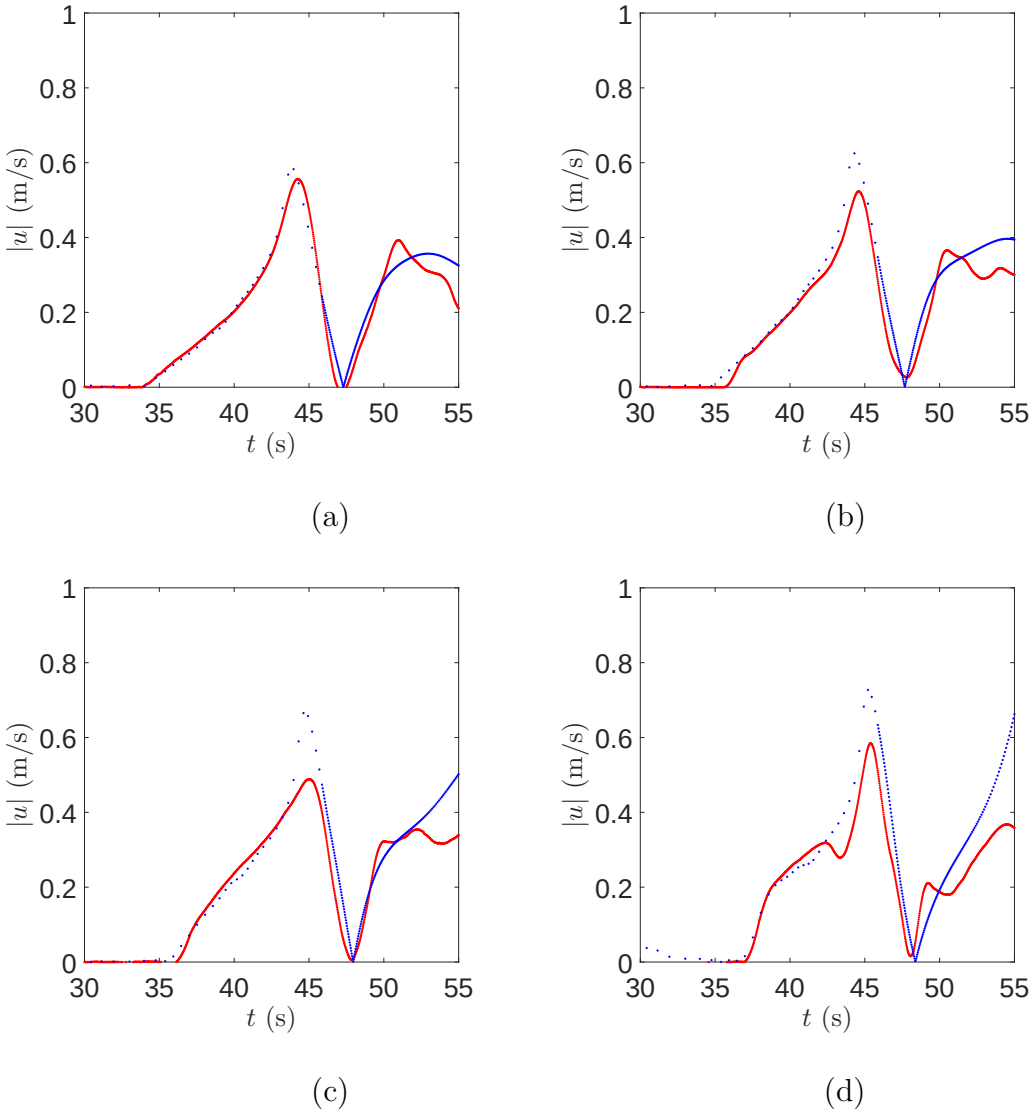

Figure D.11: *Wave 441. (a) Velocity at 9.50m, (b) 10.50m, (c) 11.50m, (d) 12.50m from the "Toe". ●, 1D numerical, ●, large-scale experimental.*

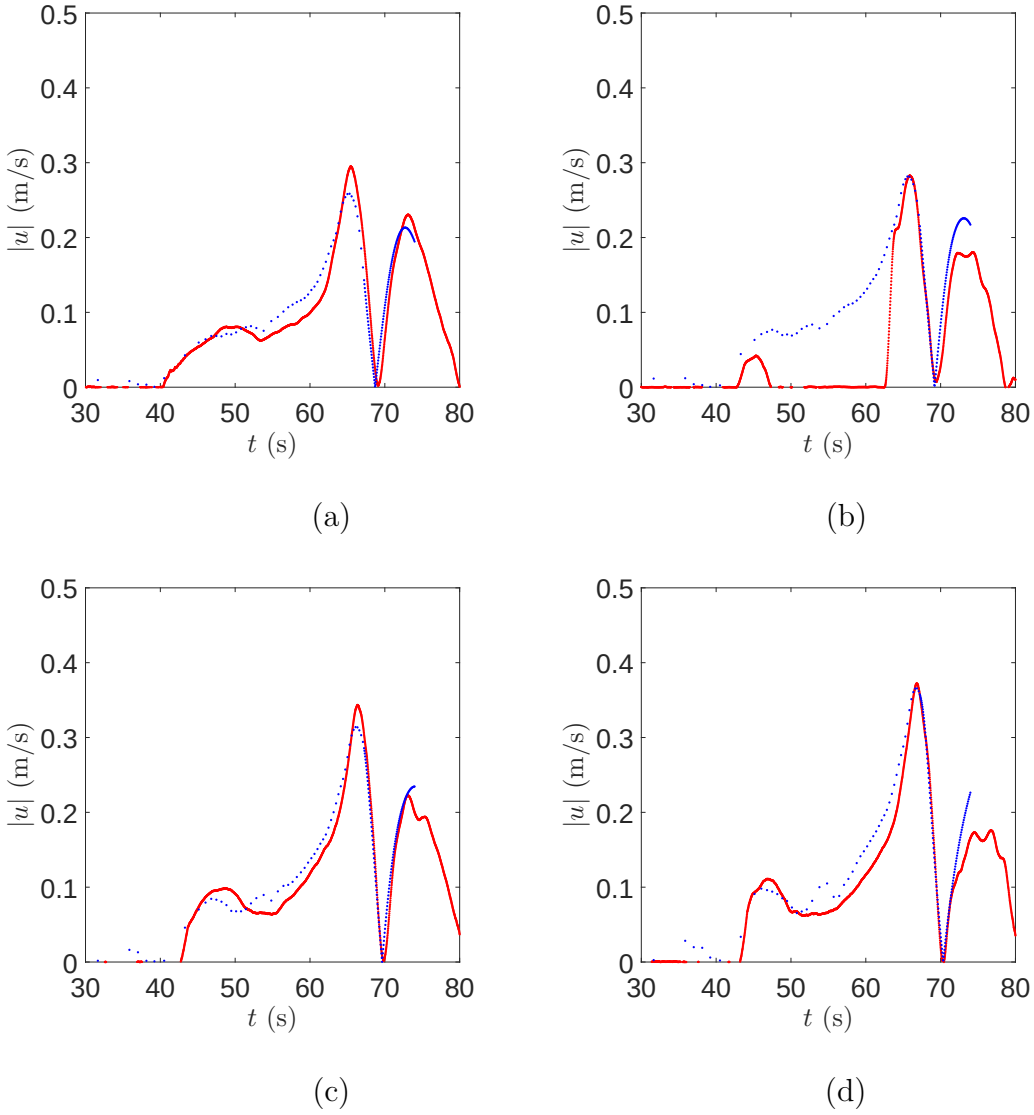

Figure D.12: *Wave 415. (a) Velocity at 9.50m, (b) 10.50m, (c) 11.50m, (d) 12.50m from the "Toe". ●, 1D numerical, ●, large-scale experimental.*

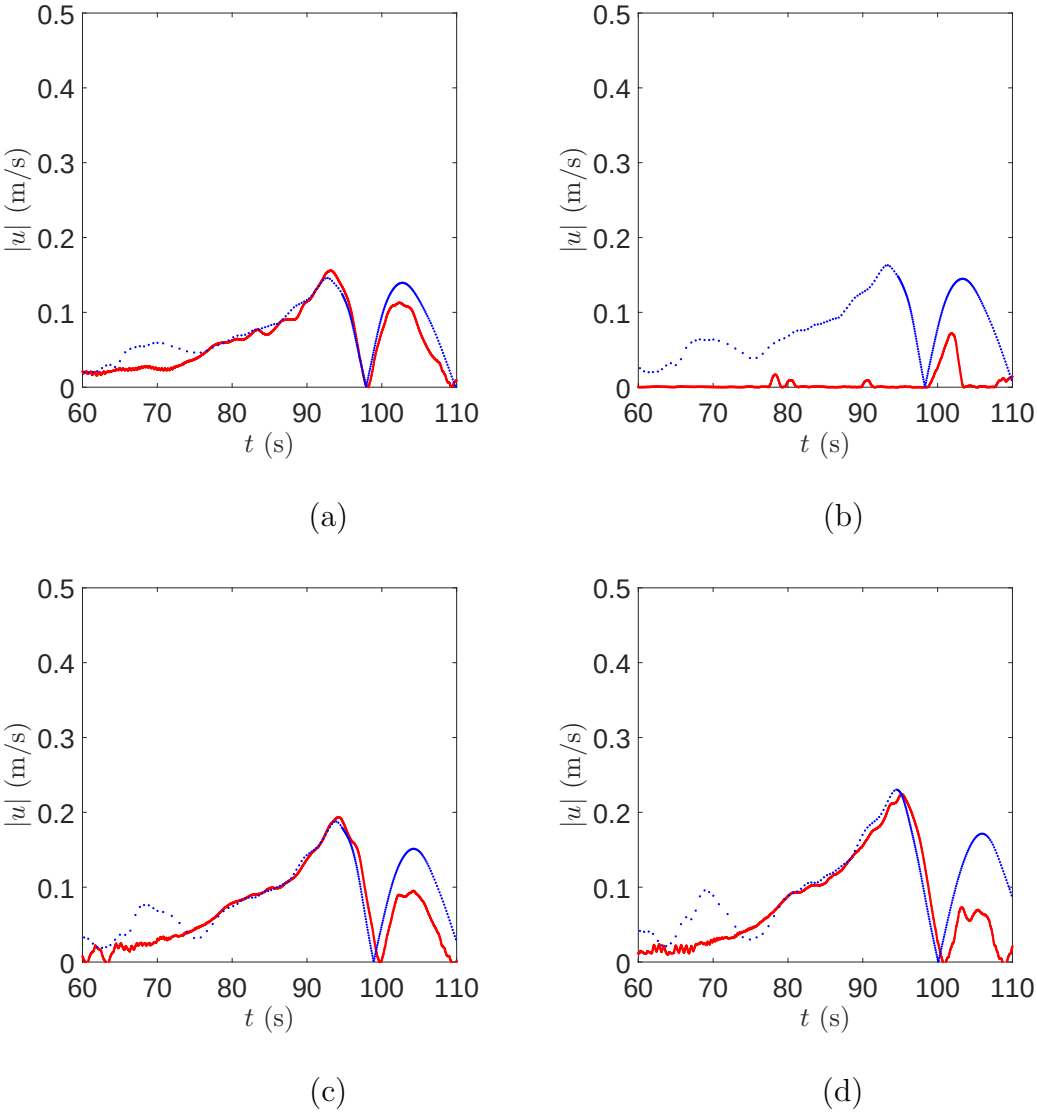

Figure D.13: *Wave 442. (a) Velocity at 9.50m, (b) 10.50m, (c) 11.50m, (d) 12.50m from the "Toe". ●, 1D numerical, ●, large-scale experimental.*

D.2.2 N-waves

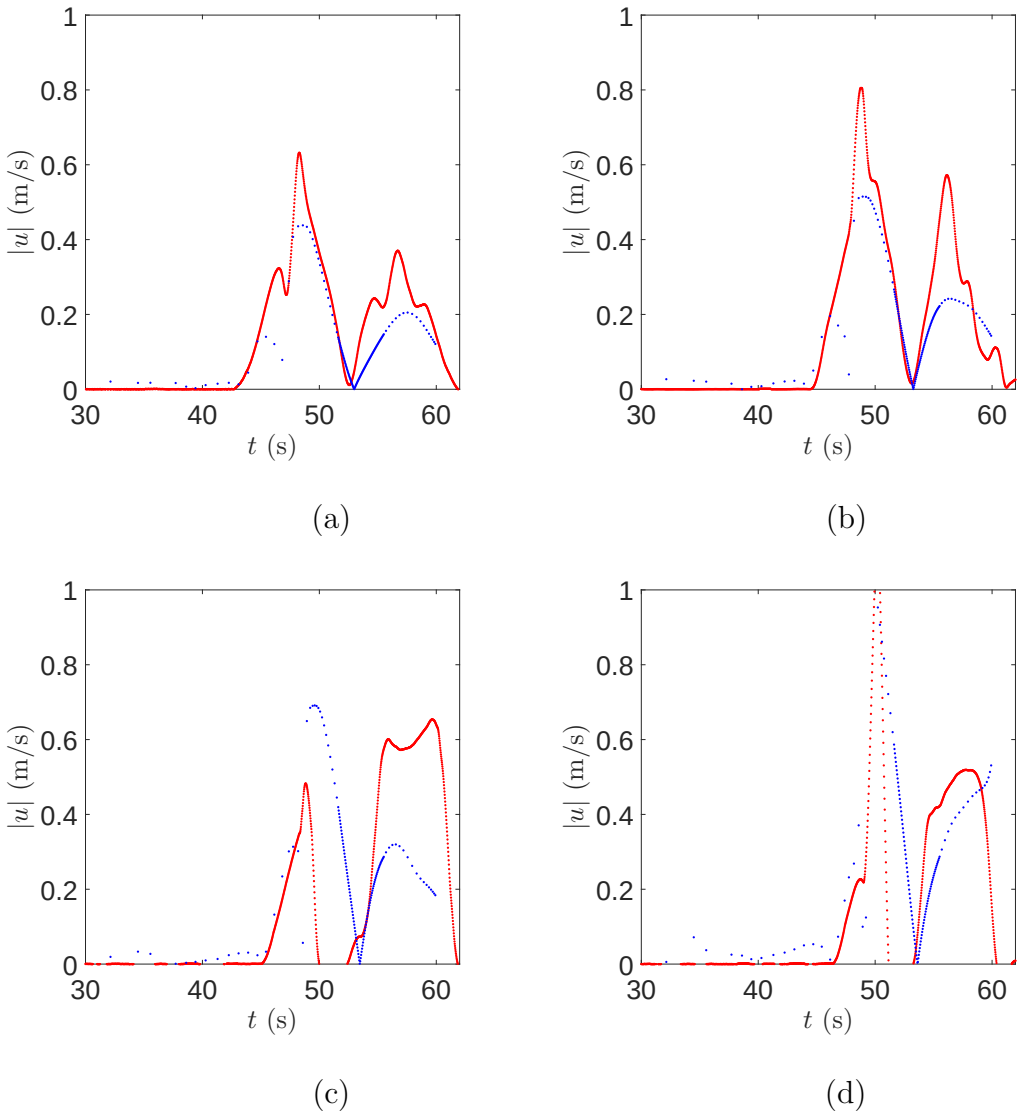

Figure D.14: *Wave 130. (a) Velocity at 9.50m, (b) 10.50m, (c) 11.50m, (d) 12.50m from the "Toe". ●, 1D numerical, ●, large-scale experimental.*

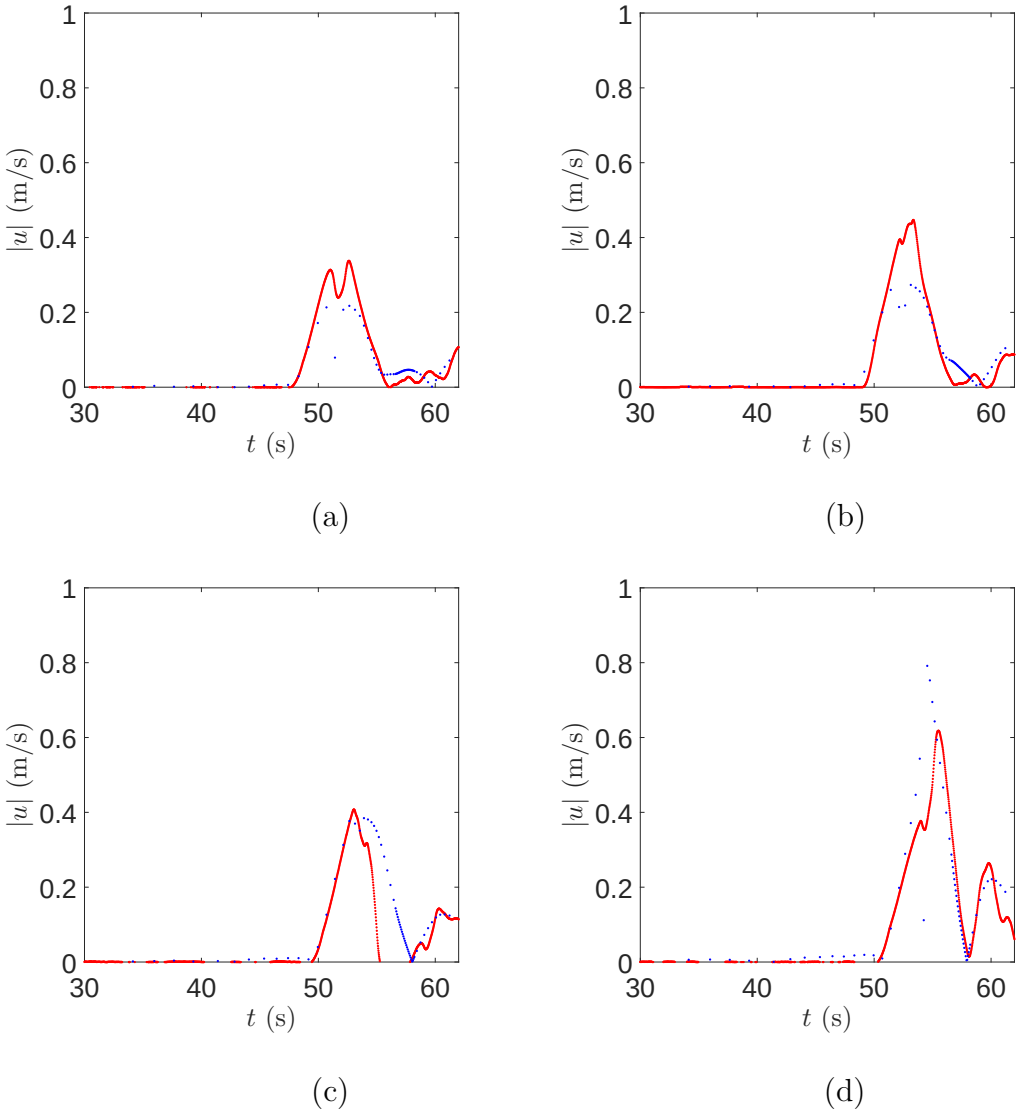

Figure D.15: *Wave 133. (a) Velocity at 9.50m, (b) 10.50m, (c) 11.50m, (d) 12.50m from the "Toe". ●, 1D numerical, ●, large-scale experimental.*

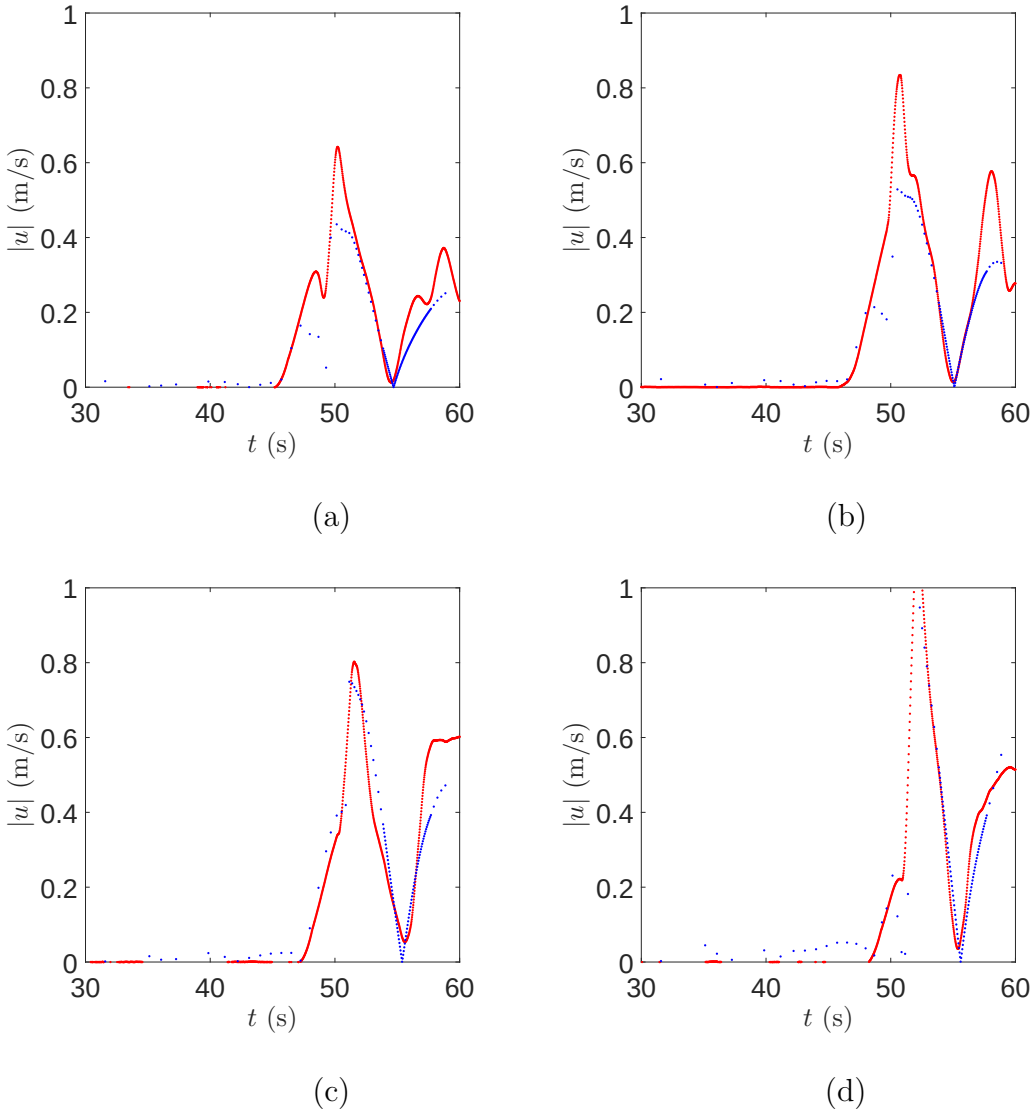

Figure D.16: *Wave 113. (a) Velocity at 9.50m, (b) 10.50m, (c) 11.50m, (d) 12.50m from the "Toe". ●, 1D numerical, ●, large-scale experimental.*

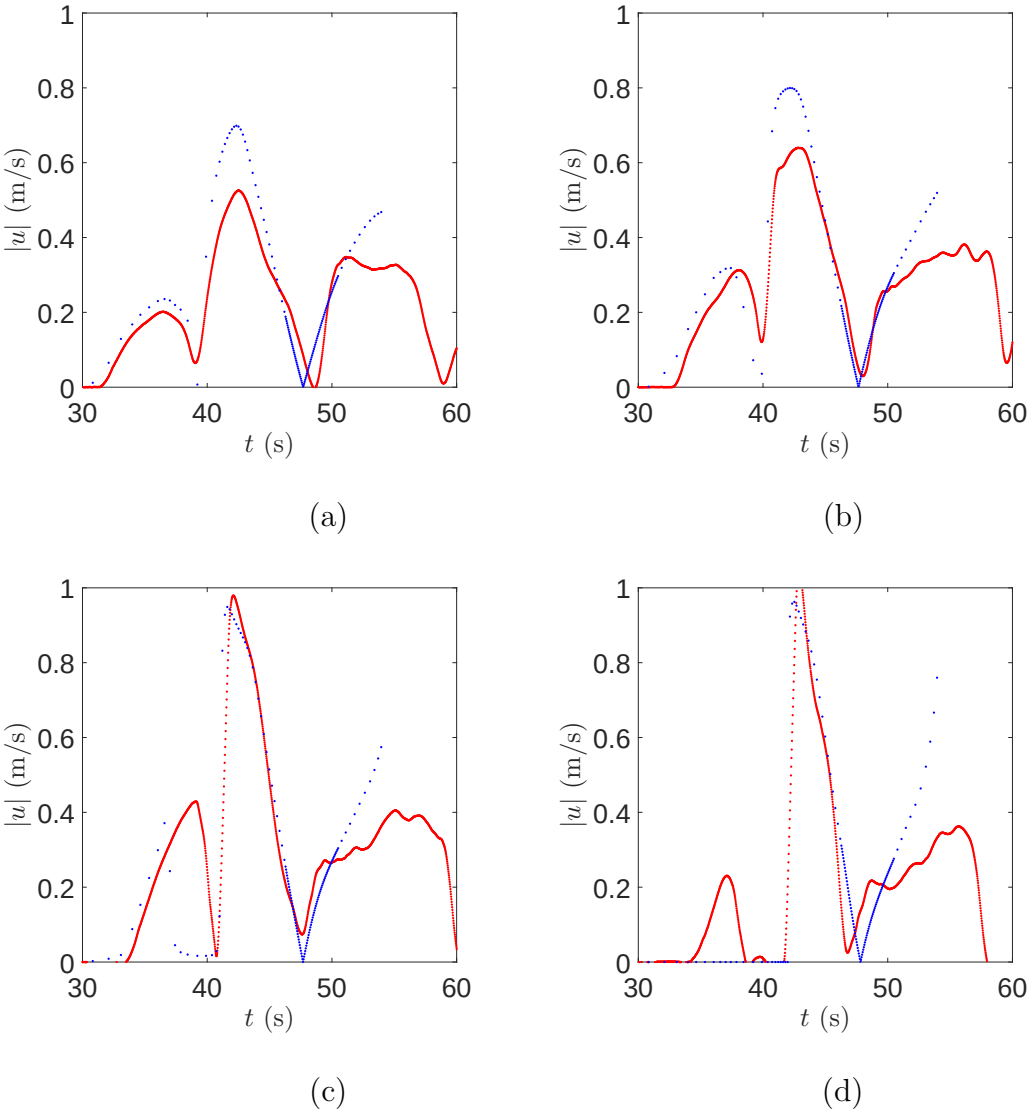

Figure D.17: *Wave 439. (a) Velocity at 9.50m, (b) 10.50m, (c) 11.50m, (d) 12.50m from the "Toe". ●, 1D numerical, ●, large-scale experimental.*

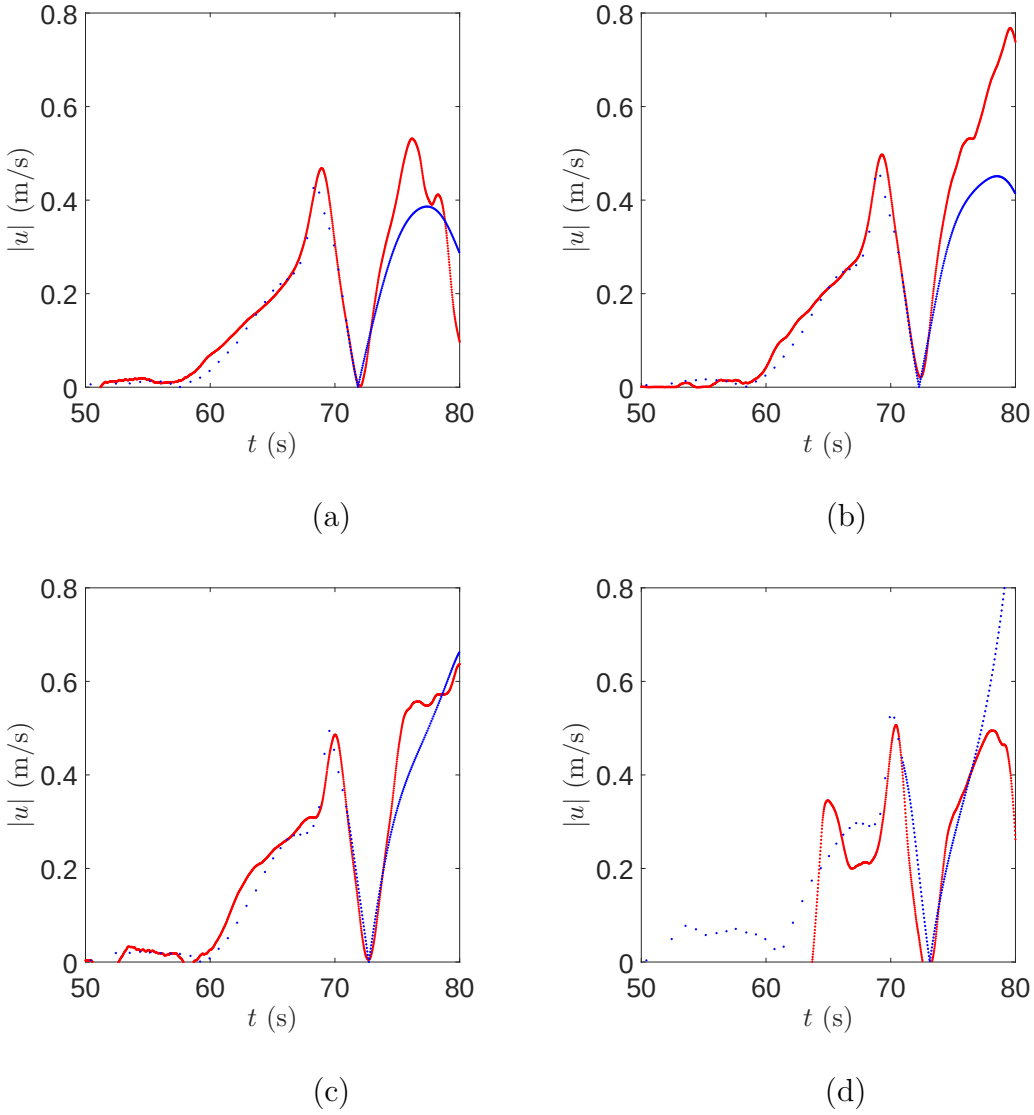

Figure D.18: *Wave 435. (a) Velocity at 9.50m, (b) 10.50m, (c) 11.50m, (d) 12.50m from the "Toe". ●, 1D numerical, ●, large-scale experimental.*

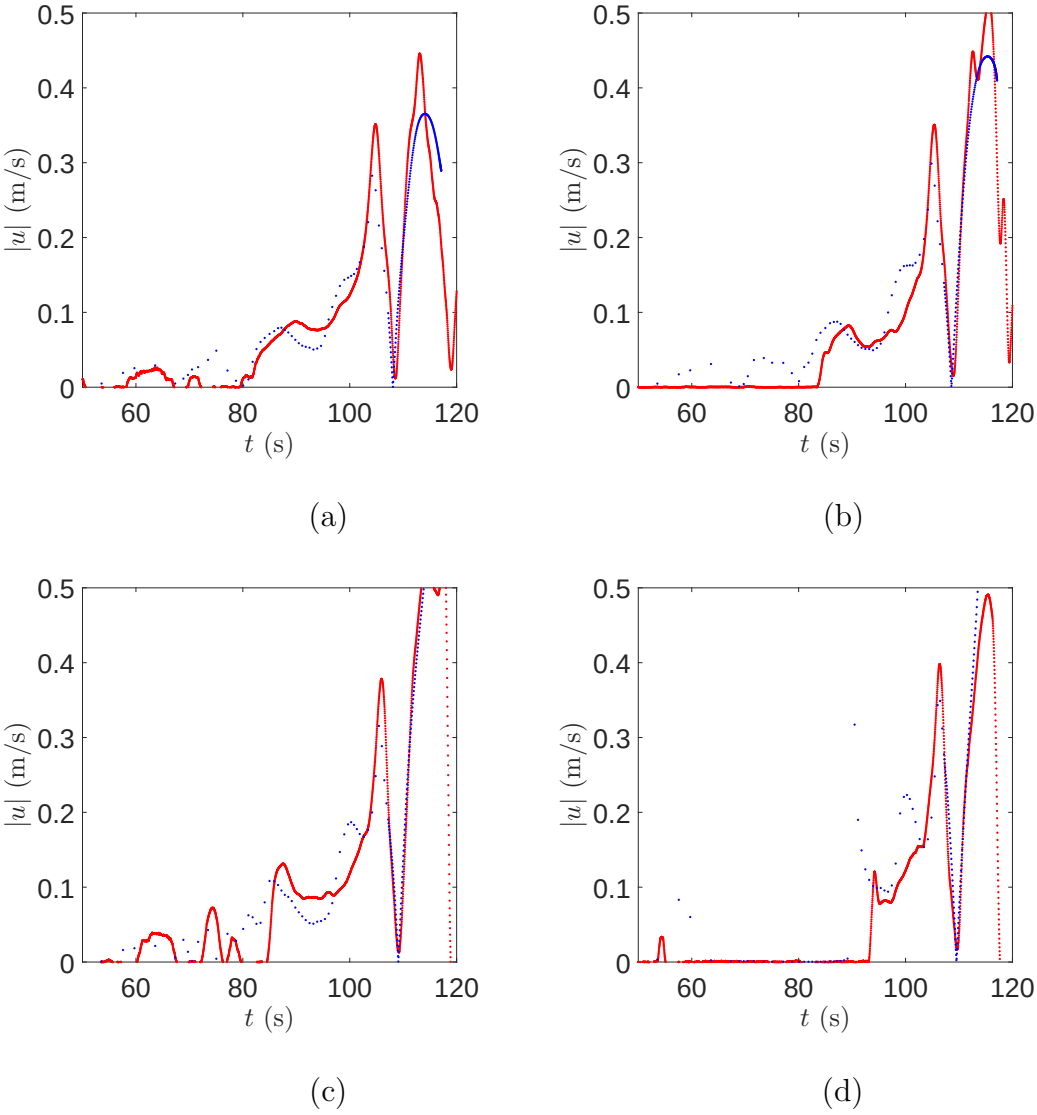

Figure D.19: *Wave 434. (a) Velocity at 9.50m, (b) 10.50m, (c) 11.50m, (d) 12.50m from the "Toe". ●, 1D numerical, ●, large-scale experimental.*

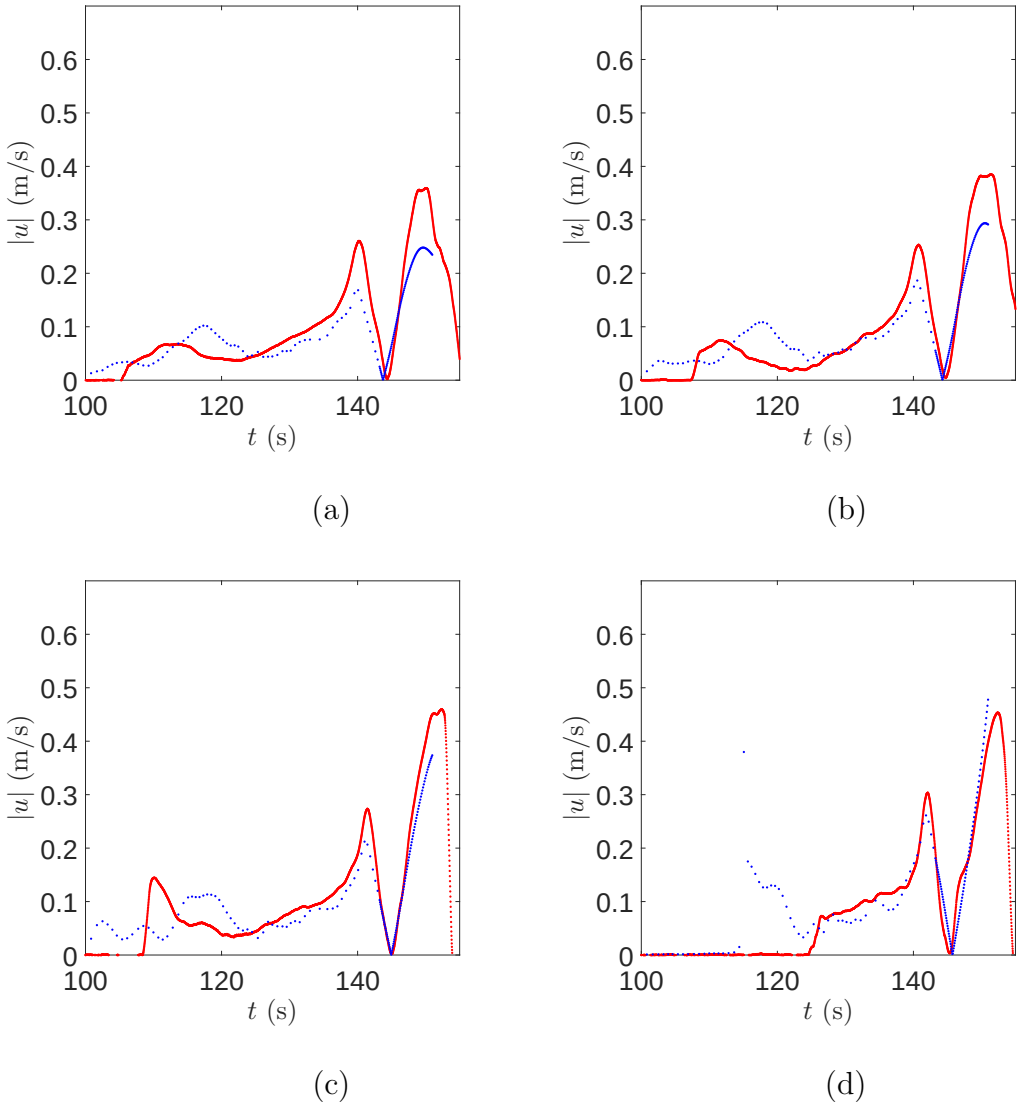

Figure D.20: *Wave 307. (a) Velocity at 9.50m, (b) 10.50m, (c) 11.50m, (d) 12.50m from the "Toe". •, 1D numerical, •, large-scale experimental.*

D.3 Onshore velocities - without building

D.3.1 Elevated waves

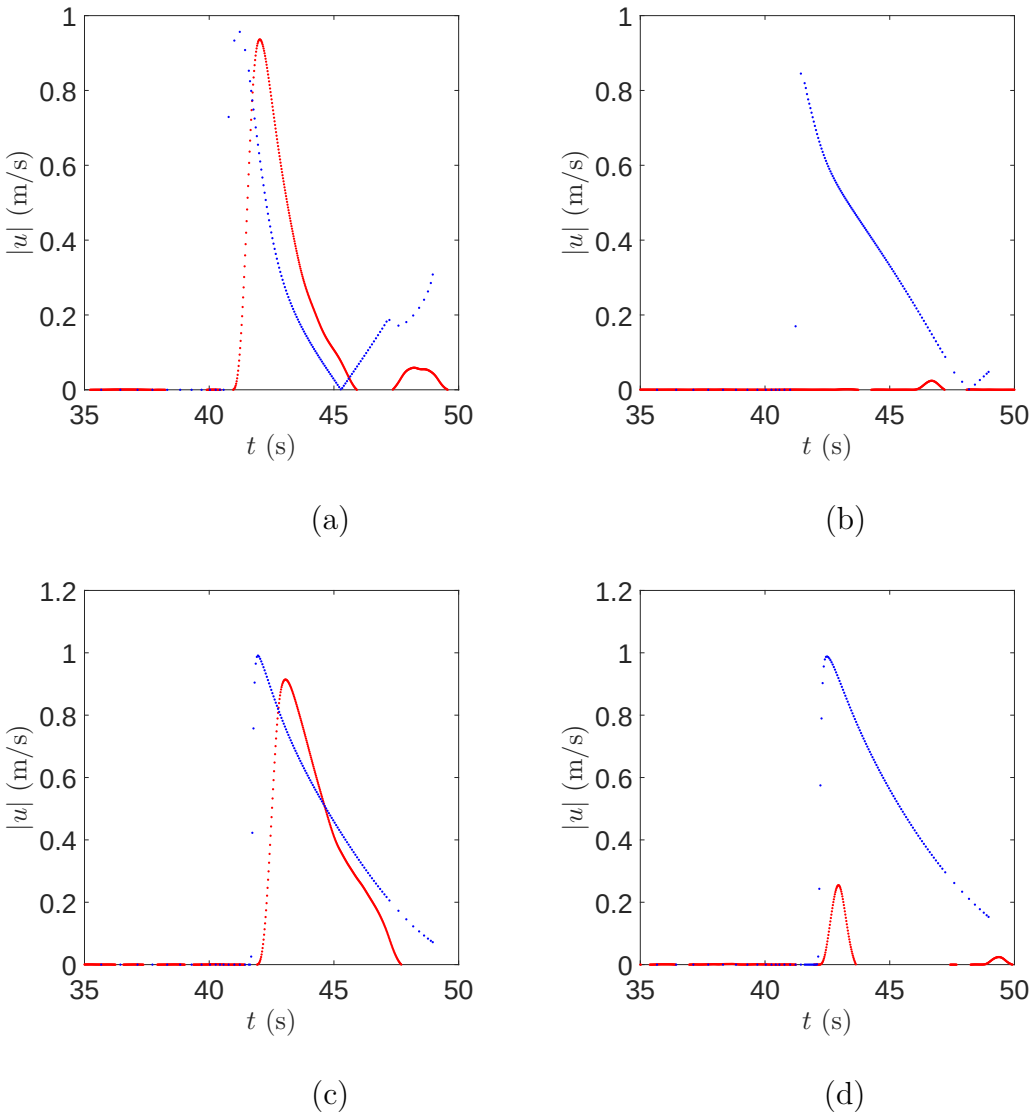

Figure D.21: *Wave 138. Onshore velocities, no building. (a) Velocity at 9.50m, (b) 10.50m, (c) 11.50m, (d) 12.50m from the "Toe". ●, 1D numerical, ●, large-scale experimental.*

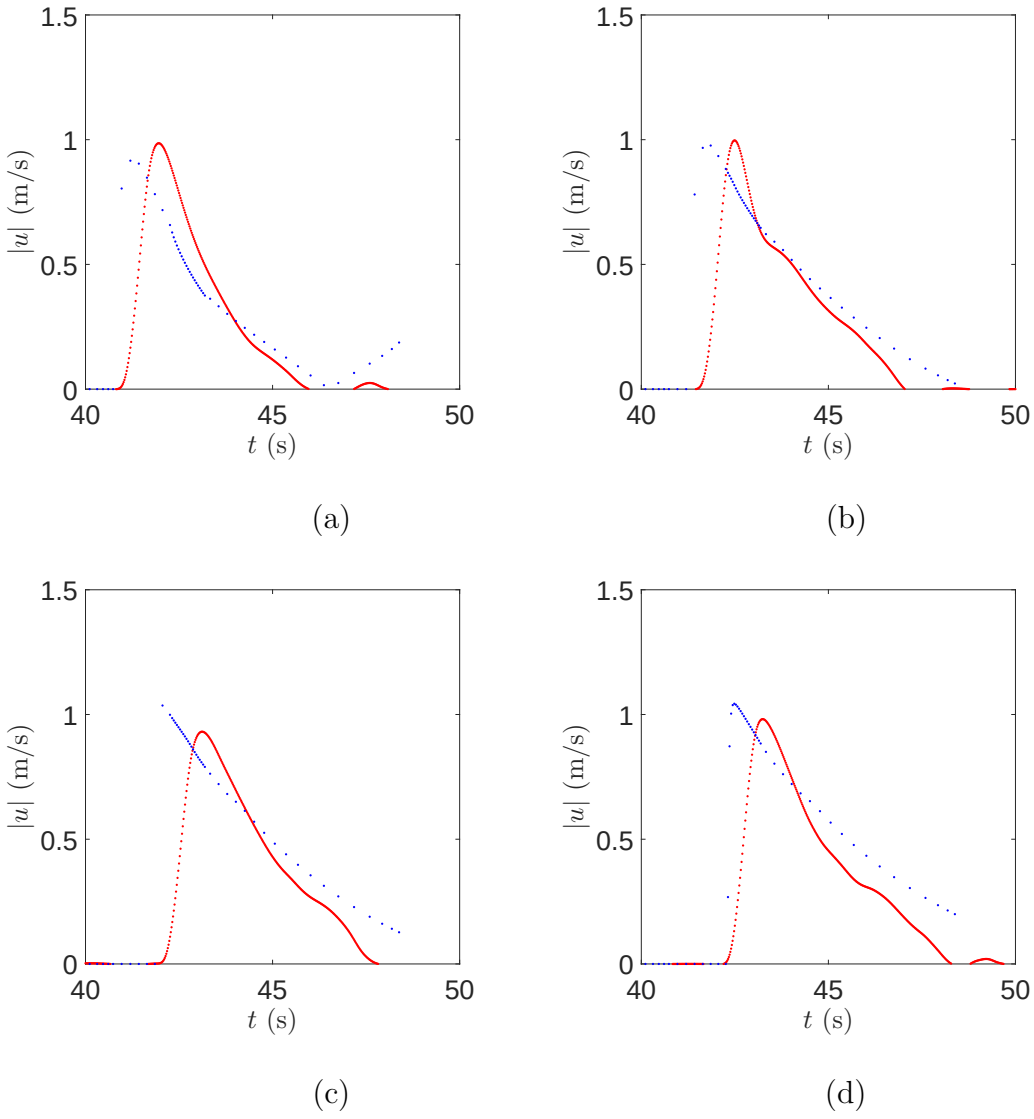

Figure D.22: *Wave 136. Onshore velocities, no building. (a) Velocity at 9.50m, (b) 10.50m, (c) 11.50m, (d) 12.50m from the "Toe". ●, 1D numerical, ●, large-scale experimental.*

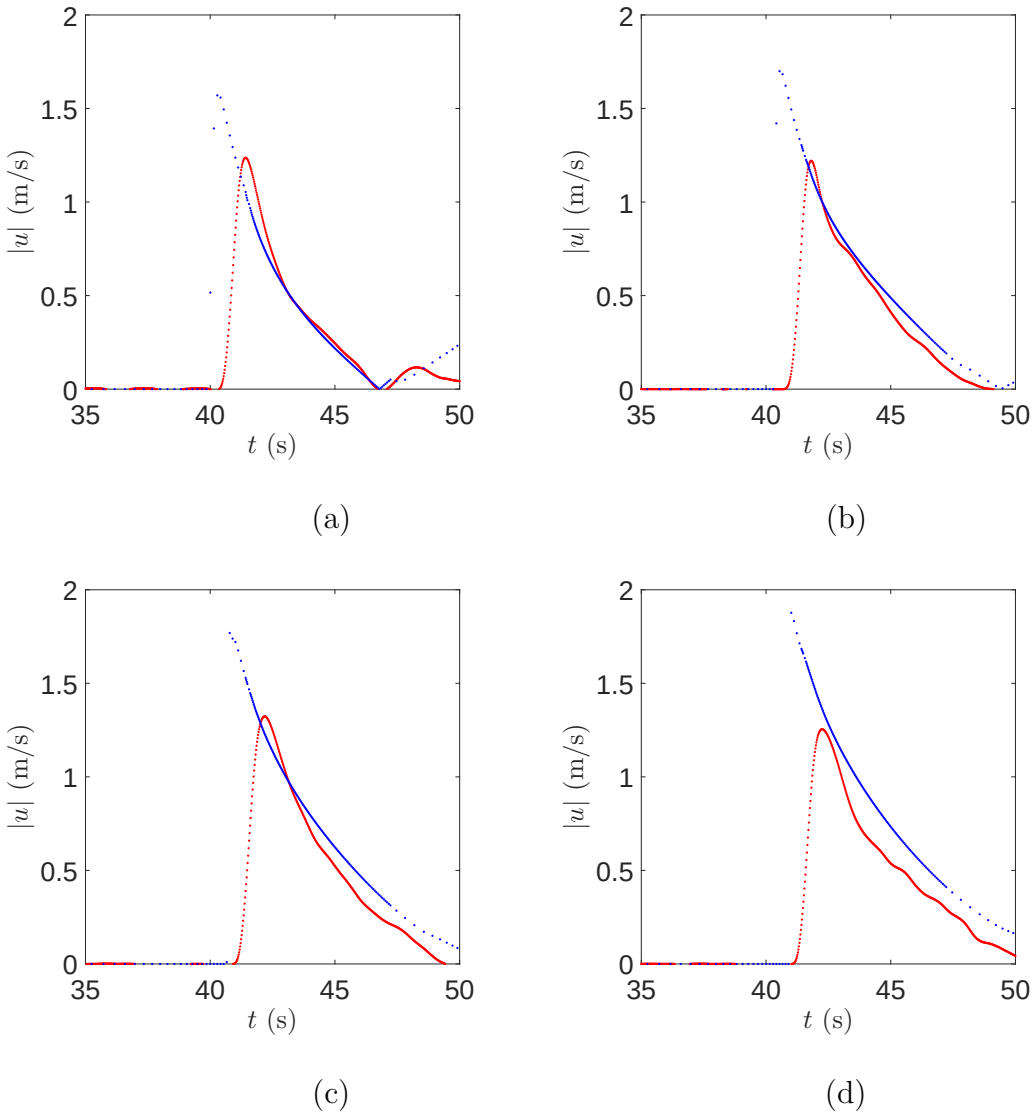

Figure D.23: *Wave 135. Onshore velocities, no building. (a) Velocity at 9.50m, (b) 10.50m, (c) 11.50m, (d) 12.50m from the "Toe". ●, 1D numerical, ●, large-scale experimental.*

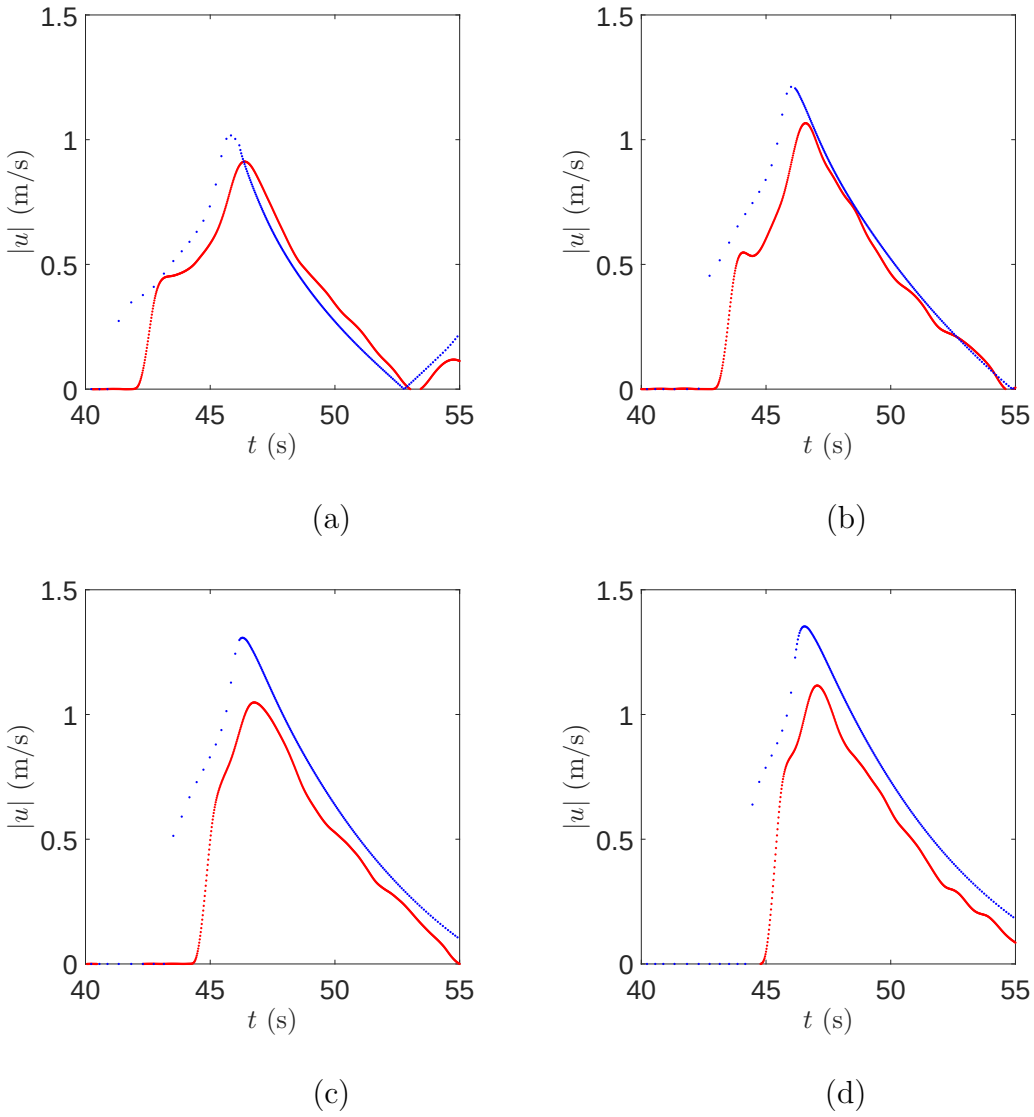

Figure D.24: *Wave 441. Onshore velocities, no building. (a) Velocity at 9.50m, (b) 10.50m, (c) 11.50m, (d) 12.50m from the "Toe". ●, 1D numerical, ●, large-scale experimental.*

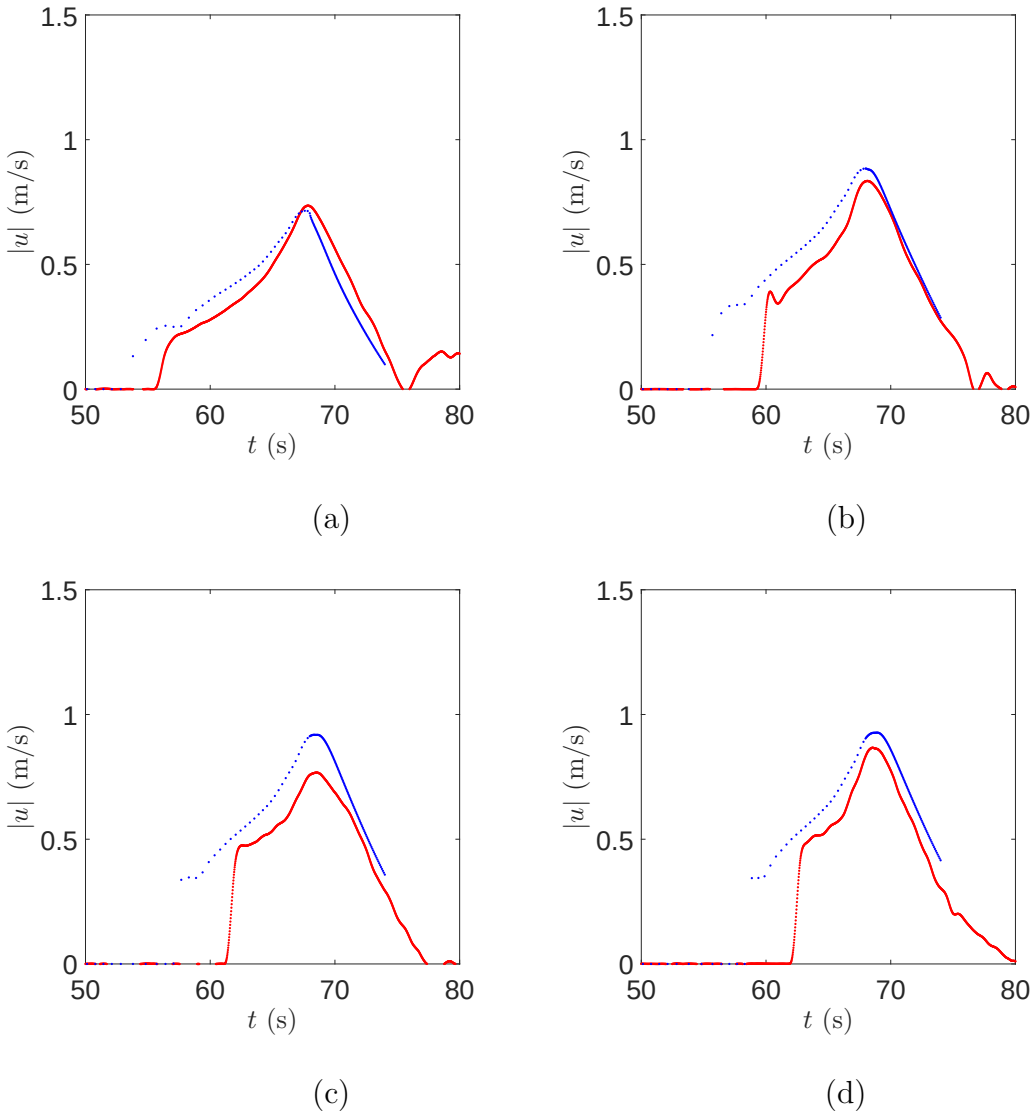

Figure D.25: *Wave 415. Onshore velocities, no building. (a) Velocity at 9.50m, (b) 10.50m, (c) 11.50m, (d) 12.50m from the "Toe". ●, 1D numerical, ●, large-scale experimental.*

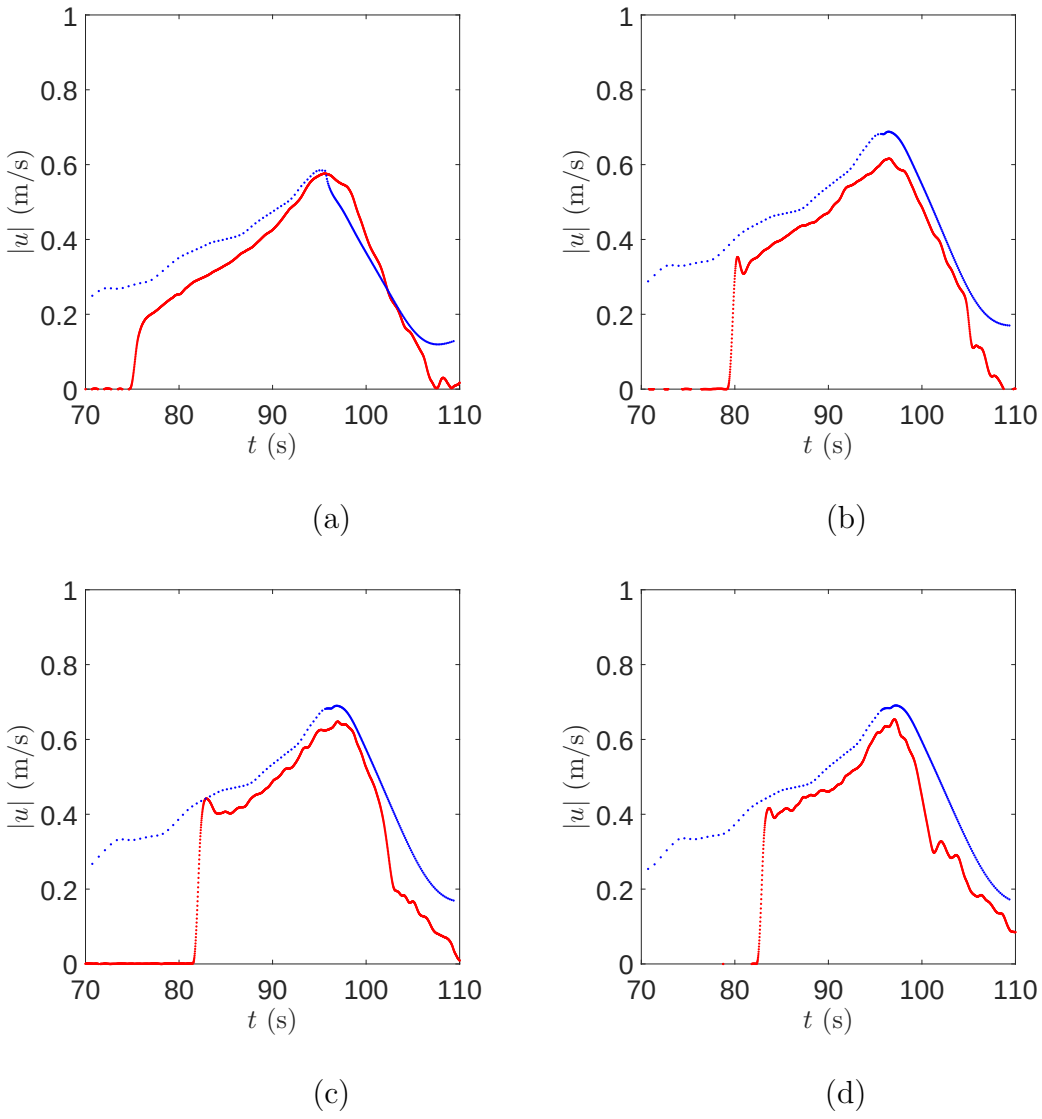

Figure D.26: *Wave 442. Onshore velocities, no building. (a) Velocity at 9.50m, (b) 10.50m, (c) 11.50m, (d) 12.50m from the "Toe". ●, 1D numerical, ●, large-scale experimental.*

D.3.2 N-waves

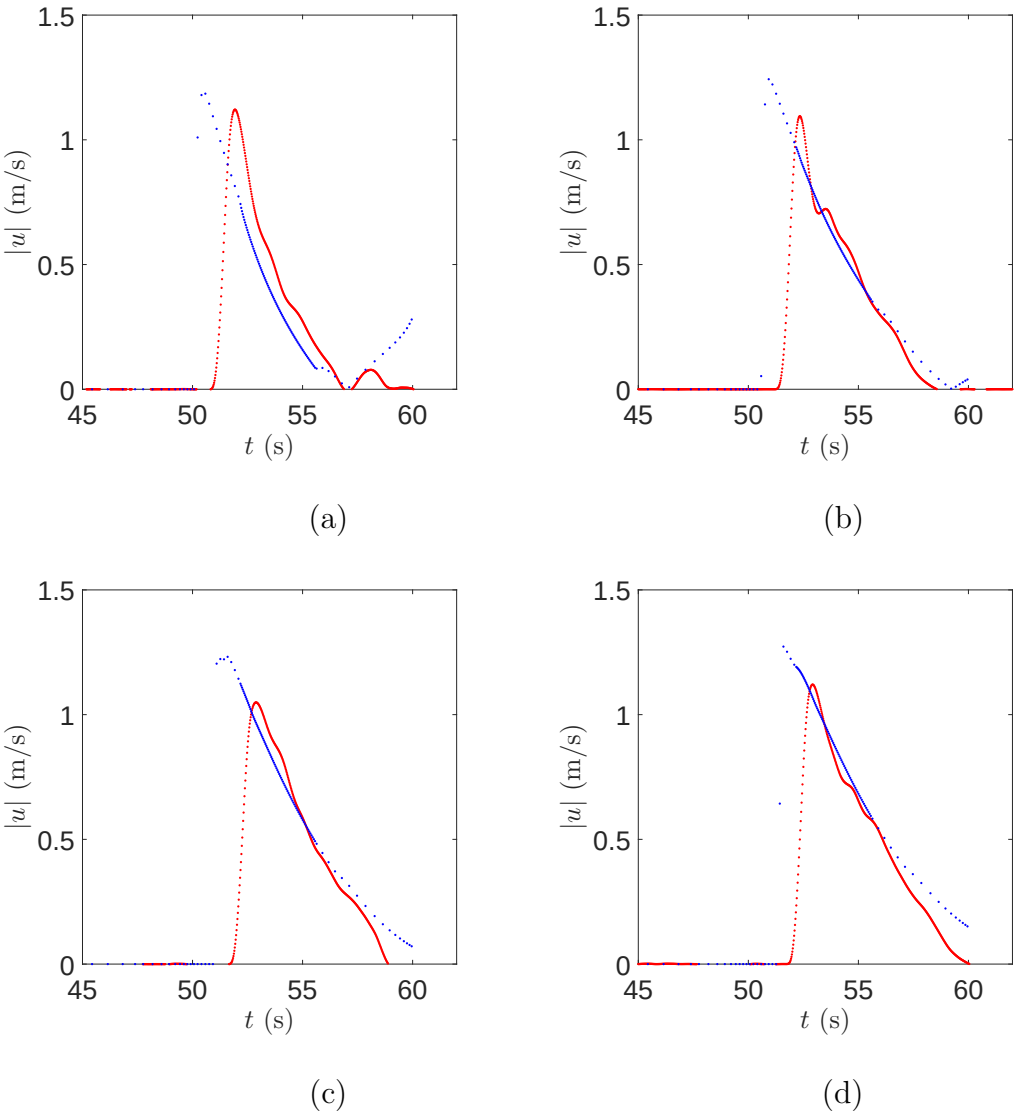

Figure D.27: *Wave 130. Onshore velocities, no building. (a) Velocity at 9.50m, (b) 10.50m, (c) 11.50m, (d) 12.50m from the "Toe". ●, 1D numerical, ●, large-scale experimental.*

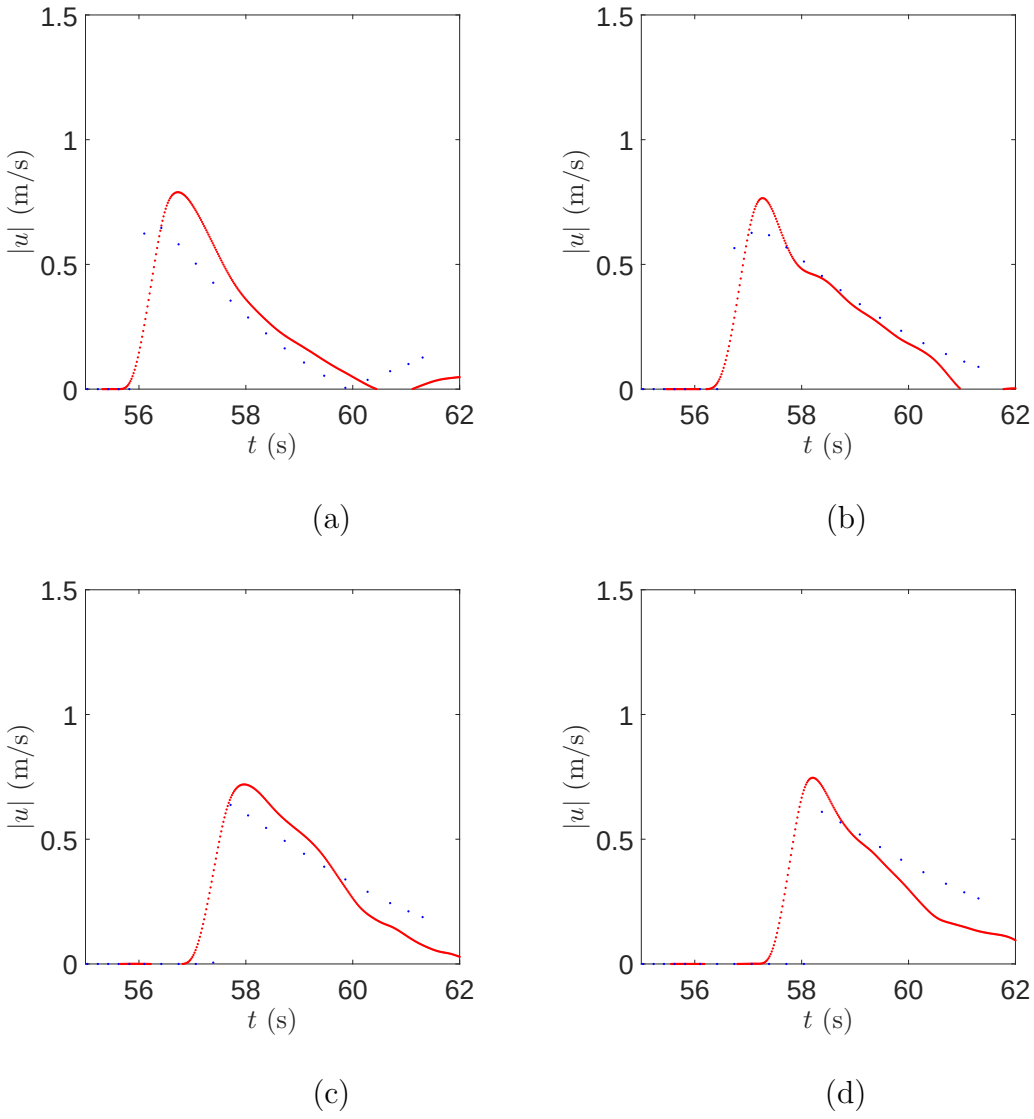

Figure D.28: *Wave 133. Onshore velocities, no building. (a) Velocity at 9.50m, (b) 10.50m, (c) 11.50m, (d) 12.50m from the "Toe". ●, 1D numerical, ●, large-scale experimental.*

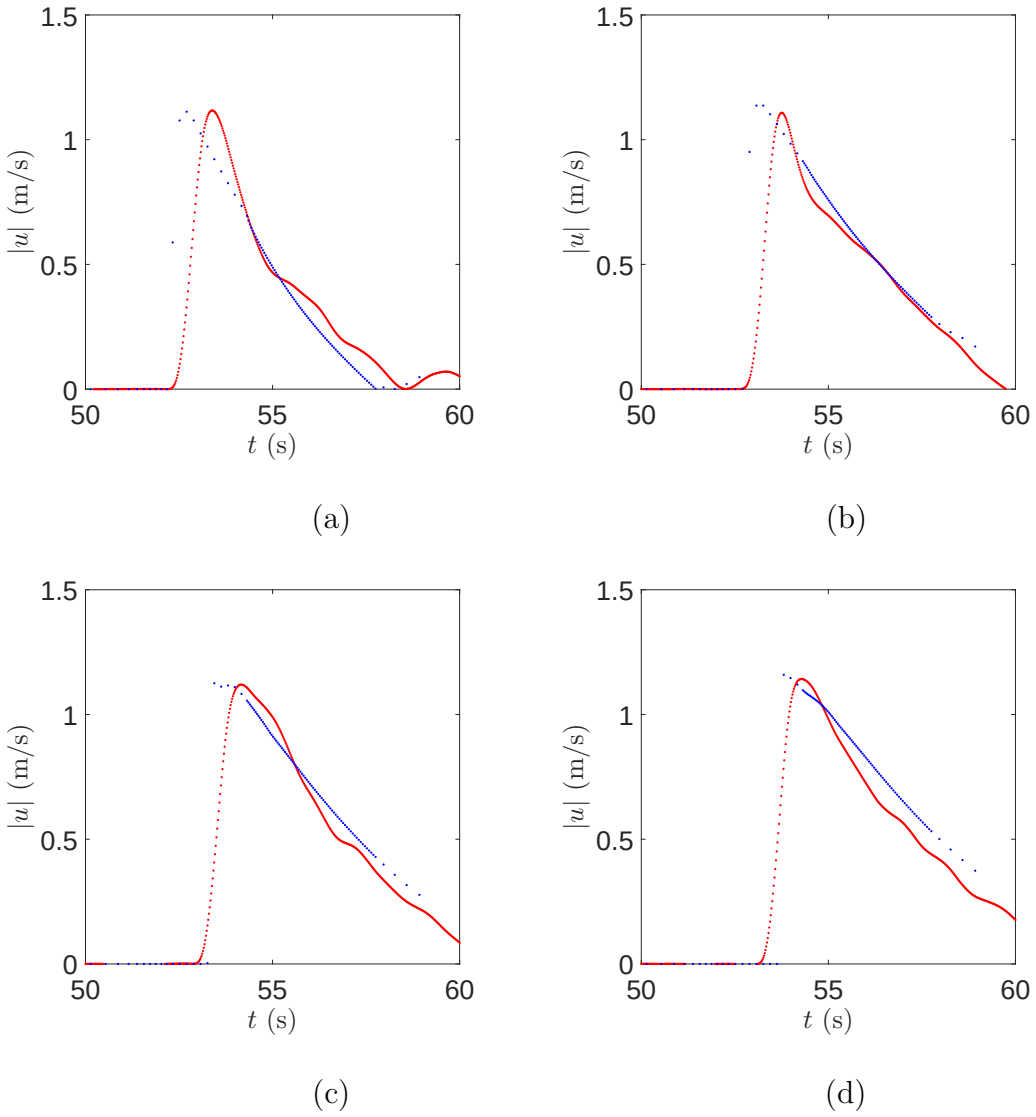

Figure D.29: *Wave 113. Onshore velocities, no building. (a) Velocity at 9.50m, (b) 10.50m, (c) 11.50m, (d) 12.50m from the "Toe". ●, 1D numerical, ●, large-scale experimental.*

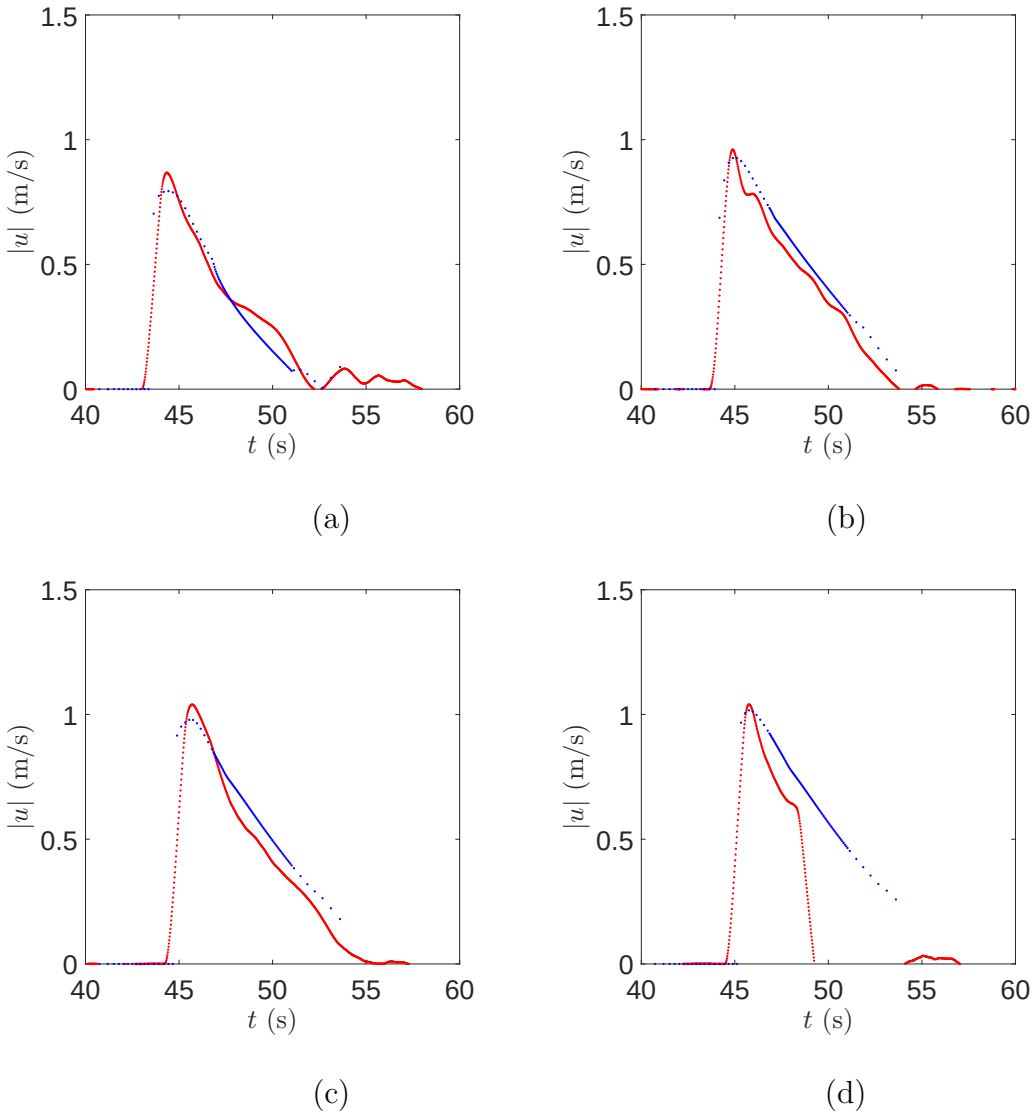

Figure D.30: *Wave 439. Onshore velocities, no building. (a) Velocity at 9.50m, (b) 10.50m, (c) 11.50m, (d) 12.50m from the "Toe". ●, 1D numerical, ●, large-scale experimental.*

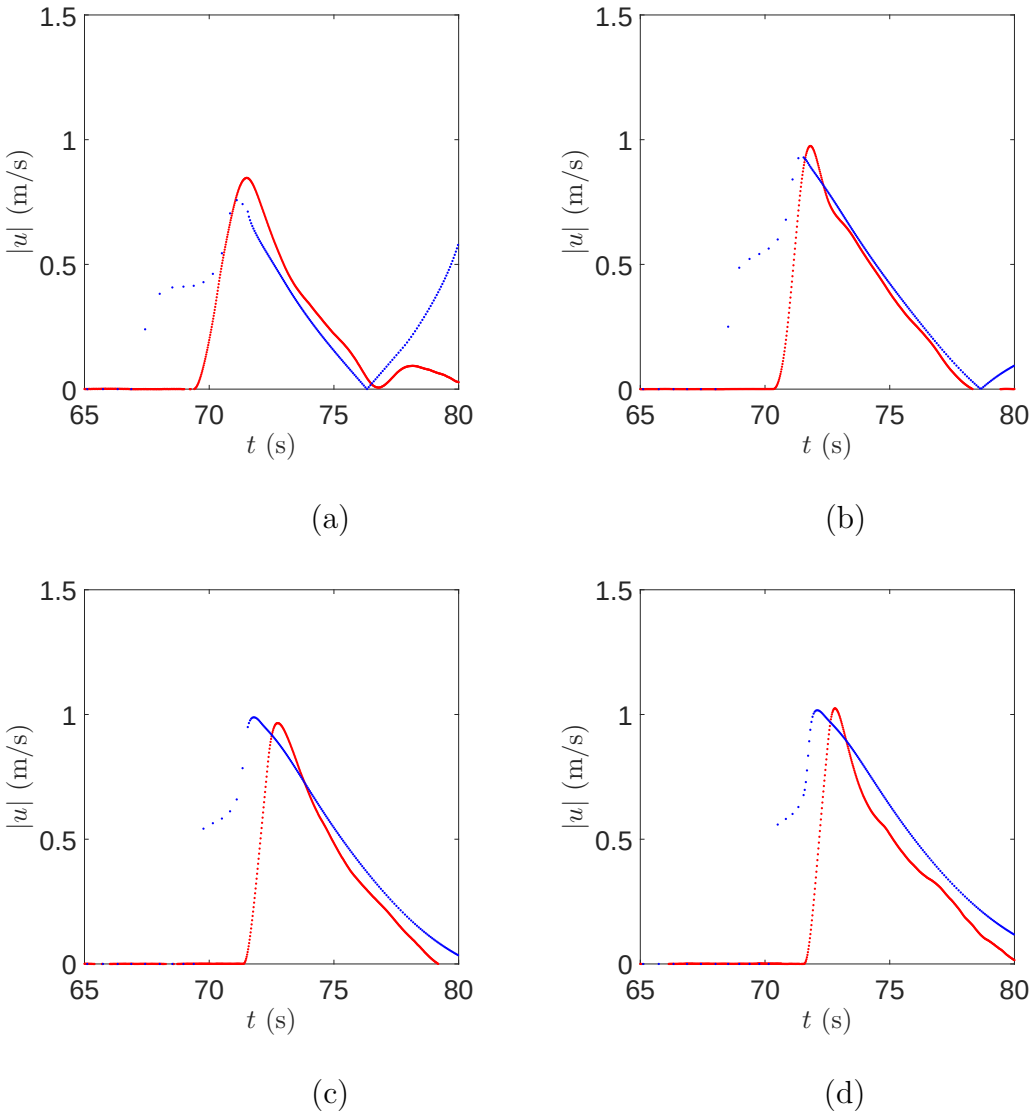

Figure D.31: *Wave 435. Onshore velocities, no building. (a) Velocity at 9.50m, (b) 10.50m, (c) 11.50m, (d) 12.50m from the "Toe". ●, 1D numerical, ●, large-scale experimental.*

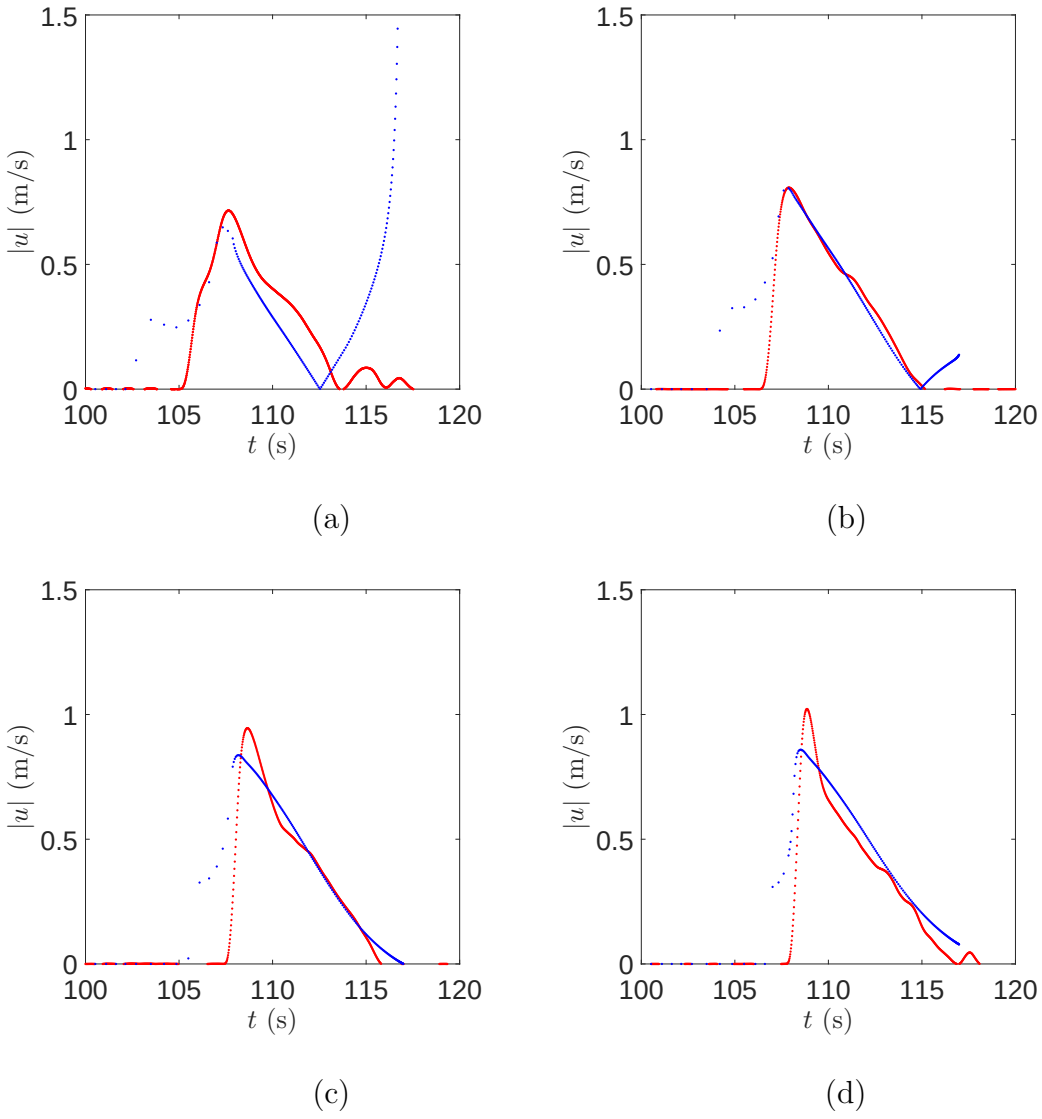

Figure D.32: *Wave 434. Onshore velocities, no building. (a) Velocity at 9.50m, (b) 10.50m, (c) 11.50m, (d) 12.50m from the "Toe". ●, 1D numerical, ●, large-scale experimental.*

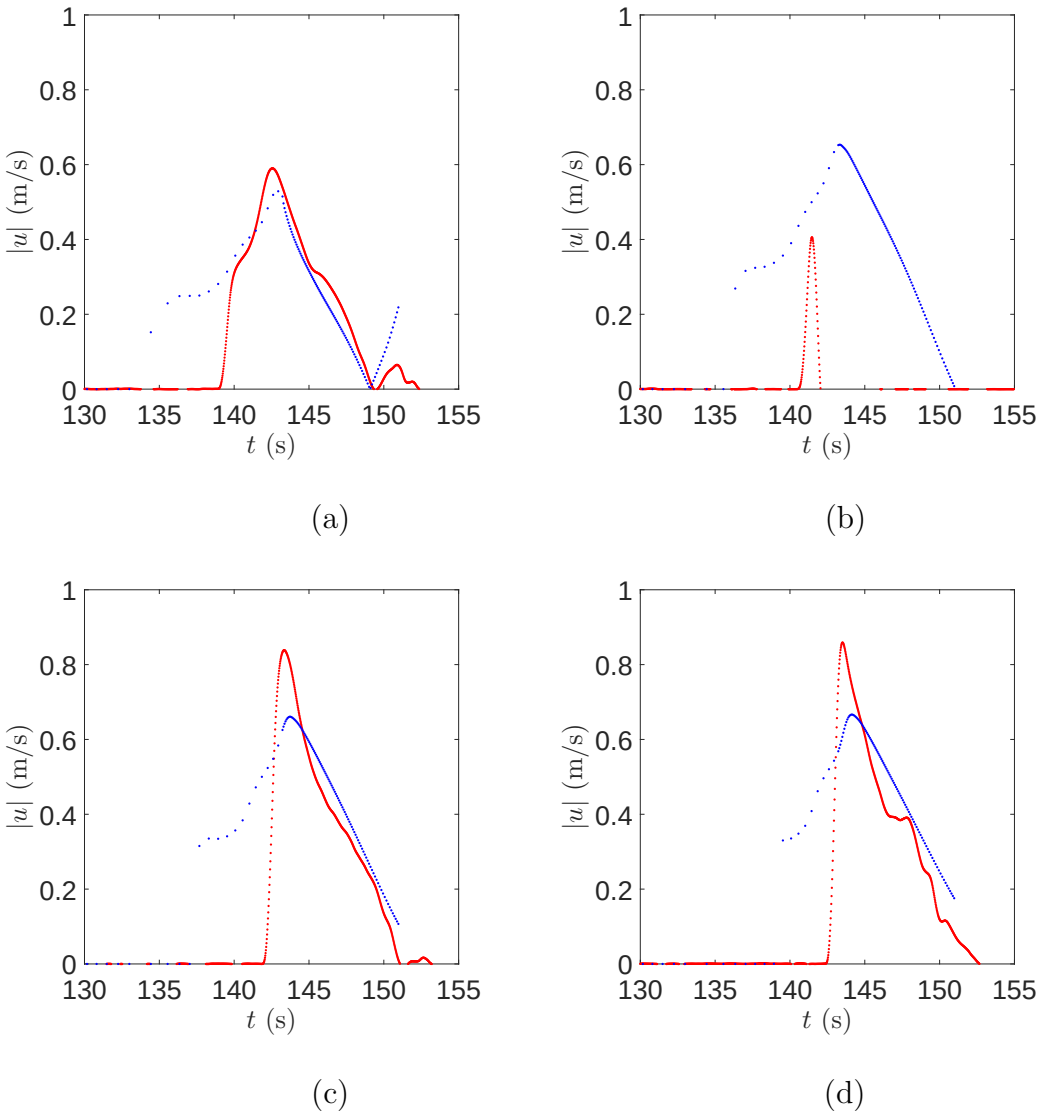

Figure D.33: *Wave 307. Onshore velocities, no building. (a) Velocity at 9.50m, (b) 10.50m, (c) 11.50m, (d) 12.50m from the "Toe". ●, 1D numerical, ●, large-scale experimental.*

D.4 Onshore velocities - around building

D.4.1 Elevated waves

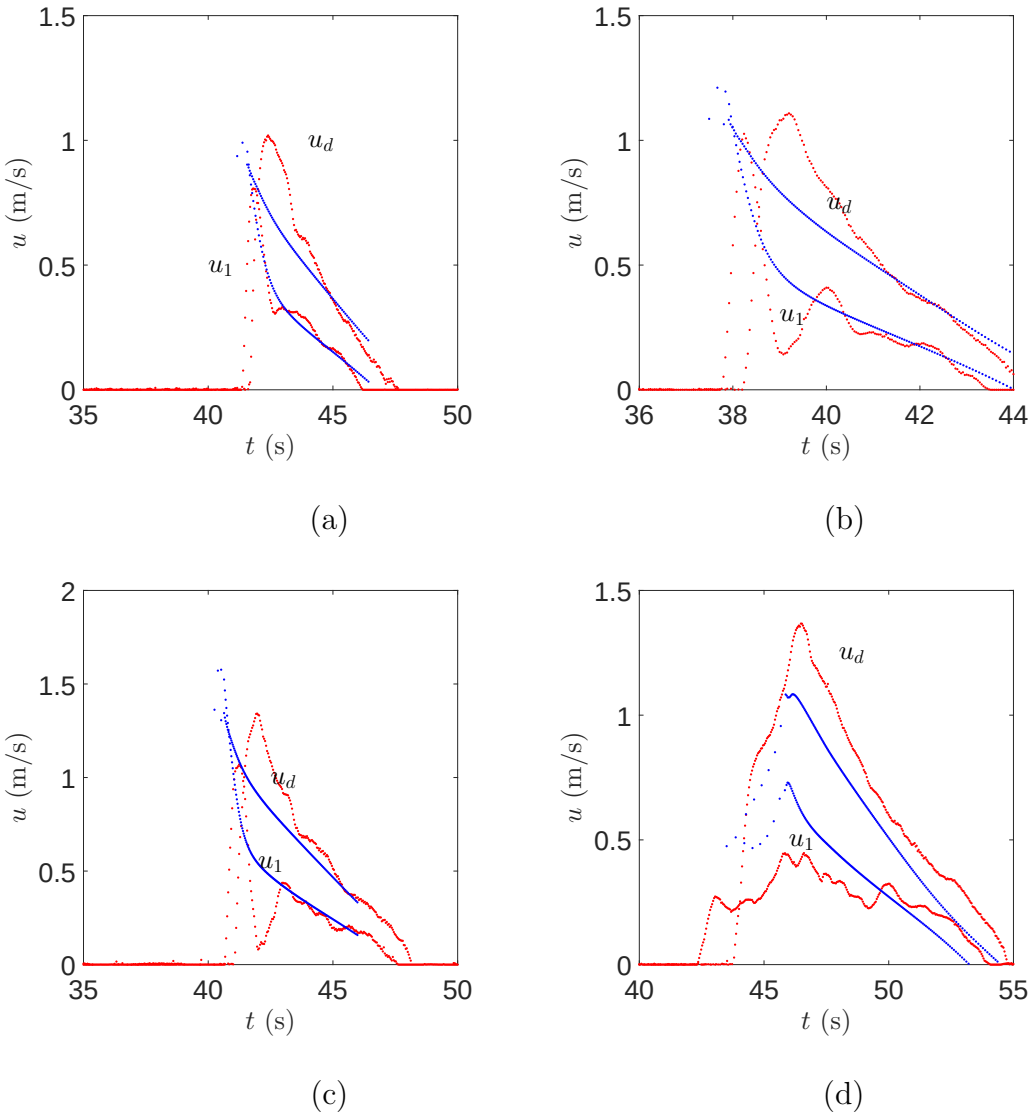

Figure D.34: *Waves 138, 136, 135 and 441. Onshore velocities, around building. (a) Wave 138, (b) Wave 136, (c) Wave 135, (d) Wave 441.* ●, *1D numerical,* ●, *large-scale experimental.*

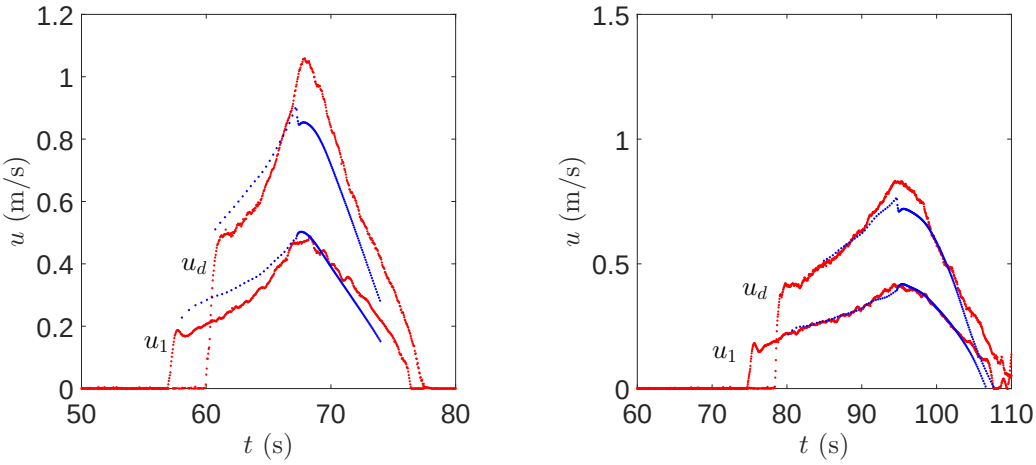

(a) (b)

Figure D.35: *Waves 415, 442. Onshore velocities, around building. (a) Wave 415, (b) Wave 442.* ●*, 1D numerical,* ●*, large-scale experimental.*

D.4.2 N-waves

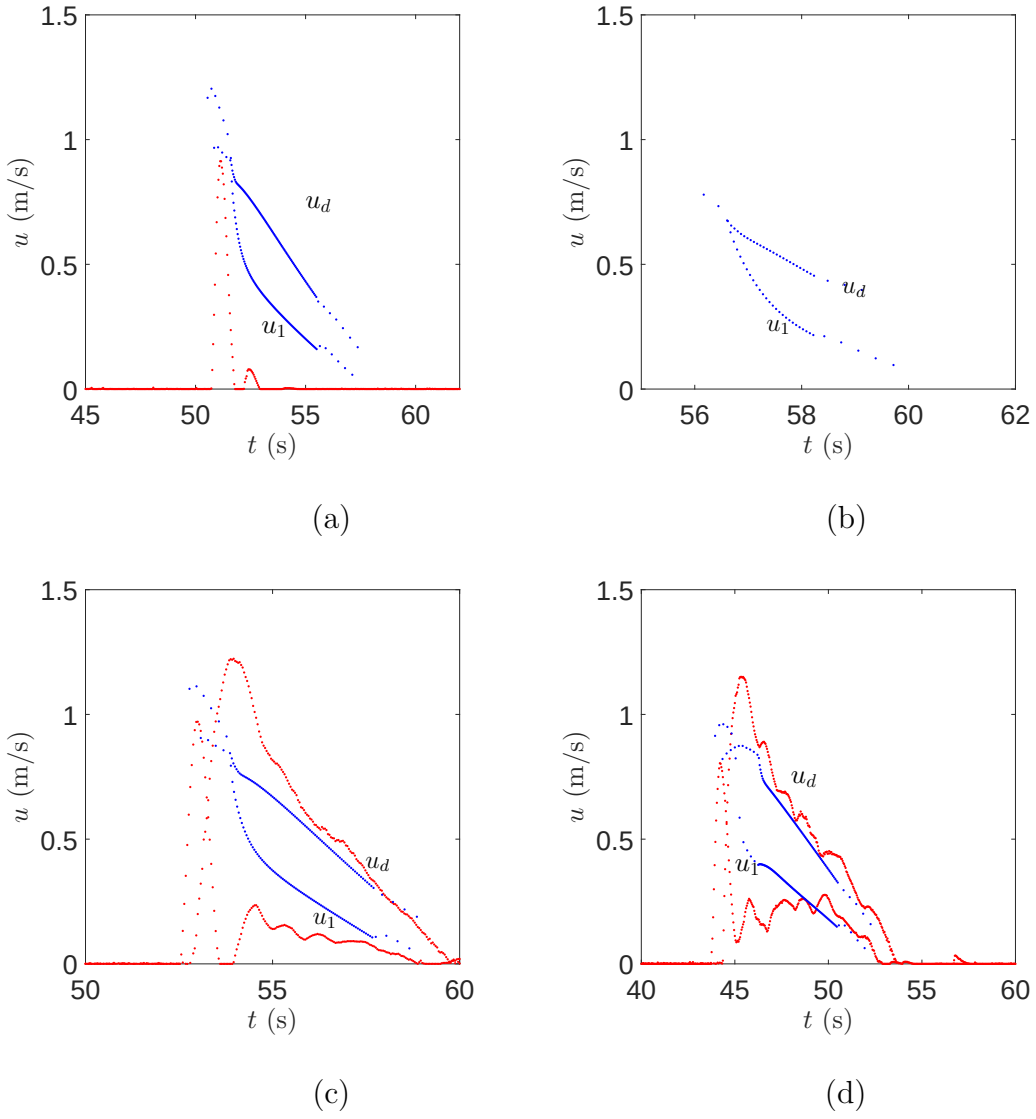

Figure D.36: *Waves 130, 133, 113 and 439. Onshore velocities, around building. (a) Wave 130 (missing rear velocity measurement due to clogging), (b) Wave 133 (missing front and rear velocity measurement due to clogging), (c) Wave 113, (d) Wave 439.* ●*, 1D numerical,* ●*, large-scale experimental.*

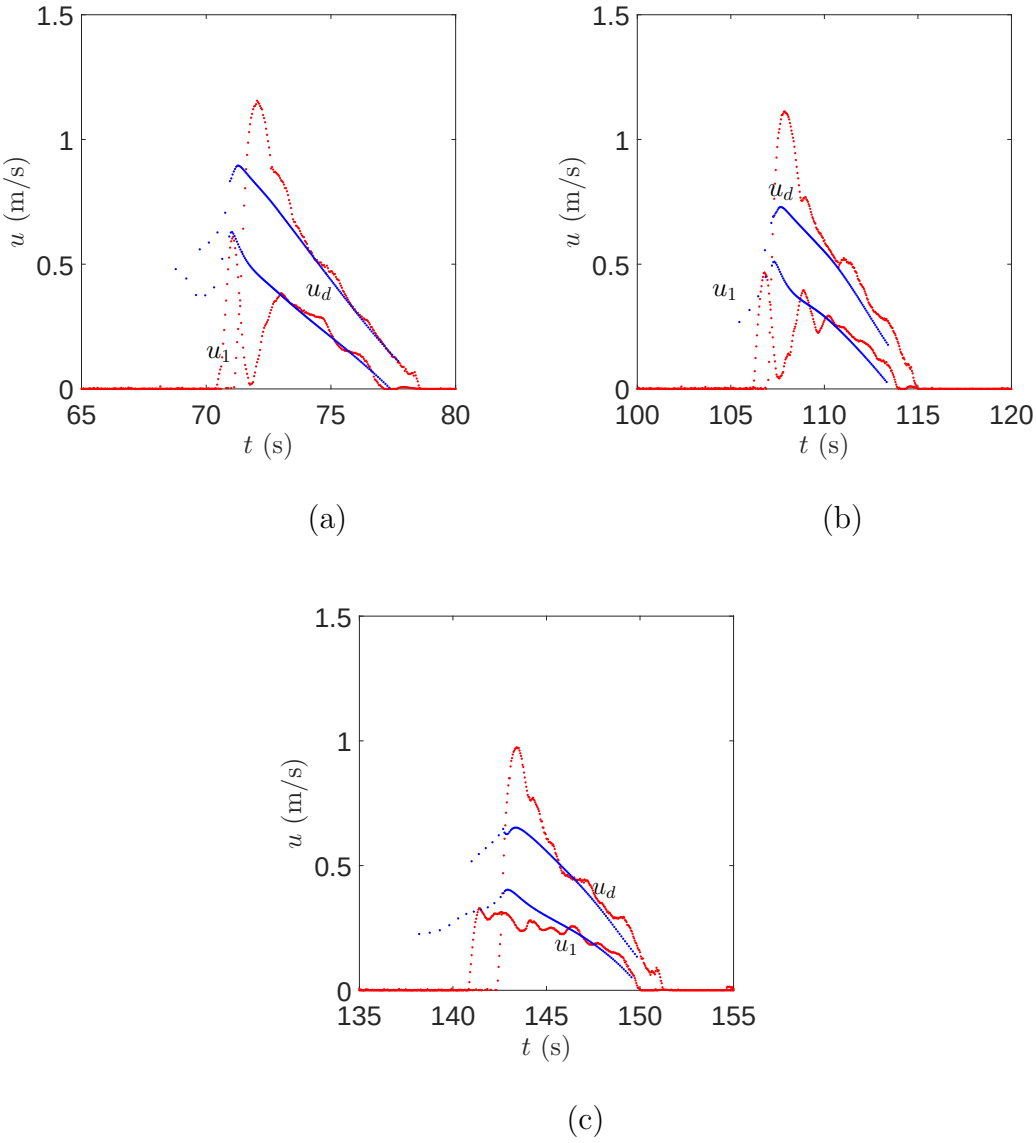

Figure D.37: *Waves 435, 434 and 307. Onshore velocities, around building. (a) Wave 435, (b) Wave 434, (c) Wave 307.* ●*, 1D numerical,* ●*, large-scale experimental.*

D.5 Front-face water level and integrated pressure distribution (force)

D.5.1 Elevated waves

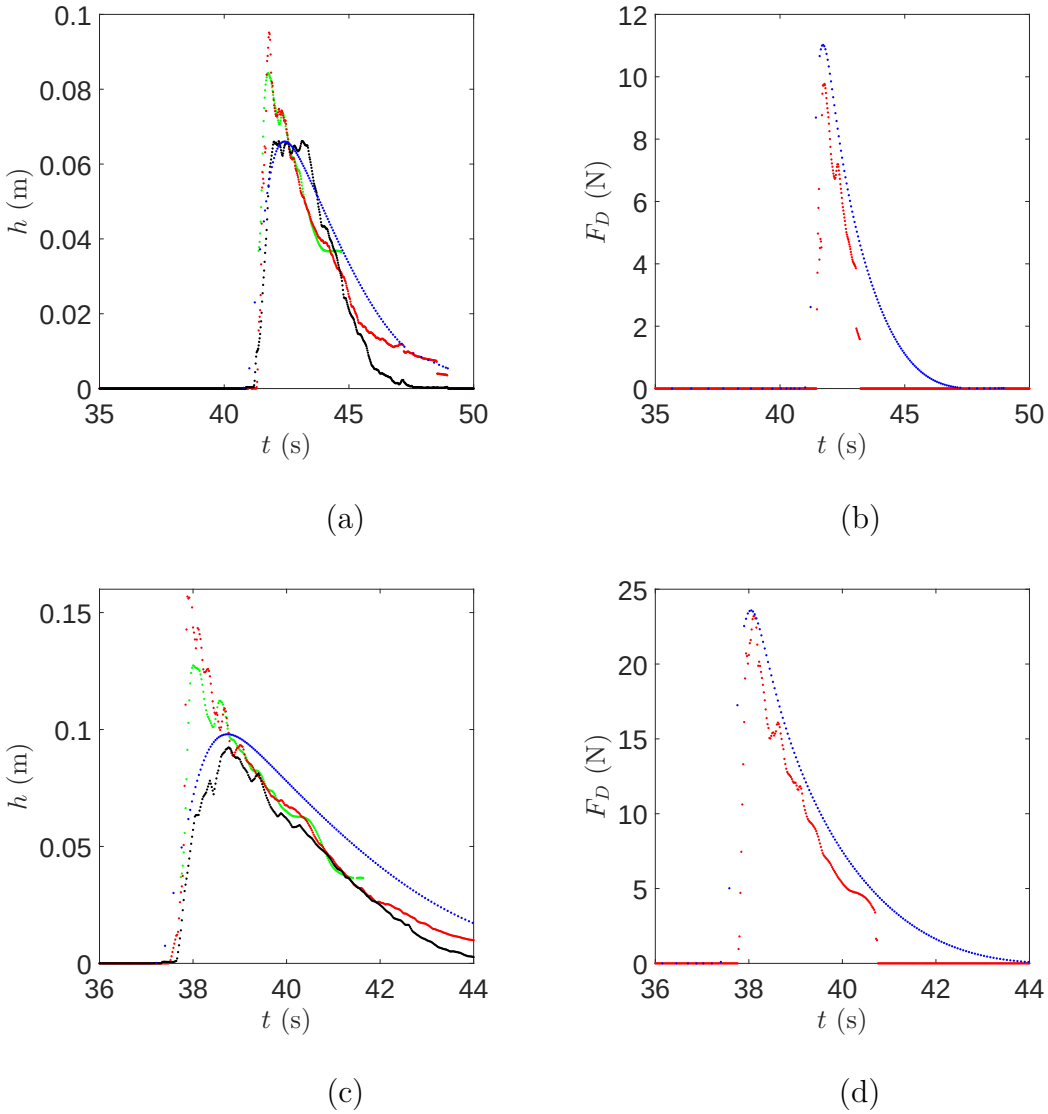

Figure D.38: *Waves 138 and 136. Front water level and integrated pressure distribution. (a) Front water level Wave 138, (b) Integrated pressure distribution Wave 138, (c) Front water level Wave 136, (d) Integrated pressure distribution Wave 136.* ●*, 1D numerical,* ●*, large-scale experimental.* ●*, height from images 10cm in front of building,* ●*, front face pressure transducer measurement (36mm off the bed).*

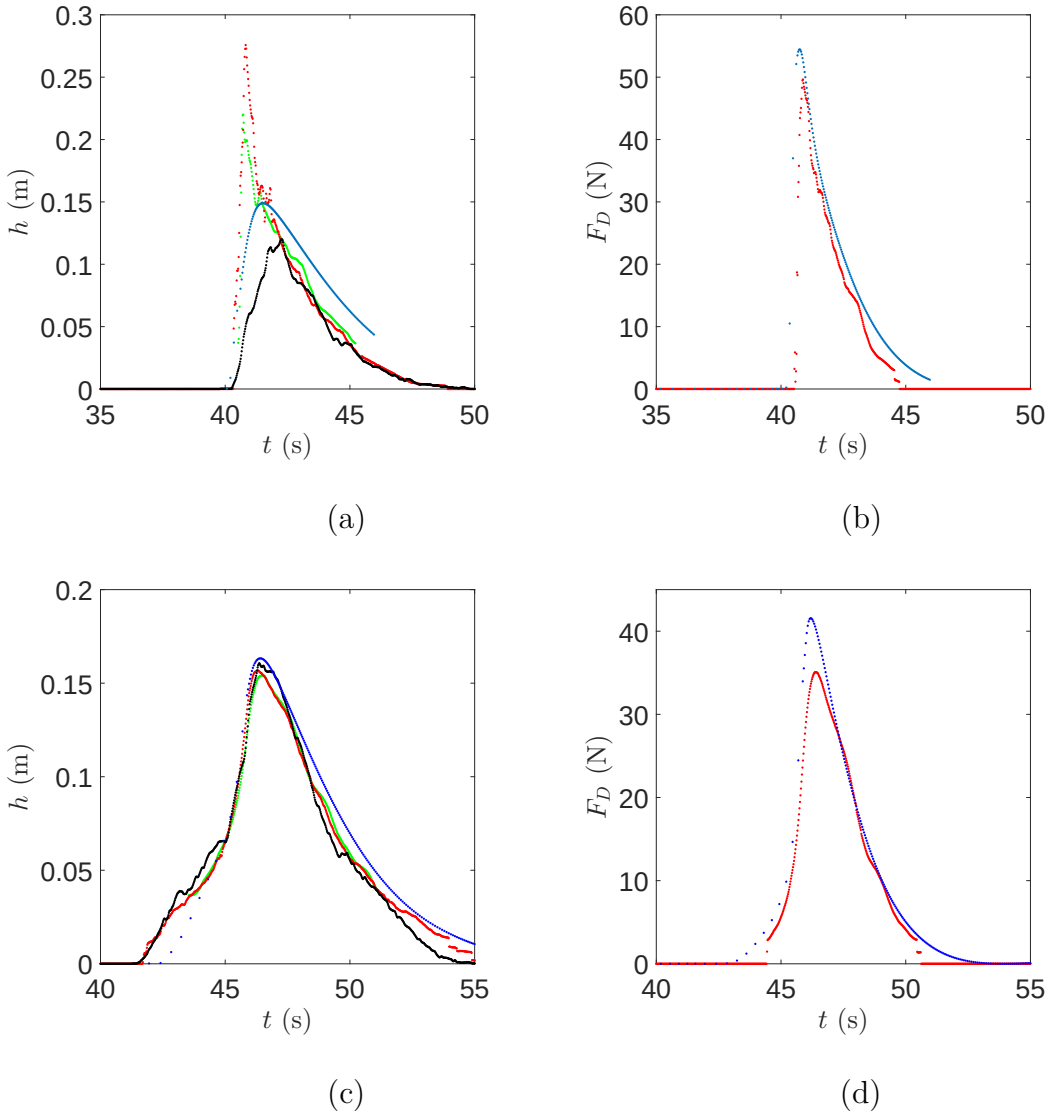

Figure D.39: *Waves 135 and 441. Front water level and integrated pressure distribution. (a) Front water level Wave 138, (b) Integrated pressure distribution Wave 138, (c) Front water level Wave 441, (d) Integrated pressure distribution Wave 441.* ●*, 1D numerical,* ●*, large-scale experimental.* ●*, height from images 10cm in front of building,* ●*, front face pressure transducer measurement (36mm off the bed).*

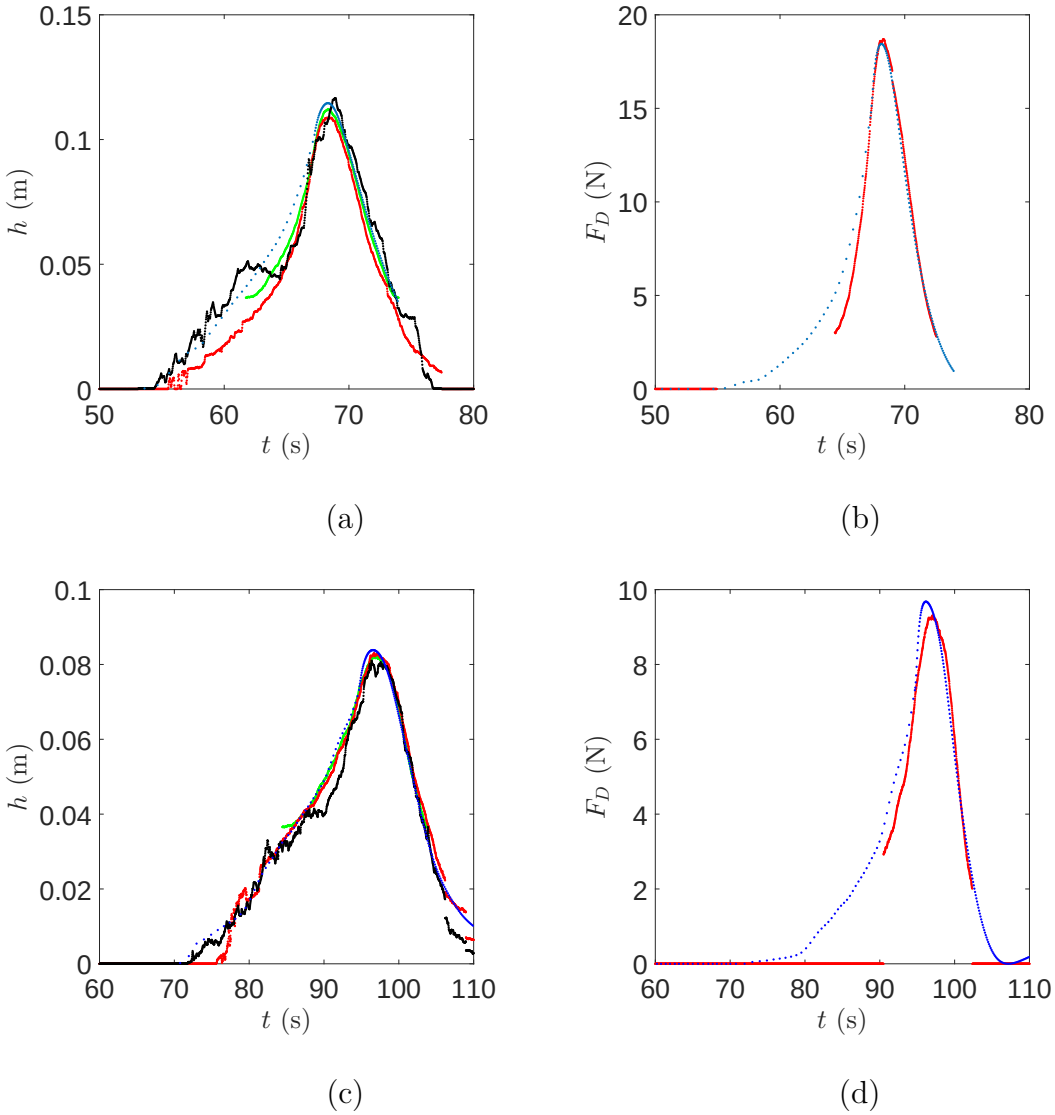

Figure D.40: *Waves 415 and 442. Front water level and integrated pressure distribution. (a) Front water level Wave 415, (b) Integrated pressure distribution Wave 415, (c) Front water level Wave 442, (d) Integrated pressure distribution Wave 442.* •, *1D numerical,* •, *large-scale experimental.* •, *height from images 10cm in front of building,* •, *front face pressure transducer measurement (36mm off the bed).*

D.5.2 N-waves

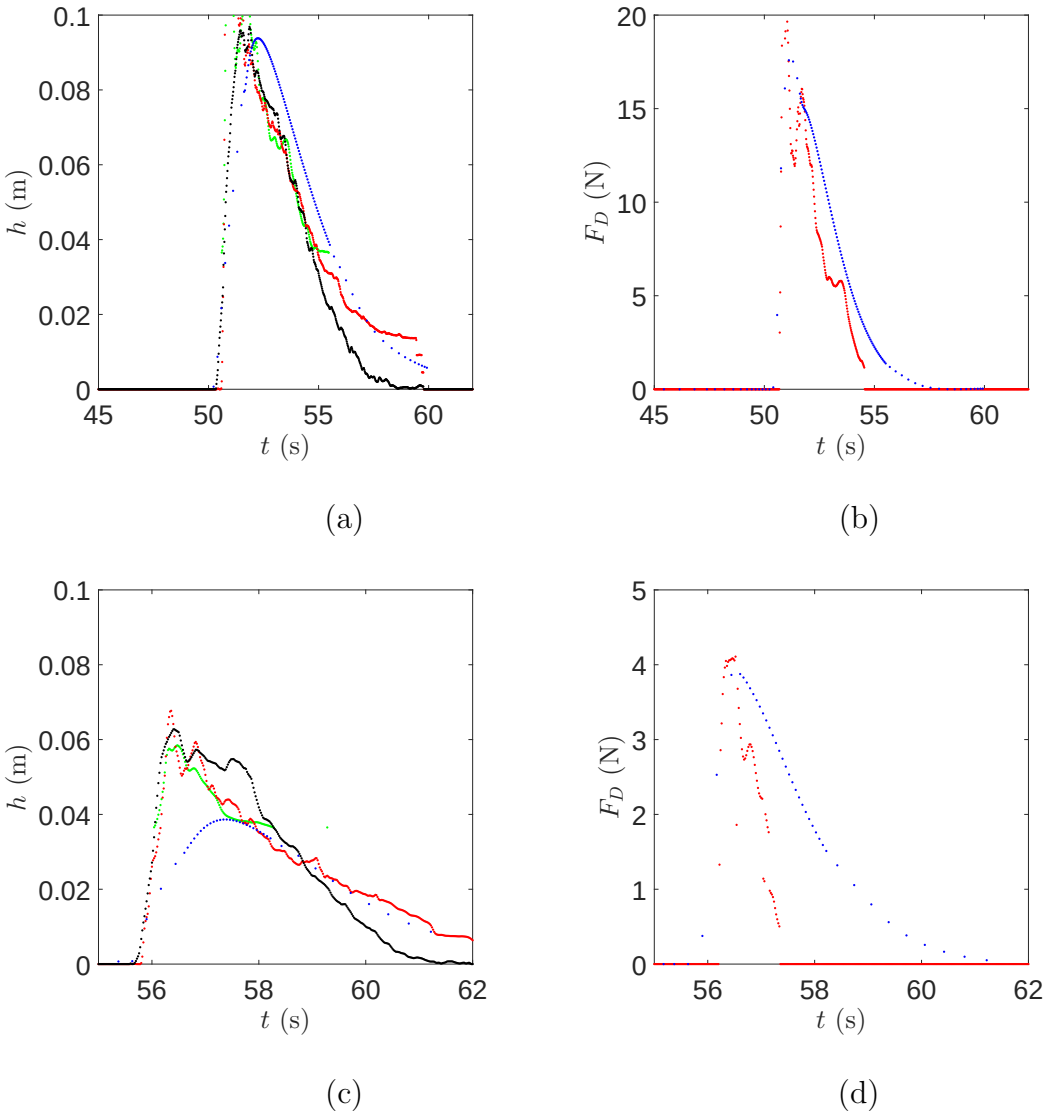

Figure D.41: *Waves 130 and 133. Front water level and integrated pressure distribution. (a) Front water level Wave 130, (b) Integrated pressure distribution Wave 130, (c) Front water level Wave 133, (d) Integrated pressure distribution Wave 133.* ●*, 1D numerical,* ●*, large-scale experimental.* ●*, height from images 10cm in front of building,* ●*, front face pressure transducer measurement (36mm off the bed).*

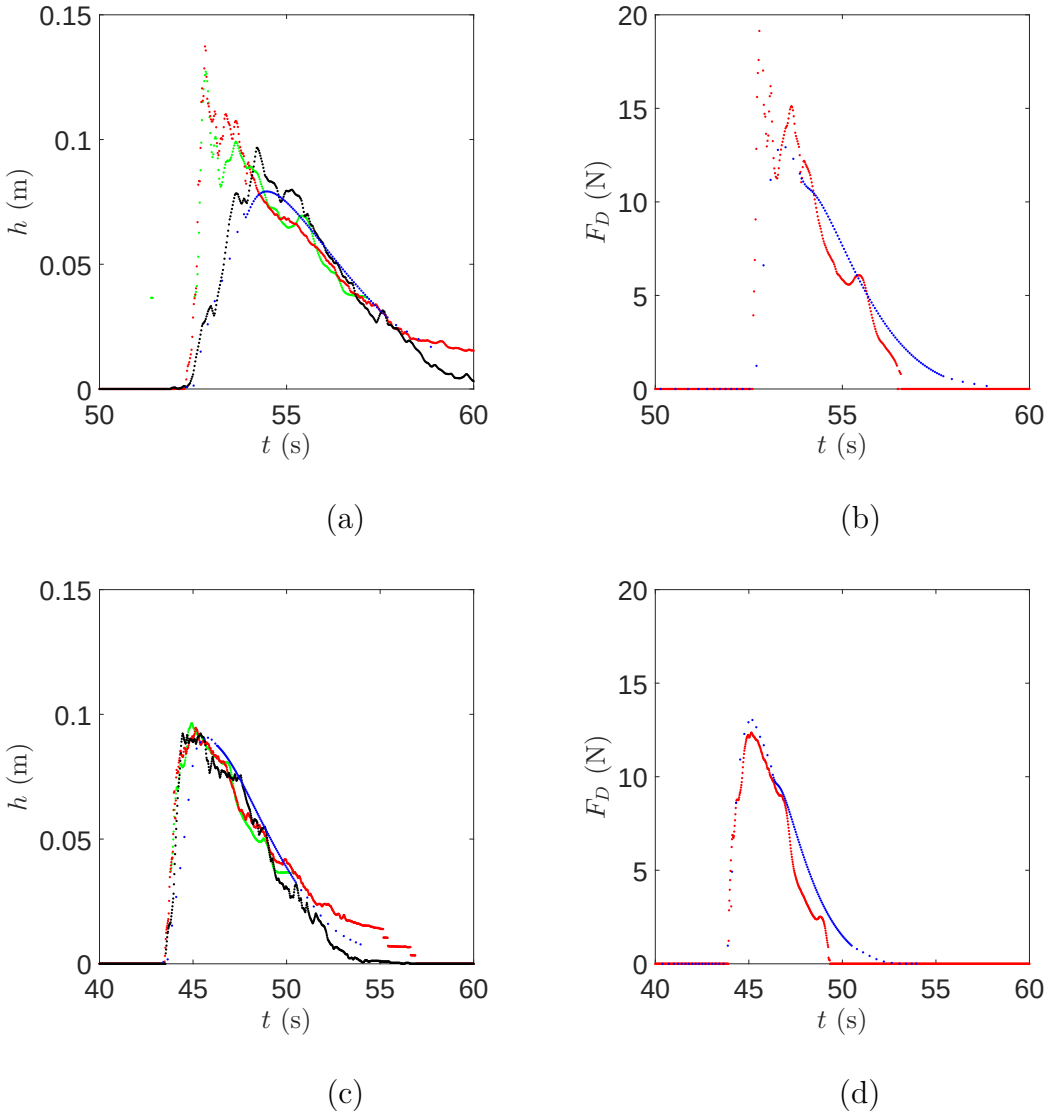

Figure D.42: *Waves 113 and 439. Front water level and integrated pressure distribution. (a) Front water level Wave 113, (b) Integrated pressure distribution Wave 113, (c) Front water level Wave 439, (d) Integrated pressure distribution Wave 439.* ●*, 1D numerical,* ●*, large-scale experimental.* ●*, height from images 10cm in front of building,* ●*, front face pressure transducer measurement (36mm off the bed).*

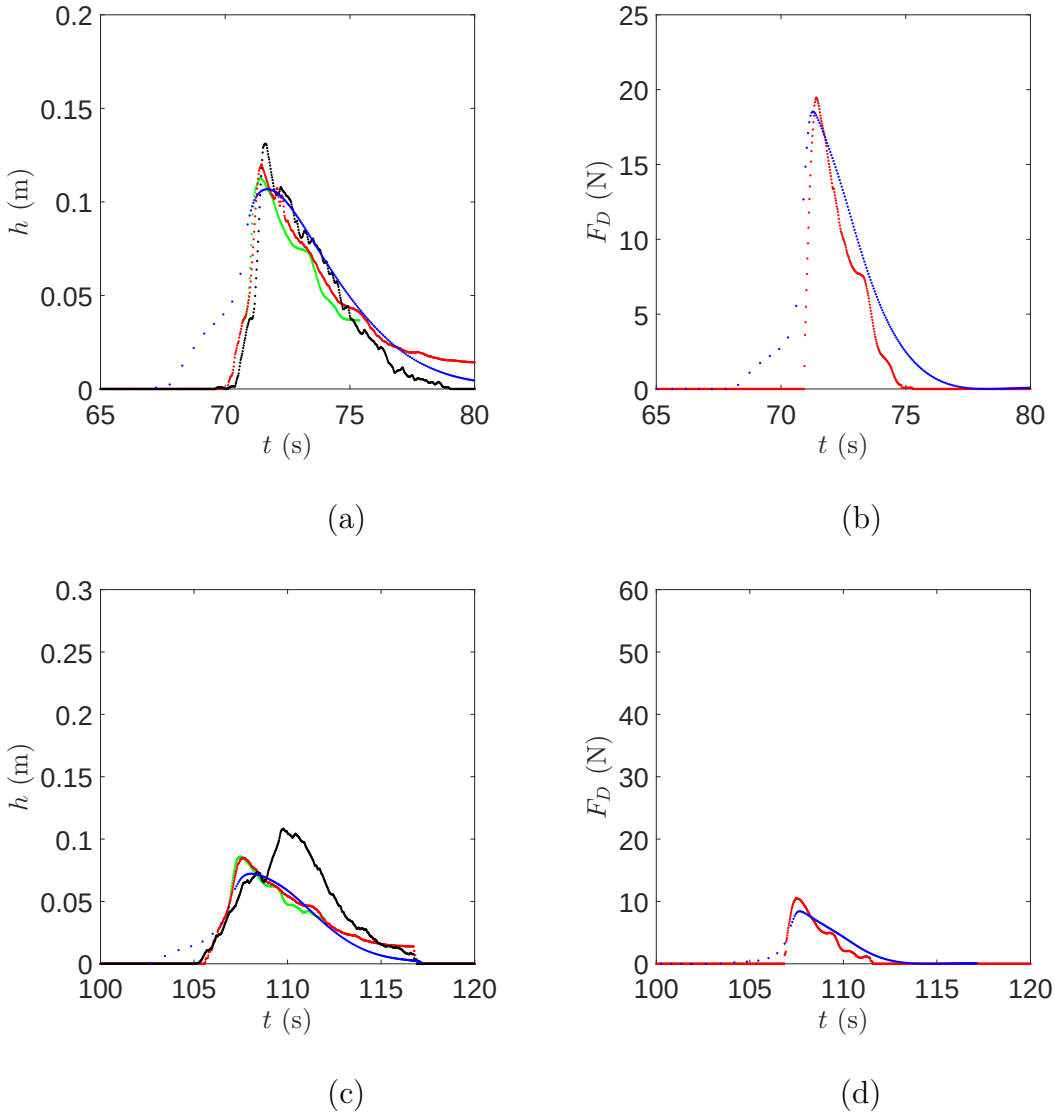

Figure D.43: *Waves 435 and 434. Front water level and integrated pressure distribution. (a) Front water level Wave 435, (b) Integrated pressure distribution Wave 435, (c) Front water level Wave 434, (d) Integrated pressure distribution Wave 434.* ●*, 1D numerical,* ●*, large-scale experimental.* ●*, height from images 10cm in front of building,* ●*, front face pressure transducer measurement (36mm off the bed).*

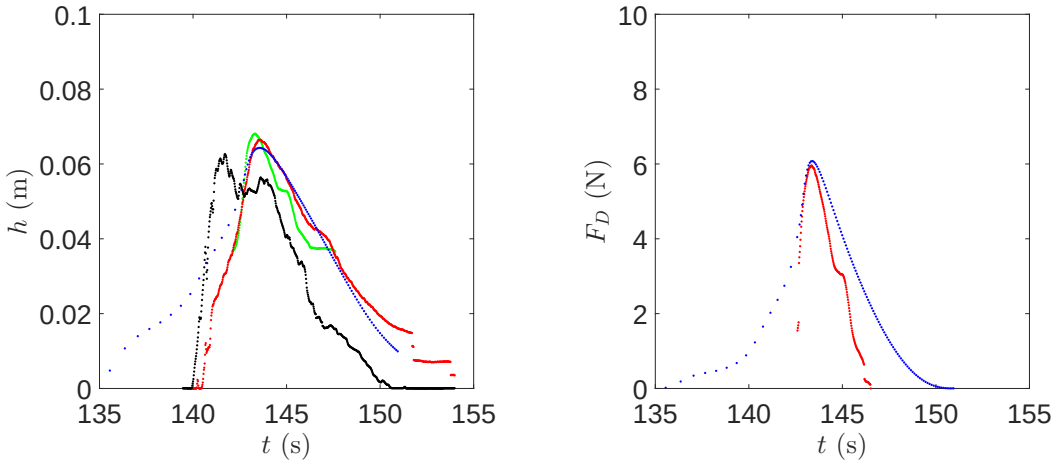

Figure D.44: *Waves 307. Front water level and integrated pressure distribution. (a) Front water level Wave 307, (b) Integrated pressure distribution Wave 307.* ●*, 1D numerical,* ●*, large-scale experimental.* ●*, height from images 10cm in front of building,* ●*, front face pressure transducer measurement (36mm off the bed).*

Appendix E

Uncertainties in instrument measurements

Table E.1: *Instrument uncertainties from the steady experiments.*

Quantity	Unit	Uncertainty	Percentage
h_1, h_2, h_d from light attenuation	mm	±2 shallow, ±6 (deep)	±2%
h_1, h_2, h_d from side wall orthorectification	mm	±2 (all)	±2%
h_i from measuring rule	mm	± 0.5	±0.5%
Q (dependent on u and h_1)	m^3s^{-1}		±2%
u from propeller meter	cms^{-1}	±2	±2%
F from mass calibration and strain gauge tolerances and accuracy of g	$kgms^{-}2$	±¡0.1	±0.25%

For combined quantities the standard error is used to derive overall uncertainties.

Table E.2: *Instrument uncertainties from the unsteady experiments.*

Quantity	Unit	Uncertainty	Percentage
h from wave probes	mm	± 0.5	$\pm$¡1%
h_1, h_2, h_d from orthorectification and image processing	mm	± 1	$\pm 1\%$
p from transducers	Pa	± 2.5	$\pm 0.25\%$
u from propeller meter	cms^{-1}	± 2	$\pm 2\%$
F from combined h_1& p data	kgms$^-$2	± 0.2	$\pm 2\%$